THE TECTONIC EVOLUTION OF THE CORE OF THE HIMALAYA, LANGTANG NATIONAL PARK, CENTRAL NEPAL

by

ALLISON MARGARET MACFARLANE

B.Sc. University of Rochester
(1986)

Submitted to the Department of
Earth, Atmospheric and Planetary Sciences
in Partial Fulfillment of the Requirements
for the Degree of

DOCTOR OF PHILOSOPHY

at the MASSACHUSETTS INSTITUTE OF TECHNOLOGY

May, 1992

Signature of Author_____
Department of Earth, Atmospheric and Planetary Sciences
May, 1992

Certified by_____
Kip V. Hodges
Supervisor

Accepted by_____
Thomas H. Jordan
Department Head

The Tectonic Evolution of the Core of the Himalaya Langtang National Park, Central Nepal

by

Allison Margaret Macfarlane

Submitted to the Department of Earth, Atmospheric and Planetary Sciences
on May 12, 1992 in partial fulfillment of the requirements for the
Degree of Doctor of Philosophy in Geology

ABSTRACT

The Himalayan mountains are one surface manifestation of continental collision between India and Asia, which initially occurred in Eocene time. Today, the Indian plate continues to move northward, resulting in active orogenesis. The core of this young orogen comprises the highest mountains on Earth, most of which are formed from high-grade crystalline rocks of the Indian plate. This thesis is the result of a multidisciplinary study of Himalayan tectonic processes in the core zone at Langtang National Park, central Nepal. This region contains excellent exposures of core zone rocks (the Greater Himalayan sequence), low grade units beneath the core zone (the Lesser Himalayan sequence) and the intervening Main Central Thrust commonly abbreviated as "MCT".

At Langtang, the MCT forms a 3.7 km wide zone of rocks with both footwall and hanging wall affinity. Two periods of distinct motion on the MCT are recognized. Early ductile motion occurred prior to 5.8 Ma, based on $^{40}Ar/^{39}Ar$ ages of muscovites from mylonites within the MCT zone. This ductile deformation is manifested in the local formation of mylonitic fabrics, with kinematic indicators that suggest top-to-the-south shear sense. The overall dominant foliation in the footwall, MCT zone and hanging wall (which strikes to the northwest and dips moderately to the northeast) is attributed to ductile movement on the MCT. A second period of brittle movement on the MCT is constrained to have occurred at approximately 2.3 Ma, based on $^{40}Ar/^{39}Ar$ ages of syn-deformational muscovites from brittle fault gouge. During this event, imbrication of MCT zone units resulted in the juxtaposition of different lithologies by brittle thrust faults. The MCT zone is interpreted as a duplex structure. The brittle deformation is attributed to represent back-breaking in response to ramping on a more southerly thrust, the Main Boundary Thrust.

The metamorphic evolution of both the MCT footwall and hanging wall rocks is very similar. Microfabric analysis distinguishes two periods or phases of metamorphism in both the Lesser and Greater Himalayan sequences. The first phase, a moderate temperature, high pressure event, occurred prior to the formation of the main foliation. The second phase was higher temperature and lower pressure and occurred syn- to post-kinematically with respect to the formation of the dominant foliation. Thermobarometric data from the second metamorphism shows a decrease in pressure but little variation in temperature across the entire core of the orogen. Within the MCT zone, there are fluctuations in the pressure estimates which probably reflects the late brittle shuffling. The lack of temperature gradient is interpreted to result from a number of different causes. Heating in the Lesser Himalayan sequence may have been caused by emplacement of a hot hanging wall on a cold footwall, whereas heating within the MCT zone may have been caused by shear heating along the fault. The heat source for the hanging wall rocks is still ambiguous.

The Greater Himalayan sequence appears to increase in metamorphic grade upsection, from kyanite grade at the base to sillimanite + K-feldspar at the top. The volume of migmatites increase upwards, with two-mica leucogranite bodies located near the top of the section. The heat source that caused the metamorphism and anatexis in the Greater Himalayan sequence is apparently located near the top of the sequence. With this in mind, an investigation of radioactive heat production in the hanging wall units was performed. U and Th concentrations were measured in a number of granites and gneisses from the Lesser Himalayan sequence through the Greater Himalayan sequence. Heat production values were calculated from this data. Simple thermal modelling of the heat production data indicates that, although radioactive heating increases the ambient temperatures, it does not bring the temperature regime to the minimum granite melting temperatures at the pressures of interest. Thus, high concentrations of radioactive elements in the gneisses may have contributed to, but did not cause, anatexis.

$^{40}Ar/^{39}Ar$ dating of twenty-five samples from MCT zone and Greater Himalayan sequence rocks establish the timing of both periods of motion along the MCT zone. Slow cooling rates are calculated for the Greater Himalayan sequence based on ages of 4.6 -9.7 Ma from $^{40}Ar/^{39}Ar$ dating of muscovites and biotites from the gneisses. Rapid unroofing of the sequence along the MCT after 4.6 Ma is suggested by the uniformity of ages across an 11 km thickness. Biotites from the uppermost Greater Himalayan sequence record an age of 19.6 Ma, based on $^{40}Ar/^{39}Ar$ dating. U-Pb ages of 20.5 - 22 Ma from granites associated with these gneisses suggest rapid cooling of the uppermost section, perhaps due to motion along the South Tibetan detachment system, a set of extensional structures that form the upper boundary of the Greater Himalayan sequence.

Thesis Supervisor: Kip V. Hodges
Title: Professor of Geology

ACKNOWLEDGEMENTS

The following piece of work wouldn't exist but for the assistance of many individuals and organizations. Of course, the actual list is terribly long, but I would like to mention certain individuals and groups. At the top of the list is Kip Hodges, who provided me with the opportunity to work with him on the Nepal project. Kip is a wonderful role model of a successful multidisciplinary scientist, which is what I hope to become one day. He has provided most of the financial support for the project and some stipend support as well. Kip graciously invited me to stay on an extra year, which I have greatly appreciated in this tough economic climate. Jane Selverstone was a great influence on me during my tenure at M.I.T. she is a superb scientist, wonderful teacher and valued friend, who also gave helpful reviews of much of this manuscript. Randy Parrish provided much appreciated insight both in the field and in the preparation of this thesis. Wiki Royden gave me the opportunity to work in northern Greece and much appreciated advice at different periods during my time here. I would also like to thank John Grotzinger and Brian Evans for their useful evaluations of the thesis during the defense. Before I go any further, let me thank Nancy Dallaire and Pat Walsh for their help in the logistical side of life at M.I.T.

Most of my financial support came from the National Science Foundation, in the form of one of their graduate fellowships. In addition, I received grants from the Geological Society of America and the Student Research Fund of the Department of Earth, Atmospheric and Planetary Sciences.

I was fortunate enough to spend three field seasons in Nepal. The Nepali government kindly granted me research permission. I have enjoyed working with Dr. Bishal Upreti, Chairman of the Geology Department at Tribhuvan University in Kathmandu, and hope the collaboration continues. I owe many debts to Surrendra Srestha for all his help at the Department of Mines and Geology in getting permission to take my rocks out of the country. Kunga Tsering, Shiva and everyone else at the Lhasa Guest House provided a home-away-from-home in Kathmandu. On my first trip to the country, I was accompanied by Kip, Randy, Sharon Carr, and Barbara Sheffels, all of whom greatly helped in easing culture shock. I would also like to thank Lhakpa Sherpa for his guidance and great food along the trail. My second field season proved much more exciting - too exciting, in fact. Carolyn Ruppel, Kip, Laurence Page and I endured Nepal's somewhat bloody revolution from a monarchy to a democracy. My third trip was definitely the easiest of all my visits to Nepal. Much of that I owe to Meg Coleman, a great field assistant and good friend, and to Mangale Sherpa, a super guide and Tika (Peanut Bhai) a mouth-watering cook! We four enjoyed many a night playing hearts in the warm confines of Mangale's tent. I would like to give special thanks to all of those people who portered for me; I can't tell you how much I appreciated their hard work. I'd also like to thank one of the Himalayan crew: Simon Inger. He made the first field season much more civilized when he shared his marmite.

The Center for Materials Research in Archaeology and Ethnology provided a diversion from geology. I thank Heather Lechtman for initially involving me (and keeping me involved) with the Center for over four years. I appreciate the encouragement and support of Dorothy Hosler, and look forward to a wonderful year of research and ideas with her. Maria Masucci enlightened me to the world of Ecuadorian ceramics, and I look forward to working with her, too.

My fellow graduate students have probably educated me as much as the faculty have and I give them special thanks. I was fortunate enough to bridge the gap between two "generations" of grad students at M.I.T., in addition to those at Harvard. The "old ones" are: David Dinter, Mary Hubbard, Barbara Sheffels, David Silverberg, Larry McKenna, Laurence Page, Carolyn Ruppel, Liz Schermer, Cathy Summa and Liz Schermer. The

"new ones" are: Deb Zervas, David Applegate (Juice!!), Meg Coleman, Martha House, David McCormick, Roy Adams, Paula Washbush, Peter Kaufman, Beverly Saylor, Erchie Wang, Dawn Sumner, C.J. Northrup and Dave Hawkins. I also would like to thank postdoc Bill Hames for help with CLAIR. And my Harvard buddies: Ximena Barrientos, Dan Holm and Gary Axen.

Very special thanks goes to those friends who have been there for me over the past month: Joan Brody, Meg Coleman and Deb Zervas - I couldn't have done it without you! Joan was there with me when I first started my undergrad education - so she knows the whole story - much more than the PhD - a better friend couldn't be found! I'd also like to thank David Silverberg for his support during my tenure at M.I.T. His friendship, companionship and all the advice - scientific and otherwise were and always will be very special to me. I'd also like to thank David's parents, Joan Podel and Jack and Eileen Silverberg for their support and encouragement throughout my endeavors here.

Of course, my greatest thanks of all goes to my family. To the big one, in South Africa, and to the smaller one, in this country. Truly, my mom and my dad have been the real source of inspiration for me. My dad loved science and conveyed that love to me. He and my mom always encouraged me to go as far as I could go and to do whatever I wanted to do. My sister, Pat, is a great friend and a wonderful sister. They all were and are my real source of strength.

To John Macfarlane,

My father and fellow scientist,
He inspired my path to academia

TABLE OF CONTENTS

Title Page.....1
Abstract.....2
Acknowledgements.....4
Dedication.....6

Chapter 1: Introduction.....10

Chapter 2: A Structural Analysis of the Main Central Thrust Zone, Langtang National Park, Central Nepal Himalaya.....13
Abstract.....14
Introduction.....15
Tectonic Setting.....17
Tectonic Stratigraphy.....19
Deformation History.....20
Deformation in the Lesser Himalayan Zone.....21
Deformation in the Main Central Thrust Zone.....21
Deformation of the Greater Himalayan Zone.....23
Correlation among Deformation Events.....24
Structural Interpretation.....26
Age of Major Thrusting Events.....28
Discussion.....30
Conclusions.....32
Acknowledgements.....33
Tables.....34
Figure Captions.....40
Figures.....44

Chapter 3: A Petrologic Examination of the Metamorphic Core of the Himalayan Orogen, Langtang National Park, Nepal.....63
Abstract.....64
Introduction.....65
Geologic Setting.....66
Regional Geology.....66
Langtang Area Geology.....68
Petrography and Phase Equilibria.....70
Descriptive Mineralogy.....71
Lesser Himalayan Sequence.....72
MCT Zone.....73
Greater Himalayan Sequence.....76
Fabric Analysis.....78
Mineral Chemistry.....79

Phase Equilibria....79
Mineral Zoning and Compositional Variability....81
Thermobarometry....83
Rim Thermobarometry....84
Inclusion Thermobarometry....85
Gibbs Method Analysis....86
Interpretations....88
Thermobarometric Data....88
PT Path Data....91
Tectonic Framework....91
Conclusions....93
Acknowledgements....94
Tables....95
Figure Captions....104
Figures....109

Chapter 4: Conditions for Granite Genesis in Collisional Orogens: The Himalayas....135
Abstract....136
Introduction....137
Geologic Setting....137
Proposed Causes of Anatexis....138
Radioactive Heat Production in the Langtang Region....139
Sample Selection and Analytical Methods....141
Results....142
Discussion....143
Conclusions....148
Acknowledgements....149
Appendix....150
Tables....152
Figure Captions....155
Figure....156

Chapter 5: The Chronology of Tectonic Events in the Crystalline Core of the Himalaya, Langtang National Park, Central Nepal....161
Abstract....162
Introduction....163
Langtang Geology....166
Analytical Procedure....168
Sample Selection and Preparation....168
Analytical Techniques....168
Results....170
Lesser Himalayan Sequence....170
MCT Zone....171
Greater Himalayan Sequence....173
Discussion....176
Data Interpretation....176

Tectonic Significance.....179
Conclusions.....180
Acknowledgements.....180
Tables.....182
Figure Captions.....191
Figures.....193

References.....222

Plate 1: Geologic map of Langtang National Park, Central Nepal.....Back Folder

Plate 2: Cross Sections from Langtang National Park, Nepal.....Back Folder

CHAPTER ONE

Introduction

The Himalayas are the youngest and highest mountain belt on earth, extending from Pakistan eastwards beyond Bhutan. The orogen represents continental collision between India and Asia that began approximately 40 Ma (Molnar and Tapponnier, 1975). Northward subduction of the Indian plate beneath the Asian plate is a continuing process, resulting in a number of devastating earthquakes recently. For the geologist, the Himalayas offer a unique setting in which a large amount of crustal section exposed in an orogen that is still active; in other words, collisional tectonics in progress.

Twenty years ago, the orogen was relatively little studied, mostly because access was limited by the governments of countries such as Nepal, Bhutan and Tibet. Nepal, in particular, did not open its borders until 1951. Prior to that, only one major geologic study of that portion of the Himalayas had been performed by Heim and Gansser (1939). By the 1960's, a handful of other studies provided a general outline of the orogen's major tectonic features (Lombard, 1953; Lombard, 1958; Bordet, 1961; Gansser, 1964; Hagen, 1969). The core of the orogen consisted of three main tectonostratigraphic units, the Lesser Himalayan sequence in the south, the Greater Himalayan sequence and the Tibetan Sedimentary sequence to the north. The Lesser Himalayan sequence, comprising low grade metasedimentary rocks, was separated from the high grade crystalline rocks of the Greater Himalayan sequence by a north-dipping thrust fault named the Main Central Thrust (MCT). An inverted metamorphic gradient associated with the MCT, has been recognized for over a century (Mallet, 1875; Oldham, 1883). Deformed and undeformed leucogranites have been emplaced into the uppermost portion of the Great Himalayan sequence. More recent studies have determined that the contact between the Tibetan Sedimentary and Greater Himalayan sequences is actually a system of low-angle north dipping normal faults (Burg et al., 1984; Burg and Chen, 1984; Brun et al., 1985; Burchfiel and Royden, 1985; Herren, 1987; Burchfiel et al., 1992).

A multidisciplinary study of the core of the Himalaya in Langtang National Park, central Nepal, is the focus of this thesis. Detailed field mapping, structural and petrologic analysis and geochronology aided in determining a portion of the tectonic evolution of the core in this location. Langtang was previously unmapped, although over the past few years, a number of workers from the Open University have begun research programs there (Inger, 1991; Massey et al., 1992; Reddy et al., 1992). Ridgetop exposures, glacial valleys and especially a well-placed roadcut result in an excellent field location. Field work for this study spanned three field seasons from 1989 to 1990.

The first chapter of this thesis focuses on the structural evolution of the MCT exposed in Langtang. Two main periods of deformation are distinguished, an earlier ductile phase and a later brittle phase. Chapter two discusses the metamorphic petrology of rocks in the hanging wall and footwall of the MCT and the relationship between metamorphism and deformation. Temperatures and pressures are calculated for footwall through hanging wall rocks by quantitative thermobarometric analysis. The heat source for the leucogranites is examined in chapter three using concentrations of U and Th to determine heat production in hanging wall gneisses and granites. Finally, chapter four provides a temporal framework for the deformation, metamorphism and anatexis with $^{40}Ar/^{39}Ar$ studies on K-feldspar, muscovite, biotite and hornblende from MCT zone and hanging wall rocks.

The chapters in this thesis are actually stand-alone papers which will be (or have been) submitted for publication; therefore, there is a certain amount of repetition among chapters. As a whole, the thesis is meant to provide an inclusive study of the tectonic evolution of the Langtang Himalaya. Understanding of such studies of tectonic processes involved in continental collision will hopefully be translated to similar events that have occurred in other mountain belts.

CHAPTER TWO

A Structural Analysis of the Main Central Thrust Zone, Langtang National Park, Central Nepal Himalaya

ABSTRACT

The Main Central Thrust (MCT) is one of the most significant structures in the Himalayan orogen. Detailed geologic mapping and structural analysis of the MCT in the Langtang National Park region of central Nepal reveals that this segment of the fault zone experienced multiple episodes of south-directed movement, under both brittle and ductile conditions, during the Tertiary period. Early (mid-Miocene) movement resulted in the development of mylonitic fabrics synchronous with amphibolite facies metamorphism. Kinematic indicators suggest hanging wall movement to the southwest relative to the footwall along the northeast-dipping fault. Late stage structures in the MCT zone at Langtang include a series of imbricate, brittle thrust faults, interpreted as a duplex structure, that separate different lithostratigraphic units and correspond to metamorphic discontinuities. Muscovite $^{40}Ar/^{39}Ar$ cooling ages from the MCT zone mylonites range from 8.9-6.9 Ma. Because the nominal closure temperature of Ar diffusion in muscovite (approximately 625 K) is higher than the apparent temperature conditions under which late brittle deformation occurred, we suggest that brittle deformation was a latest Miocene - Pliocene phenomenon. Another major Himalayan fault, the Main Boundary Thrust (MBT) was developing to the south of Langtang at roughly the same time. We speculate that brittle faulting within the MCT zone may have initiated as the MCT zone was transported over a ramp in the MBT.

INTRODUCTION

The Main Central Thrust (MCT) is a major north-dipping fault zone in the Himalayan orogen that is estimated to have accommodated at least 100 km of crustal shortening in Tertiary time (Gansser, 1966, Brunel, 1975, Pêcher, 1978). One of the most controversial issues associated with the MCT is its temporal relationship with regional metamorphism. In the Garhwal Himalaya of India (Fig. 1), the MCT corresponds to a sharp discontinuity between middle to upper amphibolite facies rocks to the north and greenschist facies units to the south (Heim and Gansser, 1939, Gansser, 1964, Valdiya, 1979, Valdiya, 1980, Hodges and Silverberg, 1988). In the Manaslu region of central Nepal (Fig. 1), the MCT has been described as a ductile shear zone across which there is no significant metamorphic break (Bordet, 1961, Le Fort, 1975, Bouchez and Pêcher, 1976, Pêcher, 1977). More recent studies have produced evidence for syn-metamorphic thrusting in the Everest region of eastern Nepal (Hubbard, 1988, Hubbard, 1989; Fig. 1), post-metamorphic thrusting in the Makalu region of eastern Nepal (Brunel and Kienast, 1986; Fig.1) and diachronous movement spanning regional metamorphic events in the Rowaling region of east-central Nepal (Schelling, 1987; Fig. 1) and the Annapurna region of central Nepal (Caby et al., 1983; Fig. 1) .

Dissimilarities in the tectonic histories of different parts of the orogen, such as Garhwal and central Nepal, have led to disagreements about the age of the MCT. If it is assumed that movements on the MCT were syn-metamorphic, then it follows that geochronologic measurements of the age of metamorphism in the hanging wall provide constraints on the age of faulting. The metamorphic core of the Himalayan orogen has experienced multiple regional metamorphic events (see Hodges et al., 1988 and

Pêcher, 1989, for reviews), but the latest and most widespread in the central Himalaya was a medium to low pressure amphibolite facies episode that included anatectic melting responsible for leucogranite plutons like the Manaslu granite of central Nepal (Le Fort, 1975). U-Pb zircon and monazite crystallization ages for the leucogranites in the central Himalaya range from Late Oligocene to Miocene (Schärer, 1984, Schärer et al., 1986, Deniel et al., 1987, Copeland et al., 1988, R. Parrish, unpublished data). Based on geochronologic data for the latest metamorphic event from the Everest region, Hubbard and Harrison (1989) established that some movement on the MCT occurred at roughly 21 Ma. In contrast, if it is assumed that most of the movement on the MCT was post-metamorphic (Gansser, 1964, Valdiya, 1979, Valdiya, 1980, Brunel, 1986, Brunel and Kienast, 1986, Schelling, 1987), then the only implication is that this faulting occurred more recently than mid-Miocene time.

There are three possible explanations for disagreements among Himalayan geologists about the relative ages of metamorphism and thrusting on the MCT. First, it is possible that the MCT has become a generic term for any fault zone that marks that physiographic break between the higher Himalaya and the lower Himalaya, such that the MCT in one region may have a different age than the MCT in another region (Hodges et al., 1988, Hodges et al., 1989). Second, the MCT may be the same structure in all areas, but the age and/or southward extent of regional metamorphism may vary along the range. Third, the relationship between faulting and metamorphism may be difficult to establish with certainty in some areas due to poor exposure. In many parts of the central Himalaya, the MCT lies in thickly wooded or extensively cultivated terrain where accessible outcrops are relatively sparse. This is not the case in the Langtang National Park region of central Nepal (Fig. 1), where extensive ridgetop exposures and a remarkable recent roadcut provide an unusual opportunity for a detailed study of the MCT. Our investigation shows that the MCT in the Langtang

area had a complex movement history involving at least two distinct periods of deformation, with initial thrusting during Miocene regional metamorphism followed by a major displacement after approximately 9-7 Ma.

TECTONIC SETTING

From western India to eastern Nepal, the core of the Himalaya is composed of three major tectonostratigraphic units separated by north-dipping structural discontinuities (Fig. 1). Northernmost and structurally highest is the Tibetan Sedimentary Sequence, dominated by a series of shallow marine continental and miogeoclinal sediments of Cambro-Ordovician to Eocene (?) age. The base of the Tibetan Sedimentary Sequence is marked by a family of Miocene, post-metamorphic normal faults collectively referred to as the South Tibetan detachment system (Burchfiel et al., 1991, Burg et al., 1984, Burchfiel and Royden, 1985, Herren, 1987). The underlying Greater Himalayan sequence consists primarily of amphibolite facies gneisses and schists of Precambrian to Cambrian (?) age that are locally migmatitic. Large leucogranite plutons, commonly containing tourmaline, occur near the top of the Greater Himalayan sequence. The Greater Himalayan sequence rocks overlie the Lesser Himalayan sequence (the "Midlands Formations" of Le Fort, 1975), a package of upper Precambrian (?) to Lower Eocene (?), greenschist to lower amphibolite facies metasedimentary and metavolcanic rocks. The contact between the Greater Himalayan sequence and the Lesser Himalayan sequence is the Main Central Thrust. As mapped and interpreted by various workers (e.g., Gansser, 1964, Le Fort, 1975, Brunel, 1975), the MCT zone ranges in thickness from <50 m to >10 km and dips moderately northward. The MCT zone is characterized by well-developed mylonitic fabrics that indicate hanging wall movement to the south relative to the footwall (Pêcher, 1978, Brunel, 1986). The Main Boundary Thrust forms the lower

contact of the Lesser Himalayan sequence. It is an active north-dipping structure that carries the Lesser Himalayan sequence over unmetamorphosed molasse units of the Subhimalayan sequence (Molnar, 1984).

Langtang National Park is located roughly 50 km north of Kathmandu, at approximately 28°10' N and 85°25' E. Figure 2 is a geologic map of part of this area, based on 1:25,000 mapping conducted in 1989 and 1990 along the Trisuli-Langtang river transect, the Trisuli-Chilime river transect, the Barabal trail transect and the Gosainkunda ridge transect. The MCT zone was best exposed along a road in the westernmost portion of the Trisuli-Langtang river transect and the southernmost portion of the Trisuli-Chilime river transect. In the northwestern part of the area, the MCT zone and lithologic contacts in the hanging wall and footwall strike generally east-west and dip northward, consistent with regional trends. However, in the central and southern parts of the Langtang area, the general strike of the units changes to north-south with an eastward dip. This variation, interpreted below as the consequence of ramping subsequent to ductile deformation, provides an important perspective on the geometry of thrust imbrication slices.

The metamorphic history of the Langtang area has been discussed in detail elsewhere (Macfarlane, submitted), but a brief summary will be useful in this paper. Evidence from microfabric analysis and Gibb's Method modelling suggests that the core of the Himalaya in the Langtang region appears to have undergone two periods of metamorphism. The earlier metamorphic event was high-pressure, moderate-temperature (M_1) and the later event was moderate-pressure, high-temperature (M_2). The second event appears to be related to the emplacement of two-mica leucogranites located in the upper portion of the Greater Himalayan sequence. M_1 is best displayed in the Lesser Himalayan sequence, where rotated garnet

porphyroblasts predate the dominant foliation. Kyanite inclusions in garnet porphyroblasts in upper MCT zone and Greater Himalayan sequence rocks are the only evidence of M_1 in these units. Maximum temperatures associated with M_2 appear to have occurred during and after the latest ductile motion on the MCT, based on the presence of syn- to post-kinematic porphyroblasts in these rocks. Quantitative thermobarometry provided estimates of the conditions of M_2 in Lesser Himalayan sequence rocks of 767-787 K and 626-665 MPa; lower MCT zone rocks of 700-785 K and 510-634 MPa; upper MCT rocks of 794-849 K and 522-899 MPa (Macfarlane, 1992).

TECTONIC STRATIGRAPHY

In the Langtang region, the Greater Himalayan sequence is characterized by pelitic gneisses and migmatites, with thin units of amphibolite and pyroxene gneisses in the uppermost portion of the section. The Lesser Himalayan sequence consists primarily of pelitic schists, (commonly containing folded quartz lenses), with less abundant calcareous metapsammites, siliceous metalimestones and amphibolites. The Lesser Himalayan sequence is separated from the Greater Himalayan sequence by a 3.7 km-wide MCT zone. The MCT zone is characterized by slices of rocks of both Greater Himalayan sequence and Lesser Himalayan sequence affinity that were juxtaposed by brittle faults. The alternation of lithologies in this zone is in stark contrast to the general lithologic monotony of the coherent Greater and Lesser Himalayan sequences. Lower units within the MCT zone have affinities with the Lesser Himalayan sequence, and upper units within the zone are associated with the Greater Himalayan sequence. Assignment of these units to the Lesser or the Greater Himalayan sequences was based primarily on lithology, mineralogy and petrologic analysis (Macfarlane, submitted). In order to facilitate mapping, the Greater

Himalayan, Lesser Himalayan and MCT zones were subdivided into a number of different tectonostratigraphic units which are described in Table 1. The unit nomenclature was devised by the authors and is pertinent to the Langtang region.

Two units in the Langtang region appear to have correlatives in other areas of Nepal. The Lesser Himalayan sequence is dominated by the chlorite to garnet grade *Dhunche schists and metapsammites*. (Table 1; Fig.s 2 & 3). This unit is probably correlative with the Midlands "formations" of Le Fort (1975) and the Okhandhunga unit of Maruo et al. (1979). In the MCT zone, the light color and large K-feldspar augen of a mylonitized augen orthogneiss, the *Syabru Bensi gneiss*, make it a distinctive unit that may be correlative with the Ulleri augen gneiss of Le Fort (1975) and the Phaplu augen gneiss of Maruo & Kizaki (1981). In central Nepal, the Ulleri augen gneiss is located in the middle of the Lower Midland formations of the Lesser Himalayan sequence. This is not the situation in Langtang, where only two units having Lesser Himalayan sequence affinities lie above the Syabru Bensi gneiss. It is possible that higher units were cut out along faults within the MCT zone.

DEFORMATION HISTORY

The tectonic evolution of the Langtang region is complex, involving at least two deformational events and two or more metamorphic events. To aid in the understanding of the sequence of these events, a specific notation for each event in each major tectonostratigraphic unit will be used. The nomenclature used to discuss different characteristics of deformation will follow the traditional format of D_1, D_2, D_3,... but the authors do not intend to imply that all "deformation events" are completely separate in time and space and relate in some way to a significant tectonic event. D_{nLH} will be used for deformational events (n = 1 - 5) in the Lesser Himalayan

sequence; D_{nMCT} will be used for events in the MCT zone, and D_{nGH} will represent events in the Greater Himalayan sequence. Note that D_{1LH} is not necessarily correlative with D_{1GH}, and so on.

Deformation in the Lesser Himalayan Zone

Four deformational events have affected the Lesser Himalayan sequence in the Langtang region (Table 1). In addition, a pre-deformation compositional layering (S_{0LH}) was identified in some of the more psammitic zones. The first deformation event in the Lesser Himalaya sequence, D_{1LH}, predated development of the dominant foliation in the rocks (S_{2LH}). It is manifested only in thin section as snowball inclusion trails in large M_1 garnets that predate S_{2LH} (Fig. 4a) and as foliation that is transposed into the dominant foliation, S_{2LH}. The second event, D_{2LH}, is the main ductile event in the Lesser Himalayan sequence. Megascopically, it is manifested by the dominant foliation, S_{2LH} (Fig. 5a & 5b), which strikes to the northwest and dips to the northeast, and an associated stretching/mineral lineation L_{2LH} (Fig. 5c) that plunges gently and trends to the north-northeast. The dominant foliation, S_{2LH}, is axial planar to mesoscopic F_{2LH} concentric folds. Smaller M_2 garnets grew syn-kinematically with respect to S_{2LH}. These garnets display asymmetric pressure shadows that indicate top-to-the-south sense of shear. The D_{3LH} event is characterized by a crenulation cleavage, S_{3LH}, and a crenulation lineation, L_{3LH} (Fig. 5d), that were found only in pelitic lithologies. Mesoscopic scale concentric folds (F_{3LH}) are less common than the crenulation cleavage. Finally, the D_{4LH} event is marked by a few late brittle faults, which strike to the northwest and dip steeply to the northeast and are of uncertain movement sense.

Deformation in the Main Central Thrust Zone

The MCT zone in the Langtang area is characterized by five periods of deformation (Table 2). Figure 4b shows the earliest foliation, S_{1MCT}, transposed into the main foliation, S_{2MCT}, which is at an angle of 45° to the bottom of the photograph. The S_{1MCT} fabric, in addition to a pre-S_{2MCT} phase of isoclinal folding present in the field, provide evidence for an early ductile event, D_{1MCT}. Helicitic inclusions in M_1 garnet indicate that syn-kinematic growth of garnet occurred during this early deformation event (Fig. 4c).

The main ductile event in the MCT zone is D_{2MCT}. Megascopically, it produced the dominant foliation, S_{2MCT}, and a stretching/mineral lineation, L_{2MCT}. S_{2MCT} strikes to the northwest and dips to the northeast, similar to S_{2LH} (Fig. 6a & 6b). L_{2MCT} trends to the northeast, subparallel to L_{2LH} (Fig. 6c). In some units (augen gneisses, quartzites and marbles) mylonitic s-c fabrics developed during D_{2MCT} (Fig. 4d). In the mylonitic quartzite lithologies (Gompagong unit and Mangol unit), sense of shear from mica fish indicate movement to the southwest (Fig. 4e). Asymmetric pressure shadows associated with D_{2MCT} also give top-to-the southwest sense of movement. Staurolite grew syn-kinematically with respect to D_{2MCT} in some lithologies. Figure 4f shows a staurolite porphyroblast surrounded by a corona of M_2 sillimanite. The main foliation runs parallel to the bottom of the page. Note that sillimanite is not aligned in the foliation; therefore, it grew post-D_{2MCT}. Similarly, kyanite also grew post-D_{2MCT}. The D_{3MCT} event is represented by a crenulation cleavage, S_{3MCT}, and lineation, L_{3MCT} (Fig. 6d). Some of the units within the MCT zone are affected by a retrograde metamorphic event that may have occurred during or just after the D_{3MCT} event.

The multiple faults in the map pattern of the MCT zone (Fig. 2) result from imbrication of lithostratigraphic units along post-metamorphic brittle thrust faults associated with D_{4MCT} deformation. Figures 8a and 8b are photographs of these faults, which are subparallel to the main foliation. Drag folds which post-date the mylonitic fabrics and earlier folding events and are adjacent to these faults suggest a reverse sense of motion. The D_{4MCT} brittle faults are 10 cm to 10 m wide zones composed of graphitic fault gouge (Fig.s 8a & 8b). The gouge is recessively weathered structurally incoherent material. The brittle faults are generally subparallel to S_{2MCT}, but demonstrably cross-cut the fabric in some places (Fig. 8a). The brittle faults strike NW and dip approximately 35° NE. No slickensides were observed. The D_{4MCT} event juxtaposed units within the MCT zone resulting in the present tectonostratigraphy. Brittle listric faulting, possibly of normal sense, constitutes the final phase of deformation, D_{5MCT}. Where the D_{5MCT} faults were encountered, they strike NW and dip steeply to the SW. Only a few D_{5MCT} faults were encountered.

Deformation in the Greater Himalayan Zone

The Greater Himalayan sequence in the Langtang region also experienced five deformational events (Table 3). D_{1GH} produced mesoscopic, F_{1GH} tight to isoclinal folds that have been overprinted by the dominant foliation, S_{2GH}. During and after D_{1GH}, there was growth of both M_1 garnet and M_1 sillimanite. D_{2GH} was the main ductile event in the Greater Himalaya sequence. The dominant foliation, S_{2GH}, and a mineral/stretching lineation, L_{2GH}, characterize D_{2GH} (Fig. 7a, 7b & 7c). The dominant foliation, S_{2GH}, strikes toward the northwest and dips toward the northeast, and L_{2GH} plunges moderately to the northeast. In the lower part of the Greater Himalayan sequence, D_{2GH} asymmetric pressure shadows suggest top-to-the southwest sense of shear, but in the upper 3-5 km of the section, the movement sense

is to the northeast. The vergence reversal is consistent with contemporaneity between ductile thrusting on the MCT and normal displacement on the structurally higher South Tibetan detachment system (c.f. Burchfiel and Royden, 1985; Burchfiel et al., 1992). At the bottom of the section, migmatitic horizons are elongate subparallel to S_{2GH} and are themselves foliated; thus, melting associated with M_2 occurred during D_{2GH}. The majority of the granites near the top of the section intruded post-D_{2GH}, based on the cross-cutting relationship of the granites to foliation and the unfoliated appearance of the granites. During and after D_{2GH}, both M_2 garnet and M_2 sillimanite grew syn- to post-kinematically.

Open to closed meso- to macroscopic folding of S_{2GH} is indicative of D_{3GH}. During this event, intrusion of granite and pegmatite associated with M_2 was probably still occurring. The D_{4GH} event is characterized by chlorite grade 1 - 5 mm wide shear zones of indeterminate displacement sense. Brittle faulting of probably small displacements occurred during the last deformational event, D_{5GH}, of unknown movement sense.

Correlation Among Deformation Events

Some correlation between deformational events in the three different tectonostratigraphic units are possible. Based on helicitic inclusion trails in M_1 garnets from both the Lesser Himalayan sequence and MCT zone, D_{1LH} and D_{1MCT} are probably correlative events, although it is not clear whether this deformation is the result of an Himalayan or older event. If the deformation is Himalayan in age, it may even then be part of a single continuous phase of ductile deformation that actually includes D_1, D_2 and D_3. It is not possible to ascertain whether D_{1GH} is the same as the first events in the Lesser Himalayan sequence and MCT zone.

The D_2 events within the three tectonostratigraphic units are probably correlative. This event is interpreted to be associated with ductile movement on the MCT and the Giyrong detachment, part of the South Tibetan detachment system exposed north of Langtang in southern Tibet (Burchfiel, et al., 1992). Figures 5-7 show stereonet plots of the main foliation in the Lesser Himalayan sequence, the MCT zone and the Greater Himalayan sequence. Note that the foliation for all three units is very similar. The stereonet plots of the mineral/stretching lineations (Fig. 5-7) show similarities between those from the MCT zone and the Greater Himalayan sequence. Although the Lesser Himalayan sequence L_2 lineation data are somewhat limited, the mean vector for the Lesser Himalayan sequence seems to be appreciably different from that of the MCT zone. This situation suggests that rotation on faults that were subparallel to the main foliation occurred between the Lesser Himalayan sequence and the MCT zone subsequent to the formation of the principle macroscopic fabric associated with D_2. The rotation may have been caused by the crenulation cleavage event (D_{3MCT}), brittle imbrication of tectonostratigraphic units within the MCT zone (D_{4MCT}) or by folding of the MCT zone (D_{3MCT}).

The D_3 event is characterized by development of a crenulation cleavage in both the Lesser Himalayan sequence and the MCT zone; thus it is probably correlative in both sequences. The crenulation cleavage may likely be part of a continuous sequence of deformation related to D_2 and possibly D_1, if D_1 is of Himalayan age. The crenulation lineation in the MCT zone (Fig.6c) is subparallel to the stretching/mineral lineation in the MCT zone. This suggests that D_3 and D_2 in the Lesser Himalayan sequence and the MCT zone may be part of a continuum of deformation. Again, it is difficult to determine whether D_{3GH} was coeval with D_{3LH} and D_{3MCT}. Because D_{4LH} brittle faults are of indeterminate movement direction, D_{4LH} may correlate with

either D_{4MCT} or D_{5MCT}. D_{5MCT} and D_{5GH} faults are also brittle and appeared to be of normal sense and similar in style; thus, they may have formed during the same event. D_{4GH}, D_{5GH}, D_{5MCT} and D_{4LH} may all be correlative, perhaps part of a single continuous brittle deformation event.

STRUCTURAL INTERPRETATION

It is important to clarify the definition of the MCT zone in the Langtang region. The base of the MCT zone in the Langtang area is defined on the basis of the first appearance of a rapid succession of different lithologic units. The top of the MCT zone is defined on the basis of the last appearance of crenulation cleavage and the first appearance of migmatites. In the Langtang Himalaya, the MCT zone experienced two distinct periods of movement: earlier ductile and later brittle. It appears that the ductile phase of deformation may have affected a larger area than the brittle phase. The extent of crenulation cleavage into the Lesser Himalayan sequence suggests that the upper portion of what is now defined as the Lesser Himalayan sequence was affected by ductile motion on the MCT and therefore was part of the "ductile" MCT zone. This portion of the Lesser Himalayan sequence was not affected by the later brittle deformation. Due to the fact that there is no metamorphic break across the MCT zone in Langtang, the majority of ductile movement on the MCT must have occurred prior to or during the D_{2MCT} event.

In the Langtang area, the MCT zone changes from the regional strike of WNW/ESE to N/S (Fig. 2). Figure 9a is a stereonet plot of two groups of the main foliation: those points that lie in the "bend" area of the MCT zone and those that lie in the north/south portion of the zone. The two regions within the MCT zone yield two distinct groups of data on the stereonet. A girdle through the data results in an axis

of 42° to N60°E. In addition, Figure 9b shows a distinction between the L_{2MCT} stretching or mineral lineations for the two structural regions within the MCT zone. Thus, it appears that bending of the MCT zone occurred some time after D_{2MCT}. Because no mesoscopic evidence for another geometrically appropriate folding event exists, the bend is interpreted as the result of lateral thrust ramping during D_4.

Figure 10 is an interpretive east-west cross-section of the MCT zone in the Langtang region. Due to N60E ramping and the average dip of 34° NE on the fault, the map pattern is essentially a cross-section looking down-dip on the fault. Down-plunge projections of the area along the N60E axis are reminiscent of a duplex structure and we have adopted such an interpretation for the MCT zone at Langtang. In addition, there are outcrop-scale duplexes related to the D_{4MCT} event faults in the field area. An alternative interpretation of the Langtang MCT is that of an imbricate structure, based on the lack of duplication of stratigrapic units within the zone. Our duplex interpretation is meant in the most general sense of duplex, not the strict definition of Boyer and Elliott (1982). Depth-to-detachment for the cross-section is 1900 m and was calculated by assuming an arbitrary horizon, calculating the excess area for a particular horse (assuming the thickness listed earlier) above that horizon, extending the unfolded length of the horse and using the difference between shortened and restored length as one side of a rectangle of area equal to the excess determined earlier. The other side of the rectangle of excess area is the depth to detachment (Marshak and Mitra, 1988). Roof fault height is inferred from the size of horses in the down-plunge projection. Cut-off angles of 15° - 25° for the floor fault were determined assuming that the depth-to-detachment was 1900 m and that bedding dips were subparallel to the brittle faults (as seen in outcrop). Roof fault cut-off angles of 35° - 45° are based on roof fault position and the assumption that compositional layering is subparallel to the faults.

AGE OF MAJOR THRUSTING EVENTS

Based on the structural and microfabric data, at least some of the D_2 ductile movement on the MCT in the Langtang area occurred synchronously with amphibolite facies metamorphism. U-Pb ages for monazite and zircon from both gneisses and leucogranites in the Greater Himalayan sequence of the Langtang region suggest that metamorphism occurred between 20 and 15 Ma (Parrish et al., 1992). These data are consistent with the conclusion of Hubbard and Harrison (1989) that ductile motion on the MCT in the Everest area was occurring at 20 Ma. The absolute age of D_4 in the Langtang area is difficult to ascertain. Experimental deformation of quartz from granite suggest that brittle deformation at low pressure and low to moderate strain rates occurs below 573-673 K (Tullis & Yund, 1977). These temperatures are lower than or in the range of the closure temperature for Ar in muscovite (625 K; McDougall & Harrison, 1988). To further constrain the age of brittle deformation (D_{4MCT} in particular) in the MCT zone, $^{40}Ar/^{39}Ar$ geochronology of muscovites from MCT zone rocks was attempted.

Three samples from the MCT zone were chosen for $^{40}Ar/^{39}Ar$ analysis: L51, an augen orthogneiss from the Syabru Bensi gneiss unit, L66, a pelitic gneiss from the Phulung augen gneiss unit and L20a, a pelitic gneiss from the Syabru gneiss (Table 5). L51 and L66 have affinities with the Lesser Himalayan sequence, while L20a has affinities with the Greater Himalayan sequence. Standard mineral separation procedures using heavy liquids and magnetic separation were followed. A detailed discussion of analytical procedures can be found in Lux (1986). Samples were irradiated at the H5 reactor at the University of Michigan for 72 hours. An in-house flux monitor, SB-51, was used to determine the J values. Plateaus were established

by using the critical value test of Dalrymple and Lanphere (1969) to assess whether age increments were different. A York 2 least squares regression technique (York, 1969) was used in determining isochron ages. All muscovites analyzed were estimated to be 99.9% pure. Muscovite ranged in composition from 9.3 to 10.6 % K_2O. Plateau and total gas ages are given with 2 sigma uncertainties; the J-value has a 0.25 % uncertainty (Table 5; Fig. 11-13).

The results from $^{40}Ar/^{39}Ar$ analysis are listed in Table 6 and Figures 11-13. Isochron ages are considered the valid ages for all the samples analyzed. Sample L51 occupies the lowest structural level within the MCT zone. Muscovite from L51 gave no plateau, but an isochron age of 8.86 ± 0.16 Ma was determined when the first and last increment points were excluded from the regression (Fig. 11). Muscovite from L66 gives a plateau age of 8.34 ± 0.08 Ma and an isochron age of 8.49 ± 0.16 Ma (Fig. 12). Sample L20a is structurally highest in the MCT zone. L20a muscovite gave a plateau age of 6.86 ± 0.16 Ma and an isochron age of 6.87 ± 0.01 Ma (Fig. 13).

Muscovite $^{40}Ar/^{39}Ar$ age data for samples from the MCT zone in Langtang suggest that the zone was still at the Ar closure temperature for muscovite (nominally 625 K; McDougall and Harrison, 1988) as late as 6.9 Ma. D_4 movement on the MCT at Langtang occurred at temperatures sufficiently low that quartz was deforming in the brittle regime, at temperatures probably lower than the muscovite closure temperature for Ar. We interpret the 6.9-8.9 Ma ages to reflect a maximum time constraint for brittle deformation (D_4) of the MCT zone. In addition, the ages decrease upsection indicating that the upper MCT zone cooled after the lower MCT zone. This age sequence leads us to speculate that either deformation proceeded in the MCT zone from structurally lower levels upwards or the upper MCT zone was reset by a later event.

DISCUSSION

In the Langtang region of central Nepal, there is abundant evidence for significant ductile *and* brittle movement on the MCT. In the Annapurna/Manaslu region to the west and the Everest area to the east of Langtang, ductile movement appears to have been dominant, with little or no evidence for brittle deformation described (Le Fort, 1975, Pêcher, 1977, Le Fort, 1981, Pêcher and Le Fort, 1986, Hubbard, 1988, Hubbard, 1989). Thus, on the scale of approximately 90 km, the distance from Manaslu to Langtang, movement on the MCT appears to be diachronous in nature, provided that the metamorphism is of the same age in both areas.

Of major importance is the relative displacement on the MCT during ductile and brittle deformation. It was not possible to estimate the amount of displacement on the MCT during D_{2MCT}. Due to the possibility that more than one episode of ductile motion occurred on the MCT with shear fabrics continuously overprinted, strain estimates on the mylonites in the MCT as exposed in Langtang would probably vastly underestimate the amount of shortening that occurred during ductile deformation. Based on field mapping and thermobarometry, no obvious large-scale metamorphic breaks occur across the MCT zone (Macfarlane, submitted). The barometry data do show a slight perturbation across the MCT, at most, 130 MPa (3.5 km). Thus, the maximum amount of brittle displacement on the MCT according to the barometry data is 3.5 km.

Figure 14 shows our interpretation of the tectonic evolution of the MCT in the Langtang region. The D_{2MCT} event is related to ductile movement on the MCT between 15 and 20 Ma (Fig. 14a). During this event, initial development of S_{2MCT}

with the folding of S_{1MCT} and the growth of staurolite porphyroblasts occurred. Further movement on the MCT may have resulted in the crenulation cleavage. Note that it is not altogether clear that D_{3MCT} is a separate event from D_{2MCT}. In the middle or latter part of D_{2MCT}, the South Tibetan detachment system developed at structurally higher levels, accommodating gravitational collapse of the growing orogen (Burchfiel and Royden, 1985, Burchfiel et al., 1992). Metamorphism and anatexis associated with M_2 outlasted D_2.

Some time after the Middle Miocene, movement began on the Main Boundary Thrust (MBT, Fig. 14b). A large ramp formed on the MBT detachment approximately below the surface expression of the MCT. Brittle movement began on the MCT in Pliocene time (Fig. 14c). The MCT as now exposed in Langtang may have been unroofed by further normal faulting in the hanging wall, bringing the section above the brittle-ductile transition. Movement over a ramp on the MBT may have caused out-of-sequence-thrusting (or back-breaking thrusting) and reactivation of the MCT (Fig. 14c). Thus, we suggest that the brittle deformation in the MCT zone may have resulted from movement on the Main Boundary Thrust. At this time, the present duplex structure of D_{4MCT} in the MCT zone formed. This hypothesis is strengthened by the situation in central Nepal. There is no evidence for a ramp structure in the MBT in central Nepal because there are no tectonic windows south of the MCT. If the out-of-sequence thrusting hypothesis for the cause of brittle movement on the Langtang MCT is correct, then there is no need for significant brittle displacement on the MCT in central Nepal. According to many workers (Bordet, 1961, Le Fort, 1975, Bouchez and Pêcher, 1976, Pêcher, 1978, Colchen et al., 1986), little evidence for brittle deformation in the MCT zone exists in central Nepal. The evidence for out-of-sequence thrusting is equivocal in eastern Nepal. The Mahabarat window lies in south-eastern Nepal and may again be the result of ramping on the MBT. Hubbard

(1988) found evidence of syn-metamorphic thrusting with no sign of later brittle movement on the MCT south of Everest; therefore, Hubbard's (1988) conclusions contradict the out-of-sequence-thrusting hypothesis. On the other hand, Brunel and Kienast (1986) who worked south of Makalu (just east of Everest) found abundant evidence for significant post-metamorphic movement. Thus, the process which created significant post-metamorphic movement on the MCT may be more complex than we suggest.

The later brittle listric extensional faulting (D_{5MCT}) may have in part accommodated continuing gravitational collapse of the range (Burchfiel and Royden, 1985, Royden and Burchfiel, 1987). Further ramping on a lower fault of the MBT in modern time may have resulted in the creation of the Kathmandu window, as previously suggested (Lyon-Caen & Molnar, 1983; Fig. 14d).

CONCLUSIONS

The data presented in this paper demonstrate that the MCT in the Langtang region had at least two major periods of movement: an early ductile phase and a later brittle phase. Ductile movement on the MCT is constrained to have begun sometime before 15 - 20 Ma. Brittle motion took place after 9-7 Ma and continued for an unknown period of time.

Based on previous work (Bordet, 1961, Le Fort, 1975, Bouchez and Pêcher, 1976, Pêcher, 1977) the MCT less than 100 km west of the Langtang region appears to have evolved quite differently, having only a strong ductile imprint, with little evidence for extensive brittle deformation. Initially, we remarked that there were three sources for the controversy over the timing relationship between deformation and metamorphism

within the MCT zone. It appears that the extent of metamorphism and later tectonic developments such as the ramp in the MBT are the major factors in the noncorrelative timing associations on the MCT. Thus, it seems that the application of one overall hypothesis for the tectonic history of the MCT is inappropriate in light of the present data.

ACKNOWLEDGEMENTS

A.M.M. would like to thank Barbara Sheffels, Sharon Carr, Randy Parrish, Lhakpa Therky Sherpa, Carolyn Ruppel, Meg Coleman, Mangale Sherpa and Tika Magar (Peanut Bhai) for support in the field, the Nepali government for research permission and D. West for help with $^{40}Ar/^{39}Ar$ analyses. Stereonets were created using the MacIntosh program *Stereonet* by R. Allmendinger. D. Silverberg, D. Applegate, M. Coleman, P. Chamberlain and an anonymous reviewer provided helpful reviews of the manuscript. This research has been supported by N.S.F. grant # EAR8721403 awarded to K.V.H. and a G.S.A. student research grant awarded to A.M.M. The majority of graduate support for A.M.M. came from an N.S.F. Fellowship.

Table 1

Structural Unit	Unit Name	Lithology	Mineral Assemblage	Grain Size	Thickness	Weathering Characteristics
Lesser Himalayan Sequence	Dhunche schists and metapsammites	pelitic and graphitic schists, calcareous metaspammite, siliceous metalimestone, amphibolite	pelitic schist: qz+bi+mu+pg ±chl±gt; calc. metapsammites: qz+calc+mu±bi±pg±chl±phl	fine to medium	≥3900 m	dark brown/black ledge-former
MCT - Lesser Himalayan Sequence affinities	Thangjet gneiss	ortho-augen gneiss	qz+pg+mu+bi+sphene+apatite	fine	≤60 m	dark gray ledge-former
	Goljhong unit	quartzite, marble, phyllite, pelitic schist, carbonaceous schist	quartzite: qz+bi+mu+pg+K-fsp phyllite: calc+qz+mu	fine to medium	≤130 m	white to gray slope-former
	Gompagong calc-quartzite	clacareous psammite alternating with pelitic schist	calc+qz+phl±pg±mu	fine to medium	≤320 m	dark gray ledge-former
	Chilime calc-schist	calcareous graphitic schist with interbeds of calcareous quartzite (5-10m)	qz+mu+bi+chl+graphite	medium	≤170 m	dark gray slope-former
	Trisuli gneiss & schist	pelitic shcists and gneisses	qz+bi+mu+pg+chl+gt±st±ky ±sill	medium	≤245 m	dark gray ledge-former
	Bhote marble	siliceous marble	calc+qz+phl+pg±mu±chl±zois ±clinozois	medium	≤250 m	tan ledge-former
	Barabal schist & gneiss	calcareous pelitic schists & gneisses	qz+mu+bi+calc+chl+pg+clino-zois	medium	≤15 m	dark gray ledge-former
	Syabru Bensi gneiss	augen orthogneiss	qz+pg+K-fsp+mu+bi	medium to coarse	≤300 m	gray/brown ledge-former
	Phulung gneiss	pelitic augen gneiss	qz+pg+bi+mu+gt+clinozois	medium	≤55 m	dark gray slope-former
	Mangol quartzite	"dirty" quartzite	qz+mu+gt	fine to medium	≤60 m	dark brown ledge-former
MCT - Greater Himalayan Sequence affinities	Syabru gneiss	pelitic gneiss	qz+pg+bi+mu+gt±ky	coarse	≤2100 m	gray/brown ledge-former
Greater Himalayan Sequence	Gosainkund gneiss	migmatitic pelitic gneiss	qz+pg+bi+mu±gt±ky	fine to coarse	3600 m	dark brown ledge-former

qz-quartz; bi-biotite; mu-muscovite; pg-plagioclase; chl-chlorite; gt-garnet; ky-kyanite; sill-sillimanite; phl-phlogopite; calc-calcite; K-fsp-K-feldspar; st-staurolite; zois-zoisite; clinozois-clinozoisite;

TABLE 2: LESSER HIMALAYA

	D1	D2	D3	D4
Deformation Style	Folded foliation, S_{LH1}	Main schistosity, S_{LH2} Pressure shadows Mineral/stretch-ing lineation, L_{LH2}	Crenulation cleavage, S_{LH3} Crenulation lineation, L_{LH3}	Brittle faults
Metamorphic Relations	Syn-kinematic garnet	Syn-kinematic garnet		

TABLE 3: MAIN CENTRAL THRUST ZONE

	D1	D2	D3	D4	D5
Deformation Style	Schistosity, S_{MCT1} F_{MCT1} isoclinal folds	Main schistosity, S_{MCT2} Mineral/stre-tching lineation, L_{MCT2} Pressure shadows Mylonitic fabrics	Crenulation cleavage, S_{MCT3} Crenulation lineation, L_{MCT3}	Brittle faults/ Imbrication of the MCT zone	Brittle listric normal faults
Metamorphic Relations	Syn-kinematic garnet	Syn-kinematic staurolite Post-kinematic kyanite & sillimanite			

TABLE 4: GREATER HIMALAYA

	D1	D2	D3	D4	D5
Deformation Style	F_{GH1} tight to isoclinal folds	Main schistosity, S_{GH2} Mineral/stre-tching lineation, L_{GH2}	F_{GH3} open to closed folds	Chlorite grade shear zones Mortar texture in quartz fabric	Brittle faulting
Metamorphic Relations	Syn- post-kinematic garnet & sillimanite	Syn- post-kinematic garnet & sillimanite growth Syn- post-kinematic migmatites			

Table 5

Sample No.	Unit	Elevation	Rock Type	Mineral	40Ar/36Ar	Isochron Age	Plateau Age
L51m	Syabru Bensi gneiss	1540 m	augen orthogneiss	muscovite	306.7 ± 6.8	8.86 ± 0.16	none
L66m	Syabru gneiss	1960 m	pelitic gneiss	muscovite	304.4 ± 4.1	8.49 ± 0.16	8.34 ± 0.08
L20am	Syabru gneiss	2750 m	pelitic gneiss	muscovite	298.5 ± 3.0	6.87 ± 0.01	6.86 ± 0.16

Table 6

Temp (K)	$^{40}Ar/^{39}Ar$	$^{37}Ar/^{39}Ar$	$^{36}Ar/^{39}Ar$ (x 10^3)	Moles ^{39}Ar (x 10^{-14})	^{39}Ar (% total)	$^{40}Ar_{rad}$ (%)	K/Ca	Apparent age (Ma)
			L51-m		J = .006232			
923	18.830	0.0073	0.056	70.4	0.6	12.1	66.80	25.35 ± 5.31
1023	5.648	0.0020	0.0155	211.2	1.8	18.3	244.79	11.61 ± 0.77
1093	2.623	0.0022	0.0060	361.6	3.1	31.3	220.59	9.19 ± 0.24
1153	1.624	0.0003	0.0027	857.6	7.5	49.5	1549.55	9.01 ± 0.17
1213	1.351	0.0008	0.0017	1555.2	13.5	60.7	594.00	9.20 ± 0.15
1273	1.177	0.0008	0.0012	2116.8	18.4	69.1	628.47	9.12 ± 0.16
1343	1.088	0.0006	0.0009	2841.6	24.7	73.2	796.78	8.93 ± 0.13
FUSE	1.070	0.0026	0.0007	3472.0	30.2	79.2	188.32	9.50 ± 0.13
			L66-m		J=.006104			
783	26.623	0.0169	0.0851	32.0	0.3	5.5	28.97	16.01 ± 5.17
923	9.960	0.0799	0.0303	76.8	0.8	10.0	6.13	10.98 ± 2.28
1023	4.715	0.0030	0.0130	285.6	2.9	17.9	165.07	9.29±0.40
1093	2.740	0.0010	0.0062	896.8	9.1	31.9	481.52	9.61 ± 0.43
1153	1.903	0.0005	0.0035	1768.0	18.0	44.2	957.07	9.25 ± 0.24
1213	1.589	0.0003	0.0026	2013.6	20.5	50.8	1511.07	8.87 ± 0.18
1273	1.485	0.0005	0.0023	1546.4	15.8	52.4	1073.69	8.55 ± 0.14
1343	1.595	0.0004	0.0027	1345.6	13.7	49.2	1259.32	8.63 ± 0.23
FUSE	1.372	0.0084	0.0019	1852.8	18.9	56.6	58.05	8.53 ± 0.24
			L20a-m		J=.006183			
923	17.373	0.0237	0.0566	56.0	0.5	3.6	20.72	6.91 ± 2.97
1023	4.648	0.0044	0.0133	156.0	1.3	14.9	111.67	7.73 ± 0.56
1093	1.994	0.0015	0.0045	1201.6	10.2	32.0	325.54	7.11 ± 0.27
1153	1.414	0.0008	0.0026	1714.4	14.5	44.6	586.66	7.02 ± 0.21
1213	1.189	0.0008	0.0018	2313.6	19.6	53.1	643.66	7.03 ± 0.19
1273	1.067	0.0009	0.0015	2004.8	17.0	57.5	558.04	6.83 ± 0.11
1343	1.053	0.0012	0.0014	1752.0	14.8	58.1	425.04	8.81 ± 0.13
FUSE	0.907	0.0018	0.0009	2622.4	22.2	68.7	278.70	6.93 ± 0.09

FIGURE CAPTIONS

Figure 1: General geologic map of Nepal. Location map of south Asia in box on top right. The Main Central Thrust (MCT) is the barbed thrust contact between The Greater Himalayan sequence and the Lesser Himalayan sequence. The Main Boundary Thrust (MBT) is the barbed thrust contact between the Lesser Himalayan sequence and the Subhimalayan sequence.

Figure 2: Geologic map of the MCT zone in the Langtang region. Units are patterned according to Figure 3. All heavy barbed lines are post-metamorphic brittle thrust faults. A-A' is the line of section for Figure 5. Locations of samples used in $^{40}Ar/^{39}Ar$ analyses are indicated with solid circles and sample number.

Figure 3: Tectonostratigraphic section of the MCT zone in the Langtang region. Unit descriptions are in text. Widths of units are actual relative thicknesses measured near the Trisuli Kosi.

Figure 4: Photomicrographs of MCT zone microfabrics. Scale bars at bottom of photographs. (a) Lesser Himalaya pelitic schist under plane light; garnet has "snowball" quartz inclusions (associated with an earlier deformational event - D_{1LH}) and pressure shadows (associated with the main foliation - D_{2LH}). Bottom of photo is 1.5 mm across; northeast is to the left side of photo. (b) MCT zone pelitic schist under crossed polars with main foliation (S_2) as indicated, folding an earlier foliation (S_1). Bottom of photo is 1.5 mm across. (c) MCT pelitic schist under plane

light; helicitic inclusion trails in garnet are associated with S_{1MCT}; pressure shadows associated with S_{2MCT}. Garnet is 5 mm in diameter. (d) MCT mylonitic augen gneisses, outcrop view. (e) "Mica fish" in MCT mylonitic quartzite, under plane light. Bottom of photo is 1.5 mm across; southwest is on left side of photo. (f) MCT pelitic schist under plane light. Here prismatic sillimanite (si) forms a corona around staurolite (st). Sillimanite is not aligned in the main foliation (S_{2MCT}; parallel to bottom of photo) and therefore grew after D_{2MCT}. Bottom of photo is 1 mm across.

Figure 5: Lower hemisphere, equal area stereographic representations of fabric data from Lesser Himalayan sequence D_{2LH} features; n is the number of data points. (a) S_{2LH} scatter plot with mean great circle. (b) S_{2LH} contour plot; contour interval = 1% per % area. (c) L_{2LH} mineral and stretching lineation plot. (d) L_{3LH} crenulation lineation plot.

Figure 6: Lower hemisphere, equal area stereographic representations of fabric data from Main Central Thrust zone D_{2MCT} features; n is the number of data points. (a) S_{2MCT} scatter plot with mean great circle. (b) S_{2MCT} contour plot; contour interval = 1% per % area. (c) L_{2MCT} mineral/stretching lineation plot. (d) L_{3MCT} crenulation lineation plot.

Figure 7: Lower hemisphere, equal area stereographic representations of fabric data from Greater Himalayan D_{2GH} features; n is the number of data points. (a) S_{2GH} scatter plot. (b) S_{2GH} contour plot; contour interval = 1% per % area. (c) L_{2GH} mineral/stretching lineation plot.

Figure 8: Photographs of the post-metamorphic brittle faults. (a) Fault zone here is approximately 5 cm wide and places the Thangjet gneiss unit (th) on top of the Dhunche schists (dh) of the Lesser Himalayan sequence; photo looking east. (b) Fault zone (fz) here is made up of 2 discrete faults, indicated by the arrows, both approximately 10 cm wide. This fault zone places the Chilime unit (ch) on top of the Gompagong unit (gom); photo is looking west. In both photos, the faults zones are subparallel to the main foliation S2 and are composed of graphitic gouge.

Figure 9: Lower hemisphere, equal area stereographic projection of data for "bend" and N/S regions of the MCT zone in the Langtang area; n is the number of data points. (a) is a plot of the foliation (S2) data; (b) is a plot of the lineation (L2) data. On (a), the data is interpreted to represent a girdle with a pole representing the fold axis of the MCT zone.

Figure 10: Cross-section across the northern part of the MCT zone if the Langtang region; A-A' as on Fig. 2. Unit names as on Fig. 3. There is no vertical exaggeration. The MCT zone in Langtang is interpreted to be a duplex structure (see text). All faults on this diagram are brittle and post-metamorphic.

Figure 11: Isotope correlation plot for sample L51. All two-sigma errors are less than the diameter of the circles that represent the increments. The intercept age for this sample was calculated after the first and last increments were omitted.

Figure 12: Isotope correlation plot for sample L66. All two-sigma errors are less than the diameter of the circles that represent the increments.

Figure 13: Isotope correlation plot for sample L20a. All two-sigma errors are less than the diameter of the circles that represent the increments.

Figure 14: Our interpretation of the tectonic evolution of the MCT zone in the Langtang region. In all frames the active faults have arrows. (a) Formation of and ductile movement on the MCT coeval with normal movement on the South Tibetan detachment system (STDS) during Miocene time. (b) Motion begins on MBT in Mio-Pliocene (?) time; exact age of initiation of movement on the MBT is unknown. (c) Reactivation of the MCT (now designated as MCT'; initiation of D_{4MCT} event) in the brittle regime due to "back-breaking" from the MBT. (d) Further movement over a ramp on a structurally lower fault associated with the MBT (now designated MBT') causes folding of the MCT. Thus, the Kathmandu window is created.

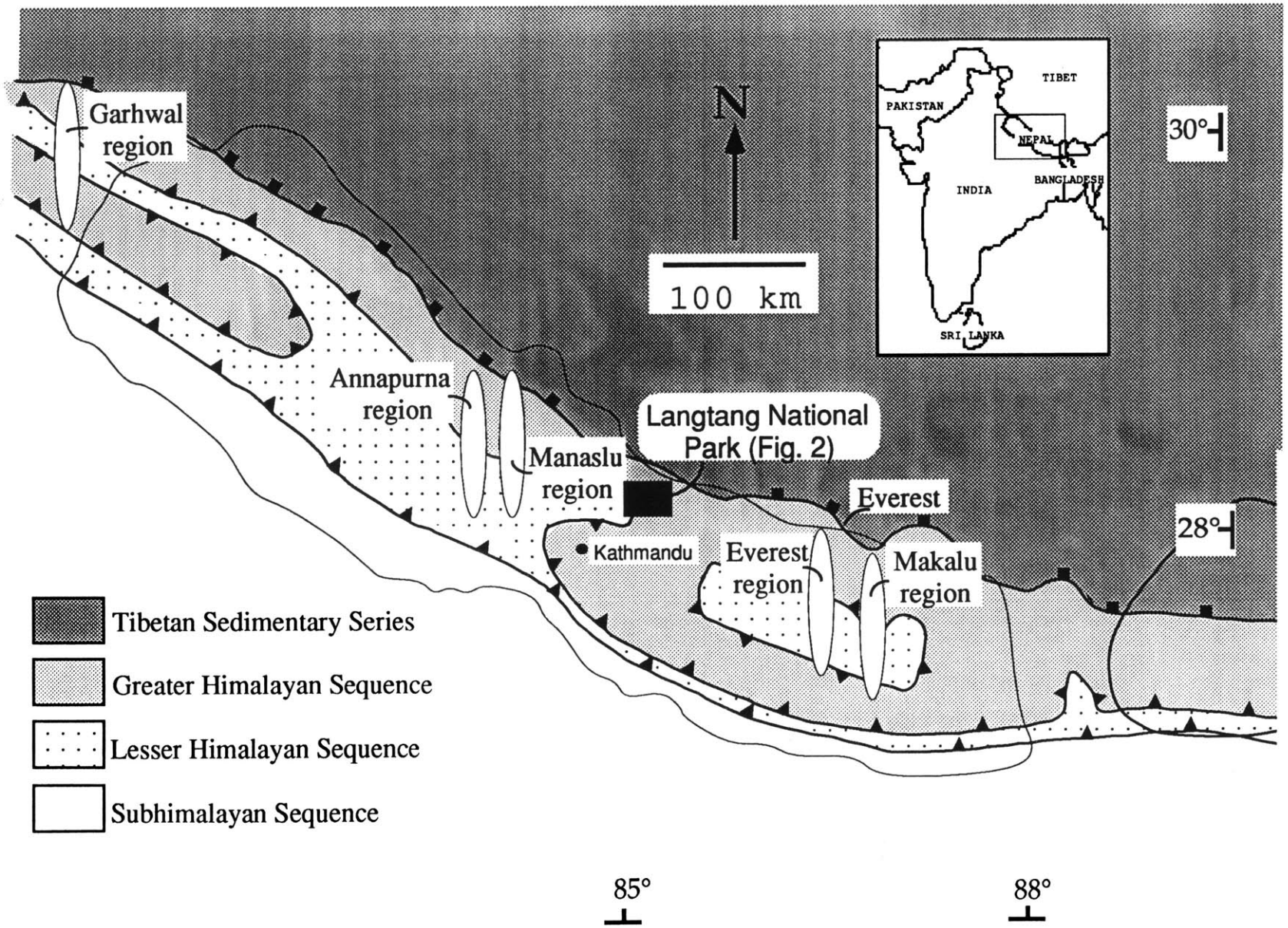
Garhwal region
Annapurna region
Manaslu region
Langtang National Park (Fig. 2)
Everest
Everest region
Makalu region
Kathmandu
N
100 km
TIBET
PAKISTAN
NEPAL
INDIA
BANGLADESH
SRI LANKA
30°
28°
85°
88°
Tibetan Sedimentary Series
Greater Himalayan Sequence
Lesser Himalayan Sequence
Subhimalayan Sequence

Figure 1

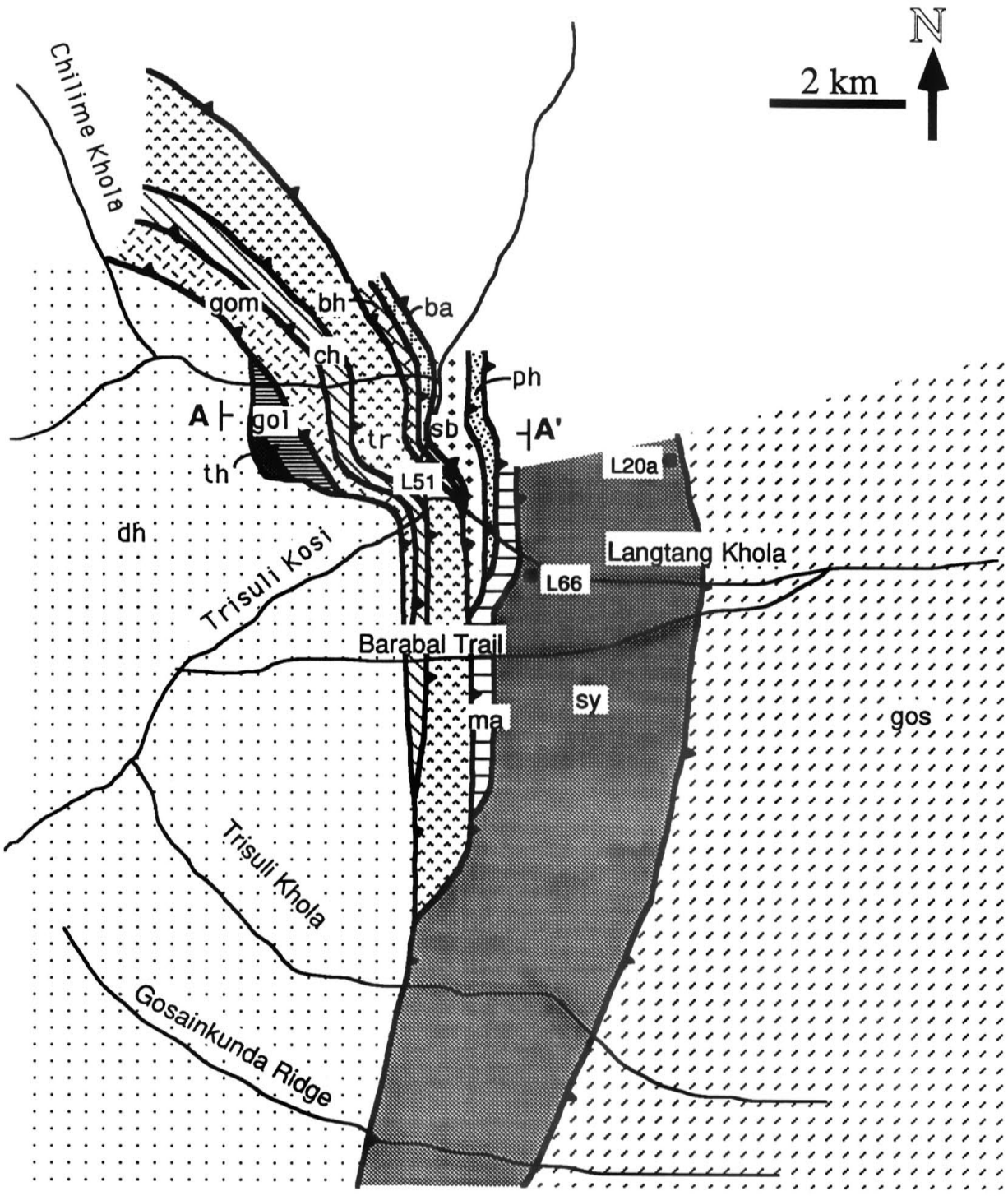
N
2 km
Chilime Khola
gom
bh
ba
ch
ph
A
goi
tr
sb
A'
th
L51
L20a
dh
Trisuli Kosi
Langtang Khola
L66
Barabal Trail
sy
ma
gos
Trisuli Khola
Gosainkunda Ridge

Figure 2

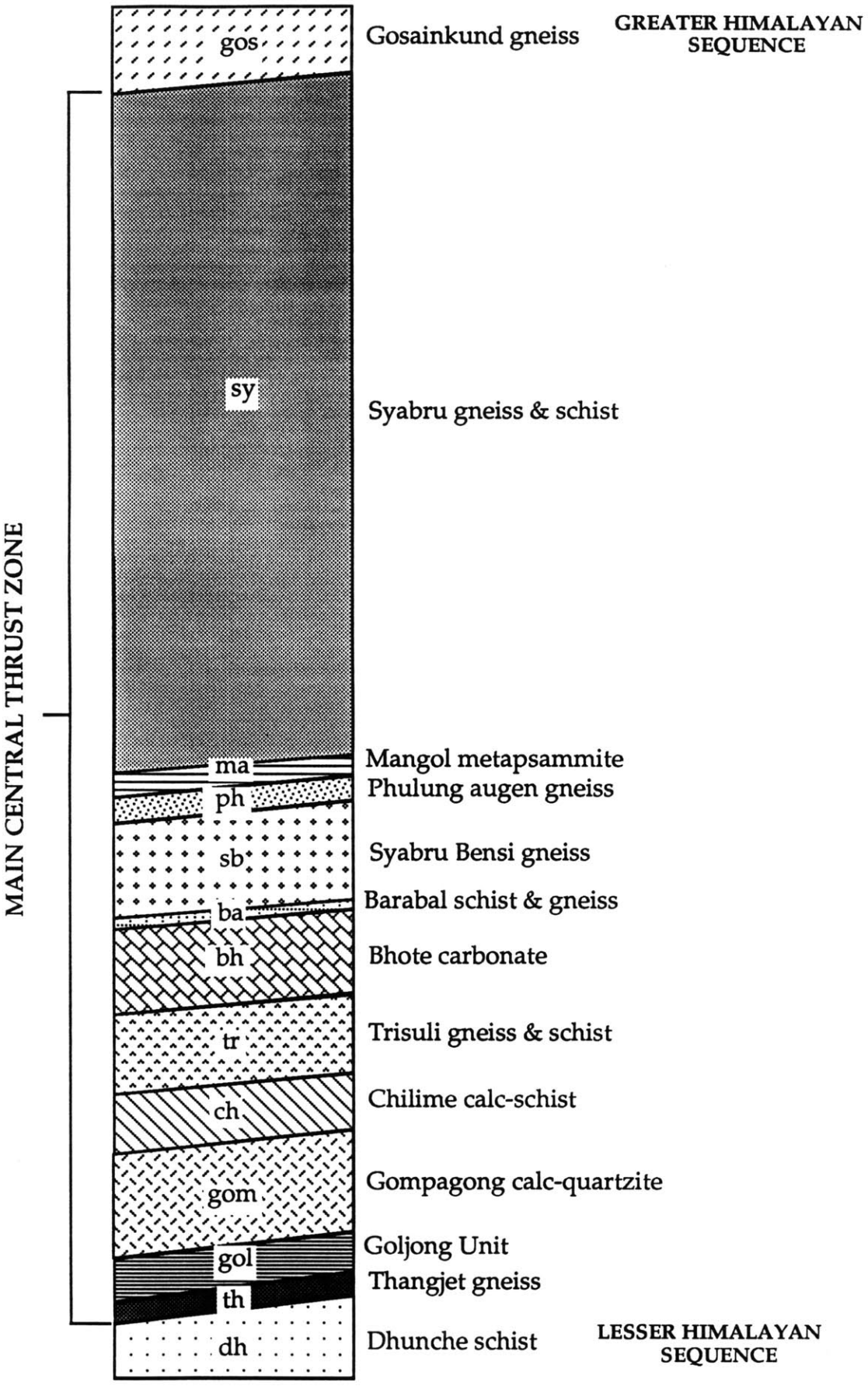
gos
Gosainkund gneiss
GREATER HIMALAYAN SEQUENCE
sy
Syabru gneiss & schist
MAIN CENTRAL THRUST ZONE
ma
Mangol metapsammite
ph
Phulung augen gneiss
sb
Syabru Bensi gneiss
ba
Barabal schist & gneiss
bh
Bhote carbonate
tr
Trisuli gneiss & schist
ch
Chilime calc-schist
gom
Gompagong calc-quartzite
gol
Goljong Unit
th
Thangjet gneiss
dh
Dhunche schist
LESSER HIMALAYAN SEQUENCE

Figure 3

a.

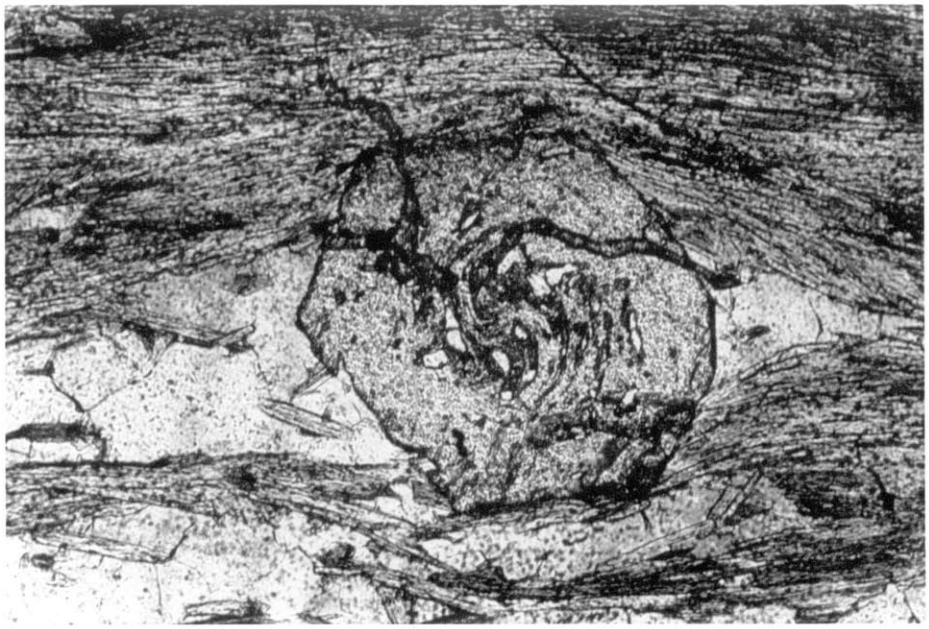

b.

Figure 4

c.

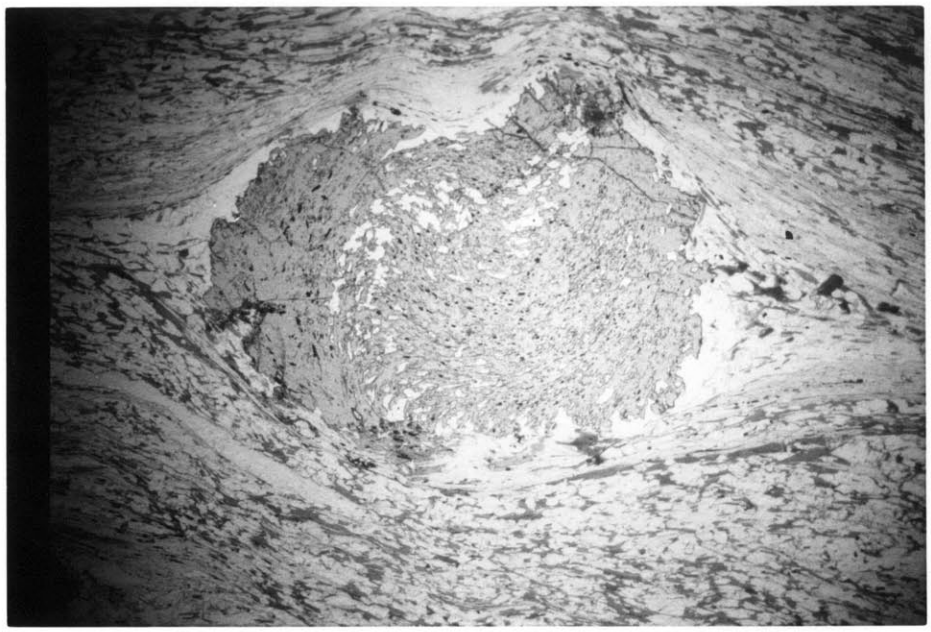

d.

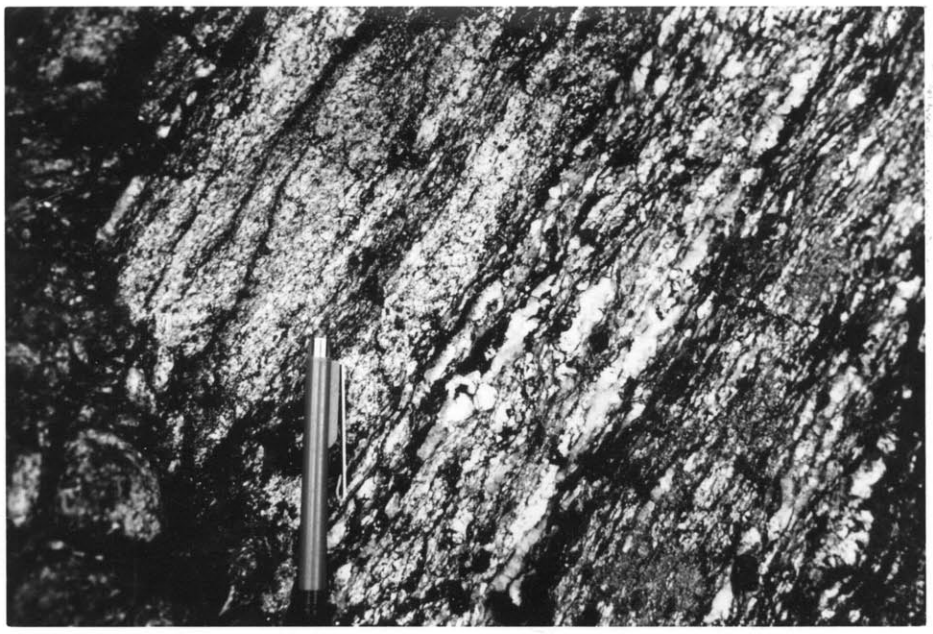

Figure 4

e.

f.

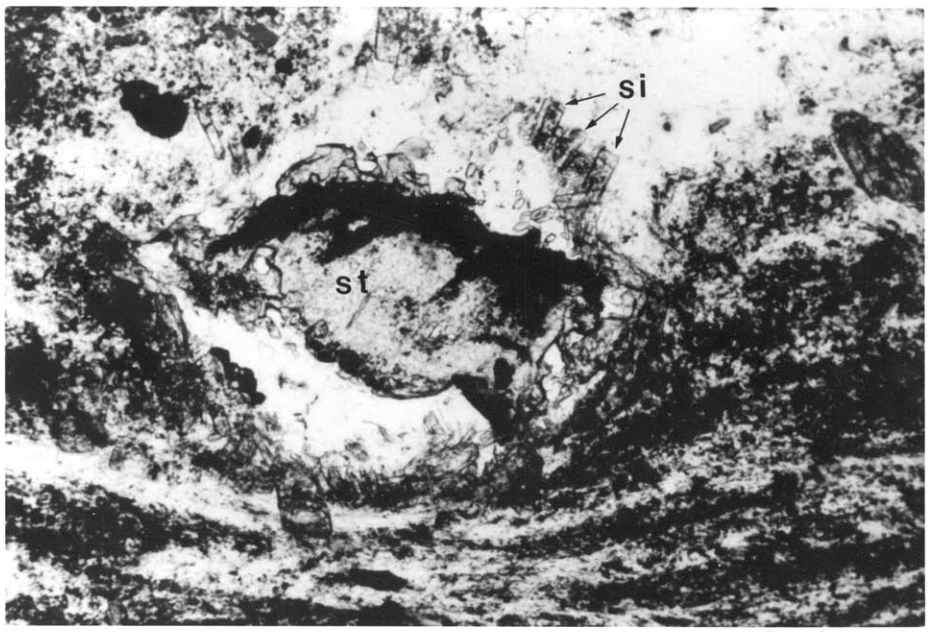

Figure 4

a.

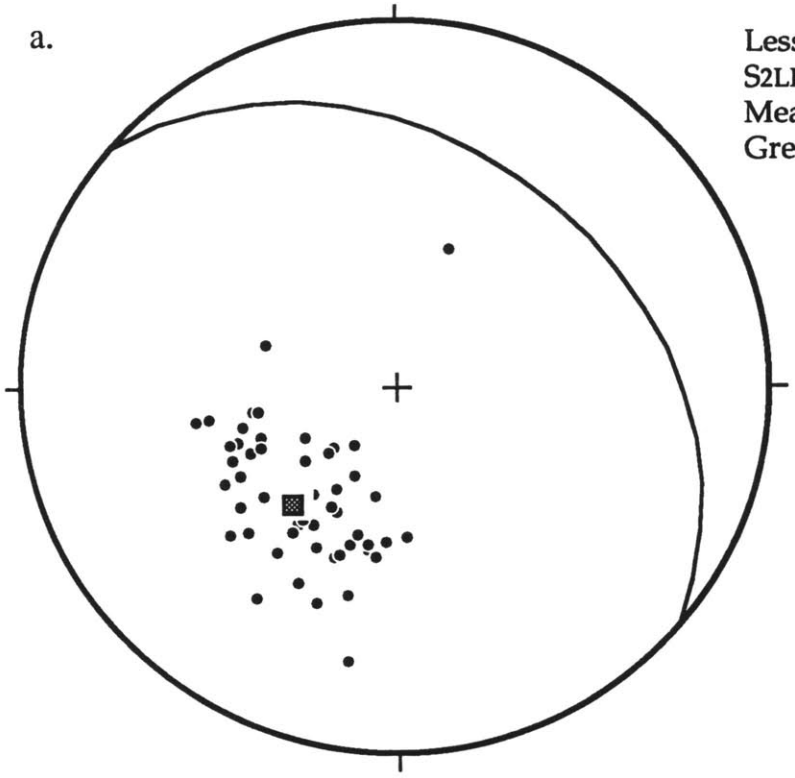

Lesser Himalaya sequence
S2LH Data, n = 53
Mean Vector: 56, S40W
Great Circle: N49W, 34NE

b.

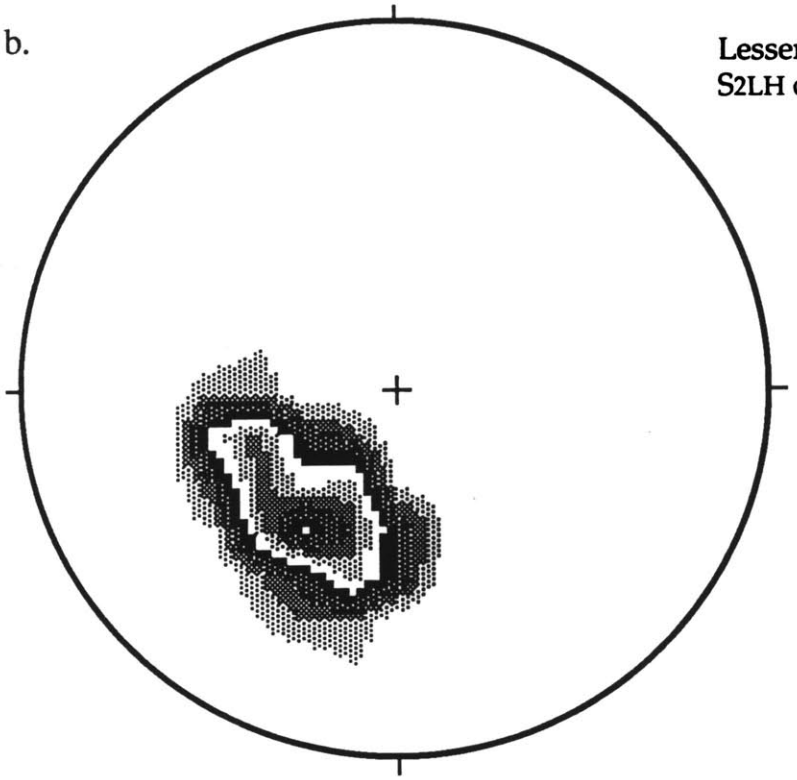

Lesser Himalaya sequence
S2LH contour interval: 1%/% area

Figure 5

c.

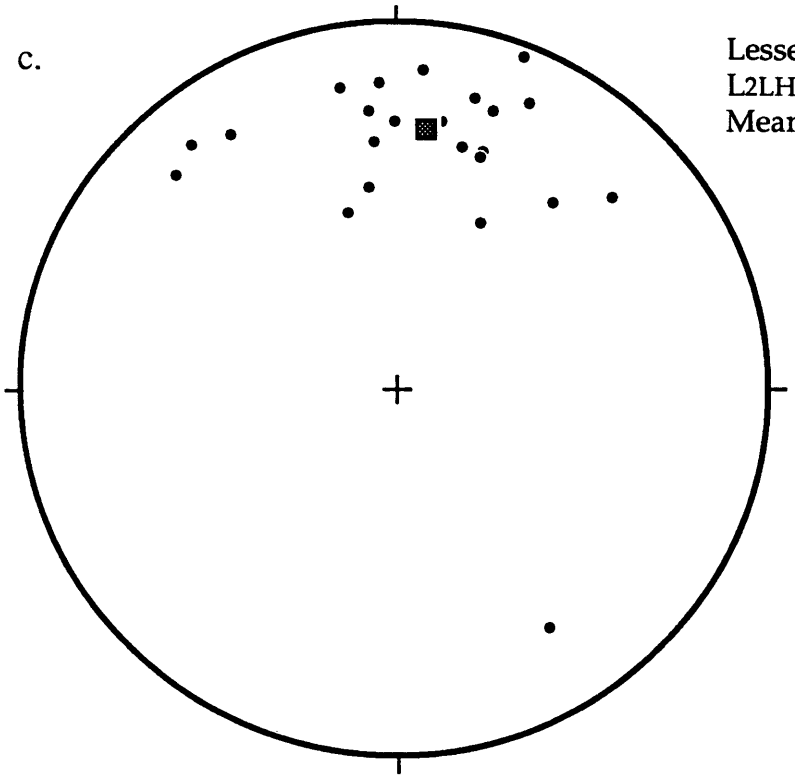

Lesser Himalaya sequence
L2LH Data, n = 23
Mean Vector: 29,N6.5E

d.

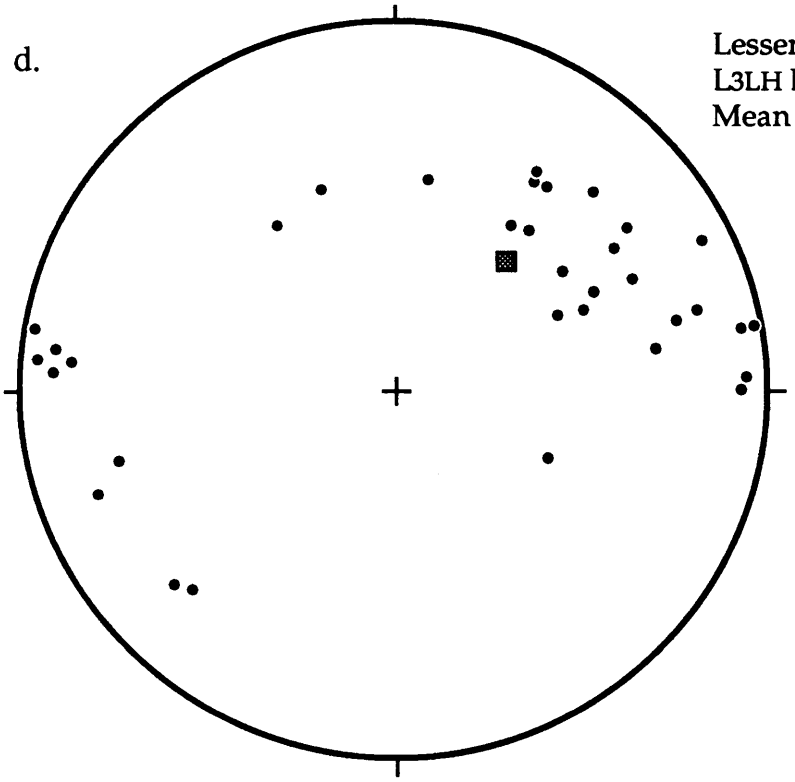

Lesser Himalaya sequence
L3LH Data, n = 34
Mean Vector: 41, N52E

Figure 5

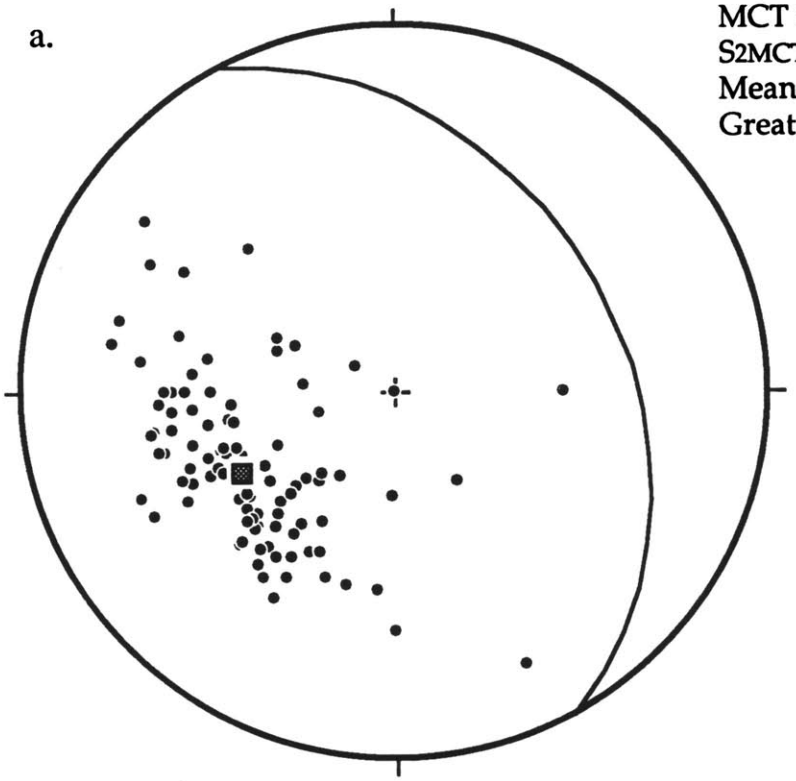
a.
MCT zone
S2MCT Data, n = 106
Mean Vector: 52, S62W
Great Circle: N28W, 38NE

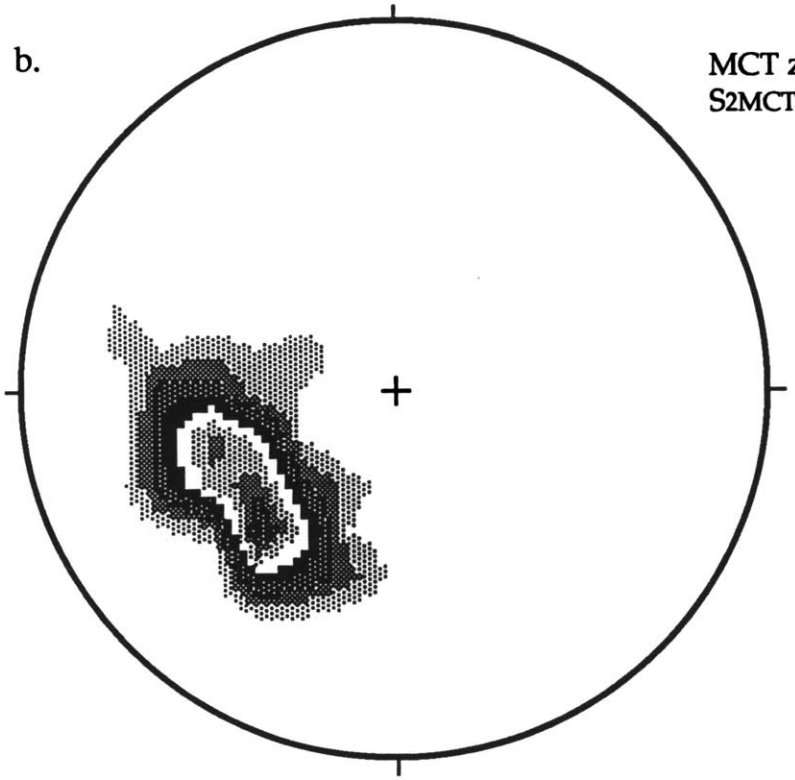
b.
MCT zone
S2MCT contour interval: 1%/% area

Figure 6

c.

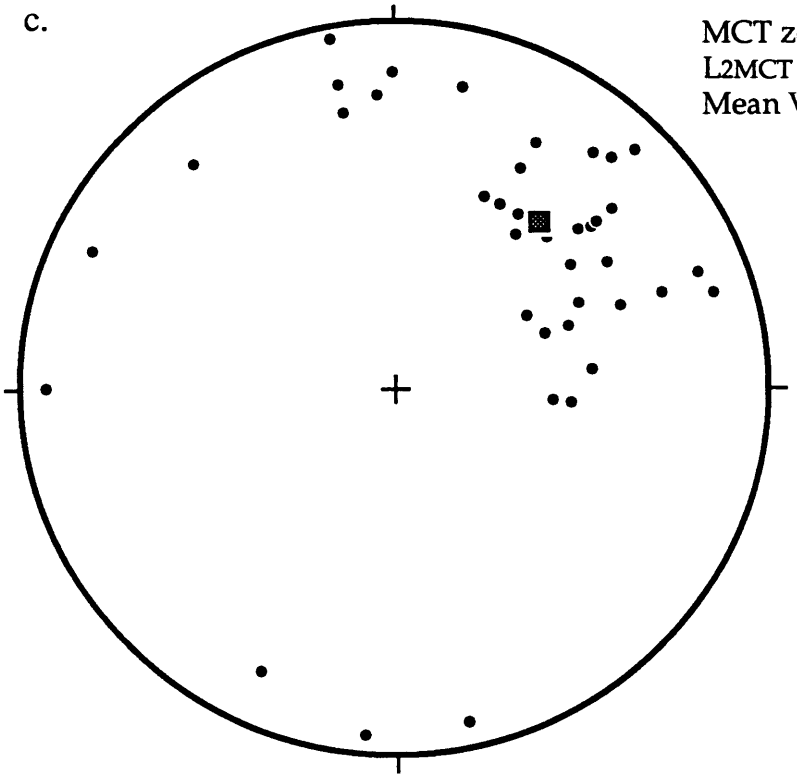

MCT zone
L2MCT Data, n = 41
Mean Vector: 40, N40E

d.

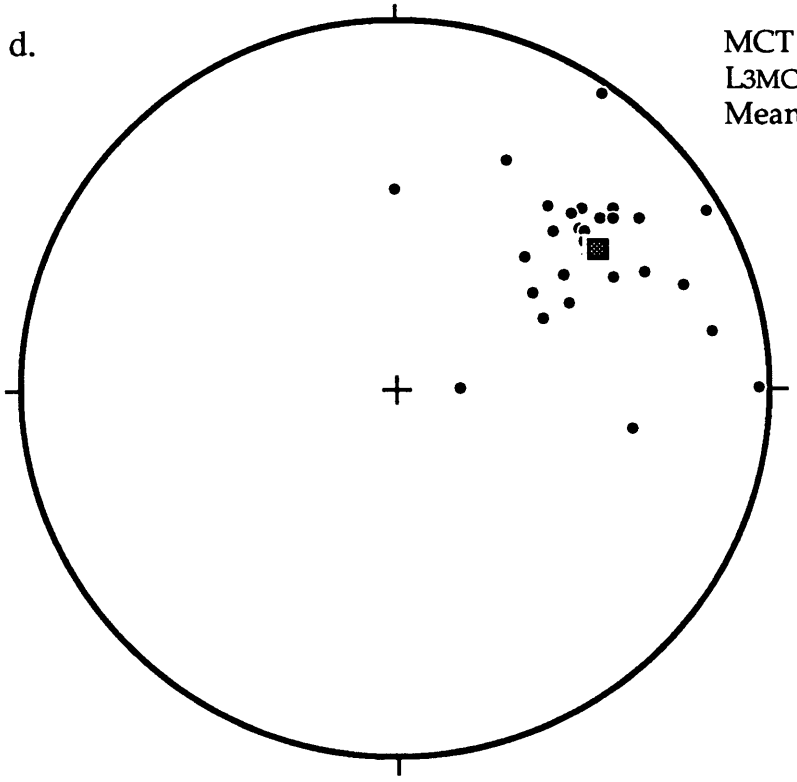

MCT zone
L3MCT Data, n = 29
Mean Vector: 34.5, N55E

Figure 6

a.

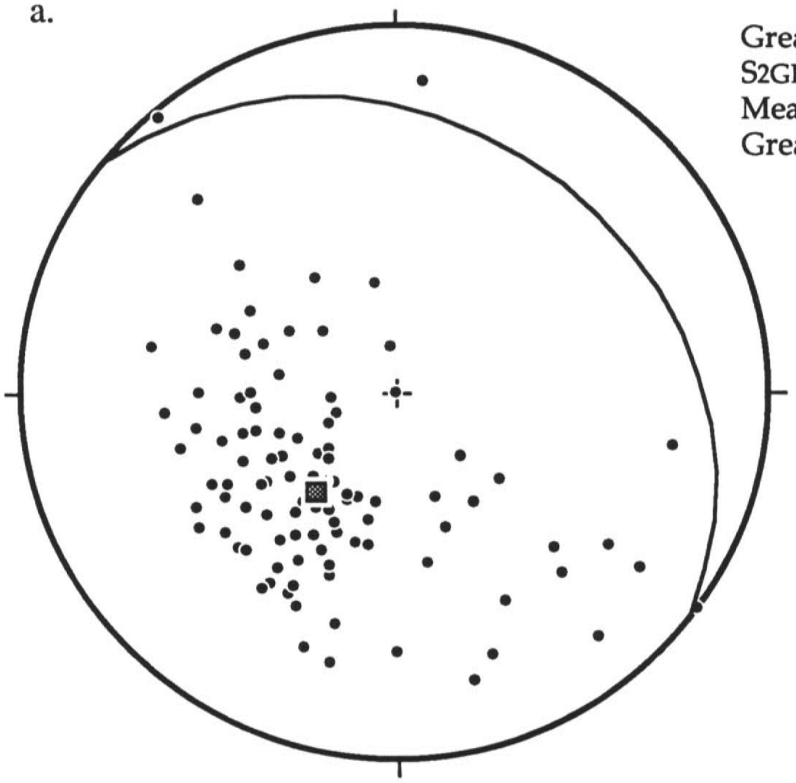

Greater Himalaya sequence
S2GH Data, n = 117
Mean Vector: 62, S39W
Great Circle: N52W, 28NE

b.

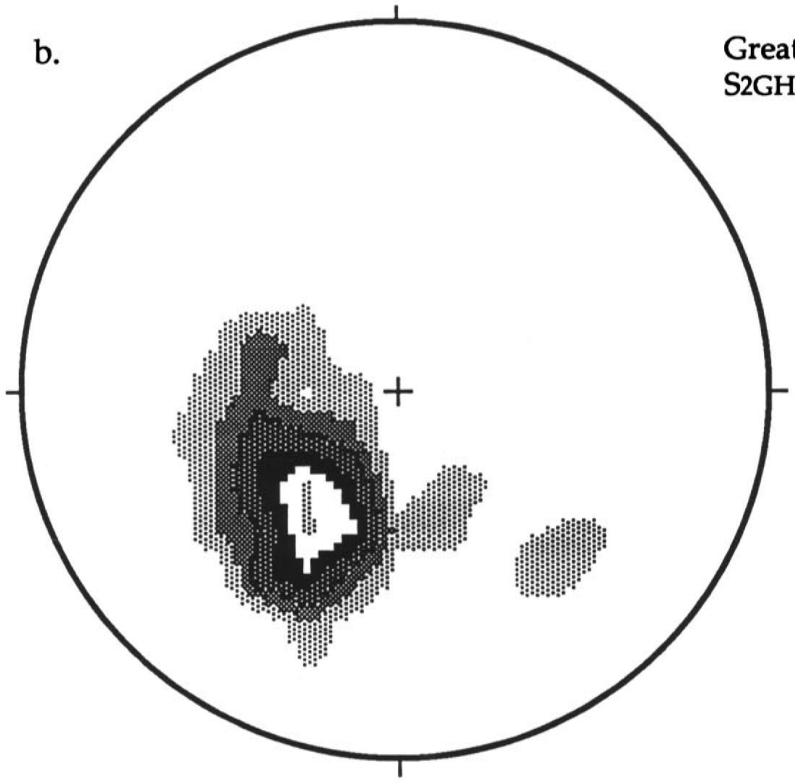

Greater Himalaya sequence
S2GH contour interval: 1%/% area

Figure 7

c.

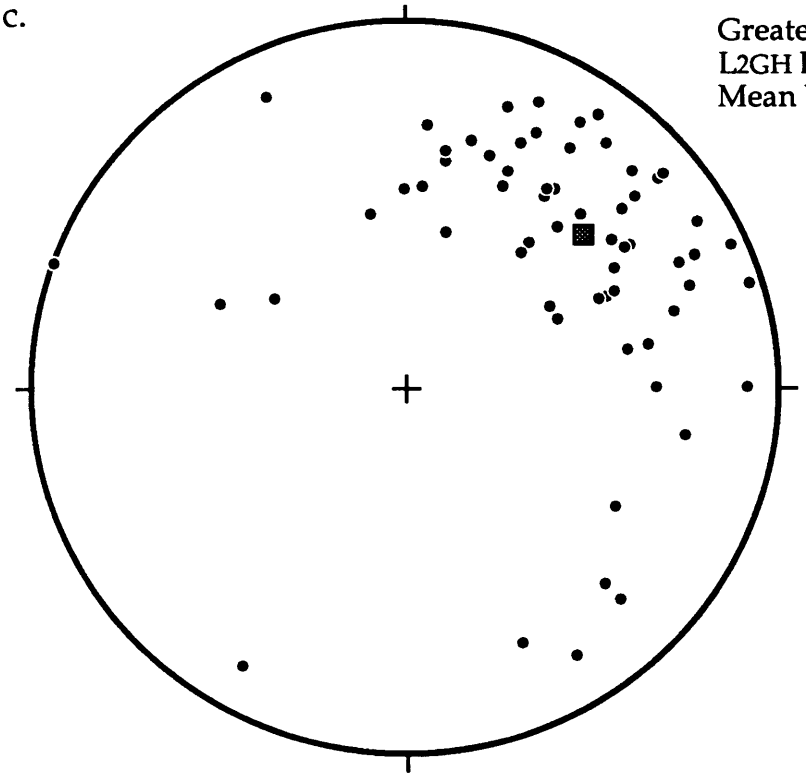

Greater Himalayan sequence
L2GH Data, n = 64
Mean Vector: 36, N49E

Figure 7

a.

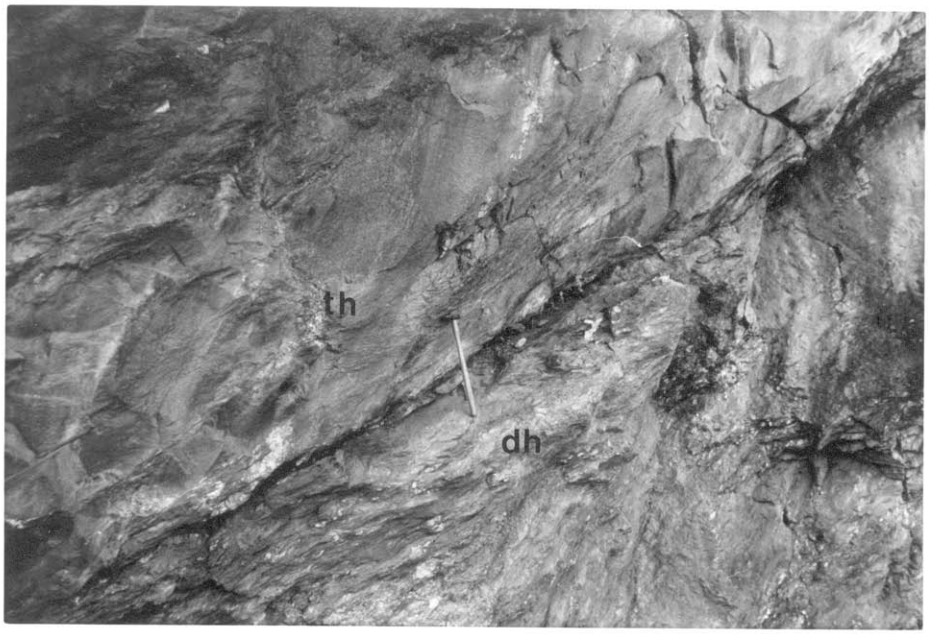

b.

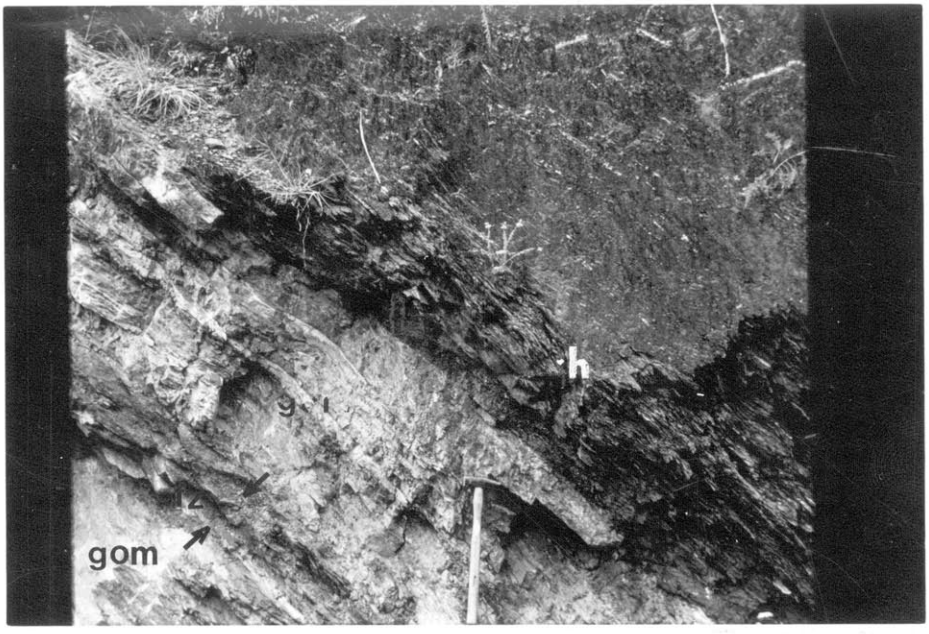

Figure 8

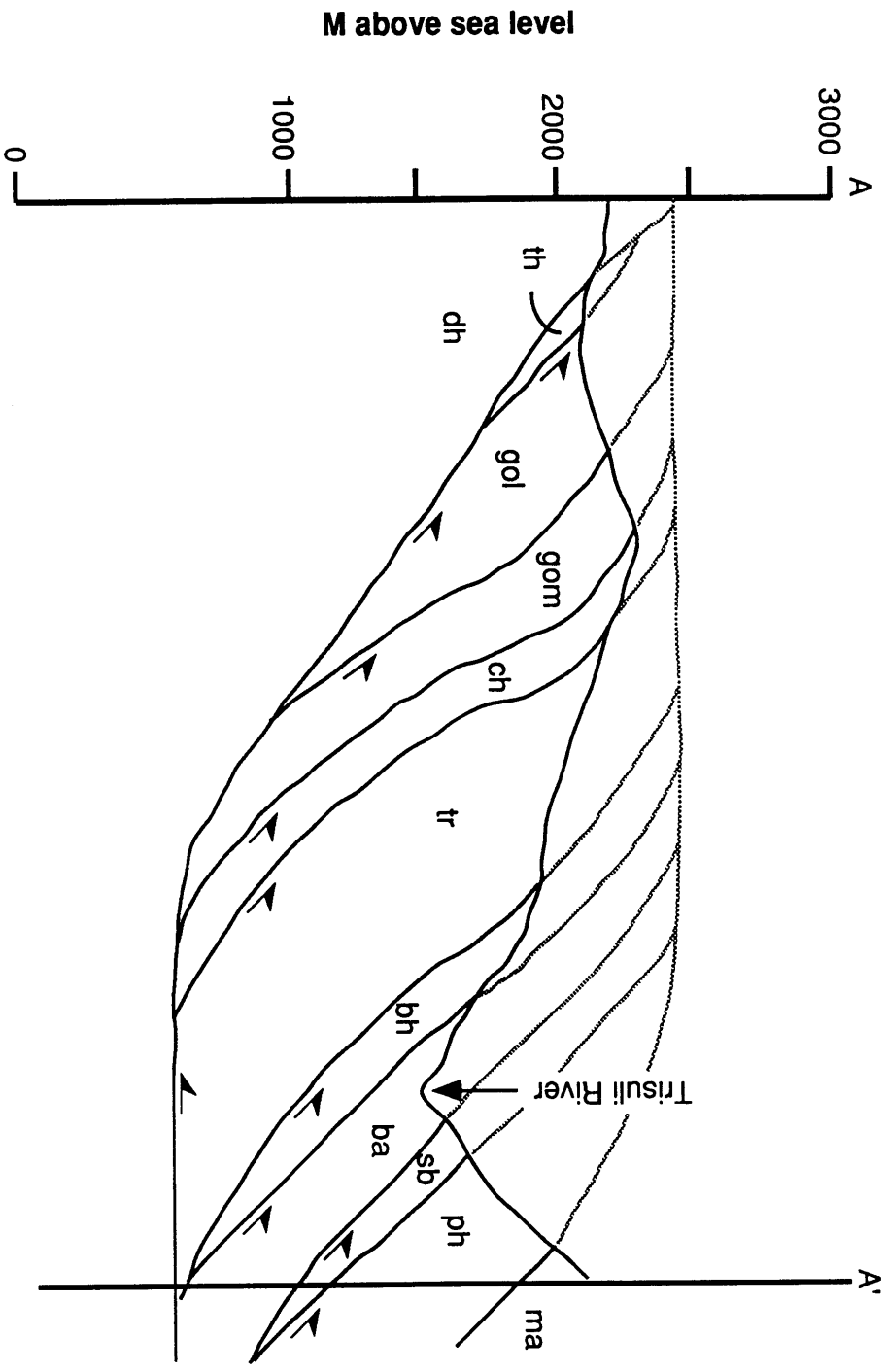
M above sea level
0
1000
2000
3000
A
th
dh
gol
gom
ch
tr
bh
Trisuli River
ba
sb
ph
ma
A'

Figure 10

a.

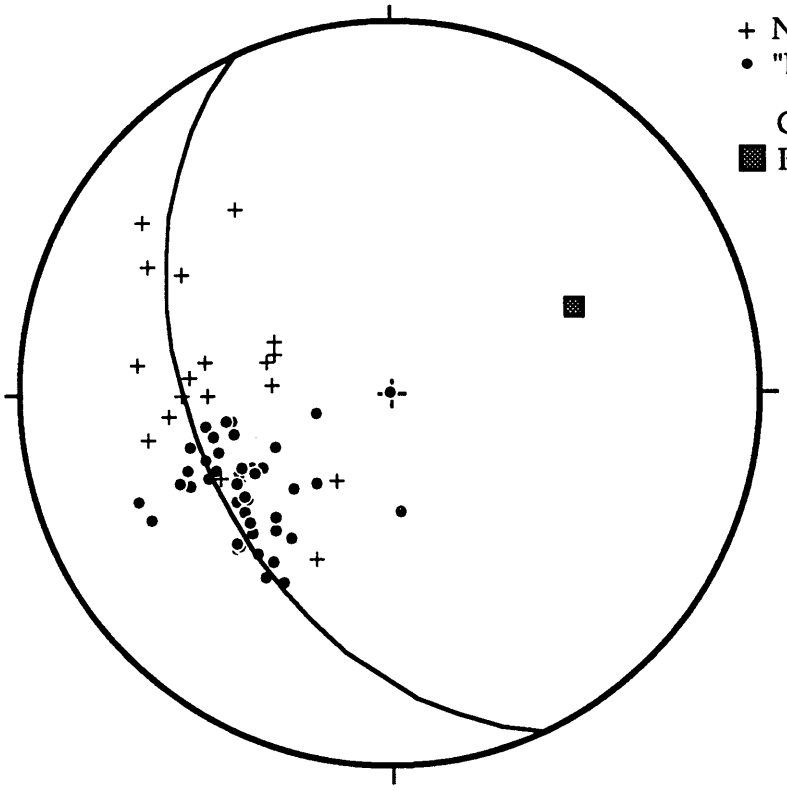

+ N/S S2 Foliations
• "Bend" S2 Foliations

Great Circle: N25W, 46SW
Pole (fold axis): 44, N60E

b.

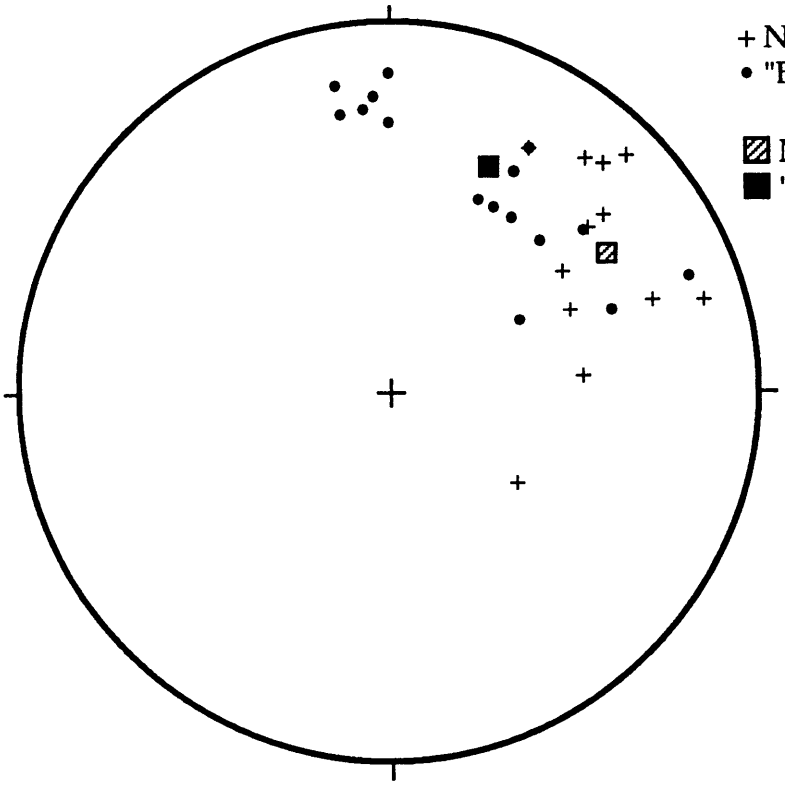

+ N/S L2 Lineations
• "Bend" L2 Lineations

N/S Mean Vector: 31,N57E
"Bend" Mean Vector: 34,N24E

Figure 9

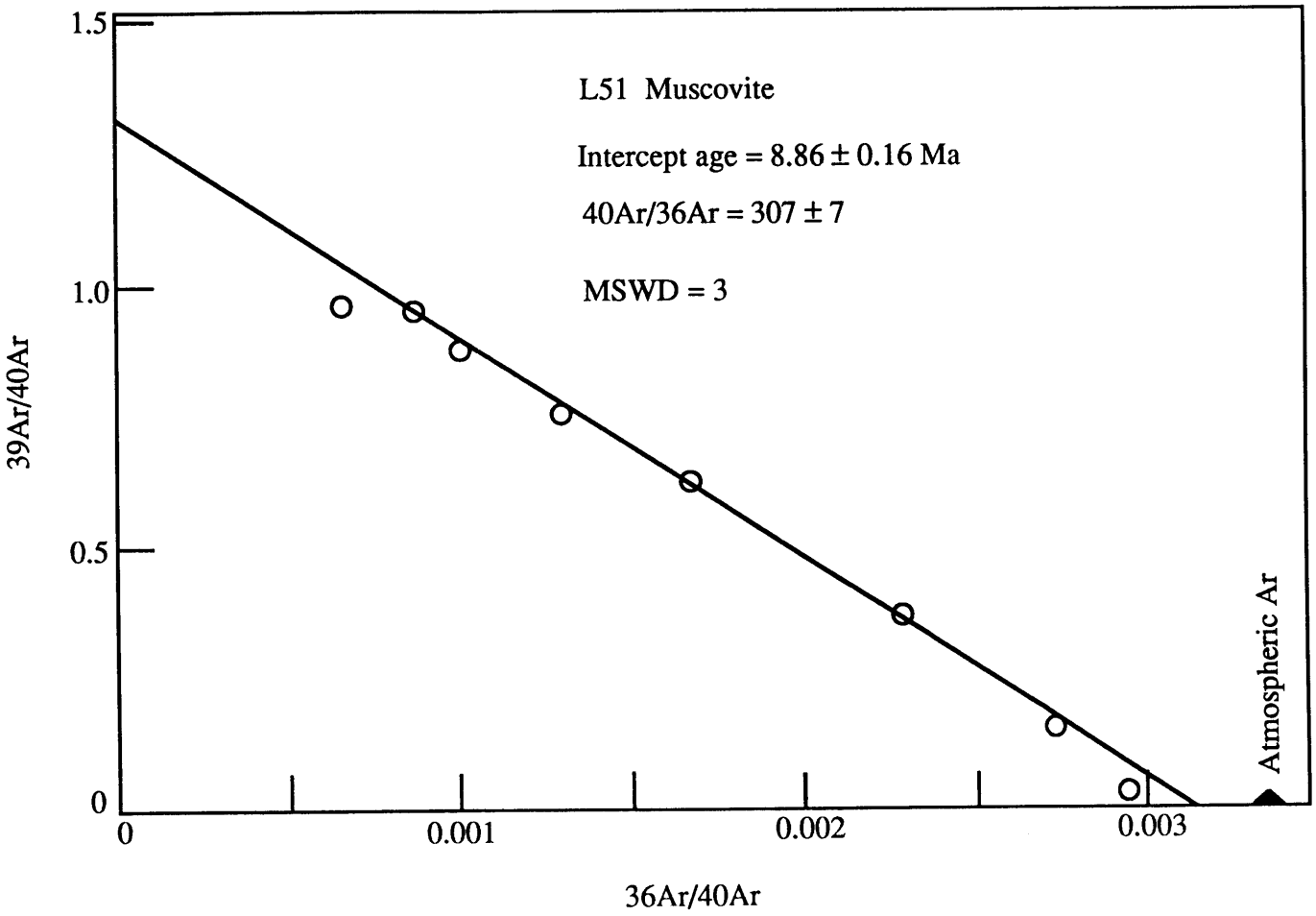
L51 Muscovite
Intercept age = 8.86 ± 0.16 Ma
40Ar/36Ar = 307 ± 7
MSWD = 3
Atmospheric Ar
39Ar/40Ar
36Ar/40Ar
1.5
1.0
0.5
0
0
0.001
0.002
0.003

Figure 11

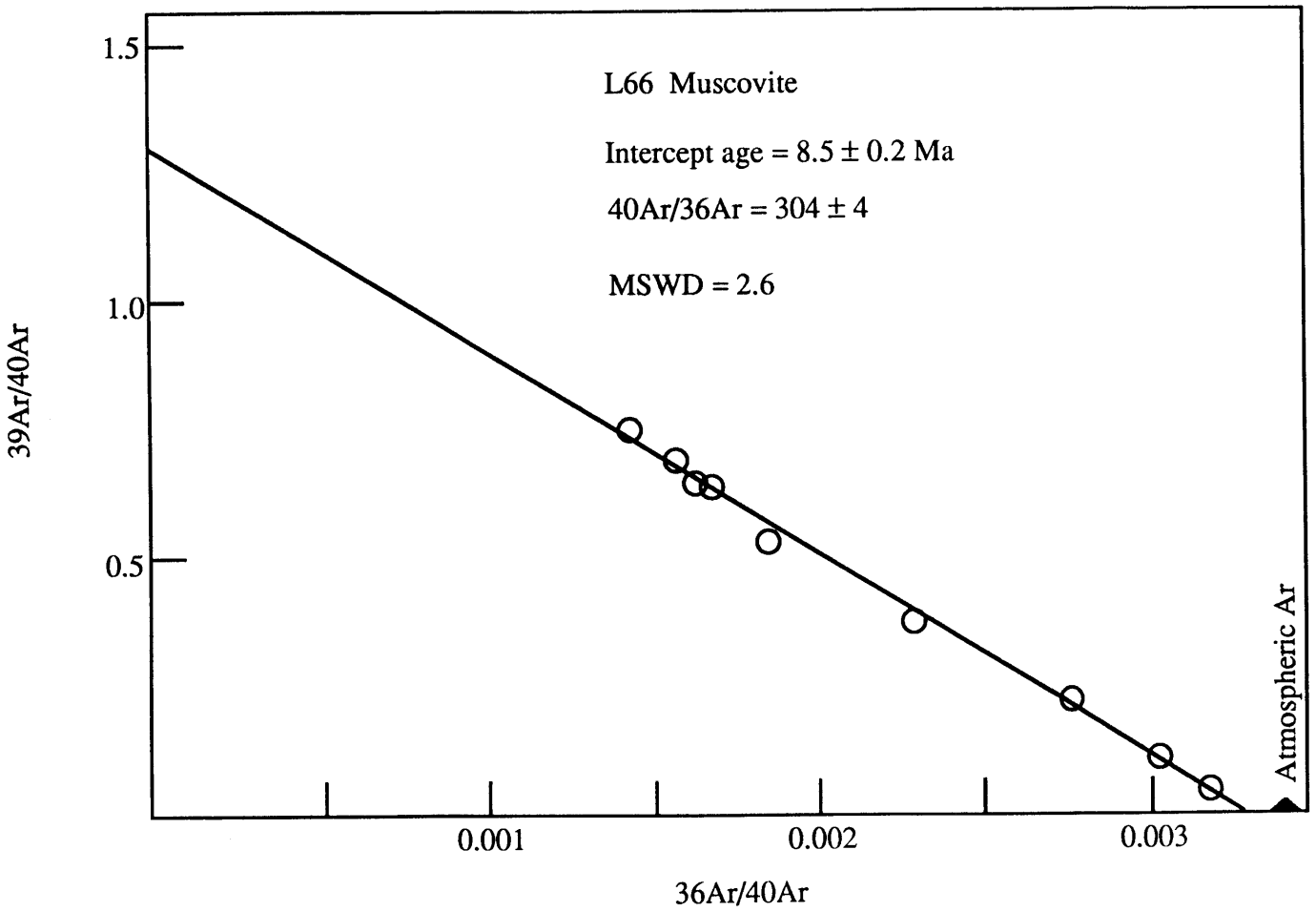
L66 Muscovite
Intercept age = 8.5 ± 0.2 Ma
40Ar/36Ar = 304 ± 4
MSWD = 2.6
39Ar/40Ar
1.5
1.0
0.5
0.001
0.002
0.003
36Ar/40Ar
Atmospheric Ar

Figure 12

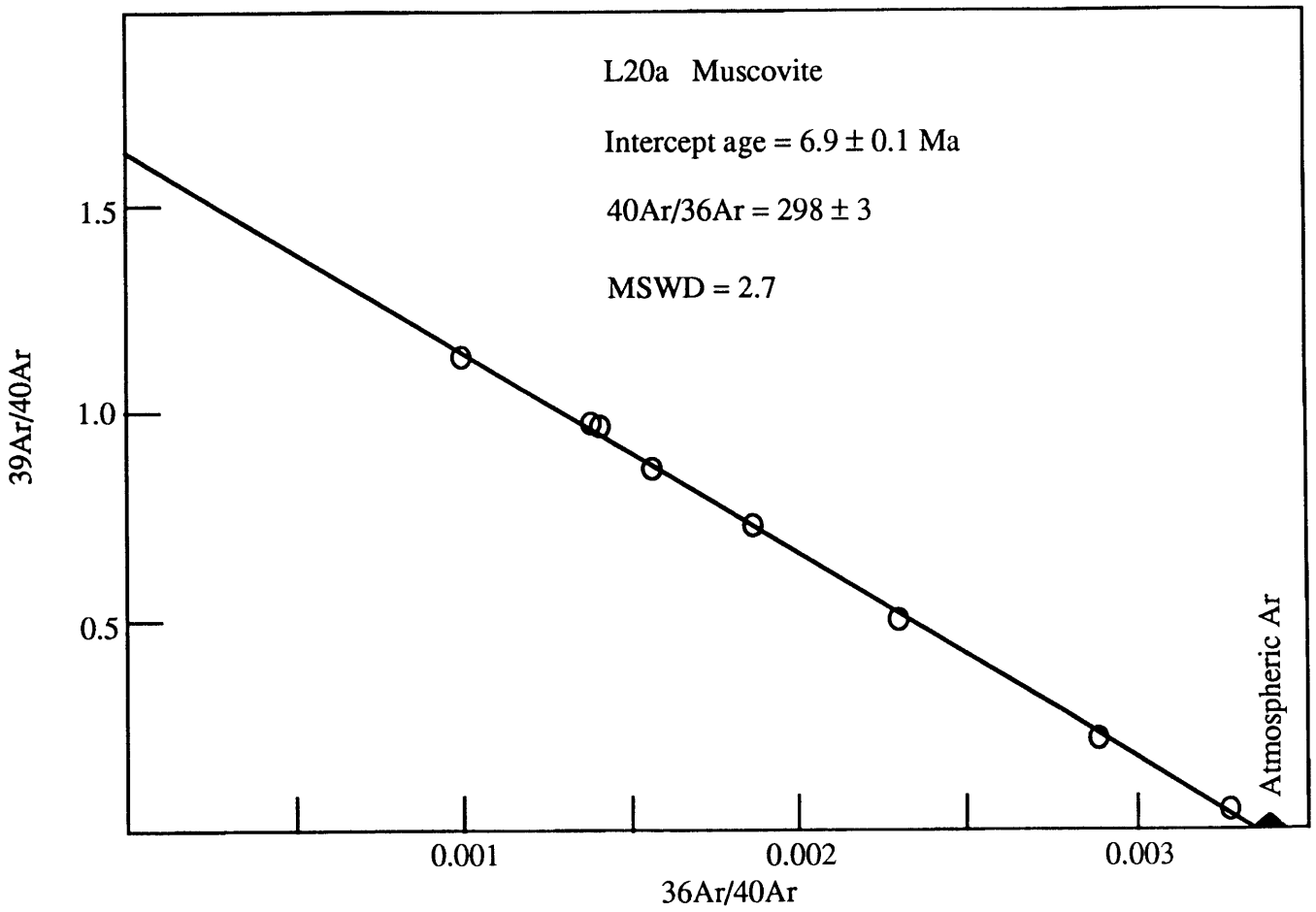
L20a Muscovite
Intercept age = 6.9 ± 0.1 Ma
40Ar/36Ar = 298 ± 3
MSWD = 2.7
39Ar/40Ar
1.5
1.0
0.5
Atmospheric Ar
0.001
0.002
0.003
36Ar/40Ar

Figure 13

Miocene

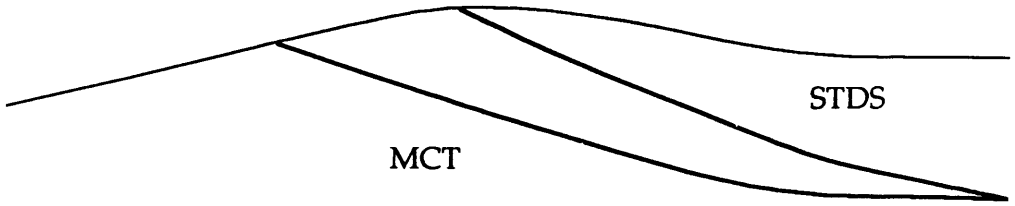

Miocene-Pliocene (?)

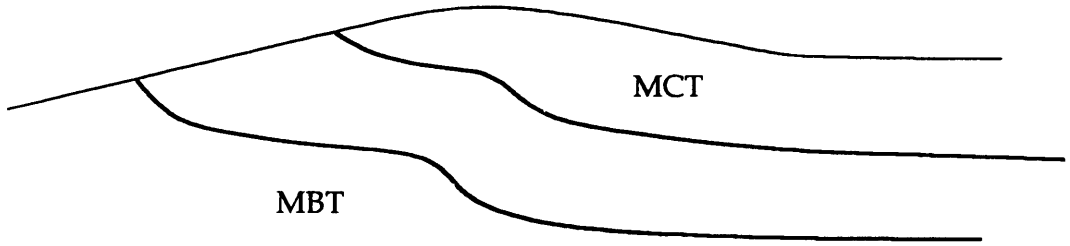

Pliocene

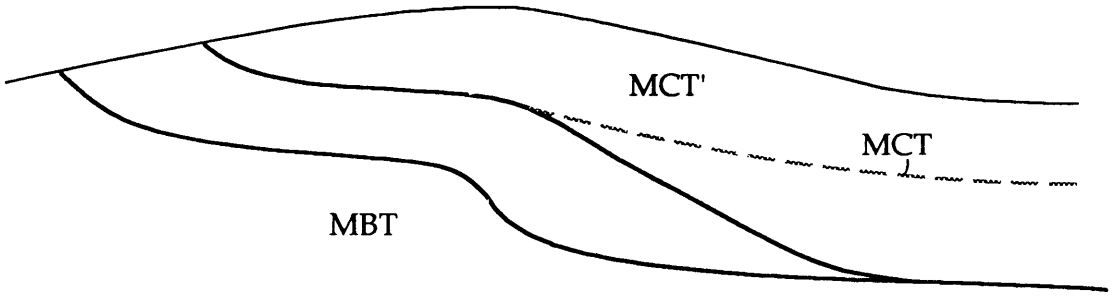

Modern

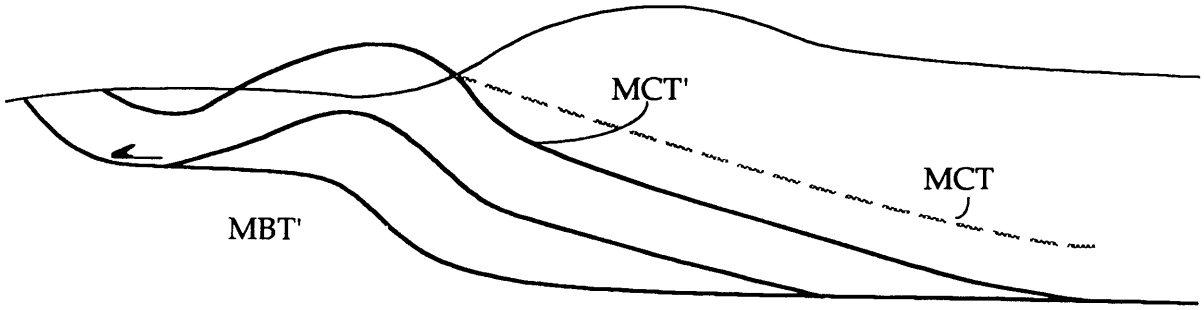

Figure 14

CHAPTER THREE

A Petrologic Examination of the Metamorphic Core of the Himalayan Orogen, Langtang National Park, Nepal

ABSTRACT

The crystalline core of the Himalayan orogen in the Langtang area of Nepal, located between the Annapurna - Manaslu region and the Everest region, contains middle to upper amphibolite-grade pelitic gneisses and schists. These rocks lie above the Main Central Thrust (MCT), one of the major compressional structures in the northern Indian plate, which forms a 3.7 km-wide zone containing rocks of both footwall and hanging wall affinity. An inverted metamorphic gradient is noticeable only in the hanging wall rocks, where metamorphic conditions increase from kyanite grade near the MCT zone to sillimanite + K-feldspar grade in the upper hanging wall. Petrographic data distinguish two metamorphic phases which have affected the area: a high pressure, moderate temperature phase (M_1) and a moderate pressure, high temperature phase (M_2). Thermobarometric results for twenty-four samples from the footwall, MCT zone and hanging wall reflect PT conditions during the M_2 phase of 300 - 700 MPa and 700 - 900 K. Estimated paleopressures show a slight decrease from footwall to hanging wall, with slight fluctuations in the MCT zone which reflect structural discontinuities, whereas paleotemperatures are indistinguishable across the entire area sampled. One viable interpretation of the lack of a paleotemperature gradient is that M_2 in the footwall, hanging wall and MCT zone resulted not from one single event, but a number of different events which affected the structural levels separately, such as heating during thrust emplacement in the footwall and shear heating in the MCT zone. Gibbs Method modeling together with the thermobarometric and microfabric data suggest that conditions for M_1 in the hanging wall were 1000 - 1200 MPa and 600 - 800 K.

INTRODUCTION

Although the Himalayan orogenic belt is over 2,500 km in length, most twentieth- century workers in the area have appealed to single unifying hypotheses to explain much of the geologic phenomena found therein (Bordet, 1961, Brunel and Kienast, 1986, Gansser, 1964, Le Fort, 1975, Valdiya, 1979). Certainly, some generalizations can be made about the geology of the range. It is truly impressive that certain structures, such as the Main Central Thrust (MCT), appear to be continuous along the length of the orogen. Relatively little geologic mapping and sample analysis have actually been done on the range due to its remote and often politically sensitive location. As more work is done, it is becoming clear that features are not as simple as first thought, and different mechanisms may create similar features in locations distant from one another. Data from this study, combined with the results of previous studies, suggest that the metamorphic evolution of the core of the orogen was not uniform along the length of the mountain belt.

Most petrologic studies of the metamorphic core of the Himalayan orogen have, in the past, concluded that an inverted paleothermal gradient is preserved across the MCT, a major zone of shortening on the Indian plate (Bordet, 1961, Bouchez and Pecher, 1976, Colchen, et al., 1981, Gansser, 1964, Heim and Gansser, 1939, Le Fort, 1975, Pecher, 1978). The widely accepted hypothesis for the inverted gradient was first discussed by Le Fort (1975), who envisioned the cause of the inversion as due to thrusting of a hot hanging wall over a cold footwall. In contrast, recent investigations of MCT zone rocks suggest a more complicated metamorphic history (Brunel and Kienast, 1986, Hodges, et al., 1988, Hodges and Silverberg, 1988, Le Fort, 1986).

To further constrain the metamorphic evolution of the core of the Himalayan orogen, I conducted research in the Langtang National Park area of east-central Nepal, located between the Manaslu region and the Everest region (Fig. 1). This paper reports the results of detailed petrographic and thermobarometric analyses of samples collected from the Lesser Himalayan sequence, the MCT zone and the Greater Himalayan sequence in the Langtang region. Structural studies in the same area indicate that significant post-metamorphic movement has occurred on the MCT (Macfarlane et al., in press). The data presented here suggest that no inverted paleothermal gradient exists across the MCT at Langtang and that the apparent increase in metamorphic grade upward in the hanging wall of the MCT is associated with emplacement of granites at high levels.

GEOLOGIC SETTING

Regional Geology

The core of the Himalayan orogen consists of three major tectonostratigraphic units, each separated by a major fault (Fig. 1). At the top of the structural pile in Tibet and northern Nepal is the Tibetan Sedimentary sequence, a Cambrian - Eocene series of deformed but generally unmetamorphosed sedimentary rocks that were deposited along the northern Indian margin prior to collision. The South Tibetan detachment system (Burchfiel, et al., 1992), a series of north-dipping normal faults, forms the contact between the Tibetan Sedimentary sequence and the Greater Himalayan sequence below (Burchfiel and Royden, 1985, Burchfiel, et al., 1992, Burg, et al., 1984, Herren, 1987). The physiographic high Himalaya encompass the Greater Himalayan sequence. This unit forms the crystalline core of the Himalaya and consists of amphibolite grade schists, gneisses and migmatites with Oligocene -

Miocene leucogranite plutons located in the upper portion. The Main Central Thrust, a major north-dipping fault zone, constitutes the basal contact of the Greater Himalayan sequence. The footwall of the MCT is the Lesser Himalayan sequence, upper Precambrian to Lower Eocene chlorite to staurolite grade metasedimentary and metavolcanic rocks. The basal contact of the Lesser Himalayan sequence is the Main Boundary Thrust (MBT), another major north-dipping fault zone which is presently active (Gansser, 1964, Molnar, 1984).

The inverted metamorphic gradient in the Himalayan orogen was first described by Oldham (1883) in north-eastern India. Gansser (1964) described this gradient within the footwall of the MCT in Garhwal, India. Based on petrographic and thermobarometric analyses on rocks from Garhwal, Hodges and Silverberg (1988) suggested that two metamorphic events affected the metamorphic core: an early high pressure, high temperature event (>960 MPa; >900 K) that affected the entire hanging wall of the MCT; and a later low pressure, high temperature event (317-523 MPa; >900 K) that affected only the upper portion of the hanging wall of the MCT.

In central Nepal, Le Fort (1975) described inverted metamorphic gradients in the footwall, the MCT zone and the lower portion of the hanging wall. Le Fort (1975) devised an elegant theory to explain the inverted gradient in the footwall and lower hanging wall of the MCT in central Nepal. He suggested that, if a hot hanging wall was thrust on top of a cold footwall, conductive cooling of the hanging wall and heating of the footwall would produce an inverted metamorphic gradient (Le Fort, 1975). Quantitative thermobarometric data for the core of the Nepalese Himalaya were first reported by Le Fort et al. (1986) for central Nepal south of Annapurna (Fig. 1). They interpreted their temperature data as showing an inverted gradient at the base of the hanging wall. Recent quantitative studies from the nearby Manaslu region of central

Nepal suggest that there is no paleothermal gradient associated with the MCT in this region (temperatures are indistinguishable at 870 ± 50 K; Hodges, et al., 1988). Hodges et al. (1988) suggested that the entire section was thermally buffered by tectonic and magmatic events. In central Nepal, petrography suggests the presence of two metamorphic events (Pecher and Le Fort, 1986). The early event is a high pressure - high temperature metamorphism and the later one is a less widespread low pressure - high temperature metamorphism probably associated with intrusion of leucogranites located in the upper part of the hanging wall and occurred syn- to post-kinematically with respect to the main foliation development (Le Fort, 1975, Pecher and Le Fort, 1986).

In eastern Nepal two contradictory data sets have been reported. South of Mt. Everest (Fig. 1), Hubbard (1988, 1989) suggested that no metamorphic break exists across the MCT zone and interpreted her thermobarometric data to indicate a normal lithostatic pressure gradient but an inverted paleothermal gradient from the base to the top of the MCT zone. In contrast, Brunel and Kienast (1986), who worked south of Makalu (Fig. 1), described a post-metamorphic MCT. They identified two metamorphic events within the hanging wall: an early high pressure - high temperature event (approximately 825 - 925 K and 600 - 900 MPa) and a later low pressure - high temperature event (approximately 785 - 990 K and 350 - 500 MPa), neither of which was associated with major movement along the MCT. Brunel and Kienast (1986) suggested that the inverted metamorphic gradient associated with the MCT is the result of post-metamorphic shuffling of rocks and thus not a true inverted metamorphic gradient.

Langtang Area Geology

In the Langtang National Park region of Nepal (Fig. 1), there are excellent exposures of the Lesser Himalayan sequence, the MCT zone and the Greater Himalayan sequence (Fig. 2). In the field area, the Lesser Himalayan sequence consists of more than 3.9 km of biotite to garnet grade pelitic schists, metapsammites and siliceous metalimestones. Spectacular exposures of the MCT zone along ridgetops and roadcuts permitted a detailed study of the zone which led to the conclusion that the MCT is presently a post-metamorphic structure in the Langtang region but experienced both ductile and brittle phases of deformation (Macfarlane et al., in press). Here, the 3.7 km-wide MCT zone is made up of a structurally distinctive package of lithotectonic units that is internally imbricated and bounded on the top and bottom by brittle faults. The map pattern and field relations suggest that the MCT in the Langtang region is a duplex structure (Macfarlane et al., in press). The MCT zone lithologic units have affinities with both the Lesser Himalayan and Greater Himalayan sequences. The top of the MCT zone is marked by the first appearance of migmatites. The Greater Himalayan sequence in the Langtang region consists of kyanite to sillimanite grade pelitic schists and gneisses including a few amphibolites and pyroxene gneisses. Migmatites and leucogranite dikes increase in volume and number toward the top of the sequence. No large plutons are present in the immediate area.

Four deformational events have affected the Greater Himalayan sequence and the MCT zone rocks and three major events have affected the Lesser Himalayan sequence (Macfarlane et al., in press). The first event led to the formation of foliation and isoclinal folding. This event, which is correlative in all units, may have occurred before movement began on the MCT. The second event in the Lesser Himalayan sequence and the MCT zone was associated with ductile movement on the MCT. In the Greater Himalayan sequence, the second event included ductile movement on the

MCT and probably concurrent normal-sense motion on the Giyrong detachment (part of the South Tibetan detachment system, Burchfiel, et al., 1992). The second deformational event in all three lithologic sequences is responsible for the dominant foliation, which strikes to the northwest and dips moderately to the northeast. The third and fourth deformational events are not necessarily correlative across all three tectonostratigraphic units. Brittle reverse-sense (top-to-the-south) movement constitutes the third deformational event in the MCT zone, which occurred post-metamorphically. The third event in the Lesser Himalayan sequence is marked by brittle faults of unknown movement direction; in the Greater Himalayan sequence it is manifested by chlorite grade shear zones of unknown movement sense. Finally, late brittle extensional motion occurred in both the MCT zone and Greater Himalayan sequence, possibly associated with late Plio-Miocene normal faulting that accounted for continued gravitational collapse of the orogen (Royden and Burchfiel, 1987, Macfarlane et al., in press).

PETROGRAPHY AND PHASE EQUILIBRIA

Figure 2 is a geologic map of the Langtang region and displays the locations and lithologic units from which the samples were collected. Over 150 thin sections of samples from this area were examined in detail. Of those, twenty-four were selected for intensive petrographic analysis and quantitative thermobarometry: two from the Lesser Himalayan sequence, eleven from the MCT zone and eleven from the Greater Himalayan sequence (Fig. 2). Samples were collected along four main transects: the Trisuli Kosi drainage, the Trisuli Khola drainage, the Langtang Khola drainage and the Chilime Khola drainage (Fig. 2). Both Lesser Himalayan sequence samples are pelitic schists. Samples from the MCT zone come from four lithotectonic units, either pelitic schists or gneisses. Four of the samples in the MCT zone originate from the

same lithotectonic unit, the Trisuli gneiss and schist (Macfarlane et al., in press). Six of the samples from the Greater Himalayan sequence were collected from the Gosainkunda pelitic gneiss (Macfarlane et al., in press). The remainder of the Greater Himalayan sequence samples come from other pelitic gneiss units.

Descriptive Mineralogy

Table 1 is a summary of the phases present in each sample listed from lowest to highest structural level. Note that in the rest of the paper, the MCT zone is informally subdivided into two parts: the lower MCT zone which has affinities with the Lesser Himalayan sequence (samples L17, L58b, L123e, L18a, L94b, L63) and the upper MCT zone, which has affinities with the Greater Himalayan sequence (samples L67, L103a, L48, L71a, L20a). Lesser Himalayan sequence and lower MCT zone samples contain the assemblage: garnet + biotite + chlorite + muscovite ± plagioclase + quartz . The assemblage for the upper MCT zone samples is garnet + biotite + chlorite + muscovite ± staurolite ± kyanite + plagioclase + quartz. Lower Greater Himalayan sequence samples contain the assemblage garnet + biotite ± chlorite + muscovite ± kyanite + plagioclase + quartz. Samples from the middle Greater Himalayan sequence all contain garnet + biotite + muscovite ± kyanite ± sillimanite + plagioclase + quartz. The assemblage for the upper Greater Himalayan sequence is garnet + biotite ± muscovite + sillimanite + K-feldspar + plagioclase + quartz . In addition, in the upper Greater Himalayan sequence samples, abundant myrmekitic intergrowths are present. As structural depth decreases, the grade appears to increase from initially garnet to staurolite + kyanite to kyanite to kyanite + sillimanite and finally to K-feldspar + sillimanite. This apparent inverted gradient may not be an accurate reflection of the relative peak conditions, and this point will be addressed later.

Lesser Himalayan sequence

Garnets are generally small (up to 0.75 mm diameter), sub- to euhedral and contain inclusions of quartz, biotite, chlorite and opaque phases aligned in helicitic trails that lie inside an inclusion-free rim (Fig. 3a). The modal percentage of garnet in these samples is approximately 5% - 10%. The Lesser Himalayan sequence garnets are all pre-kinematic with respect to the main foliation; these garnets are enveloped by pressure shadows of quartz + muscovite + biotite within the dominant schistosity.

Biotite occurs in all Lesser Himalayan sequence samples and defines the main foliation in each sample. Biotite makes up approximately 20% - 30% modal proportion and crystal lengths range from 0.025 mm to 0.75 mm. In some samples late biotite grains grew across the main fabric. In the Lesser Himalayan sequence, the biotite is an orange - brown color under plane light.

Muscovite is present in all Lesser Himalayan sequence samples. It defines the foliation in all samples and makes up 20% - 25% modal proportion. Muscovites have a similar size range to the Lesser Himalayan biotites.

Chlorite is euhedral to subhedral, appears to be primary and is aligned in the main foliation. Chlorite makes up <1% - 10% modal proportion and grains reach 0.75 mm in length. Garnets in some of the samples have been slightly altered to chlorite on their rims.

Plagioclase is rare in the Lesser Himalayan sequence samples and occurs as very small grains, <0.5 mm in diameter. It makes up only 1%-3% of the modal proportion. Plagioclase grains display few deformational effects.

Quartz is the predominant phase in the Lesser Himalayan sequence samples, making up 30% - 40% modal proportion. Most crystals are fine-grained, with diameters <0.5 mm. Most quartz grains have straight edges and exhibit a slight undulose extinction under crossed polars; larger grains show deformation bands.

Accessory phases in the Lesser Himalayan sequence are zoisite, ilmenite, zircon, and tourmaline. Ilmenite and tourmaline crystals are abundant (~1% modal proportion) and are aligned in the foliation. Tourmaline grains have blue cores with green rims under plane light.

MCT zone

Garnets from the MCT zone are euhedral to anhedral. They range in size from 0.5 mm to 1 cm in diameter. Large garnets (>2.5 mm diameter) usually contain abundant inclusions (quartz + opaques ± tourmaline ± biotite ± staurolite ± zoisite ± rutile ± chlorite ± muscovite ± kyanite) aligned in an internal foliation that is not parallel to the external foliation (Fig. 3b). Garnets make up 1% - 15% modal proportion. Pressure shadows of biotite + muscovite + quartz + chlorite are always present around larger garnets. Smaller garnets (<< 2 mm diameter) often do not contain inclusions. In the lower part of the MCT zone, garnets are pre-kinematic with respect to the main foliation; in the upper MCT zone most of the garnets are syn- to post-kinematic, but larger garnets are often pre-kinematic.

Biotite is present in all MCT zone samples. It defines the dominant schistosity and composes 10% - 25% modal proportion. Generally, biotite is finer-grained in the lower MCT zone than in the upper MCT zone; the grain length range is 0.1 - 2.0 mm. In the MCT zone biotite ranges in color from green to orange - brown under plane light. Petrographically, a change in biotite composition is noticeable in some samples in which the biotite adjacent to garnet is green in color whereas the matrix biotite is orange - brown.

Muscovite is present in ten of the samples from the MCT zone. It does not occur in sample L103a. When present, it helps to define the main foliation. It makes up between <1% - 20% modal proportion. Muscovite displays the same size range as biotite within the MCT zone.

Chlorite occurs mostly in the lower MCT zone samples, where it is present as both primary and secondary generations in modal proportions of <1% - 5%. When primary, chlorite is aligned in the dominant schistosity; in grain size it ranges up to 0.5 mm. When secondary, it occurs on garnet rims or cracks.

Plagioclase is found almost throughout the section, but it is absent in three samples from the lower MCT zone (L123e, L18a, L94b). In the lower MCT zone, it is rare (<1% - 35%) and fine grained (<.75 mm). Plagioclase grains exhibit little deformation in the lower MCT zone. Plagioclase in the upper MCT zone rocks is coarse-grained (0.75 - 2.0 mm) and makes up 15 - 30% of the assemblage. Plagioclase grains display undulose extinction and slightly embayed edges in the upper MCT zone.

Quartz is the main constituent in all MCT zone samples, making up 20% - 45% modal proportion. The amount of plastic deformation in quartz grains increases structurally upwards in the MCT zone. The grain size range is <0.25 - 2.0 mm, depending upon the amount of subgrain development. Generally, lower MCT zone samples have fine grained quartz exhibiting undulose extinction; larger grains have deformation bands. In the upper MCT zone, the quartz is coarser grained and grains display embayed edges with well-developed deformation bands.

Staurolite is found only in samples from the lower MCT zone. In general, it is subhedral to euhedral, up to 1 mm in length and makes up 5 - 8 modal percent of the assemblage. Staurolite contains abundant opaque and quartz inclusions, often arranged in helicitic inclusion trails. Some staurolite porphyroblasts are surrounded by pressure shadows, while others are not; therefore, staurolite is interpreted to be pre- to post-kinematic with respect to the main foliation.

Kyanite in the MCT zone is usually euhedral and ranges in size from 1 to 5 mm in length. In general, kyanite porphyroblasts are not aligned in the main foliation. Kyanite makes up <5% modal proportion. Some MCT zone kyanite porphyroblasts contain inclusions of quartz ± biotite ± opaque. In the lower part of the MCT zone kyanite porphyroblasts are post-kinematic with respect to the main foliation. Kyanite occurs as both inclusions in garnets and as a matrix phase in sample L94b, where the kyanite exhibits a blue color under plane light.

Accessory phases in the MCT zone samples are tourmaline, ilmenite, apatite, zircon, graphite, rutile and clinozoisite. Tourmalines are usually aligned in the dominant schistosity and have blue or green cores with green or yellow rims. In the lower MCT zone samples, ilmenite and graphite are also aligned in the main foliation.

Greater Himalayan sequence

Garnets are generally subhedral to anhedral in the Greater Himalayan sequence. They range in size from 0.5 to 7 mm in diameter and make up <1% - 5% modal proportion. Again, larger garnets contains more abundant inclusions than small ones. Inclusions in garnet are quartz ± plagioclase ± biotite ± rutile ± muscovite ± kyanite. These inclusions rarely form an internal fabric. Most of the garnets are syn- to post-kinematic with respect to the main foliation, although some of the very large garnets appear to be pre-kinematic.

Biotite defines the main foliation in all samples. Biotite occurs in modal proportions of 10% - 20% and varies in length from 0.5 - 3 mm. Matrix biotite is always orange - brown under plane light, but some biotites adjacent to garnet or as inclusions in garnet are green.

Muscovite occurs in the lower Greater Himalayan samples, but is absent in the uppermost Greater Himalayan sequence. Where present, muscovite is always aligned in the main foliation. It makes up 3% - 20% modal proportion and is up to 3 mm in length. A symplectite of muscovite and plagioclase is formed in some samples from the upper Greater Himalayan sequence.

Chlorite is rare in the Greater Himalayan sequence, occurring only in samples L21 and L171. Here it is an anhedral secondary phase, not affected by deformation.

Plagioclase occurs in almost all Greater Himalayan sequence samples except L36b. It makes up 1% - 25% modal proportion of the rocks. Plagioclase grains range

in size from 0.3 - 3.0 mm. Intensity of deformation in plagioclase grains increases structurally upwards from the MCT zone to well-developed undulose extinction, embayed edges and subgrain formation at the top of the sequence.

Quartz is the dominant phase in all Greater Himalayan sequence samples, constituting 20% - 40% modal proportion. The style of deformation increases structurally upwards within the Greater Himalayan sequence from embayed edges and deformation bands to a well-developed mortar texture near the top of the sequence. The grain size ranges from 0.3 - 3.0 mm in diameter.

K-feldspar occurs in significant modal proportions (<1% - 10%) only near the structural top of the Greater Himalayan sequence. K-feldspar grains reach sizes up to 3.0 mm across. Near the top of the sequence they display undulose extinction and embayed edges.

Kyanite occurs within samples from the lower Greater Himalayan sequence in modal proportions of 1% - 5%. In the Greater Himalayan sequence, kyanite is generally euhedral and ranges up to 3 cm in length. Kyanite occurs as subhedral inclusions within garnets in samples L157. Matrix kyanite is interpreted to be syn- to post-kinematic with respect to the main foliation.

Sillimanite occurs as prismatic crystals and fibrolitic mats in several samples from the Greater Himalayan sequence. It often is found as tiny (<0.01 mm length) prisms on grain boundaries between plagioclase grains. The majority of sillimanite is pre- to syn-kinematic with respect to the main foliation, although some tiny laths are not aligned in the main foliation and are probably post-kinematic. Sillimanite makes up 1% - 8% of the modal percentage.

Accessory phases that occur in the Greater Himalayan sequence are: tourmaline, rutile, ilmenite, scheelite, zircon, apatite and monazite.

Fabric Analysis

From the above petrographic analysis, it is possible to conclude that at least two metamorphic phases affected the Langtang region. Figure 4 shows timing relationships between the two major ductile deformational events affecting the area and porphyroblast growth for all three lithotectonic units. The earlier metamorphic phase is most obvious in the Lesser Himalayan sequence, where garnet porphyroblasts are demonstrably pre-kinematic with respect to the main foliation which was formed during ductile movement on the MCT. Evidence of M_2 within the Lesser Himalayan sequence is inclusion-free rims on garnet and the presence of tiny inclusion-free garnets. The existence of kyanite inclusions in garnets from both the MCT zone and the Greater Himalayan sequence provides evidence of either two separate metamorphic events preserved within these rocks or one protracted event with continuous garnet growth. Thus, the term metamorphic "phase" will be employed, with the first metamorphic phase referring to the early portion of the PT path and the second phase referring to the later portion of the PT path. Kyanite and sillimanite porphyroblasts in MCT zone and Greater Himalayan sequence rocks are associated with M_2. In the upper MCT zone and the Greater Himalayan sequence, fabric analysis suggests that the maximum temperatures were attained during and after ductile thrust motion on the MCT and normal movement on the South Tibetan detachment system. The second metamorphic phase was most intense in the upper Greater Himalayan sequence, where it was associated with widespread anatexis and leucogranite plutonism.

Mineral Chemistry

Thermobarometrically important mineral compositions were determined using the JEOL 733 Superprobe at the Massachusetts Institute of Technology. Rim compositions were measured approximately 2 - 3 μm from the edge of the phase. Two garnets per sample were analyzed adjacent to biotite and plagioclase and then checked adjacent to quartz and muscovite. At least two separate biotite, muscovite and plagioclase grains were measured next to each garnet. In a few samples (L17, L48, L52a, L63, L71a), no plagioclase grains were adjacent to garnet and plagioclase rims were measured adjacent to quartz no further than 50-100 μm away from garnet . Tables 2 - 5 contain compositional analyses for garnet, biotite, plagioclase and muscovite for all samples from the Lesser Himalayan sequence, the MCT zone and the Greater Himalayan sequence. The compositions in these tables represent the averages of all analyses for a particular phase in a sample. The errors reported in this table represent the sample standard deviation of the analyses for a particular phase.

Phase Equilibria

Compositions of garnet and biotite are plotted on Thompson (1957) AFM diagrams in Figures 5a - 5f. In the Lesser Himalayan sequence plot (Fig. 5a), crossing tie lines are present, suggesting that either the mineral compositions did not attain equilibrium at similar pressures and temperatures, or another component not considered in the diagram is stabilizing the assemblage. Figure 5b is a plot of the lower MCT zone samples, which are lithologically similar, and a few crossing tie lines are present. The compositions of the upper MCT zone samples are not consistent with equilibration at approximately the same temperature and pressure (Fig. 5c).

That the MCT zone samples did not reach final equilibration at similar pressure and temperature conditions is not surprising. The zone has been disrupted by later post-metamorphic faults that may be juxtaposing units that were once distant (Macfarlane et al., in press). The lower Greater Himalayan sequence samples display crossing tie lines on an AFM projection (Fig. 5d), but when plotted on an Al'-Fe-Mg-Mn diagram (Spear and Peacock, 1989), some of the crossing tie lines are eliminated (Fig. 5e). Additional components and structural distance of different samples best explain the crossing tie lines in the lower Greater Himalayan sequence. Crossing tie lines are also apparent in the upper Greater Himalayan sequence (L36b and L25, Fig. 5f). These samples are separated by a minimum of 7 km structural distance; therefore, it is very likely that they did not reach final equilibration at similar temperature and pressure.

The appearance of index minerals is not always an accurate indicator of metamorphic grade in the MCT zone and the lower Greater Himalayan sequence. One unit within the lower MCT zone, the Trisuli gneiss and schist, contains garnet to staurolite to kyanite "grade" rocks within a structural distance of 80 m. In Figure 5b, all samples belong to the Trisuli gneiss with the exception of L94b. The phase compositions of samples from this unit are consistent with final equilibration at similar pressure and temperature conditions, but they have very different bulk compositions. Thus it is most likely that difference in bulk composition results in the appearance of different index minerals. The question of bulk composition versus metamorphic grade is well illustrated by the lowermost Greater Himalayan sequence unit, the Gosainkunda gneiss. This unit alternates between the assemblages garnet + biotite + muscovite + plagioclase + quartz and kyanite + garnet + biotite + muscovite + plagioclase + quartz on the order of 50 to 200 m. Such alternation is most likely not

the result of fluctuating temperature, but of differences in overall bulk composition as demonstrated in Figure 5e.

Although bulk composition accounts for some of the apparent changes in metamorphic grade, field studies reveal that the overall temperature gradient increases upwards from the lower Greater Himalayan sequence to the upper Greater Himalayan sequence. The petrographic data suggest that the Lesser Himalayan sequence through the lower Greater Himalayan sequence experienced, at maximum, amphibolite grade metamorphism. In the lowermost Greater Himalayan sequence, kyanite is the stable index mineral. In three samples from the upper part of the lower Greater Himalayan sequence (L22, L22a, L25) sillimanite occurs together with kyanite, but does not overgrow it, suggesting the stable coexistence of kyanite and sillimanite. In the upper Greater Himalayan sequence, muscovite is replaced by K-feldspar and tiny sillimanite laths are often found on plagioclase grains. These petrographic features can be explained by the second sillimanite isograd reaction:

(K, Na)-muscovite + quartz = K-feldspar + sillimanite + water.

Sample L157 contains an inclusion suite of quartz + plagioclase + biotite + rutile + kyanite. The stable matrix assemblage is garnet + biotite + K- feldspar + plagioclase + quartz + sillimanite. The inclusion suite is a high pressure reaction assemblage stable at pressures of 900-1600 MPa over the 673-1373 K interval (Ghent & Stout, 1984). This suggests that L157 experienced a decrease in pressure until it reached the conditions recorded by its matrix phases.

Mineral Zoning and Compositional Variability

Plagioclase has a composition of An_{10}-An_{20} within the Lesser Himalayan sequence; An_{10} in the lower MCT zone; and An_{15}-An_{25} in the upper MCT zone. Two samples from the Lesser Himalayan sequence and the MCT zone reveal only slight normal zoning across the grains. In the Greater Himalayan sequence, plagioclase has a composition of An_{15}-An_{35}. Two samples from the Greater Himalayan sequence show slight zoning profiles. L142 becomes slightly more albitic toward the core (from An_{17} to An_{12}) and L171 displays an increase in anorthite content in the vicinity of the rim (from core to rim: An_{19} - An_{21} - An_{18}).

Compositional profiles across garnet were completed for all the samples listed. Profiles were measured on one garnet per sample at 10 μm intervals near the rim and 20 - 30 μm intervals toward the core. Most of the garnets are unzoned except near their rims, suggesting that the samples were affected by diffusional re-equilibration (Fig. 6). Only a few of the samples show significant chemical zoning, illustrated in Figures 7-9. Two samples from the Lesser Himalayan sequence reveal distinct and similar growth zoning profiles (Fig. 7). In both samples almandine and pyrope content increase from core to rim, while grossular and spessartine decrease from core to rim. Changes in the almandine and grossular profiles near the rims suggest diffusional re-equilibration or resorption. The lower MCT zone samples lack compositional gradients with the exception of sample L123e, which has a chemically distinct core and a 0.5 mm rim defined by changes in all components except pyrope (Fig. 8). The distinct core of L123e and the near-rim compositional changes in L7a and L52a suggest either a prolonged period of metamorphism with fluctuating pressure and temperature or two distinct phases of metamorphism. Upper MCT zone samples are homogeneous or show only minimal zoning.

For the most part, the Greater Himalayan sequence garnets are similar in that they display relatively flat zoning profiles. The exceptions are L171 and L36b. L171 shows a relatively flat core and a reversal in trend near the rims in all components (Fig. 9a). L36b reveals an almost sinusoidal pattern in all components except pyrope, but is best displayed by grossular (Fig. 9b). The reversal in composition in the profiles of both L171 and L36b may reflect one prolonged period of metamorphism with dissolution then regrowth or two separate metamorphic events.

THERMOBAROMETRY

Three well-calibrated thermobarometers can be applied to the assemblages of the Langtang samples. The garnet - biotite (GARB) thermometer of Ferry and Spear (1978) with modifications of Hodges and McKenna (1987):

$Mg_3Al_2Si_3O_{12}$ (garnet) + $KFe_3AlSi_3O_{10}(OH)_2$ (biotite)= $Fe_3AL_2Si_3O_{12}$ (garnet) + $KMg_3AlSi_3O_{10}(OH)_2$ (biotite)

was used to determine the temperatures of final equilibration for all samples. Pressures were determined using either the garnet - muscovite - biotite - plagioclase (GMPB) barometer of Ghent and Stout (1981) as modified by Hodges and Crowley (1985):

$Fe_3AL_2Si_3O_{12}$ (garnet) + $Ca_3Al_2Si_3O_{12}$ (garnet) + $KAl_3Si_3O_{10}(OH)_2$ (muscovite) = $3CaAl_2Si_2O_8$ (plagioclase) + $KFe_3AlSi_3O_{10}(OH)_2$ (biotite)

or the garnet - aluminum silicate - quartz - plagioclase (GASP) barometer of Ghent (1976) as modified by McKenna and Hodges (1988):

$Ca_3Al_2Si_3O_{12}$ (garnet) + $2Al_2SiO_5$ (aluminum silicate) + SiO_2 (quartz) = $3CaAl_2Si_2O_8$ (plagioclase).

The solution models used in the Langtang analysis are from Hodges and Royden (1984) and Hodges and Crowley (1985).

Rim Thermobarometry

Table 6 lists the results of rim thermobarometry on the Langtang samples. When complete assemblages were present for the solution of the GASP and GMPB barometers, both solutions are shown in the table. Solution of GARB with both GASP and GMPB give the same pressures within uncertainty. The pressure - temperature data are shown in Figures 10 - 12. The solutions depicted are those of GARB - GMPB where possible with the exceptions of: L67, L103a, L159, L157 (in which little or no muscovite was present, thus GASP was substituted) and L123e, L18a, L94b and L36b. In the latter samples there was no plagioclase, thus no barometer was available and only the GARB equilibrium is plotted. To facilitate reading of the figures, error ellipses of the data are presented first, followed by analytical solutions which are labeled by sample number. The ellipses represent 95% confidence precision of the thermobarometric calculation based on the propagation of analytical uncertainties (Hodges and McKenna, 1987).

Although only two samples from the Lesser Himalayan sequence were analyzed, there is a good correspondence between the two in both pressure and temperature (Figs. 10a & 10b). There appears to be complete overlap between PT conditions for samples from the Lesser Himalayan sequence and the MCT zone (Figs.

10a & 11a; 10b & 11b). The lower MCT zone samples all plot in the same general temperature range (700-790 K) as do the upper MCT zone samples (790-850 K). There is overlap in the pressure range for the lower (510 - 630 MPa) and upper (550 - 900 MPa) MCT zone. The MCT zone samples with kyanite (L94b, L67, L103a, L71a) consistently plot in the kyanite field on the graph (Fig. 11b).

The Greater Himalayan sequence samples plot in two general groups: most samples cluster in a moderate pressure, high temperature region (410-590 MPa; 800-870 K), but two samples yield significantly lower pressures and higher temperatures (220-260 MPa; 750-810 K; Figs. 12a & 12b). Samples of the first group were collected from the lower and middle structural levels of the Greater Himalayan sequence and the other two were collected from significantly higher structural levels. The three samples that contain both kyanite and sillimanite (L22, L22a, L25) plot directly on the kyanite-sillimanite join of the aluminum silicate stability fields (Fig. 12b). Other samples that are structurally close to these (i.e., L21, L73a, L142, L26) plot very close to the kyanite-sillimanite join. L171, which is approximately 2.5 - 3.0 km structurally above L22, L22a and L25 plots well within the sillimanite field (Fig. 12b). The PT estimates determined for the uppermost Greater Himalayan sequence samples (L157, L159) suggest disequilibrium: sillimanite is the stable aluminum silicate present, but both plot well within the andalusite field (Figs. 12a & 12b).

Inclusion Thermobarometry

Inclusion thermobarometry was performed unsuccessfully on one Greater Himalayan sequence sample (L25). One garnet in this sample has a biotite inclusion and a plagioclase inclusion that are equidistant from the core, but not adjacent. Solution of GARB - GASP gives 799 ± 110 K and 492 ± 190 MPa and solution of

GARB - GMPB results in 795 ± 160 K and 372 ± 290 MPa. This is an increase in temperature of 5-10 K and either a decrease in pressure of 20 MPa for the GASP solution or an increase in pressure of 50 MPa for the GMPB solution from inclusions to rim. Thus, the thermometry indicates essentially no change in temperature from core to rim and depending on the barometer used, the barometry results contradict each other and the exercise was unsuccessful.

GIBBS METHOD ANALYSIS

Five samples proved appropriate for modeling of pressure - temperature paths following the Gibbs Method of Spear and Selverstone (1983). Data from one sample from the MCT zone (L67) and three Greater Himalayan sequence samples (L73a, L22a and L25) were used in Spear's (1989) program for Gibbs Method modeling. L67 and L73a contain the assemblage: garnet + kyanite + biotite + muscovite + plagioclase + quartz + water and are quadravariant in the system K_2O + CaO + FeO + MgO + MnO + Na_2O + SiO_2 + Al_2O_3 + H_2O. The entire assemblage was assumed to have been present during garnet growth. Samples L22a and L25 contain the matrix assemblage garnet + kyanite + sillimanite + biotite + muscovite + plagioclase + quartz, although only one aluminum silicate phase was assumed to be present during garnet growth. The aluminum silicate phase was permitted to change during the modelling depending on pressure, temperature and the assumed stability fields of kyanite and sillimanite (Berman, 1989). Table 7 lists the mineral compositions used in the modeling of the assemblages. Four monitors were needed for the modeling of each sample. When biotite was the inclusion phase, almandine, grossular, spessartine and annite were the monitors used; for plagioclase inclusions, monitors were anorthite, almandine, grossular and spessartine.

Although garnet cores from the samples used in the Gibbs modeling are relatively homogeneous, their flat profiles may not be the result of diffusive homogenization. If we assume that the flat profiles *do* result from diffusive re-equilibration, use of the Gibbs Method in this case is not completely obviated. If the core of the garnet changes composition then it is probable that biotite inclusions would change composition in concert with the garnet through volume diffusion. If plagioclase inclusions re-equilibrated with garnet, there should be textural evidence from the net transfer reaction. There is no such textural evidence on the Langtang samples. Application of the Gibbs Method using a biotite inclusion in garnet would give us the temperature and pressure conditions of diffusive re-equilibration, assuming that the system is quadravariant. Used together with the rim thermobarometric data which record final equilibration (not maximum temperature), we would recover a part of the pressure - temperature path experienced by the sample. In other words, maximum temperatures would not be recovered, but two PT points on the retrograde path would. In the following discussion, both biotite and plagioclase inclusions were used in Gibbs Method modeling to test the above hypothesis.

The results of quantitative modeling of assemblages are presented in Figure 13 and Table 7. As suspected, biotite and plagioclase inclusions give very different results. In all cases, modeling of biotite inclusions predicts an increase in temperature with either a decrease or no change in pressure from core to rim, whereas plagioclase inclusions indicate decrease in temperature with a decrease in pressure. In the two samples (L22a and L25) where both a biotite and plagioclase inclusion were modeled, contradictory results were obtained. In sample L73a, two biotite inclusions were modeled. The pressure - temperature path for this sample is an isothermal decrease in pressure followed by an isobaric increase in temperature.

INTERPRETATIONS

Thermobarometric Data

The thermobarometric data appear to be reliable with the exception of the upper Greater Himalayan sequence samples, L157 and L159. These samples plot well within the andalusite field in Figures 12a and 12b. Because sillimanite, not andalusite is the aluminum silicate phase, rim compositions of phases in these samples probably do not reflect equilibrium. The thermobarometric data for the rest of the Greater Himalayan sequence appear to represent a major metamorphic episode whose conditions of final equilibration fell near the kyanite sillimanite join. These data are supported by the mineralogy of the samples, three of which contain both kyanite and sillimanite. In addition, granite samples collected in the vicinity of L22 to L25 contain kyanite as the aluminum silicate phase. This suggests that melting occurred in the kyanite field. Figure 12a shows that the wet granite minimum melt curve (Le Breton, 1988) falls within error of the loci of the Greater Himalayan sequence samples. The MCT zone and Lesser Himalayan sequence samples record higher pressures than the Greater Himalayan sequence samples, which is consistent with their structural position. On the other hand, the temperature range of the two groups is very similar. Because the thermobarometric results are consistent with the phase equilibria, the estimates of PT conditions are assumed to be valid.

In light of the microfabric and garnet profile data, it appears that the thermobarometric data record the second metamorphic phase (M_2). Only the cores of garnets may be considered remnants of the earlier metamorphic phase (M_1). Two samples, one from the MCT zone (L94b) and one from the Greater Himalayan sequence (L157) contain inclusions suites of kyanite + biotite ± plagioclase + rutile +

ilmenite + quartz. The presence of such an inclusion assemblage suggests the reaction: garnet + rutile = ilmenite + kyanite + quartz. Thus the conditions of M_1 can be estimated as passing through the above reaction boundary, as illustrated in Figures 14 and 15.

When the pressure and temperature data are plotted as a function of structural distance from the base of the MCT zone (defined as the distance from the basal brittle thrust fault), two important features are apparent: pressures increase somewhat structurally downwards, while temperatures show no systematic variation (Fig. 16). The pressure versus distance plot (Fig. 16b) shows a slight decrease in pressure from the Lesser Himalayan sequence through the middle Greater Himalayan sequence. Within error, these data are consistent with a lithostat of 27 MPa/km, although the large errors make it difficult to distinguish any trend with certainty (Fig. 16b). Within the MCT zone, minor reversals in the prevailing paleopressure gradient may reflect slight structural discontinuities associated with late brittle imbrication (Macfarlane et al., in press). Note that the two structurally highest points in these plots represent samples L157 and L159, which probably are not valid PT conditions.

The thermobarometric data suggest no obvious paleothermal gradient from the Lesser Himalayan sequence through the Greater Himalayan sequence. The apparent *lack* of a gradient becomes a challenge to explain. Possible interpretations of the temperature and pressure versus distance data include:

1) Due to known and unknown tectonic factors, similar temperatures were attained by all samples, but not necessarily at the same time.

2) Thermal buffering of the entire sequence caused a lack of thermal gradient, as discussed by Hodges et al. (1988).

3) Shuffling of rock packages along late brittle faults within the MCT zone produced the pattern of thermobarometric data, as suggested by Brunel and Kienast (1986) for eastern Nepal and Brunel (1989) for central Nepal.

4) The samples analyzed did not actually attain final equilibrium.

As discussed above, there is no reason to believe that the samples did not attain equilibrium with the exception of L157 and L159, so we can probably eliminate hypothesis number four. Shuffling within the MCT zone may account for the lack of paleothermal gradient within the zone and does perturb the PT trend slightly (Fig. 16), but this phenomenon does not explain the lack of paleothermal gradient from the Lesser Himalayan sequence to the Greater Himalayan sequence, 18 km away. Thermal buffering during anatexis (as envisioned by Hodges, et al., 1988) is inconsistent with the lack of evidence for partial melting in the MCT zone at Langtang.

We are left with the somewhat vague explanation of tectonic factors affecting the sequence. The idea behind this hypothesis is that Lesser Himalayan sequence rocks, which form the footwall of the MCT, may have reached final equilibration early during thrust movement. Due to shear heating effects, rocks within the MCT zone may have reached final equilibrium later than those from the Lesser Himalayan sequence (Molnar and England, 1990). Greater Himalayan sequence units were likely affected by the same heating event that caused anatexis and the formation of the granites. Field relations suggest that granite intrusion in the Langtang area outlasted movement on the MCT and the South Tibetan detachment system, because the larger granite bodies are unfoliated (Macfarlane et al., in press). Thus, these rocks probably equilibrated last. One of the "little known" tectonic factors in this scenario is the South Tibetan detachment system, which does not outcrop in the immediate Langtang area but has been mapped just north of the area in Tibet (Burchfiel et al., 1992). The

thermal effects of this major structure, part of which was probably active during M_2 (Macfarlane et al., in press), are not yet fully understood.

PT Path Data

Contradictory results from inclusion thermobarometry and Gibbs Method modeling were obtained for sample L25 as shown in Figure 15. The inclusion thermobarometry data for sample L25 are unreliable in light of the discussion on the Gibbs Method modeling. The most reasonable PT path results were obtained from Gibbs Method modeling of garnets using biotite as a monitor. If the core conditions that were determined do not represent peak conditions, they may at least represent a smaller portion of the PT path, from the time the core of the garnet was internally homogenized to when its rim reached final equilibrium. Modelled paths begin at high pressure (1000-1200 MPa) and moderate temperature (700-800 K) and reach final equilibrium at moderate pressure (400-700 MPa) and higher temperature (800-900 K). Figures 14 and 15 show that the modeled paths are consistent with the path suggested by the kyanite+ rutile + ilmenite + quartz inclusions in garnet. All quantitative data thus indicate that the Greater Himalayan sequence in the Langtang area experienced an early high pressure, moderate temperature event followed by a moderate pressure, high temperature event.

Tectonic Framework

In the Langtang region, microfabrics suggest that M_2 began during movement on the MCT but continued after motion ceased (Macfarlane et al., in press). The second metamorphic phase is also most probably associated with the anatectic event that produced foliation-parallel migmatites and leucogranite pods. The age of M_2 is

constrained by 16-20.5 Ma U-Pb dates from zircons and monazites from pelitic gneisses, and 15-22 Ma ages from monazites and xenotimes from migmatites and granite dikes within the Greater Himalayan sequence (Parrish, 1992). Late brittle motion on the MCT is constrained to have occurred after 7-9 Ma based on $^{40}Ar/^{39}Ar$ ages of muscovites from the MCT zone (Macfarlane et al., in press).

The tectonic history of the Langtang region can be envisioned as follows: in the absence of absolute evidence, we shall assume that M_1 occurred sometime prior to M_2 (before or near 15-22 Ma) at the conditions of 1000-1200 MPa and 600-800 K. Movement began on the MCT sometime before 15-22 Ma and by 15-22 Ma M_2 attained peak thermal conditions, reaching final equilibration conditions of 300-700 MPa and 700-900 K. Sometime after motion on the MCT began, the South Tibetan detachment system began to move. Anatexis and metamorphism continued after motion had ceased on both the MCT and the South Tibetan detachment system, although later brittle, probably normal-sense motions occurred in the upper Greater Himalayan sequence. M_2 ceased sometime before 7 Ma brittle motion on the MCT (Macfarlane et al., in press).

As noted above, although there appears to have been significant post-metamorphic movement on the MCT (Macfarlane et al., in press), there is no obvious metamorphic break across the MCT zone as is described for Garhwal (Gansser, 1964, Hodges and Silverberg, 1988, Valdiya, 1979). Given uncertainties in the thermobarometric data, a maximum of 8-9 km (250 MPa) of tectonostratigraphic throw is possible for post-metamorphic displacement on the MCT (Fig. 14b).

CONCLUSIONS

Based on microfabric data, two metamorphic phases (M_1 and M_2) have affected the crystalline core of the Himalaya in the Langtang region. Both phases are probably Himalayan in age and may be part o a single, protracted metamorphic event. M_1 was a high pressure, moderate temperature phase. The rim thermobarometry data presented in this paper pertain only to the later phase, a moderate pressure, high temperature phase. The results show that final equilibration temperatures are statistically indistinguishable through 16 km of section, from the upper Lesser Himalayan sequence to the upper Greater Himalayan sequence. M_2 in all units is interpreted to be the result of not one single thermal pulse, but the combination of many factors. Movement on the MCT, shear heating on the MCT, motion on the South Tibetan detachment system, radioactive heating and other unknown agents may have come together to produce M_2.

Quantitative modeling of mineral assemblages provided the high-pressure portion of the PT path for the Langtang samples. It is not certain whether the cores of the garnets were formed during M_1 or M_2; it may vary from sample to sample and garnet to garnet. There is general agreement among the models produced from four different samples that garnet composition evolved during decreasing pressure and increasing temperature. Inclusion thermobarometry appears to have failed on both samples where it was attempted.

Finally, the inverted metamorphic gradient that has been described elsewhere in the Himalaya as associated with the MCT (Bordet, 1961, Gansser, 1964, Le Fort, 1975, Pecher, 1978) is not present *sensu stricto* in the Langtang region. In the field, the Lesser Himalayan sequence and the MCT zone reach amphibolite grade, with

minor fluctuations that most probably reflect changes in bulk composition, not temperature. The occurrence of sillimanite + K-feldspar grade rocks in the Greater Himalayan sequence is not accompanied by an inversion in the paleotemperatures obtained thermobarometrically. Thus, no inverted paleothermal gradient exists in any of the rocks in the Langtang region. Considering the data from central Nepal to the west of Langtang and the Everest region to the east, the metamorphic evolution of the core of the Himalaya varies on the scale of 100 km.

ACKNOWLEDGEMENTS

A.M.M. wishes to thank all her supportive field assistants (B. Sheffels, C. Ruppel and M. Coleman); her hard-working guides, cooks and porters; Surrendra Shrestha at the Dept. of Mines and Geology for all his help; and the Nepali government for research permission. This research was supported by N.S.F. grant # EAR8721403 awarded to K.V. Hodges and a G.S.A. Research grant awarded to A.M.M. A.M.M. was supported by an N.S.F. fellowship.

Table 1: Phases Present in Samples

Sample	Garnet	Staur	Biotite	Chlor	Plag	Musc	K-spar	Kya	Sillim
L7a	*		*	*	*	*			
L52a	*		*	*	*	*			
L17	*		*	*	*	*			
L58b	*		*	*	*	*			
L123e	*	*	*	*		*			
L18a	*	*	*	*		*			
L103a	*		*		*			*	
L94b	*	*	*	*		*		*	
L63	*		*		*	*			
L67	*		*		*	*		*	
L48	*		*		*	*			
L71a	*		*	*	*	*		*	
L20a	*		*		*	*			
L73a	*		*		*	*		*	
L21	*		*	*	*	*			
L22	*		*		*	*		*	*
L22a	*		*		*	*		*	*
L142	*		*		*	*			
L25	*		*		*	*		*	*
L26	*		*		*	*			*
L171	*		*	*	*	*			*
L159	*		*		*	*			*
L157	*		*		*		*		*
L36b	*		*				*		*

Note that quartz is present in all samples.

Table 2: Garnet analyses: weight percent oxides

	L7a	L52a	L17	L58b	L123e	L18a	L103a	L94b	L63	L67	L48	L71a	L20a	L73a	L21	L22	L22a	L142	L25	L26
MgO	1.65	1.96	2.37	2.36	3.27	3.27	3.77	1.7	1.53	3.78	3.42	4.02	2.21	3.3	2.48	2.76	2.95	2.57	3.05	1.98
	±0.09	±0.16	±0.17	±0.20	±0.27	±0.32	±0.51	±0.10	±0.23	±0.57	±0.35	±0.27	±0.25	±0.60	±0.40	±0.30	±0.45	±0.48	±0.32	±0.27
Al2O3	20.79	21.05	20.95	20.93	21.28	20.85	21	21.15	20.95	21.08	21.07	21.4	20.7	21.01	20.88	21.05	20.95	20.81	21.06	20.45
	±0.10	±0.16	±0.26	±0.20	±0.28	±0.25	±0.17	±0.19	±0.20	±0.38	±0.17	±0.25	±0.22	±0.22	±0.40	±0.16	±0.17	±0.24	±0.24	±0.21
SiO2	37.25	37.21	37.72	37.45	37.8	37.64	37.97	37.05	37.58	38.09	37.68	38.48	37.87	37.83	37.35	37.8	37.69	36.81	37.65	37.2
	±0.23	±0.18	±0.31	±0.27	±0.41	±0.32	±0.26	±0.27	±0.27	±0.37	±0.40	±0.23	±0.35	±0.26	±0.33	±0.18	±0.21	±0.35	±0.18	±0.22
CaO	3.00	4.05	2.07	2.32	0.87	3.22	5.01	0.26	4.44	1.68	3.19	2.55	3.71	1.86	1.53	1.53	1.56	1.33	0.87	1.59
	±0.45	±0.54	±0.09	±0.24	±0.22	±0.95	±0.47	±0.02	±0.30	±0.12	±0.18	±0.10	±0.30	±0.14	±0.10	±0.07	±0.07	±0.12	±0.05	±0.15
TiO2	0.01	0.03	0.03	0.06	0.06	0.06	0.1	0	0.05	0.01	0.02	0.06	0.08	0.02	0.03	0.07	0.05	0.12	0.03	0.03
	±0.02	±0.02	±0.03	±0.03	±0.03	±0.03	±0.03	±0.01	±0.03	±0.02	±0.03	±0.04	±0.04	±0.03	±0.03	±0.02	±0.16	±0.03	±0.03	±0.04
MnO	1.20	1.07	0.58	1.24	0.64	0.34	2.19	0.14	5.45	2.13	2.68	4.55	1.43	1.75	1.47	2.39	2.15	1.67	4.1	1.68
	±0.21	±0.54	±0.10	±0.26	±0.11	±0.06	±1.11	±0.05	±1.31	±0.31	±0.50	±0.37	±0.19	±0.21	±0.19	±0.21	±0.43	±0.23	±0.41	±0.22
FeO	36.60	34.87	37.79	36.5	37.8	35.08	30.21	40.99	30.87	34.28	32.01	31.03	35.69	35.19	36.84	35.74	35.2	36.68	34.08	37.24
	±0.48	±0.59	±0.36	±0.46	±0.40	±0.80	±0.49	±0.22	±1.11	±0.64	±0.34	±0.45	±0.49	±0.99	±0.41	±0.40	±0.41	±0.56	±0.40	±0.41
Total	100.50	100.24	101.51	100.86	101.72	100.46	100.25	101.29	100.87	101.05	100.07	102.09	101.69	100.96	100.58	101.34	100.55	99.99	100.84	100.17
	Garnet analyses: Cations per 12 oxygens																			
Mg	0.199	0.235	0.282	0.282	0.386	0.389	0.446	0.204	0.183	0.446	0.407	0.469	0.262	0.391	0.298	0.324	0.352	0.310	0.364	0.240
	±0.011	±0.019	±0.019	±0.024	±0.031	±0.036	±0.059	±0.011	±0.028	±0.065	±0.040	±0.030	±0.029	±0.069	±0.046	±0.324	±0.054	±0.056	±0.038	±0.033
Al	1.979	1.998	1.970	1.979	1.989	1.964	1.963	2.012	1.979	1.970	1.984	1.973	1.942	1.972	1.981	1.977	1.978	1.989	1.985	1.957
	±0.008	±0.011	±0.014	±0.015	±0.015	±0.010	±0.009	±0.008	±0.017	±0.020	±0.013	±0.020	±0.010	±0.010	±0.026	±0.011	±0.012	±0.009	±0.015	±0015
Si	3.008	2.997	3.010	3.004	2.999	3.007	3.011	2.990	3.012	3.020	3.010	3.010	3.014	3.013	3.007	3.012	3.019	2.986	3.011	3.020
	±0.011	±0.012	±0.010	±0.012	±0.012	±0.009	±0.012	±0.008	±0.008	±0.012	±0.016	±0.009	±0.010	±0.010	±0.019	±0.010	±0.010	±0.010	±0.014	±0.016
Ca	0.260	0.350	0.177	0.200	0.074	0.276	0.426	0.022	0.381	0.143	0.273	0.214	0.316	0.159	0.132	0.130	0.134	0.116	0.075	0.138
	±0.038	±0.047	±0.007	±0.020	±0.019	±0.082	±0.038	±0.001	±0.026	±0.011	±0.015	±0.009	±0.025	±0.012	±0.009	±0.006	±0.006	±0.011	±0.005	±0.013
Ti	0.001	0.001	0.002	0.004	0.004	0.004	0.006	0.000	0.003	0.001	0.001	0.003	0.005	0.001	0.002	0.004	0.003	0.007	0.002	0.001
	±0.001	±0.001	±0.002	±0.002	±0.002	±0.002	±0.002	±0.000	±0.002	±0.001	±0.002	±0.002	±0.002	±0.002	±0.002	±0.001	±0.003	±0.002	±0.002	±0.002
Mn	0.082	0.073	0.039	0.084	0.043	0.023	0.147	0.009	0.370	0.143	0.181	0.302	0.097	0.118	0.101	0.164	0.146	0.115	0.279	0.116
	±0.014	±0.036	±0.007	±0.018	±0.007	±0.004	±0.075	±0.003	±0.089	±0.021	±0.035	±0.025	±0.013	±0.015	±0.013	±0.014	±0.029	±0.016	±0.008	±0.015
Fe	2.472	2.349	2.522	2.449	2.508	2.344	2.003	2.766	2.069	2.273	2.139	2.030	2.376	2.344	2.481	2.385	2.358	2.489	2.280	2.528
	±0.032	±0.037	±0.024	±0.026	±0.029	±0.046	±0.034	±0.020	±0.073	±0.052	±0.024	±0.024	±0.036	±0.072	±0.040	±0.029	±0.030	±0.045	±0.028	±0.030
Total	8.001	8.003	8.002	8.002	8.003	8.007	8.002	8.003	7.997	7.996	7.995	8.001	8.012	7.998	8.002	7.996	7.990	8.012	7.996	8.000
Xalm	0.820	0.781	0.835	0.812	0.833	0.773	0.663	0.922	0.689	0.756	0.713	0.673	0.779	0.778	0.824	0.794	0.789	0.821	0.761	0.837
	#DIV/0!																			
Xpyr	0.066	0.078	0.093	0.094	0.128	0.128	0.148	0.068	0.061	0.148	0.136	0.156	0.086	0.130	0.099	0.108	0.118	0.102	0.121	0.079
Xgros	0.086	0.116	0.059	0.066	0.025	0.091	0.141	9.000	0.127	0.048	0.091	0.071	0.104	0.053	0.044	0.043	0.045	0.038	0.025	0.046
Xspes	0.027	0.024	0.013	0.028	0.014	0.008	0.049	0.003	0.123	0.048	0.060	0.100	0.032	0.039	0.034	0.055	0.049	0.038	0.093	0.038
Fe/Mg+Fe	0.925	0.909	0.899	0.897	0.867	0.858	0.818	0.931	0.919	0.836	0.840	0.812	0.901	0.857	0.893	0.880	0.870	0.889	0.862	0.913

Table 2

L171	L159	L157	L36b
2.58	1.89	3.682	2.78
±0.29	±0.36	±1.02	±0.11
21.1	20.75	20.23	21.18
±0.16	±0.18	±0.36	±0.16
37.27	36.9	37.66	37.34
±0.22	±0.25	±0.35	±0.18
1.03	0.89	1.62	1.69
±0.03	±0.05	±0.51	±0.40
0.02	0.06	0.07	0.05
±0.02	±0.03	±0.02	±0.02
2.05	7.93	3.5	3.4
±0.34	±0.74	±0.60	±0.23
36.88	31.71	33.31	34.44
±0.60	±0.39	±0.63	±0.60
100.93	100.13	100.07	100.88
0.309	0.229	0.441	0.332
±0.033	±0.043	±0.119	±0.013
1.997	1.989	1.917	1.999
±0.009	±0.012	±0.026	±0.010
2.993	3.000	3.028	2.991
±0.008	±0.010	±0.017	±0.010
0.089	0.078	0.140	0.145
±0.003	±0.005	±0.044	±0.034
0.001	0.004	0.004	0.003
±0.001	±0.002	±0.001	±0.001
0.139	0.546	0.239	0.231
±0.023	±0.053	±0.041	±0.016
2.478	2.156	2.240	2.307
±0.047	±0.020	±0.055	±0.039
8.006	8.002	8.009	8.008
0.822	0.717	0.732	0.765
0.102	0.076	0.144	0.110
0.030	0.026	0.046	0.048
0.046	0.181	0.078	0.077
0.889	0.904	0.836	0.874

Table 3: Biotite analyses: weight percent oxides

	L7a	L52a	L17	L58b	L123e	L18a	L103a	L94b	L63	L67	L48	L71a	L20a	L73a	L21	L22	L22a
MgO	7.19	8.77	10.39	10.01	11.55	13.07	12.43	7.11	7.19	11.24	11.61	11.80	8.27	9.43	8.57	9.39	9.91
	±1.16	±0.19	±0.10	±0.543	±0.542	±0.594	±0.560	±0.80	±0.15	±0.29	±0.28	±0.63	±0.28	±0.23	±0.49	±0.82	±0.37
Al2O3	19.41	19.09	19.06	18.72	19.62	19.65	19.60	19.59	18.84	19.11	19.26	19.60	18.53	18.35	19.16	19.31	18.90
	±0.35	±0.41	±0.30	±0.335	±0.468	±0.609	±0.978	±0.71	±0.44	±0.78	±0.50	±1.06	±0.23	±0.35	±0.52	±0.40	±0.74
SiO2	34.83	35.63	36.50	35.89	36.70	37.16	36.92	34.34	35.75	37.04	36.70	37.58	36.03	36.45	35.51	36.07	35.43
	±0.99	±0.42	±0.41	±0.458	±0.732	±0.642	±0.482	±1.08	±0.53	49.00	±0.53	±0.60	±0.37	±0.50	±0.84	±0.46	±1.61
CaO	0.02	0.08	0.00	0.03	0.05	0.05	0.10	0.01	0.05	0.07	0.04	0.02	0.02	0.01	0.02	0.07	0.05
	±0.02	±0.02	±0.01	±0.061	±0.023	±0.046	±0.030	±0.01	±0.038	±0.02	±0.02	±0.02	±0.02	±0.02	±0.03	±0.05	±0.04
TiO2	1.00	1.30	1.13	1.31	0.98	0.93	1.17	1.09	2.21	1.87	2.14	1.64	3.03	3.20	1.61	1.55	1.50
	±0.07	±0.49	±0.40	±0.296	±0.561	±0.253	±0.304	±0.57	±0.61	±0.27	±0.43	±0.82	±0.54	±0.45	±0.57	±0.84	±0.98
MnO	0.15	0.12	0.04	0.07	0.00	0.03	0.07	0.01	0.33	0.04	0.07	0.15	0.04	0.07	0.07	0.05	0.05
	±0.11	±0.02	±0.04	±0.042	±0.011	±0.029	±0.049	±0.02	±0.05	±0.05	±0.03	±0.08	±0.03	±0.06	±0.06	±0.07	±0.4
FeO	23.44	21.45	20.07	20.45	18.01	16.10	16.08	24.70	22.57	17.36	16.56	16.53	21.96	19.13	22.28	20.40	19.65
	±1.50	±0.48	±0.71	±0.630	±0.792	±0.479	±0.371	±1.88	±0.54	±0.90	±0.71	±0.74	±0.83	±0.46	±1.58	±1.69	±1.83
Na2O	0.05	0.12	0.25	0.19	0.38	0.40	0.18	0.05	0.02	0.31	0.27	0.27	0.15	0.12	0.11	0.16	0.32
	±0.04	±0.05	±0.05	±0.054	±0.045	±0.048	±0.070	±0.03	±0.03	±0.05	±0.04	±0.06	±0.04	±0.04	±0.10	±0.06	±0.06
K2O	8.75	9.37	8.93	9.16	8.66	8.28	8.29	9.02	9.04	8.63	8.83	9.17	8.91	8.74	8.10	8.23	8.04
	±0.35	±0.15	±0.35	±0.345	±0.631	±0.252	±0.486	±1.28	±0.2	±0.24	±0.31	±0.26	±0.17	±0.16	±0.74	±0.33	±0.51
Total	94.84	95.93	96.37	95.83	95.95	95.66	94.83	95.92	96.00	144.67	95.48	96.76	96.94	95.50	95.43	95.23	93.85
												Biotite analyses: cations per 11 oxygens					
Mg	0.832	0.997	1.162	1.132	1.282	1.437	1.379	0.821	0.820	1.246	1.288	1.291	0.929	1.059	0.975	1.061	1.121
	±0.121	±0.024	±0.015	±0.061	±0.063	±0.052	±0.067	±0.096	±0.018	±0.033	±0.030	±0.074	±0.028	±0.026	±0.049	±0.087	±0.041
Al	1.778	1.716	1.685	1.674	1.721	1.708	1.718	1.788	1.698	1.675	1.690	1.695	1.646	1.630	1.724	1.724	1.780
	±0.037	±0.037	±0.020	±0.030	±0.034	±0.041	±0.072	±0.055	±0.041	±0.057	±0.047	±0.090	±0.026	±0.033	±0.049	±0.039	±0.092
Si	2.706	2.717	2.737	2.723	2.732	2.741	2.747	2.659	2.734	2.755	2.731	2.757	2.716	2.747	2.711	2.733	2.686
	±0.025	±0.016	±0.017	±0.020	±0.037	±0.027	±0.019	±0.042	±0.019	±0.016	±0.034	±0.025	±0.013	±0.028	±0.046	±0.015	±0.082
Ca	0.002	0.007	0.000	0.002	0.004	0.004	0.008	0.001	0.004	0.006	0.003	0.001	0.001	0.001	0.002	0.005	0.004
	±0.002	±0.002	±0.000	±0.005	±0.002	±0.004	±0.003	±0.001	±0.003	±0.002	±0.002	±0.002	±0.002	±0.001	±0.003	±0.004	±0.003
Ti	0.058	0.074	0.064	0.074	0.054	0.052	0.065	0.063	0.113	0.105	0.119	0.090	0.172	0.181	0.092	0.088	0.085
	±0.003	±0.028	±0.023	±0.017	±0.031	±0.014	±0.017	±0.033	±0.035	±0.015	±0.024	±0.045	±0.030	±0.025	±0.003	±0.047	±0.054
Mn	0.010	0.007	0.003	0.005	0.000	0.002	0.004	0.001	0.022	0.002	0.005	0.009	0.003	0.005	0.004	0.003	0.003
	±0.007	±0.001	±0.002	±0.003	±0.001	±0.002	±0.003	±0.002	±0.003	±0.003	±0.002	±0.005	±0.002	±0.004	±0.004	±0.005	±0.003
Fe	1.525	1.368	1.259	1.297	1.121	0.993	1.001	1.601	1.444	1.084	1.031	1.015	1.385	1.206	1.423	1.293	1.248
	±0.125	±0.033	±0.053	±0.045	±0.058	±0.030	±0.025	±0.144	±0.040	±0.064	±0.047	±0.051	±0.057	±0.027	±0.111	±0.012	±0.134
Na	0.007	0.018	0.037	0.028	0.055	0.057	0.025	0.007	0.003	0.045	0.039	0.038	0.022	0.018	0.017	0.024	0.047
	±0.006	±0.007	±0.007	±0.008	±0.006	±0.007	±0.010	±0.004	±0.004	±0.007	±0.006	±0.008	±0.006	±0.006	±0.014	±0.009	±0.009
K	0.867	0.912	0.854	0.887	0.822	0.779	0.787	0.890	0.883	0.817	0.838	0.858	0.857	0.840	0.788	0.796	0.778
	±0.025	±0.017	±0.029	±0.029	±0.055	±0.028	±0.048	±0.120	±0.015	±0.019	±0.030	±0.019	±0.014	±0.015	±0.069	±0.026	±0.042
Total	7.785	7.816	7.801	7.822	7.791	7.773	7.734	7.831	7.721	7.735	7.744	7.754	7.731	7.687	7.736	7.727	7.752
Xann	0.644	0.577	0.519	0.533	0.467	0.408	0.420	0.661	0.632	0.465	0.444	0.438	0.598	0.531	0.592	0.549	0.526
Xphlog	0.351	0.420	0.479	0.465	0.533	0.591	0.578	0.339	0.359	0.534	0.554	0.558	0.401	0.467	0.406	0.450	0.473
XMn-Bi	0.004	0.003	0.001	0.002	0.000	0.001	0.002	0.000	0.010	0.001	0.002	0.004	0.001	0.002	0.002	0.001	0.001

Table 3

L142	L25	L26	L171	L159	L157	L36b
7.96	10.13	7.40	7.90	7.59	12.66	10.77
±0.2	±0.24	±0.43	±0.36	±0.11	±0.86	±0.57
19.38	19.33	18.56	20.04	19.82	18.21	20.25
±0.93	±0.66	±0.71	±0.88	±0.47	±0.57	±0.51
35.05	36.36	35.10	34.31	34.62	36.42	35.26
±0.88	±0.17	±0.51	±1.06	±0.21	±0.63	±0.79
0.04	0.04	0.03	0.03	0.03	0.02	0.03
±0.02	±0.03	±0.06	±0.03	±0.03	±0.02	±0.03
3.16	2.89	2.54	2.19	2.61	1.67	1.47
±0.44	±0.59	±0.80	±1.01	±0.58	±0.47	±0.51
0.05	0.11	0.11	0.09	0.27	0.08	0.10
±0.03	±0.11	±0.03	±0.04	±0.04	±0.03	±0.04
20.47	18.51	23.18	22.37	21.55	17.25	18.58
±0.64	±0.89	±1.24	±0.97	±0.65	±1.13	±1.07
0.16	0.16	0.09	0.22	0.10	0.35	0.14
±0.03	±0.04	±0.05	±0.04	±0.02	±0.07	±0.08
8.98	8.62	8.35	8.63	9.49	8.53	9.36
±0.19	±0.09	±0.72	±0.85	±0.24	±0.21	±0.49
95.25	96.15	95.36	95.78	96.08	95.19	95.96
0.906	1.125	0.850	0.902	0.864	1.415	1.207
±0.022	±0.027	±0.052	±0.043	±0.015	±0.085	±0.062
1.744	1.698	1.685	1.809	1.785	1.609	1.794
±0.076	±0.062	±0.061	±0.094	±0.034	±0.038	±0.040
2.676	2.709	2.704	2.627	2.645	2.731	2.650
±0.051	±0.008	±0.019	±0.053	±0.007	±0.027	±0.035
0.003	0.003	0.003	0.003	0.002	0.001	0.002
±0.002	±0.002	±0.003	±0.003	±0.002	±0.001	±0.002
0.181	0.162	0.147	0.126	0.150	0.094	0.083
±0.25	±0.033	±0.046	±0.057	±0.033	±0.027	±0.029
0.003	0.007	0.007	0.006	0.018	0.005	0.007
±0.002	±0.007	±0.002	±0.002	±0.003	±0.002	±0.003
1.308	1.153	1.494	1.434	1.377	1.082	1.169
±0.049	±0.051	±0.090	±0.079	±0.045	±0.078	±0.079
0.023	0.023	0.014	0.033	0.016	0.051	0.020
±0.005	±0.006	±0.007	±0.005	±0.004	±0.009	±0.012
0.875	0.819	0.820	0.842	0.925	0.816	0.897
±0.02	±0.009	±0.067	±0.075	±0.023	±0.018	±0.041
7.719	7.699	7.724	7.782	7.782	7.804	7.829
0.590	0.505	0.635	0.612	0.610	0.432	0.491
0.409	0.492	0.362	0.385	0.382	0.566	0.507
0.001	0.003	0.003	0.003	0.008	0.002	0.003

Table 4: Muscovite analyses: weight percent oxides

	L7a	L52a	L17	L58b	L63	L48	L71a	L20a	L73a	L21	L22	L22a	L142	L25	L26	L171
MgO	0.44	0.71	0.73	0.65	0.73	1.10	0.85	0.84	0.87	0.76	0.72	0.79	0.76	0.82	0.66	0.64
	±0.06	±0.05	±0.13	±0.13	±0.12	±0.43	±0.18	±0.08	±0.06	±0.13	±0.02	±0.04	±0.13	±0.12	±0.10	±0.12
Al2O3	35.51	34.99	34.43	34.74	33.95	33.31	33.45	33.60	33.63	34.28	35.02	34.22	34.22	33.98	33.72	34.80
	±0.34	±0.34	±0.44	±0.45	±0.77	±0.72	±0.81	±0.29	±0.64	±0.65	±0.42	±0.35	±0.31	±0.50	±0.43	±0.34
SiO2	46.67	47.14	47.68	46.89	46.94	47.13	47.22	47.22	47.40	47.92	48.54	47.31	46.74	46.92	47.57	46.71
	±0.33	±0.45	±0.78	±0.76	±0.44	±1.06	±0.81	±0.31	±0.38	±0.90	±1.02	±0.77	±1.03	±0.53	±0.52	±0.287
CaO	0.00	0.03	0.03	0.06	0.01	0.04	0.02	0.02	0.01	0.00	0.00	0.03	0.01	0.04	0.00	0.01
	±0.00	±0.04	±0.05	±0.06	±0.013	±0.02	±0.02	±0.02	±0.01	±0.00	±0.01	±0.03	±0.01	±0.02	±0.00	±0.02
TiO2	0.17	0.22	0.25	0.27	0.49	0.76	0.71	0.61	1.34	0.83	0.76	1.15	0.96	1.07	0.75	0.90
	±0.05	±0.06	±0.07	±0.10	±0.15	±0.09	±0.38	±0.27	±0.13	±0.17	±0.28	±0.31	±0.14	±0.49	±0.12	±0.33
MnO	0.07	0.03	0.05	0.06	0.05	0.06	0.08	0.02	0.04	0.05	0.00	0.05	0.01	0.03	0.00	0.03
	±0.03	±0.05	±0.03	±0.05	±0.05	±0.04	±0.04	±0.03	±0.05	±0.03	±0.00	±0.06	±0.01	±0.03	±0.00	±0.02
FeO	1.34	1.52	2.29	2.40	1.88	2.08	3.26	2.01	1.47	1.28	1.25	1.60	1.57	1.73	1.48	1.57
	±0.08	±0.17	±0.48	±0.49	±0.35	±0.63	±0.40	±0.23	±0.20	±0.11	±0.16	±0.50	±0.61	±0.60	±0.14	±0.58
Na2O	1.33	0.93	1.41	1.53	0.57	0.85	0.99	0.57	0.51	1.12	1.05	1.03	0.67	1.00	0.82	0.82
	±0.20	±0.09	±0.21	±0.14	±0.10	±0.04	±0.09	±0.03	±0.07	±0.09	±0.05	±0.12	±0.05	±0.08	±0.05	±0.10
K2O	9.19	9.59	8.99	9.12	9.99	9.54	9.55	10.43	10.06	9.19	9.42	9.19	9.90	9.33	9.71	9.76
	±0.29	±0.19	±0.26	±0.21	±0.25	±0.50	±0.10	±0.15	±0.57	±0.24	±0.17	±0.22	±0.20	±0.29	±0.12	±0.22
Total	94.72	95.16	95.86	95.72	94.61	94.87	96.13	95.32	95.33	95.43	96.76	95.37	94.84	94.92	94.71	95.24
	Muscovite analyses: cations per 11 oxygens															
Mg	0.044	0.071	0.072	0.064	0.073	0.110	0.084	0.083	0.086	0.075	0.070	0.078	0.075	0.081	0.065	0.063
	±0.006	±0.005	±0.013	±0.012	±0.013	±0.045	±0.018	±0.008	±0.006	±0.013	±0.001	±0.003	±0.013	±0.012	±0.010	±0.012
Al	2.784	2.735	2.677	2.713	2.679	2.622	2.616	2.641	2.630	2.663	2.682	2.668	2.691	2.667	2.648	2.724
	±0.025	±0.014	±0.015	±0.028	±0.040	±0.030	±0.055	±0.029	±0.035	±0.044	±0.012	±0.025	±0.018	±0.024	±0.026	±0.018
Si	3.104	3.126	3.145	3.107	3.143	3.148	3.133	3.149	3.146	3.158	3.154	3.129	3.119	3.125	3.170	3.103
	±0.017	±0.011	±0.017	±0.018	±0.013	±0.030	±0.038	±0.009	±0.020	±0.026	±0.018	±0.021	±0.029	±0.023	±0.016	±0.013
Ca	0.000	0.003	0.002	0.005	0.001	0.003	0.001	0.029	0.001	0.000	0.000	0.002	0.001	0.003	0.000	0.001
	±0.000	±0.003	±0.003	±0.004	±0.001	±0.002	±0.002	±0.074	±0.001	±0.000	±0.000	±0.002	±0.001	±0.002	±0.000	±0.001
Ti	0.008	0.011	0.013	0.013	0.025	0.038	0.036	0.031	0.067	0.041	0.037	0.057	0.048	0.054	0.038	0.045
	±0.003	±0.003	±0.004	±0.005	±0.008	±0.004	±0.019	±0.013	±0.007	±0.008	±0.014	±0.015	±0.008	±0.025	±0.006	±0.016
Mn	0.004	0.002	0.003	0.004	0.003	0.004	0.004	0.001	0.002	0.003	0.000	0.003	0.001	0.002	0.000	0.002
	±0.002	±0.003	±0.002	±0.003	±0.003	±0.002	±0.002	±0.001	±0.003	±0.002	±0.000	±0.003	±0.001	±0.002	±0.000	±0.001
Fe	0.075	0.084	0.127	0.133	0.106	0.117	0.181	0.112	0.082	0.071	0.068	0.089	0.088	0.097	0.083	0.087
	±0.005	±0.010	±0.027	±0.029	±0.021	±0.037	±0.024	±0.013	±0.012	±0.007	±0.008	±0.029	±0.035	±0.034	±0.008	±0.033
Na	0.172	0.120	0.181	0.197	0.074	0.110	0.127	0.074	0.066	0.144	0.133	0.133	0.087	0.129	0.106	0.105
	±0.026	±0.011	±0.027	±0.017	±0.013	±0.005	±0.012	±0.004	±0.009	±0.012	±0.007	±0.017	±0.007	±0.010	±0.006	±0.013
K	0.780	0.811	0.756	0.771	0.853	0.814	0.808	0.888	0.852	0.773	0.781	0.775	0.843	0.793	0.825	0.827
	±0.025	±0.014	±0.017	±0.018	±0.019	±0.048	±0.010	±0.014	±0.050	±0.027	±0.019	±0.015	±0.009	±0.023	±0.007	±0.020
Total	6.971	6.963	6.976	7.007	6.957	6.966	6.990	7.008	6.932	6.928	6.925	6.934	6.953	6.951	6.935	6.957
Xmarg	0.000	0.003	0.002	0.005	0.001	0.003	0.001	0.029	0.001	0.000	0.000	0.002	0.001	0.003	0.000	0.001
Xparag	0.181	0.128	0.193	0.202	0.080	0.119	0.136	0.075	0.072	0.157	0.146	0.146	0.093	0.139	0.114	0.113
Xmusc	0.819	0.868	0.805	0.792	0.919	0.878	0.863	0.896	0.927	0.843	0.854	0.852	0.905	0.857	0.886	0.886

Table 5: Plagioclase analyses: weight percent oxides

	L7a	L52a	L17	L58b	L103a	L63	L67	L48	L71a	L20a	L73a	L21	L22	L22a	L142	L25	L26	L171	L159	L157
MgO	0.01	0.00	0.00	0.03	0.01	0.03	0.03	0.01	0.02	0.02	0.01	0.03	0.02	0.00	0.01	0.02	0.00	0.00	0.04	0.00
	±0.01	±0.01	±0.01	±0.03	±0.01	±0.01	±0.03	±0.04	±0.02	±0.02	±0.01	±0.03	±0.01	±0.01	±0.01	±0.01	±0.00	±0.01	±0.02	±0.01
Al2O3	21.91	23.14	21.56	21.35	23.98	22.27	22.09	23.64	24.08	25.18	22.90	22.44	23.20	22.97	22.64	21.78	22.63	22.81	23.17	24.80
	±0.51	±0.20	±0.24	±0.58	±0.34	±0.40	±0.20	±0.51	±0.24	±0.59	±0.11	±0.32	±0.70	±0.35	±0.35	±0.23	±0.39	±0.52	±0.62	±0.60
SiO2	64.57	62.76	66.53	66.33	61.28	64.94	65.69	62.20	62.97	60.51	63.07	64.05	63.42	63.61	63.15	65.49	63.13	63.57	62.17	59.34
	±0.90	±0.32	±0.41	±0.99	±0.65	±0.48	±0.32	±0.65	±0.58	±0.99	±0.27	±0.81	±1.07	±0.53	±0.27	±0.66	±0.35	±0.88	±1.02	±0.71
CaO	2.86	4.26	2.37	1.85	5.59	3.39	2.94	5.14	5.28	6.94	4.30	3.63	4.45	4.18	3.74	2.55	4.08	3.92	4.42	7.06
	±0.67	±0.12	±0.27	±0.84	±0.27	±0.07	±0.09	±0.36	±0.25	±0.75	±0.13	±0.47	±0.79	±0.38	±0.11	±0.34	±0.47	±0.58	±0.72	±0.53
FeO	0.30	0.17	0.14	0.47	0.36	0.10	0.35	0.16	0.05	0.38	0.28	0.13	0.23	0.28	0.17	0.43	0.29	0.15	0.44	0.35
	±0.24	±0.04	±0.12	±0.24	±0.29	±0.07	±0.11	±0.15	±0.03	±0.06	±0.07	±0.07	±0.06	±0.16	±0.09	±0.15	±0.04	±0.10	±0.11	±0.11
Na2O	10.24	9.45	10.77	10.90	8.63	9.97	10.39	8.93	8.97	7.94	9.08	9.77	9.30	9.54	9.57	10.45	9.18	9.48	9.16	7.60
	±0.37	±0.06	±0.24	±0.47	±0.20	±0.20	±0.16	±0.21	±0.20	±0.48	±0.12	±0.35	±0.53	±0.16	±0.14	±0.20	±0.27	±0.42	±0.37	±0.31
K2O	0.13	0.12	0.01	0.02	0.05	0.09	0.05	0.08	0.07	0.07	0.19	0.05	0.05	0.05	0.09	0.03	0.08	0.05	0.14	0.01
	±0.22	±0.02	±0.01	±0.03	±0.03	±0.02	±0.02	±0.03	±0.02	±0.03	±0.07	±0.02	±0.02	±0.03	±0.01	±0.02	±0.03	±0.01	±0.09	±0.02
Total	100.02	99.90	101.38	100.95	99.90	100.79	101.54	100.16	101.44	101.04	99.83	100.10	100.67	100.63	99.37	100.75	99.39	99.98	99.54	99.16
	Plagioclase analyses: cations per 8 oxygens																			
Mg	0.001	0.000	0.000	0.002	0.001	0.002	0.002	0.001	0.001	0.001	0.000	0.002	0.001	0.000	0.001	0.001	0.000	0.000	0.002	0.000
	±0.001	±0.001	±0.001	±0.002	±0.001	±0.001	±0.002	±0.003	±0.001	±0.001	±0.001	±0.002	±0.001	±0.000	±0.001	±0.001	±0.000	±0.000	±0.001	±0.000
Al	1.140	1.209	1.103	1.097	1.258	1.149	1.132	1.234	1.241	1.312	1.197	1.167	1.202	1.191	1.187	1.123	1.186	1.188	1.217	1.315
	±0.030	±0.005	±0.013	±0.032	±0.017	±0.017	±0.008	±0.026	±0.015	±0.034	±0.005	±0.020	±0.039	±0.018	±0.017	±0.018	±0.015	±0.030	±0.035	±0.029
Si	2.850	2.783	2.888	2.893	2.728	2.842	2.855	2.755	2.753	2.673	2.797	2.825	2.789	2.798	2.809	2.866	2.808	2.809	2.771	2.670
	±0.029	±0.005	±0.013	±0.035	±0.017	±0.016	±0.009	±0.026	±0.014	±0.034	±0.007	±0.021	±0.039	±0.021	±0.013	±0.019	±0.018	±0.029	±0.035	±0.029
Ca	0.135	0.203	0.110	0.086	0.266	0.159	0.137	0.244	0.248	0.329	0.204	0.172	0.210	0.197	0.178	0.120	0.194	0.186	0.211	0.341
	±0.032	±0.006	±0.013	±0.039	±0.013	±0.003	±0.004	±0.017	±0.013	±0.037	±0.006	±0.023	±0.038	±0.018	±0.005	±0.016	±0.022	±0.028	±0.035	±0.025
Fe	0.011	0.006	0.005	0.017	0.013	0.004	0.013	0.006	0.002	0.014	0.010	0.005	0.008	0.010	0.006	0.016	0.011	0.006	0.016	0.013
	±0.009	±0.001	±0.004	±0.009	±0.011	±0.003	±0.004	±0.005	±0.001	±0.002	±0.003	±0.002	±0.002	±0.006	±0.004	±0.006	±0.001	±0.004	±0.004	±0.004
Na	0.879	0.815	0.909	0.925	0.747	0.849	0.878	0.770	0.763	0.683	0.783	0.839	0.796	0.816	0.828	0.890	0.794	0.815	0.795	0.666
	±0.029	±0.008	±0.019	±0.038	±0.016	±0.015	±0.012	±0.015	±0.015	±0.039	±0.010	±0.026	±0.043	±0.013	±0.012	±0.012	±0.026	±0.034	±0.031	±0.027
K	0.008	0.007	0.000	0.001	0.003	0.005	0.003	0.004	0.004	0.004	0.011	0.003	0.003	0.003	0.005	0.002	0.004	0.003	0.008	0.001
	±0.012	±0.001	±0.001	±0.001	±0.002	±0.001	±0.001	±0.001	±0.001	±0.001	±0.004	±0.001	±0.001	±0.002	±0.001	±0.001	±0.002	±0.001	±0.005	±0.001
Total	5.024	5.023	5.015	5.021	5.016	5.010	5.020	5.014	5.012	5.016	5.002	5.013	5.009	5.015	5.014	5.018	4.997	5.007	5.020	5.006
Xal	0.860	0.795	0.892	0.914	0.735	0.838	0.862	0.756	0.752	0.672	0.785	0.827	0.789	0.803	0.819	0.879	0.800	0.812	0.784	0.661
Xan	0.132	0.198	0.108	0.085	0.262	0.157	0.135	0.240	0.244	0.324	0.204	0.170	0.208	0.194	0.176	0.119	0.196	0.185	0.208	0.338
Xor	0.008	0.007	0.000	0.001	0.003	0.005	0.003	0.004	0.004	0.004	0.011	0.003	0.003	0.003	0.005	0.002	0.004	0.003	0.008	0.001

Table 6: Langtang Thermobarometric Data

Tectonic Unit	*Stratigraphic Unit*	*Sample No.*	*Temperature (K)*	*Pressure (MPa)*	*Thermometer / Barometer*
Lesser Himalaya	Dhunche	L7a	668 ± 30	788 ± 150	GB/GMPB
	Dhunche	L52a	767 ± 50	626 ± 110	GB/GMPB
Main Central Thrust Zone	Trisuli	L17	725 ± 40	510 ± 100	GB/GMPB
	Trisuli	L58b	752 ± 60	634 ± 180	GB/GMPB
	Trisuli	L123e	730-765 ± 60		GB
	Trisuli	L18a	700-730 ± 50		GB
	Trisuli	L103a	830 ± 70	899 ± 160	GB/GASP (kya)
	Barabal	L94b	750-785 ± 80		GB
	Phulung	L63	810 ± 70	767 ± 230	GB/GMPB
	Syabru	L67	829 ± 100	686 ± 200	GB/GASP (kya)
	Syabru	L48	794 ± 50	599 ± 120	GB/GMPB
	Syabru	L71a	852 ± 40	689 ± 90	GB/GASP (kya)
	Syabru	L20a	818 ± 60	621 ± 240	GB/GMPB
Greater Himalaya	Gosainkund	L73a	864 ± 110	663 ± 200	GB/GASP (kya)
	Gosainkund	L21	830 ± 90	504 ± 170	GB/GMPB
	Gosainkund	L22	818 ±70	501 ± 160	GB/GASP (kya)
	Gosainkund	L22a	812 ± 90	510 ±150	GB/GASP (kya)
	Gosainkund	L142	838 ± 100	484 ± 150	GB/GMPB
	Gosainkund	L25	809 ± 80	499 ± 170	GB/GASP (sill)
	Ghora Tabela	L26	821 ± 80	551 ±160	GB/GASP (sill)
	Ghora Tabela	L171	868 ± 70	482 ± 100	GB/GASP (sill)
	Kyangjin	L159	808 ± 100	258 ± 140	GB/GASP (sill)
	Kyangjin	L157	757 ± 100	217 ± 140	GB/GASP (sill)
	Kyangjin	L36b	745-780 ± 50		GB

Table 7: Compositions used in Gibb's Method modeling

Component	L67			L73a					L22a					L25				
	Xrim	Xbi inc	ΔX	Xrim	Xbi inc 1	ΔX.1	Xbi inc 2	ΔX.2	Xrim	Xpg inc	ΔX.1	Xbi inc	ΔX.2	Xrim	Xpg inc	ΔX.1	Xbi inc	ΔX.2
Almandine	0.756	0.743	-0.013	0.778	0.776	-0.002	0.745	-0.033	0.789	0.746	-0.042	0.775	-0.013	0.761	0.724	-0.037	0.755	-0.006
Pyrope	0.148	0.183	0.034	0.130	0.110	-0.020	0.159	0.029	0.118	0.160	0.042	0.130	0.013	0.121	0.142	0.020	0.104	-0.018
Grossular	0.048	0.044	-0.003	0.053	0.069	0.016	0.068	0.015	0.045	0.047	0.002	0.043	-0.002	0.025	0.025	0.000	0.024	-0.001
Spessartine	0.048	0.029	-0.018	0.039	0.045	0.006	0.029	-0.011	0.049	0.047	-0.002	0.052	0.003	0.093	0.109	0.016	0.117	0.024
Annite	0.465	0.365	-0.099	0.531	0.533	0.002	0.381	-0.151	0.526			0.407	-0.119	0.505			0.488	-0.017
Phlogopite	0.534	0.635	0.100	0.467	0.467	0.001	0.615	0.149	0.473			0.593	0.120	0.492			0.506	0.014
Mn-Biotite	0.001	0.000	-0.001	0.002	0.000	-0.002	0.004	0.002	0.001			0.000	-0.001	0.003			0.006	0.003
Anorthite									0.194	0.071	-0.123			0.119	0.108	-0.011		
Albite									0.806	0.929	0.123			0.881	0.892	0.011		
Core Temperature (K)		792			807		771			818		722			832		744	
Core Pressure (MPa)		1124			639		1224			838		959			567		545	

FIGURE CAPTIONS

Figure 1: Geologic map of Nepal. Location map of Nepal and India in box on right. Thin solid line is delineates boundaries of Nepal. The Main Central Thrust (MCT) is the barbed line between the Greater Himalayan sequence and the Lesser Himalayan sequence. The Main Boundary Thrust (MBT) is the barbed contact between the Lesser Himalayan sequence and the Subhimalayan sequence. The South Tibetan detachment system is the normal fault located between the Greater Himalayan sequence and the Tibetan Sedimentary sequence. Shaded ovals are regions discussed in the text.

Figure 2: Geologic map of the Langtang National park region. Samples used in thermobarometry are indicated by solid circles with samples numbers. The upper MCT zone is enlarged in box on right for clarification.

Figure 3: Photomicrographs of garnets form the Langtang sample set. (a) Lesser Himalayan sequence garnet displaying snowball quartz inclusions and a pressure shadow associated with a later deformational event. Bottom of photo is 1.5 mm across. (b) MCT zone garnet with helicitic inclusion trails and later pressure shadow. Garnet is 5 mm in diameter.

Figure 4: Fabric - porphyroblast relations for the Lesser Himalayan sequence, MCT zone and Greater Himalayan sequence. (a) D_{1LH} refers to the first deformational event in the Lesser Himalayan sequence. D_{2LH} refers to the main foliation-forming event in the Lesser Himalayan sequence. (b)

D_{1MCT} refers to the deformational event the preceded the dominant schistosity-forming event, D_{2MCT} in the MCT zone. (c) D_{1GH} and D_{2GH} are as in the MCT zone and Lesser Himalayan sequence.

Figure 5: Phase diagrams for the Langtang samples. In the following, Gt is garnet; Bt is biotite, St is staurolite, Chl is chlorite, A or AlSi is aluminum silicate. (a) AFM projection from quartz, water and muscovite for Lesser Himalayan samples. Chlorite composition is not known; it is estimated. (b) AFM projection from quartz, water and muscovite for the lower MCT zone samples. Staurolite composition is not known; it is estimated. (c) AFM projection from quartz, water and muscovite for upper MCT zone samples. (d) AFM projection from quartz, water and muscovite for the lower Greater Himalayan sequence samples (L73a, L21, L22, L22a, L142). The A apex is kyanite in this case. (e) Al'-Fe-Mg-Mn projection quartz, water and muscovite for the lower Greater Himalayan sequence samples. L73a no longer crosses with L22. (f) AFM projection from quartz, water and K-feldspar for the upper Greater Himalayan sequence samples (L25, L26, L171, L159, L157, L36b).The A apex is sillimanite for this projection.

Figure 6: Representative compositional profile across a relatively homogeneous garnet in sample L25.

Figure 7: Compositional profiles from Lesser Himalayan garnets. (a) Sample L7a. (b) Sample L52a.

Figure 8: Compositional profile across one garnet in sample L123e from the lower MCT zone.

Figure 9: Compositional profile across two garnets from the upper Greater Himalayan sequence. (a) Sample L171 and (b) Sample L36b display similar component patterns.

Figure 10: Pressure - temperature plots of Lesser Himalayan sequence rim thermobarometric data. Ellipses represent 95% precision limits that reflect the uncertainty in the analytical data. The aluminum silicate stability fields of Holdaway (1971) are plotted in the background. (a) Ellipse plot for the Lesser Himalayan sequence samples. (b) PT plot of analytical solutions with points labeled.

Figure 11: Pressure - temperature plots of MCT zone rim thermobarometric data. Ellipses represent 95% precision limits that reflect the uncertainty in the analytical data. The aluminum silicate stability fields of Holdaway (1971) are plotted in the background. Subvertical lines are Keq's for samples in which only the garnet-biotite thermometer was solved. (a) Ellipse plot for MCT zone samples. Shaded samples are those that were determined using GAPQ instead of GMPB. (See text for discussion.). Granite wet melting curve from Le Breton and Thompson (1988). (b) Analytical solutions of thermometer and barometer are labeled by sample number.

Figure 12: Pressure - temperature plot of Greater Himalayan sequence rim thermobarometric data. Ellipses represent 95% precision limits that reflect the uncertainty in the analytical data. The aluminum silicate triple

point of Holdaway (1971) is plotted in the background. Subvertical lines are Keq's for samples in which only the garnet-biotite thermometer was solved. (a) Ellipse plot for all Greater Himalayan sequence samples. Shaded samples are those that were determined using GASP instead of GMPB. (See text for discussion.). Muscovite - out reaction based on data from Berman (1988) after Spear & Cheney (1989). Granite wet melting curve from Le Breton and Thompson [, 1988 #141]. (b) Analytical solutions of thermometer and barometer are labeled by sample number.

Figure 13: Plot of results from quantitative modeling of pressure - temperature paths. Rim points are indicated by large open diamonds and were determined by thermobarometry. Core points calculated from plagioclase inclusions are shown with solid squares. Core points determined from biotite inclusions are shown with open circles. Rim points are labeled diamonds. Arrows indicate the calculated PT path direction from core to rim.

Figure 14: Gibbs Method modeling and inclusion thermobarometry results. Inclusion thermobarometry data are indicated as open diamonds with arrows to rim points, indicated by circles. Gibbs method modeling paths are shown as arrows from shaded diamonds (cores) to circles (rims). Equilibria plotted are aluminum silicate stability fields, based on data from Holdaway (1971); Granite wet melting curve; muscovite - out reaction based on data from Berman (1988) and garnet - rutile - aluminum silicate - ilmenite - quartz reaction based on data from Ghent and Stout (1984).

Figure 15: Interpretation of data presented in this paper. Shaded boxes include entire spread of analytical rim thermobarometry data for Lesser Himalayan sequence and MCT zone, and Greater Himalayan sequence. Equilibria plotted are aluminum silicate stability fields, based on data from Holdaway (1971); Granite wet melting curve; muscovite - out reaction based on data from Berman (1988) and garnet - rutile - aluminum silicate - ilmenite - quartz reaction based on data from Ghent and Stout (1984). Large shaded arrow shows progression from M1 at high pressure - moderate temperature to M_2 at moderate pressure and high temperature.

Figure 16: Temperature and pressure plotted as a function of structural distance in km from the base of the MCT, which is defined as the lowermost brittle fault encountered. Shaded area is the MCT zone; to the left is the Lesser Himalayan sequence; to the right, the Greater Himalayan sequence. Structural distance is calculated from the thicknesses of units, i.e., perpendicular to layering. (a) Temperature versus distance plot displays no thermal gradient from the upper Lesser Himalayan sequence to the upper Greater Himalayan sequence. (b) Pressure versus distance plot shows a slight structural break within the MCT zone and a more obvious decrease in pressure in the upper Greater Himalayan sequence. The upper two samples in the Greater Himalayan sequence are anomalous (see text). The line represents a lithostatic pressure gradient of 27 MPa/km for reference.

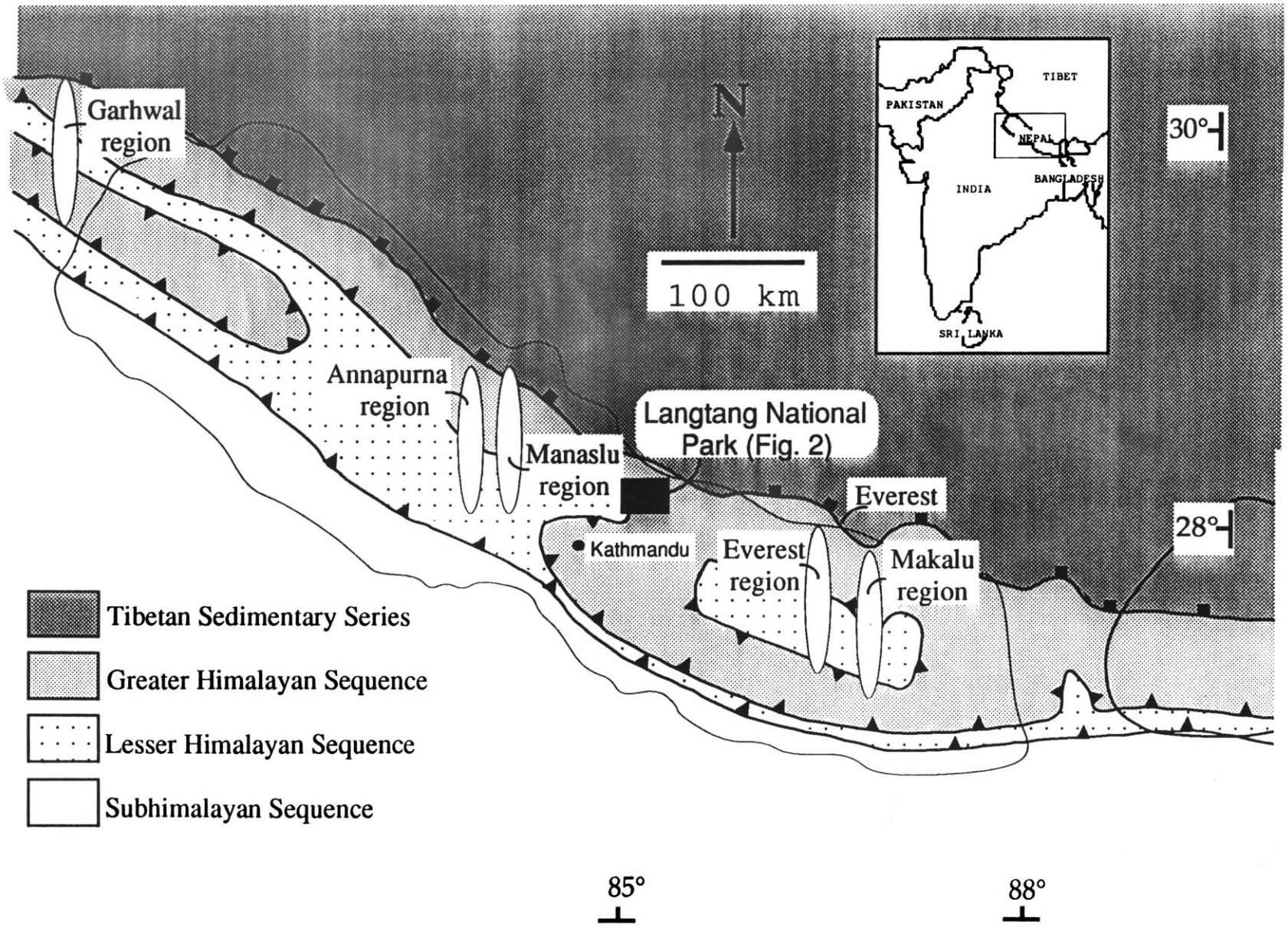
Garhwal region
Annapurna region
Manaslu region
Langtang National Park (Fig. 2)
Everest
Everest region
Makalu region
Kathmandu
N
100 km
TIBET
PAKISTAN
NEPAL
INDIA
BANGLADESH
SRI LANKA
30°
28°
85°
88°
Tibetan Sedimentary Series
Greater Himalayan Sequence
Lesser Himalayan Sequence
Subhimalayan Sequence

Figure 1

N
5 km
L103a
L159
L157
L36b
Langtang Khola
L171
L20a
L21
L22
L25
L26
L48
L7a
Trisuli Kosi
L71a
L73a
Trisuli Khola
L142
L94b
L58b
L18a
L17
L123
L51
L52a
L63
L67
Greater Himalayan Sequence
Main Central Thrust Zone
Lesser Himalayan Sequence
Thrust contact
Lithologic contact
Landslide contact
River

Figure 2

a.

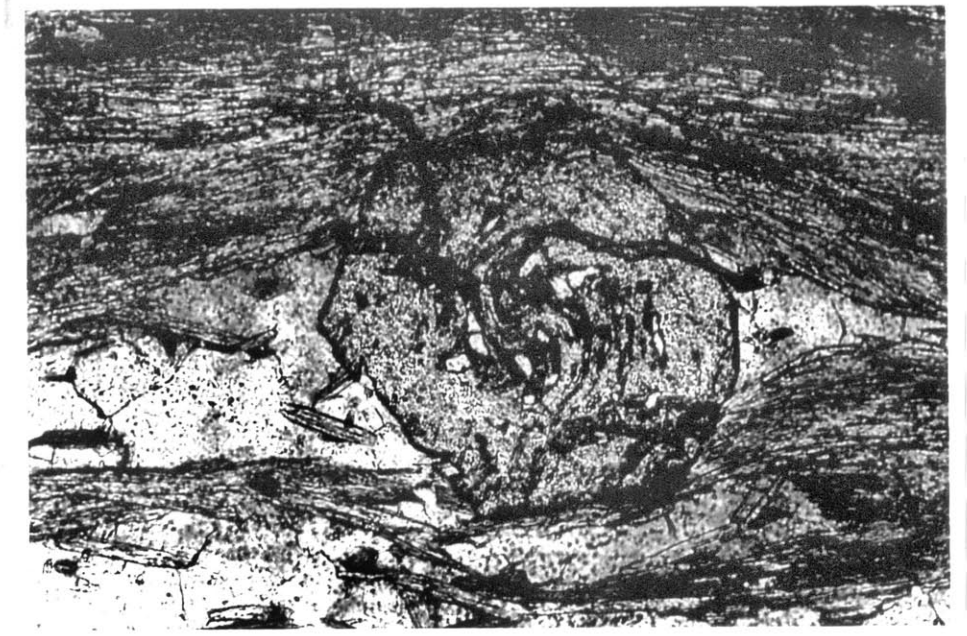

b.

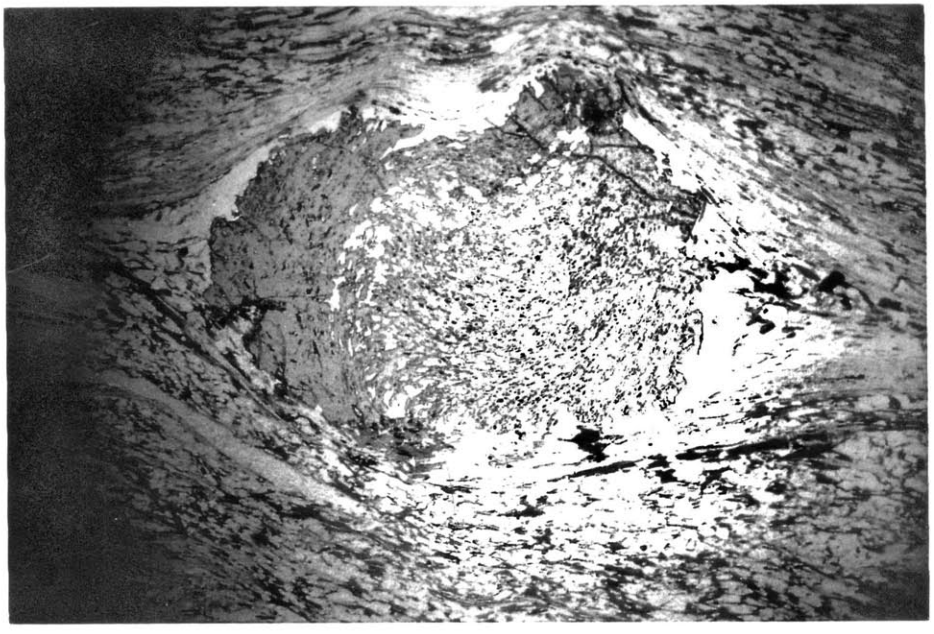

Figure 3

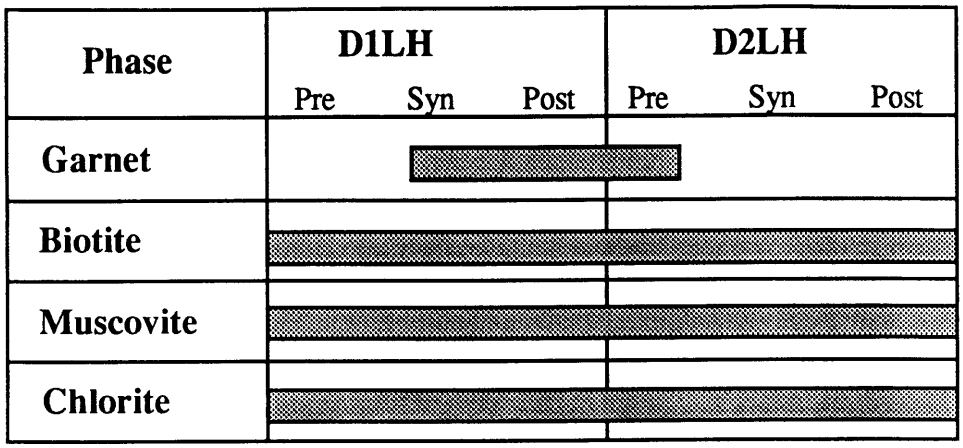
Phase
D1LH
Pre
Syn
Post
D2LH
Pre
Syn
Post
Garnet
Biotite
Muscovite
Chlorite

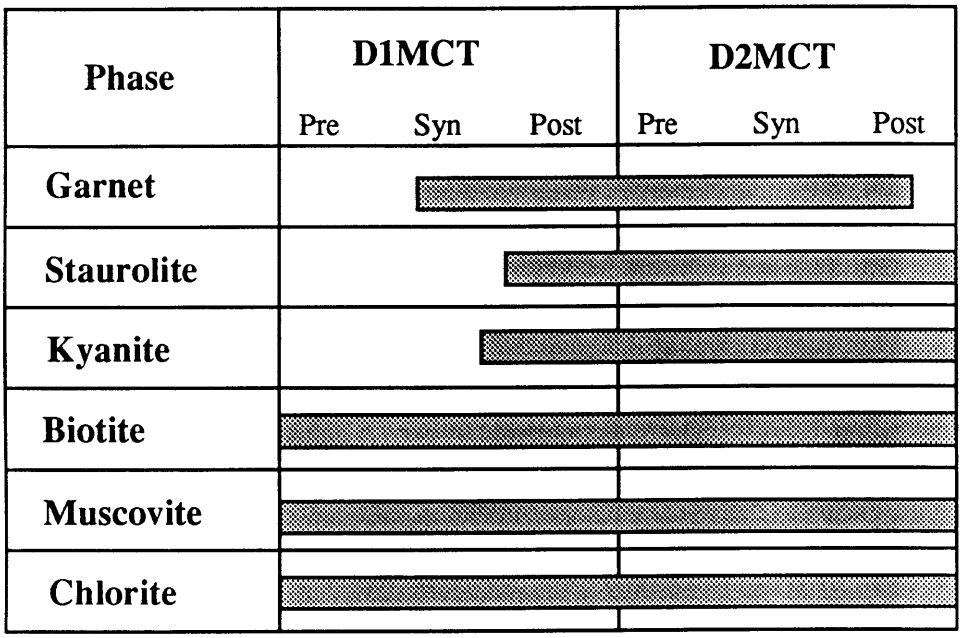
Phase
D1MCT
Pre
Syn
Post
D2MCT
Pre
Syn
Post
Garnet
Staurolite
Kyanite
Biotite
Muscovite
Chlorite

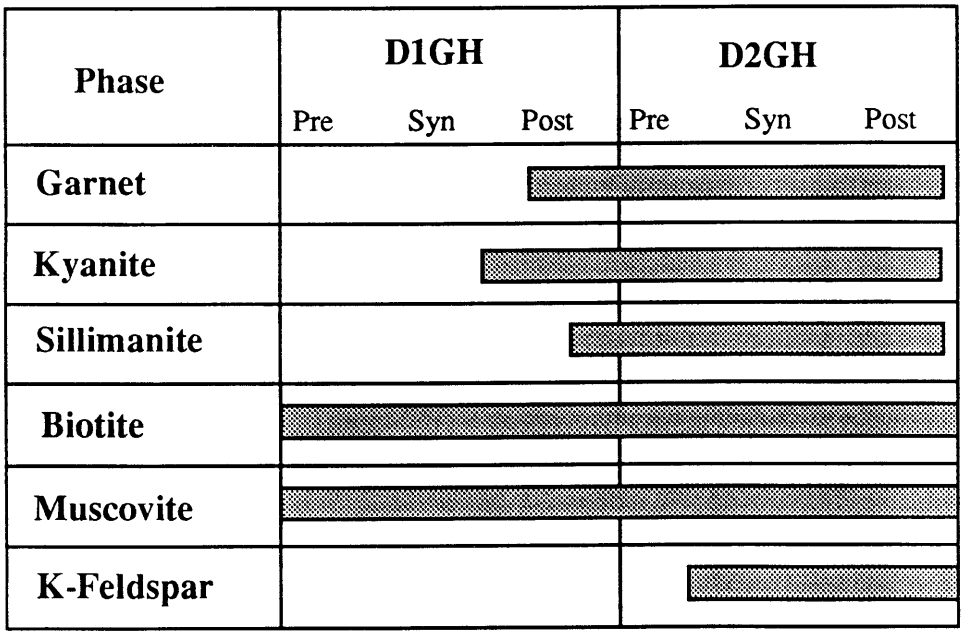
Phase
D1GH
Pre
Syn
Post
D2GH
Pre
Syn
Post
Garnet
Kyanite
Sillimanite
Biotite
Muscovite
K-Feldspar

Figure 4

Lesser Himalayan sequence AFM

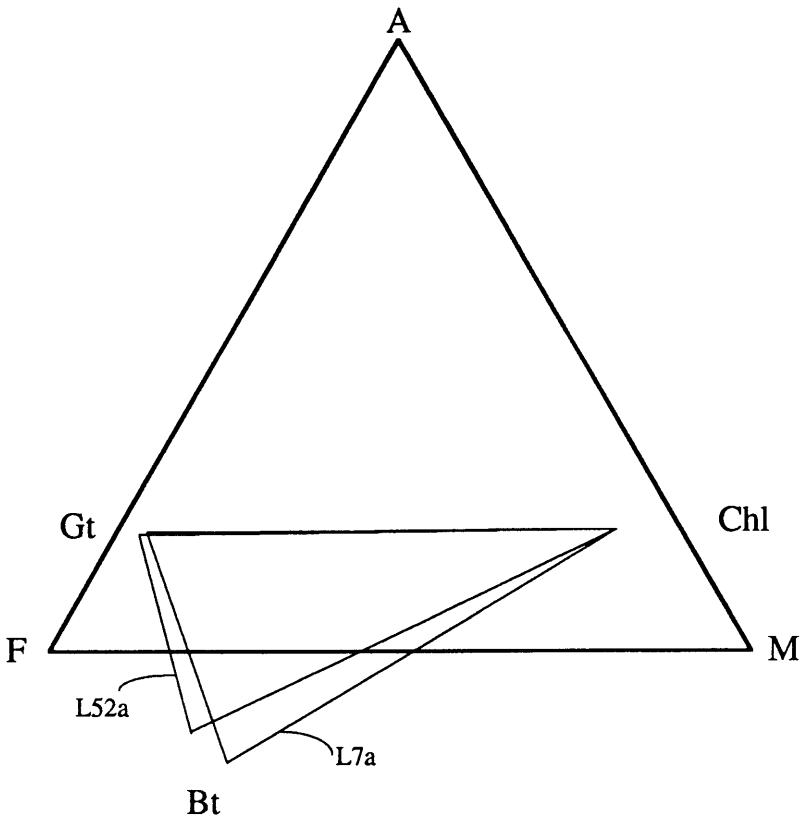

Figure 5a

MCT Zone AFM

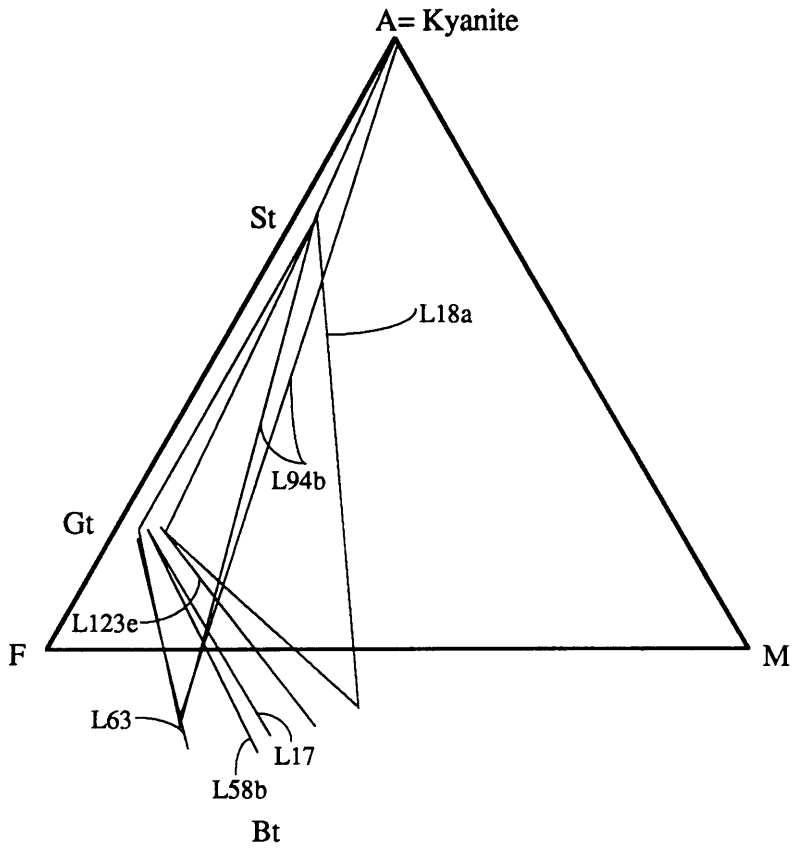

Figure 5b

MCT Zone AFM

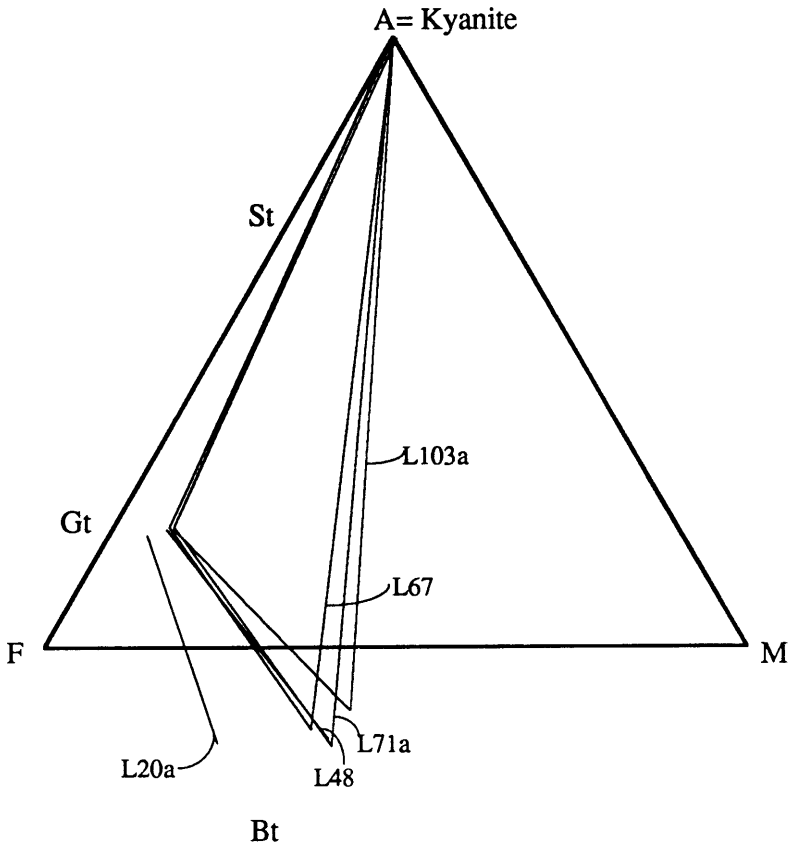

Figure 5c

Greater Himalayan Sequence AFM

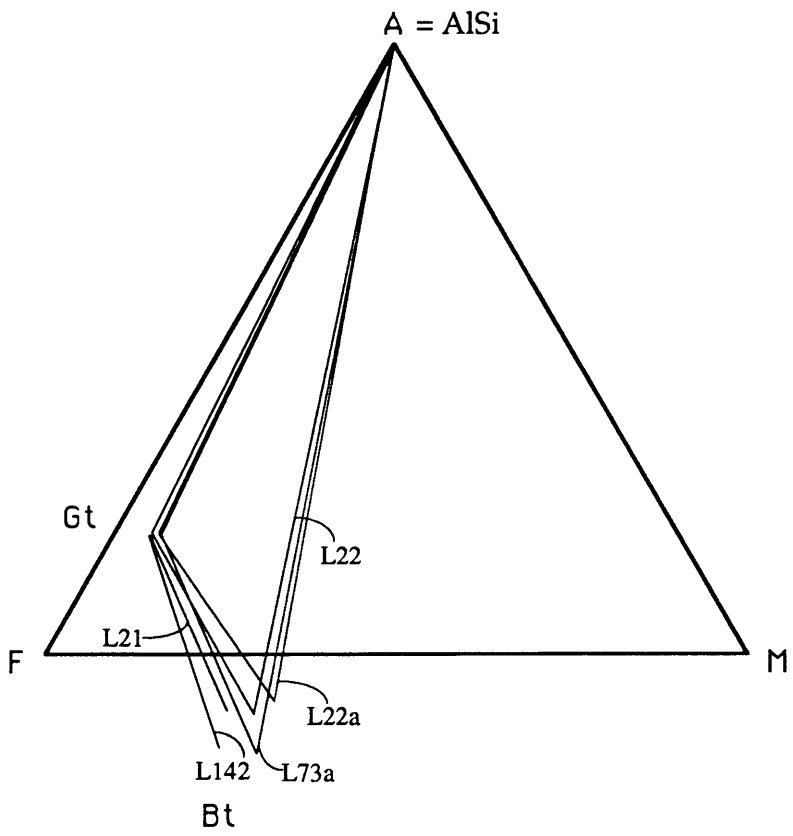

Figure 5d

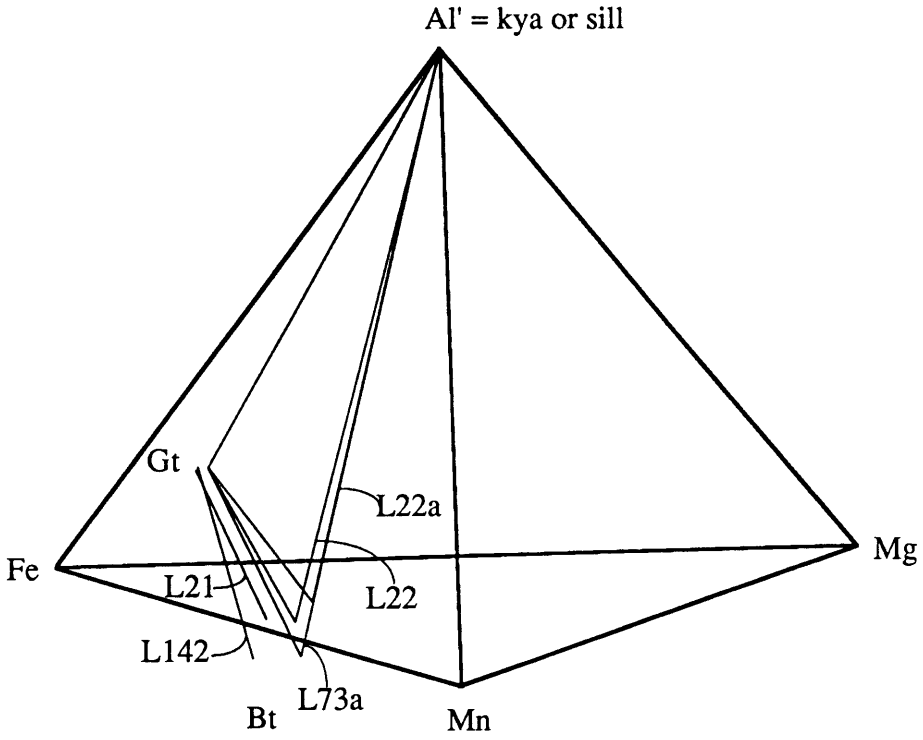

Figure 5e

Greater Himalayan Sequence AFM

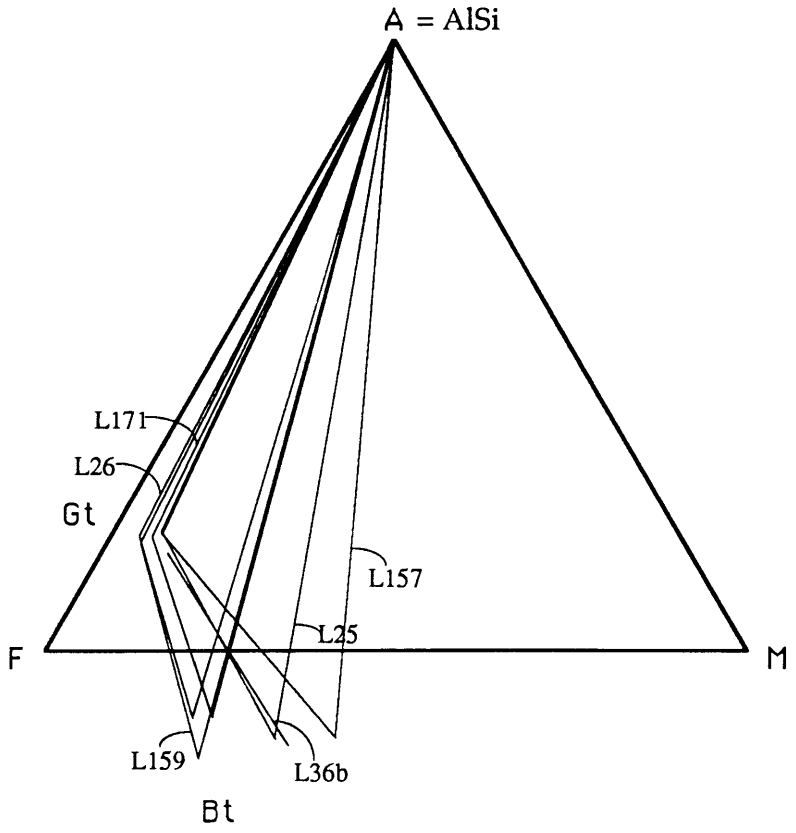

Figure 5f

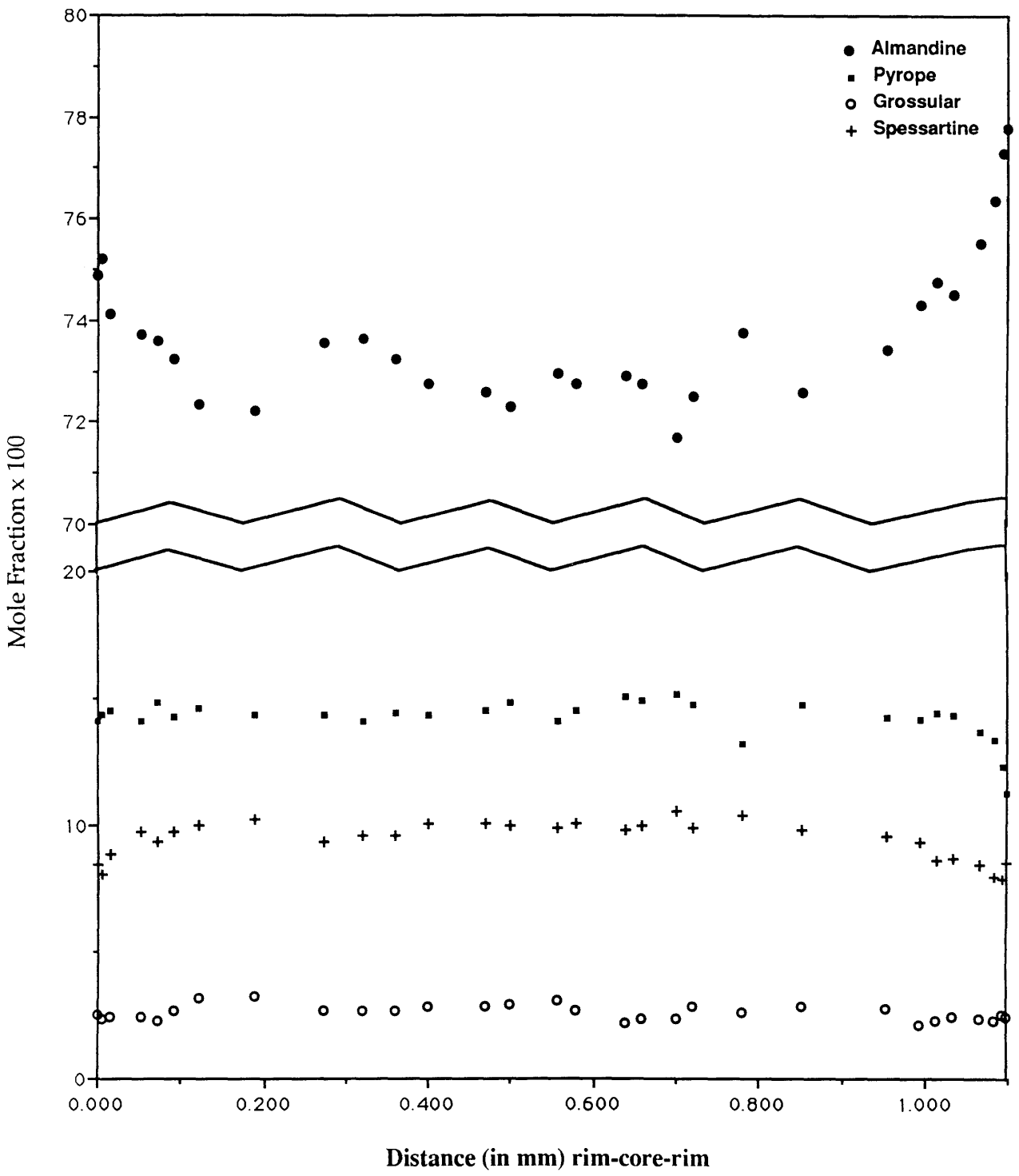
L25 Garnet Profile
Almandine
Pyrope
Grossular
Spessartine
Mole Fraction x 100
80
78
76
74
72
70
20
10
0
0.000
0.200
0.400
0.600
0.800
1.000
Distance (in mm) rim-core-rim

Figure 6

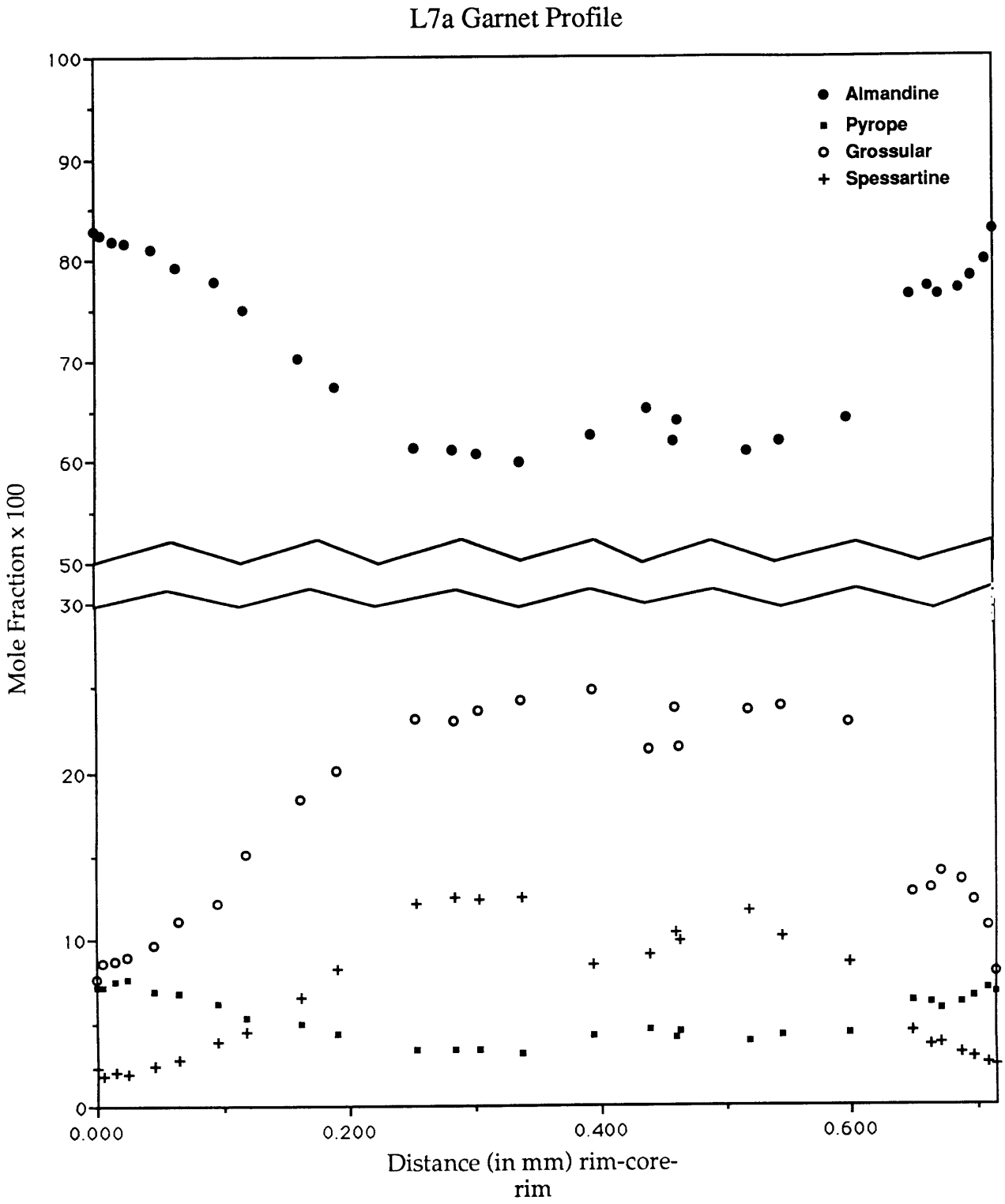
L7a Garnet Profile
Almandine
Pyrope
Grossular
Spessartine
Mole Fraction x 100
100
90
80
70
60
50
30
20
10
0
0.000
0.200
0.400
0.600
Distance (in mm) rim-core-rim

Figure 7a

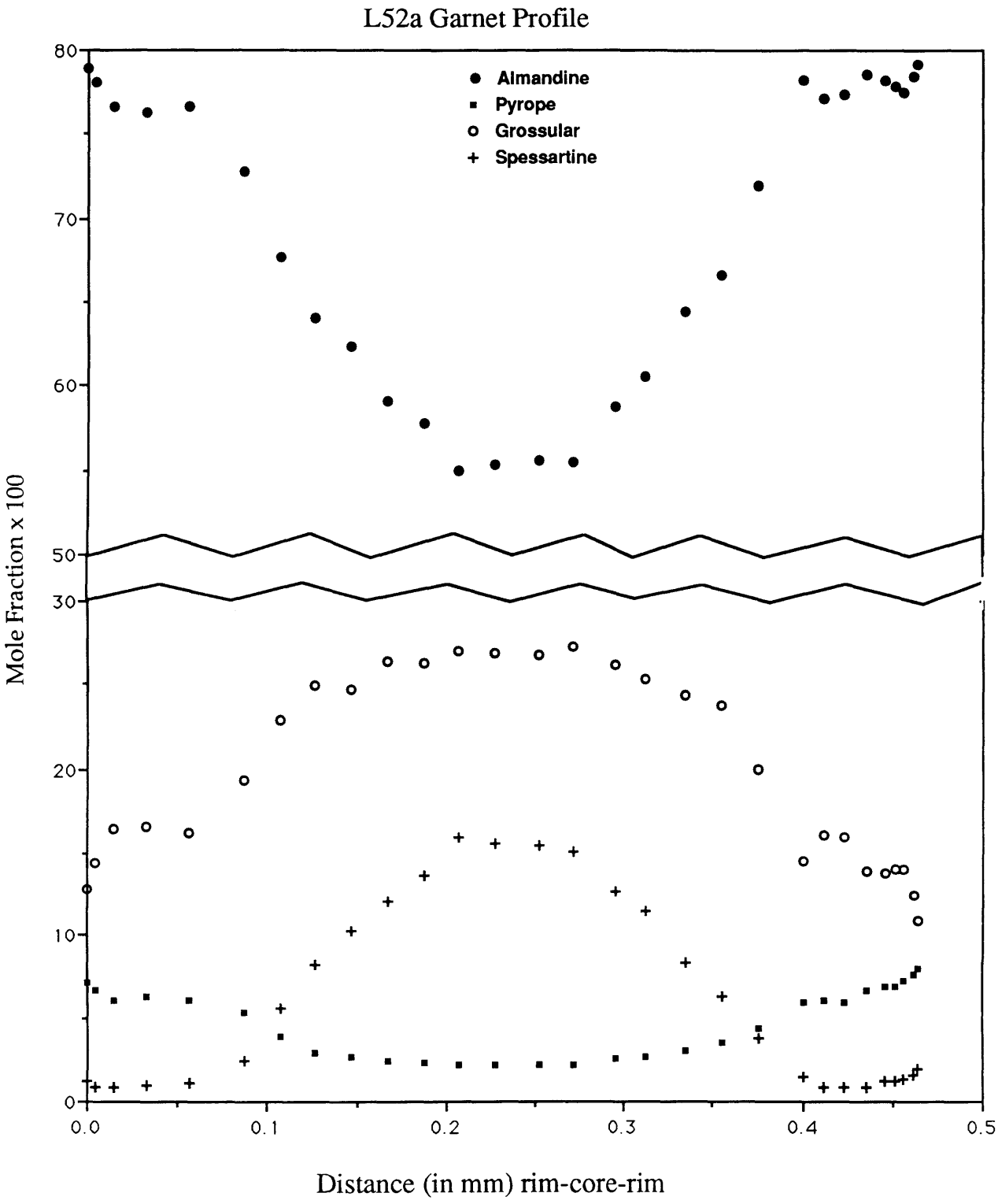
L52a Garnet Profile
Almandine
Pyrope
Grossular
Spessartine
Mole Fraction x 100
80
70
60
50
30
20
10
0
0.0
0.1
0.2
0.3
0.4
0.5
Distance (in mm) rim-core-rim

Figure 7b

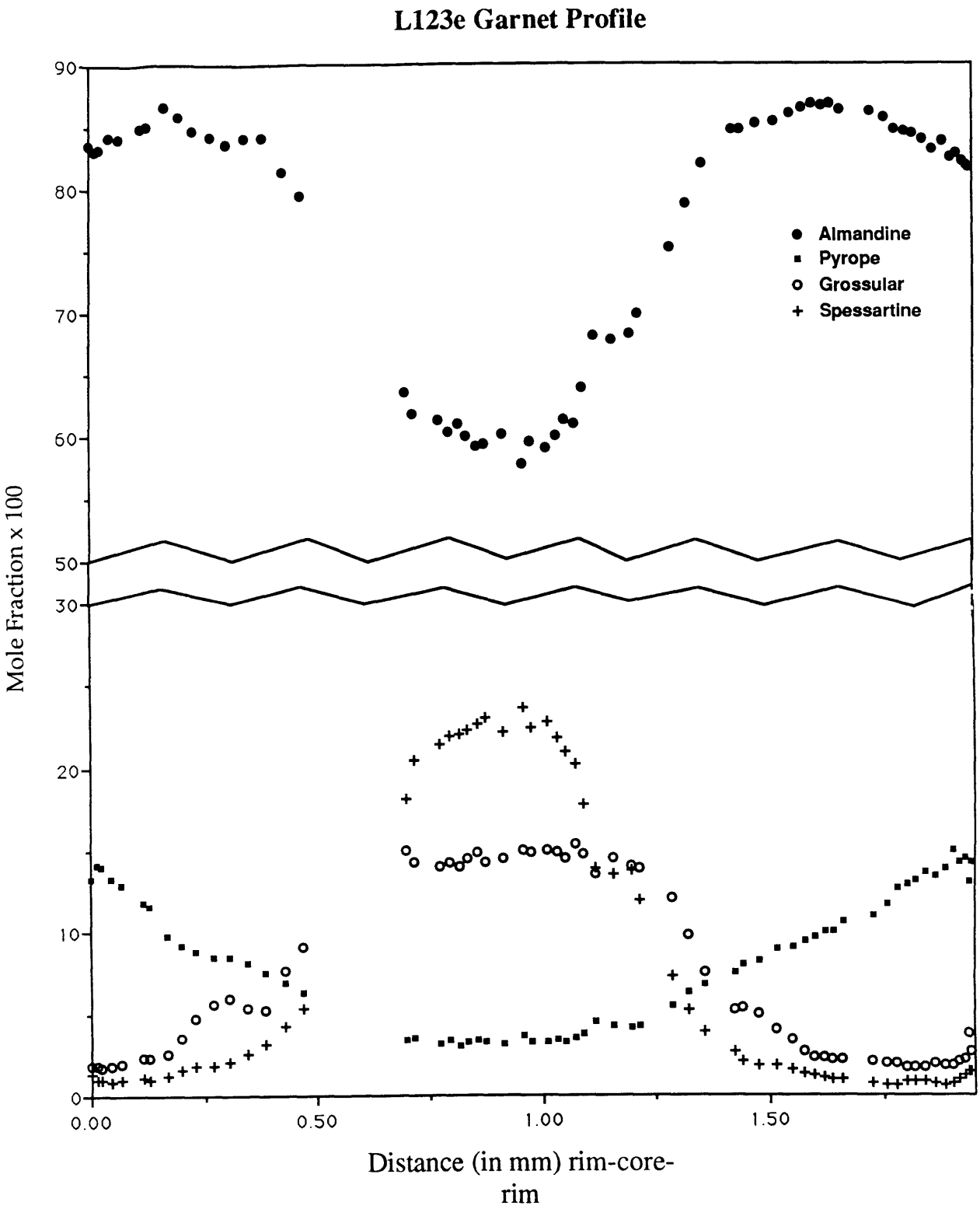
L123e Garnet Profile
Mole Fraction x 100
90
80
70
60
50
30
20
10
0
0.00
0.50
1.00
1.50
Distance (in mm) rim-core-rim
Almandine
Pyrope
Grossular
Spessartine

Figure 8

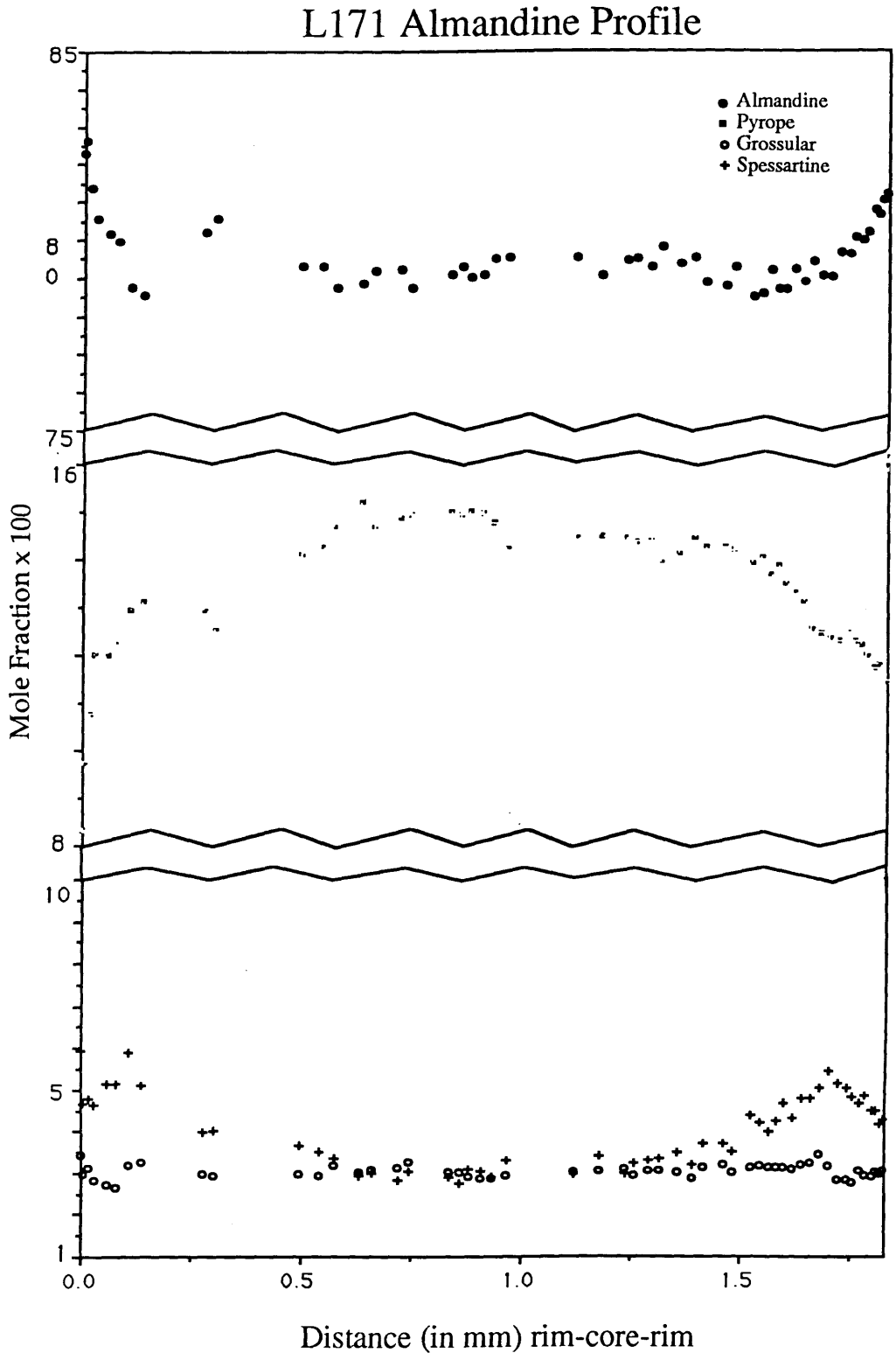
L171 Almandine Profile
Almandine
Pyrope
Grossular
Spessartine
Mole Fraction x 100
85
80
75
16
8
10
5
1
0.0
0.5
1.0
1.5
Distance (in mm) rim-core-rim

Figure 9a

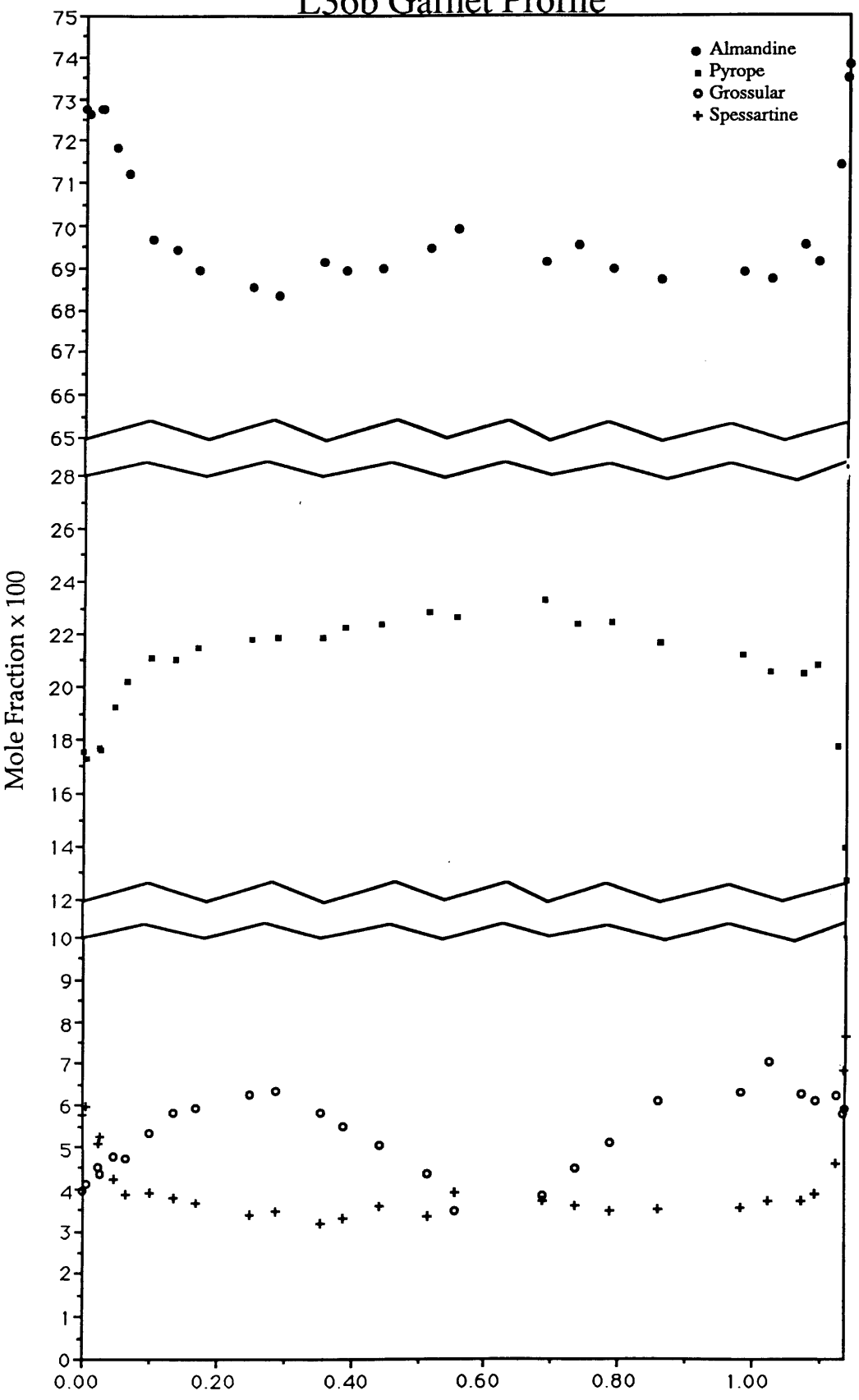
L36b Garnet Profile
Almandine
Pyrope
Grossular
Spessartine
Mole Fraction x 100
Distance (in mm) rim
core-rim

Figure 9b

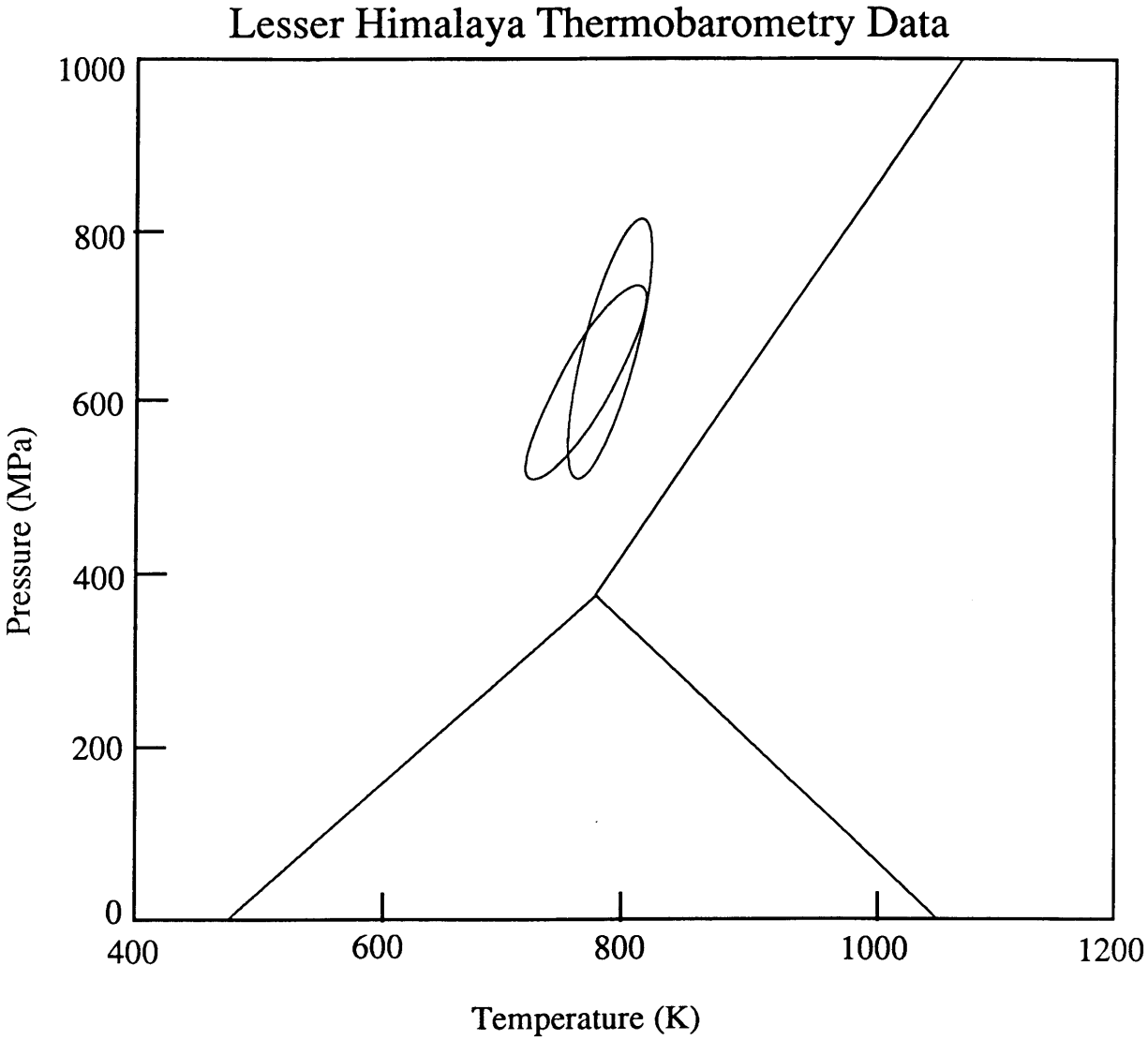
Lesser Himalaya Thermobarometry Data
1000
800
600
400
200
0
Pressure (MPa)
400
600
800
1000
1200
Temperature (K)

Figure 10a

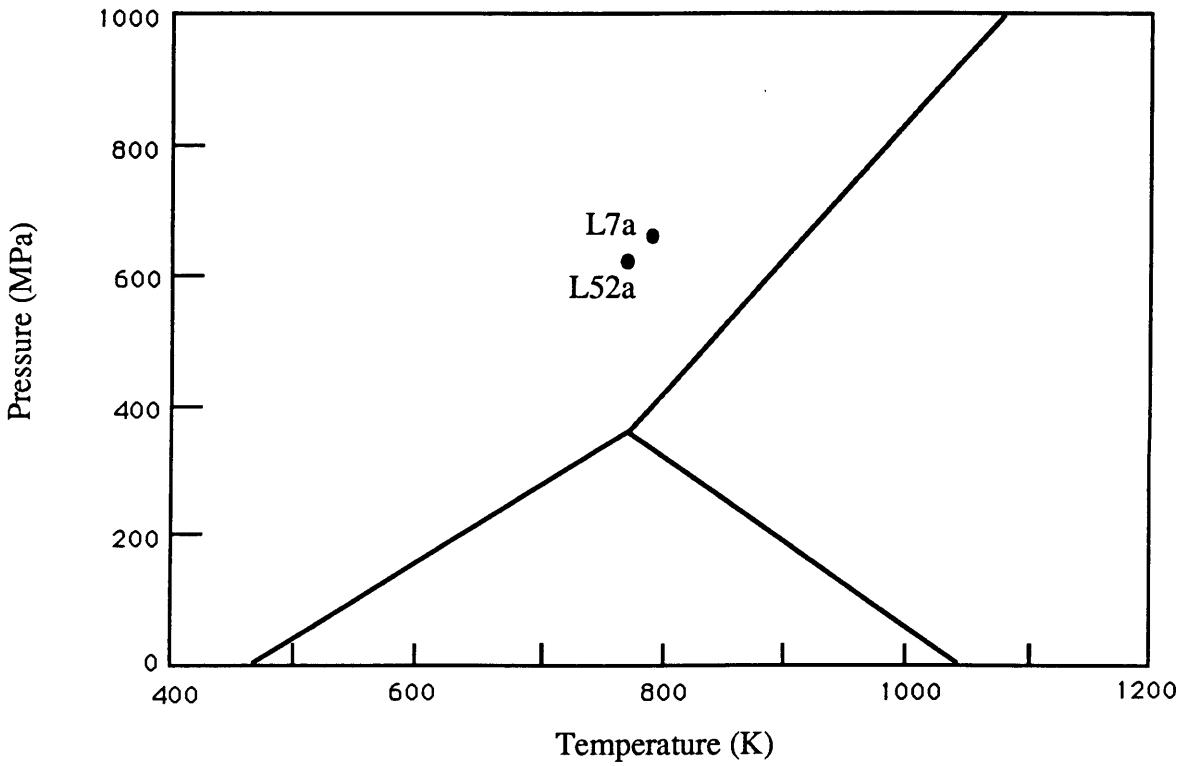
1000
800
600
400
200
0
Pressure (MPa)
L7a
L52a
400
600
800
1000
1200
Temperature (K)

Figure 10b

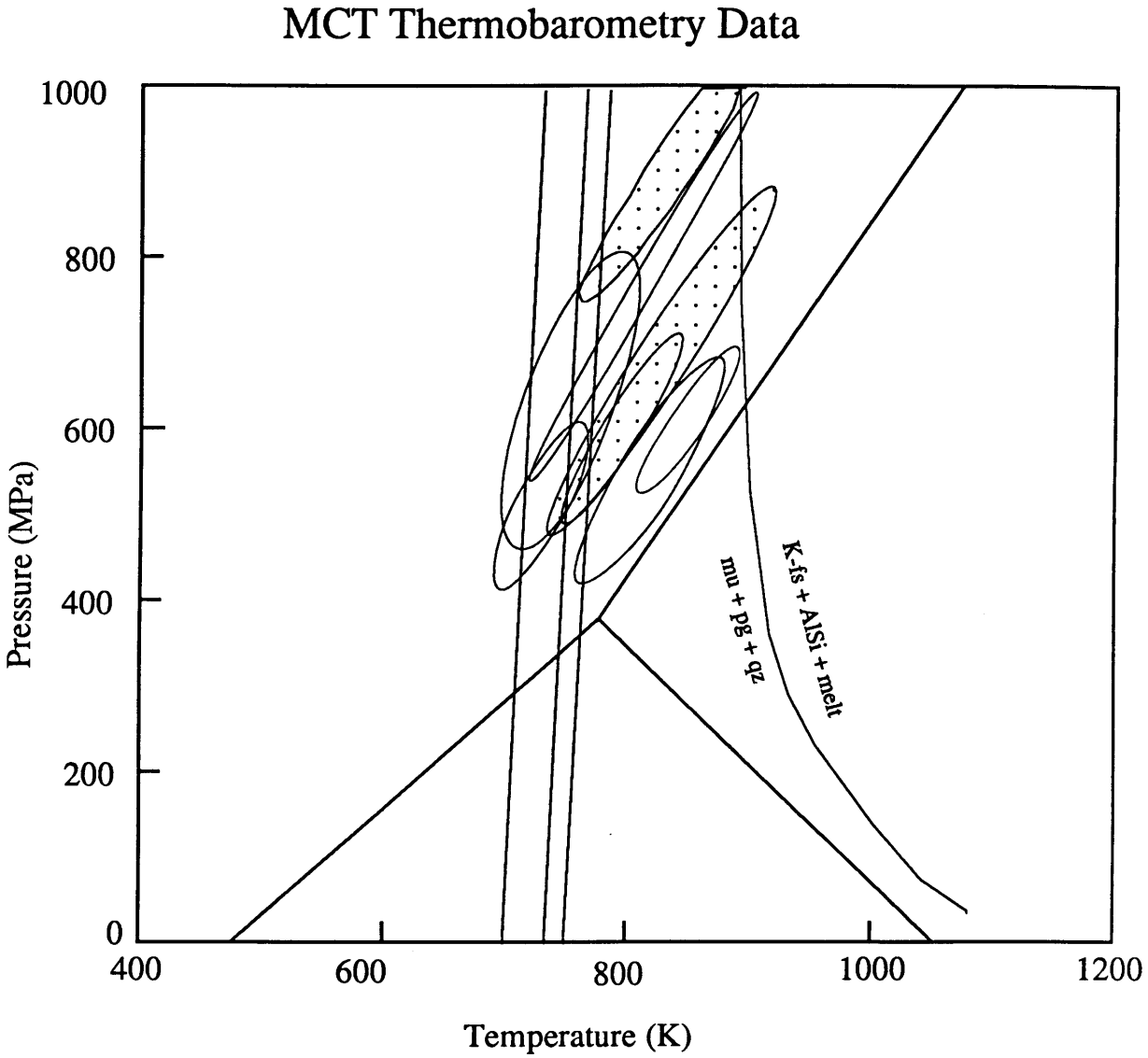
MCT Thermobarometry Data
1000
800
600
400
200
0
Pressure (MPa)
400
600
800
1000
1200
Temperature (K)
mu + pg + qz
K-fs + AlSi + melt

Figure 11a

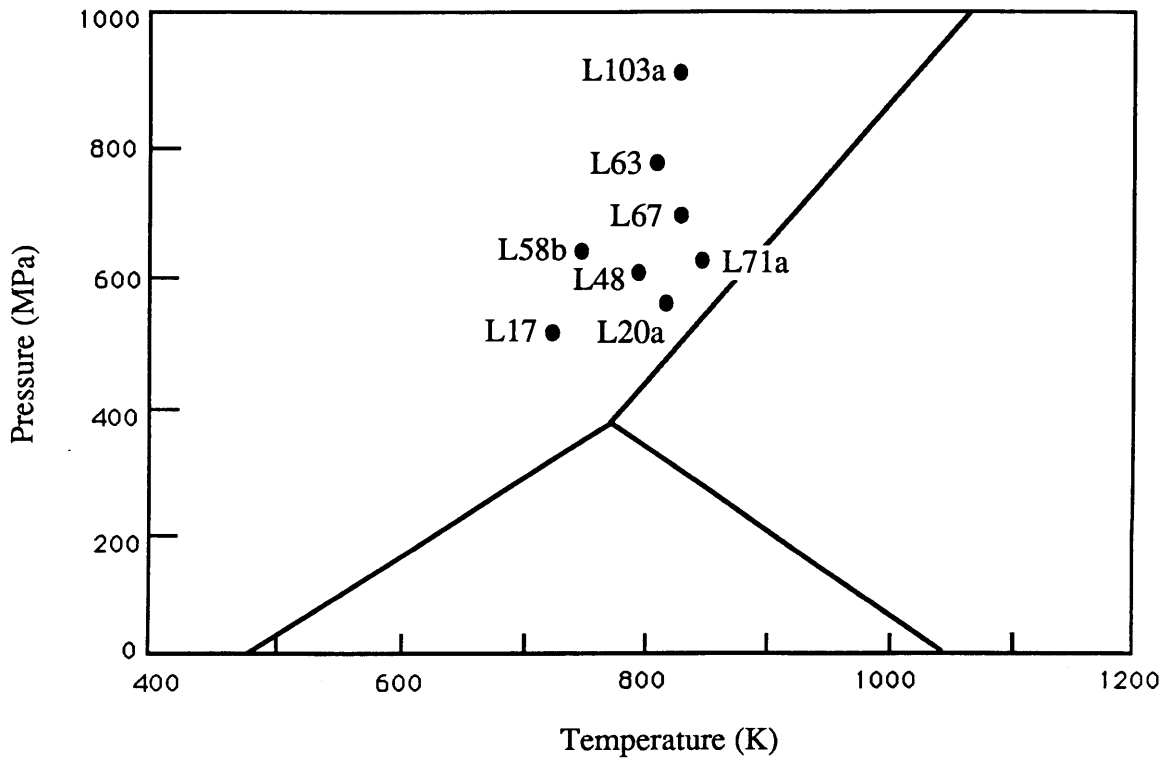
1000
800
600
400
200
0
Pressure (MPa)
400
600
800
1000
1200
Temperature (K)
L103a
L63
L67
L58b
L48
L71a
L17
L20a

Figure 11b

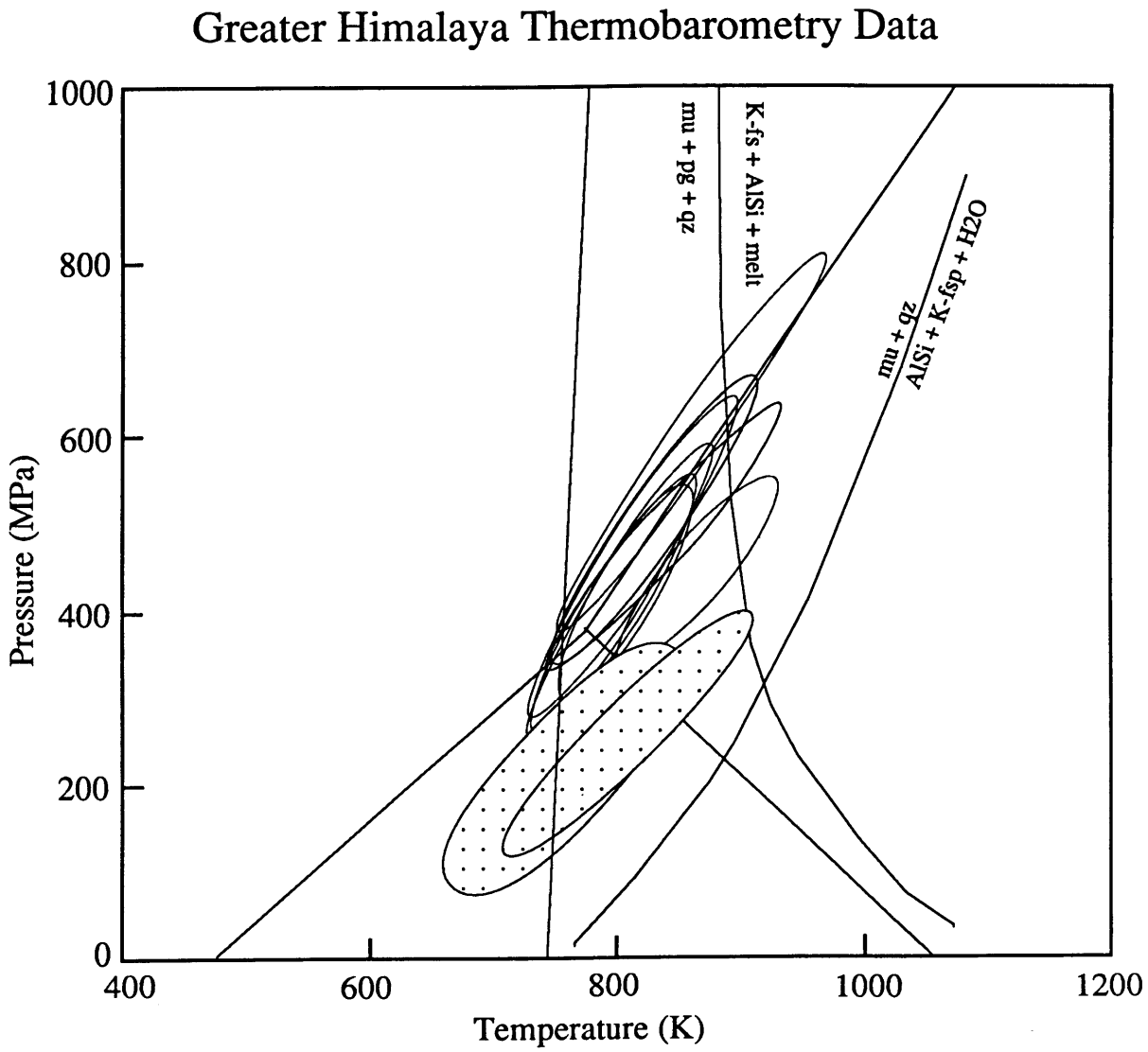
Greater Himalaya Thermobarometry Data
1000
800
600
400
200
0
Pressure (MPa)
400
600
800
1000
1200
Temperature (K)
mu + pg + qz
K-fs + AlSi + melt
mu + qz
AlSi + K-fsp + H2O

Figure 12a

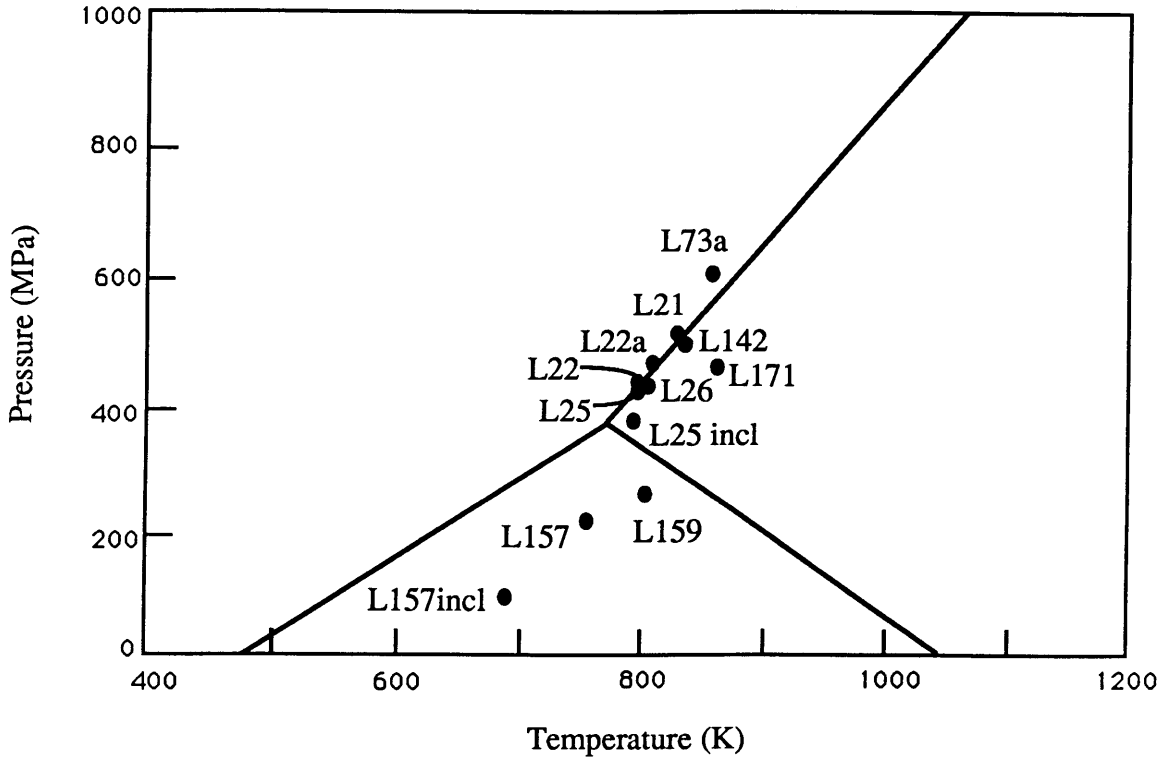
1000
800
600
400
200
0
Pressure (MPa)
400
600
800
1000
1200
Temperature (K)
L73a
L21
L22a
L142
L22
L171
L26
L25
L25 incl
L157
L159
L157incl

Figure 12b

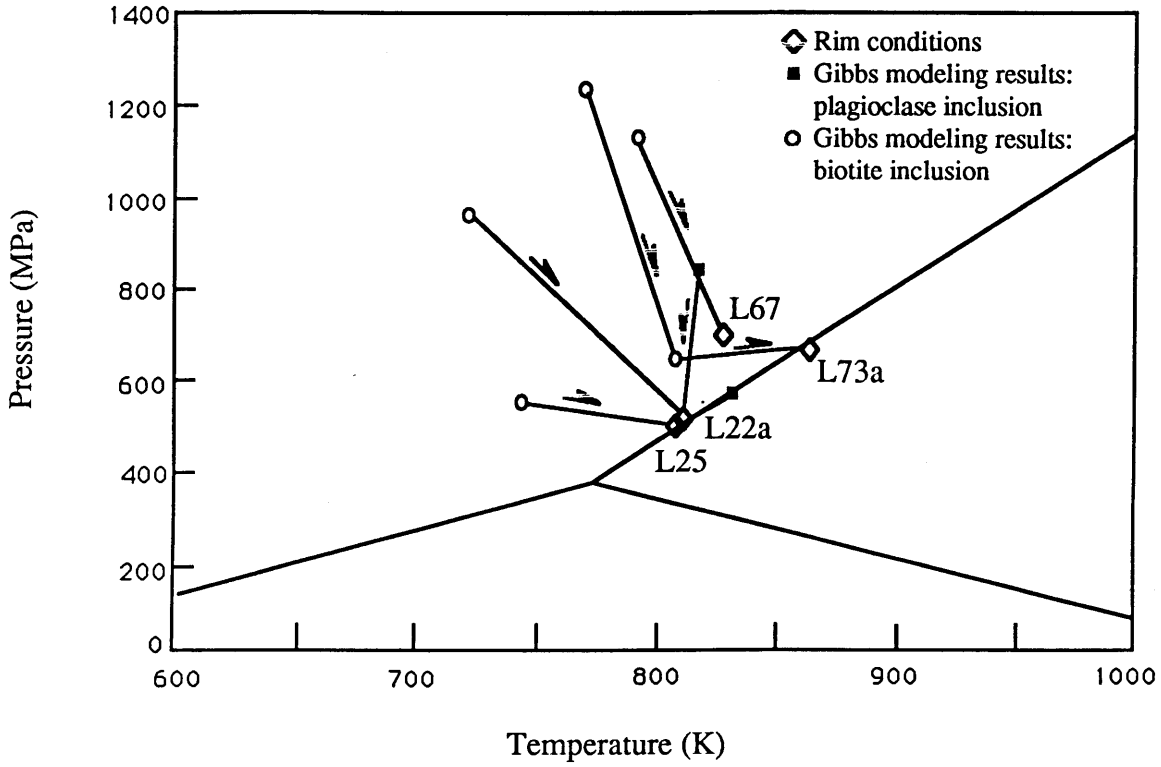
Rim conditions
Gibbs modeling results: plagioclase inclusion
Gibbs modeling results: biotite inclusion
L67
L73a
L22a
L25
Pressure (MPa)
Temperature (K)
1400
1200
1000
800
600
400
200
0
600
700
800
900
1000

Figure 13

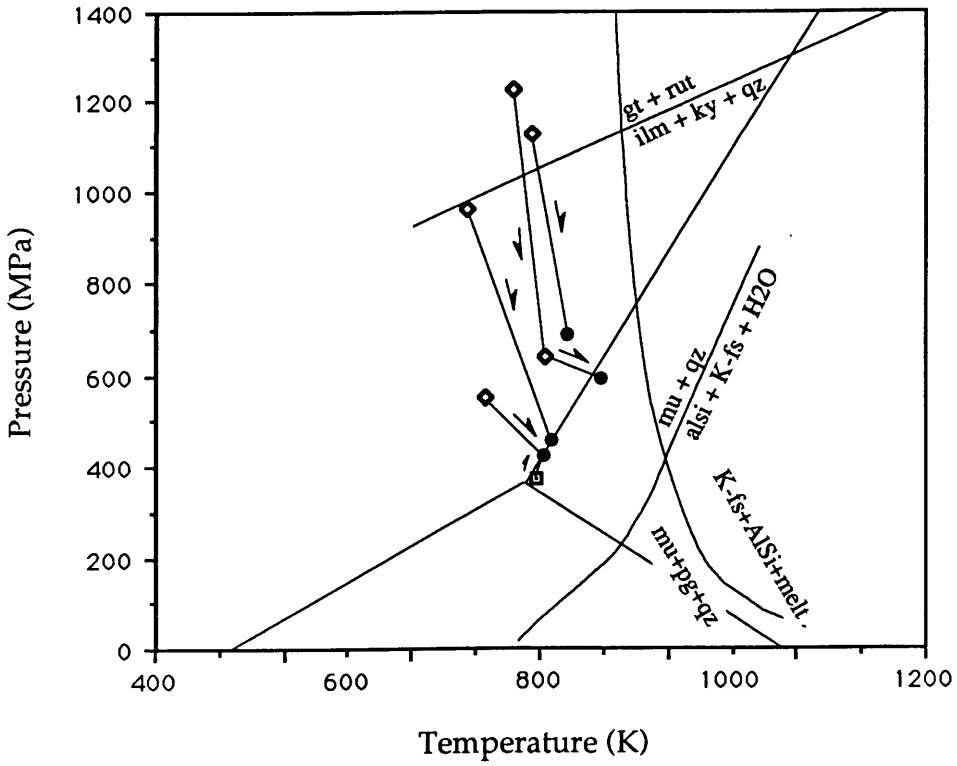
1400
1200
1000
800
600
400
200
0
400
600
800
1000
1200
Pressure (MPa)
Temperature (K)
gt + rut
ilm + ky + qz
mu + qz
alsi + K-fs + H2O
K-fs+AlSi+melt
mu+pg+qz

Figure 14

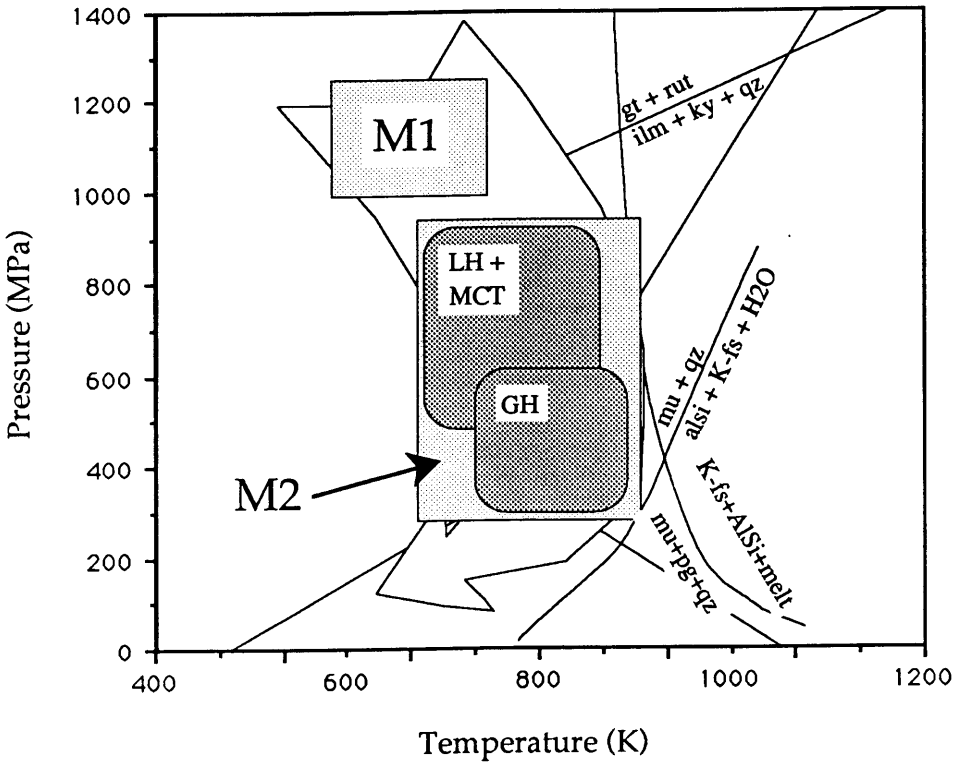
1400
1200
1000
800
600
400
200
0
400
600
800
1000
1200
Pressure (MPa)
Temperature (K)
M1
LH +
MCT
GH
M2
gt + rut
ilm + ky + qz
mu + qz
alsi + K-fs + H2O
K-fs+AlSi+melt
mu+pg+qz

Figure 15

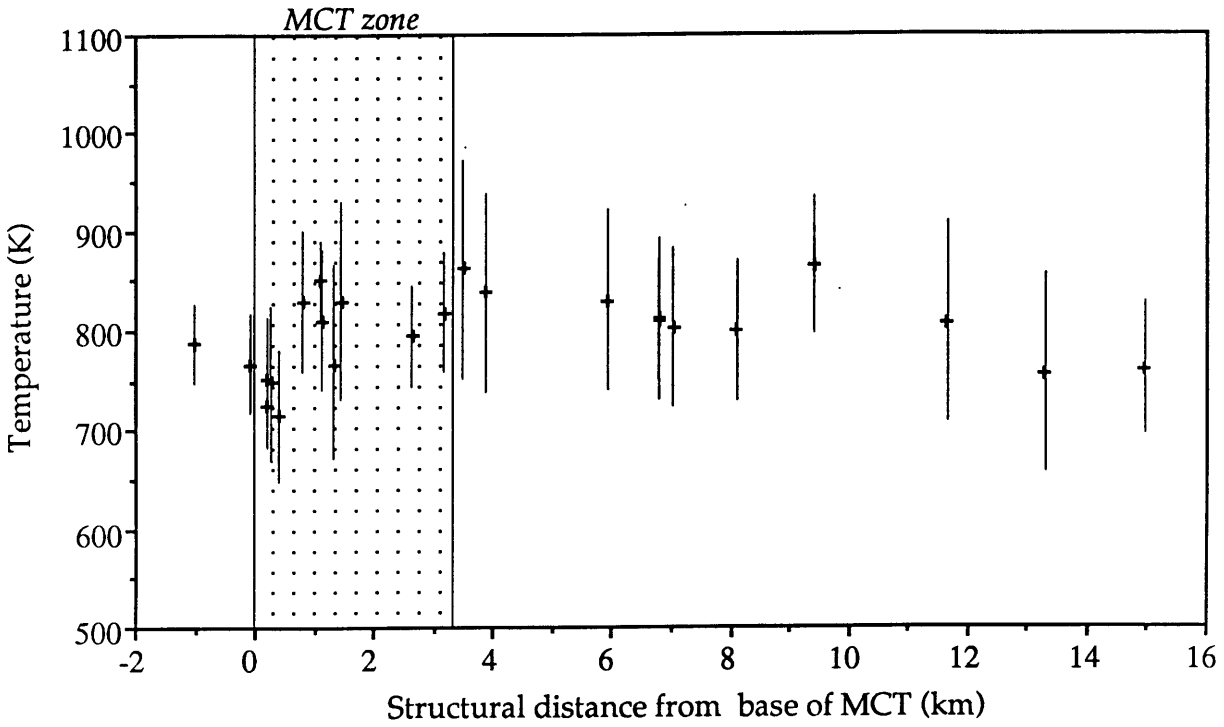
MCT zone
1100
1000
900
800
700
600
500
Temperature (K)
-2
0
2
4
6
8
10
12
14
16
Structural distance from base of MCT (km)

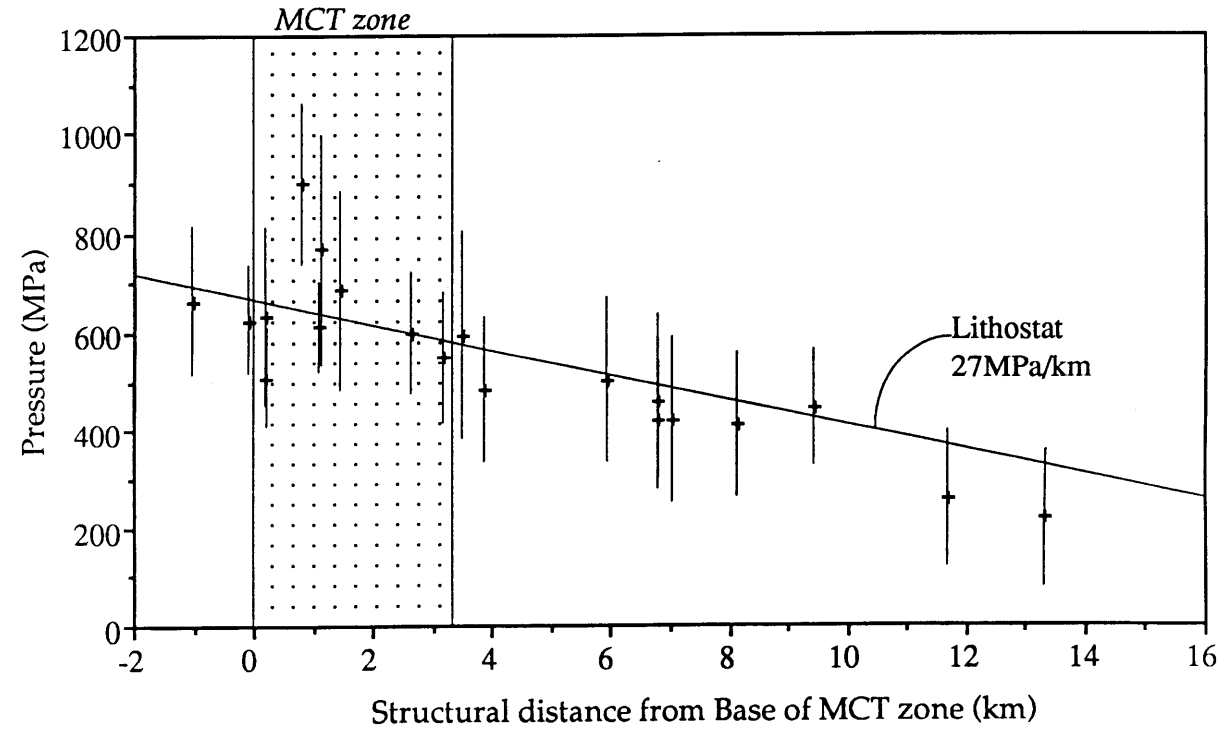
MCT zone
1200
1000
800
600
400
200
0
Pressure (MPa)
Lithostat
27MPa/km
-2
0
2
4
6
8
10
12
14
16
Structural distance from Base of MCT zone (km)

Figure 16

CHAPTER FOUR

Conditions for Granite Genesis in Collisional Orogens: The Himalayas

ABSTRACT

In the core of the Himalaya, Miocene age leucogranites are emplaced into the structural top of the hanging wall of the Main Central Thrust (MCT), a major zone of shortening in the Indian plate. The leucogranites are s-type granites that may have formed from anatectic melting of the hanging wall gneisses. The mechanism by which melting of the gneisses occurred is controversial. Most of the controversy centers on the source of heat required for anatexis. This paper focuses on radioactivity, a potentially significant heat source in the Himalayas, and explores the possibility that radioactive heating played a dominant role in anatexis. Heat production values calculated from measured concentrations of U and Th and assumed potassium contents in gneisses and granites from the Langtang National Park region of central Nepal suggest that radioactivity significantly contributes to the heat budget of the area, but must have been augmented by other heat sources (e.g., increased mantle heat flux or shear heating associated with deformation) for Miocene melting to have occurred.

INTRODUCTION

Leucogranite bodies form a discontinuous belt in the hinterland of the Himalayas. The leucogranites are emplaced into the upper portion of the hanging wall of a major intracontinental subduction zone, the Main Central Thrust (MCT). The metamorphic grade and degree of migmatization increase upsection in the hanging wall, culminating in granite bodies located at the top of the section (Gansser, 1964; Le Fort, 1975). These granites are thought to have formed from anatectic melting of hanging wall gneisses (see Le Fort, 1986 for a review). Thus, it appears that the heat source for the metamorphism and anatexis may be located near the top of the hanging wall. Fluid fluxing, thermal conductivity contrasts, shear heating, the mantle heat flux and radioactive heating have been suggested as possible explanations for anatexis (Le Fort, 1981; Jaupart and Provost, 1985; Pinet and Jaupart, 1987; Molnar and England, 1990; England, 1992). This paper presents data from the Langtang National Park area, Nepal, pertaining to heat production in hanging wall gneisses and granites in order to assess the importance of radioactive heating in the production of Himalayan leucogranites.

GEOLOGIC SETTING

The core of the Himalayan orogen is composed of three major tectonostratigraphic units (Fig. 1). The Tibetan Sedimentary sequence, consisting of highly deformed Cambrian to Eocene sedimentary rocks, constitutes the hanging wall of the South Tibetan detachment system (STDS; Burchfiel et al., 1992), a north-dipping system of Miocene and perhaps younger low angle normal faults. The Greater Himalayan sequence forms the footwall of the STDS and the hanging wall of the Main Central Thrust (MCT). It is made up of amphibolite to upper amphibolite grade metamorphic rocks, predominantly gneisses and schists, with two-mica leucogranite

plutons scattered near the structural top of the sequence. The leucogranites form an orogen-parallel band from northern India eastwards to Bhutan. The MCT is one of the major structures that accommodated much of the shortening in the Indian plate. The Lesser Himalayan sequence forms the footwall of the MCT and is composed of Precambrian to Lower Eocene age chlorite to garnet grade metasedimentary and metavolcanic rocks.

In most areas of the Himalaya, there is evidence for two major metamorphic phases which affected the footwall and hanging wall of the MCT (eg., Brunel and Kienast, 1986; Pecher and Le Fort, 1986; Hodges and Silverberg, 1988). The first phase (M_1) has been tentatively associated with initial collision of India and Asia (Hodges and Silverberg, 1988), and affected both the footwall and hanging wall. The second phase (M_2), in some regions more localized in the upper Greater Himalayan sequence, is thought to be associated with movement on the MCT and leucogranite emplacement (Pecher and Le Fort, 1986; Hodges et al., 1988; Hodges and Silverberg, 1988). The age of the granites is fairly well constrained to be in the range 15 - 22 Ma based on U-Pb dating of monazite and zircon (Scharer, 1984; Scharer et al., 1986; Copeland et al., 1988; Parrish, 1992). Oxygen, Rb-Sr, Nd-Sm and Pb isotope studies suggest that the source of the leucogranites is the lowermost gneisses of the Greater Himalayan sequence (see France-Lanord and Le Fort, 1988 for a review).

PROPOSED CAUSES OF ANATEXIS

Le Fort (1975; 1981) suggested that fluid fluxing caused anatexis by lowering the melting temperature of the Greater Himalayan sequence gneisses. He proposed that a hot hanging wall was thrust over a cool footwall, heating the upper footwall and cooling the lowermost hanging wall, resulting in an "inverted metamorphic gradient" associated with the MCT. Metamorphism dewatered the footwall and the resulting fluids rose through the hanging wall, which was still warm (Le Fort, 1981; France-

Lanord and Le Fort, 1988; Le Fort, 1988). Jaupart and Provost (1985) and later Pinet and Jaupart (1987) suggested that the thermal conductivity contrast between the crystalline rocks of the Greater Himalayan sequence and the sedimentary rocks of the Tibetan Sedimentary sequence provided a situation where melting of the gneisses would occur at the contact between the Greater Himalayan and Tibetan Sedimentary sequences (Jaupart and Provost, 1985). Pinet and Jaupart (Pinet and Jaupart, 1987) suggested that the early formation of the granites and thus the location of the larger bodies depended on the local variations in abundances of radioactive elements. Molnar and England (1990) and England et al., (1992) recently explored the effects of shear heating along the MCT and the mantle heat flux on anatexis. Through thermal models, they suggest that dissipative heating from shear stresses of about 100 MPa caused both metamorphism and anatexis in central Nepal (England, 1992).

Radioactive Heat Production in the Langtang Region

In order to explore further the contribution of radioactivity to the thermal budget during Himalayan anatexis, I have calculated radioactive heat production rates for thirteen samples from the Langtang National Park region of central Nepal. The upper Lesser Himalayan sequence, a 3.7 km wide MCT zone and the Greater Himalayan sequence are exposed at Langtang (Fig. 2). The Lesser Himalayan sequence consists of a monotonous series of chlorite to garnet grade calcareous quartzites, pelitic schists and some silty metalimestones. The MCT zone is an imbricate sequence of pelitic schists and gneisses, calcareous metapsammites and schists, silty limestones and augen orthogneisses of both footwall and hanging wall affinity. The Greater Himalayan sequence is dominated by pelitic gneisses and schists. The Greater Himalayan sequence gneisses are kyanite grade at the base and increase to sillimanite + K-feldspar grade at the top.

Migmatites and granites are found throughout the Greater Himalayan sequence in the Langtang region. The lowest units contain foliation-parallel migmatites (leucosomes ≤ 5 cm wide) with a few late cross-cutting pegmatites. Leucosomes and restites from migmatitic samples contain the same assemblage (plagioclase + quartz + biotite + muscovite + sillimanite + kyanite) but in very different modal proportions. Zircon is more plentiful in the restite than the leucosome, although it is still present in the leucosome. Pegmatites contain the assemblage: quartz + plagioclase + K-feldspar ± garnet + tourmaline. Aplite dikes (containing the assemblage: quartz + plagioclase + K-feldspar + muscovite + biotite ± kyanite ± sillimanite) occur in the lower portion of the section. They are weakly foliated and concordant with the dominant foliation. The presence of kyanite in the granitoid rocks as well as the host gneisses at this structural level suggests that anatexis of the lower portion of the Greater Himalayan sequence occurred at pressures of at least 400 MPa. Thermobarometric analysis of gneiss samples from this outcrop and nearby result in PT points that fall on the kyanite - sillimanite join of the aluminum silicate stability field, at conditions of approximately 800 K and 500 MPa. In the middle of the sequence, the volume of migmatite increases, and the upper middle section contains foliated granites. Near the top of the sequence there are small granite bodies, no larger than 10 m by 10 m, which cut across the main foliation and are undeformed. Xenoliths of country rock (pelitic gneiss) are found in these granites. Petrographic examination of the granites from the upper portion of the Greater Himalayan sequence reveals the mineral assemblage: K-feldspar + plagioclase ± perthite ± antiperthite + quartz + biotite + muscovite ± tourmaline. Sillimanite and chlorite are both secondary phases in all granites and accessory phases included zircon, monazite, xenotime and rutile. Zircon is not present in the granites in the same high modal proportions as in some of the gneiss samples. An approximate modal proportion for plagioclase is 25-35%; for K-feldspar 25-35%; for perthite/antiperthite, 20-30%; for quartz 10%; for

biotite<5-8%; for muscovite <1-5%; for chlorite <1%; for sillimanite <5-8%; and for tourmaline 0-10%. Fibrolitic sillimanite overgrows muscovite in many samples. This reaction texture suggests that, after granite formation, the muscovite-breakdown reaction was crossed, implying an increase in temperature or decrease in pressure after crystallization.

SAMPLE SELECTION AND ANALYTICAL METHODS

Figure 2 shows the locations of thirteen samples chosen for U and Th analysis using the inductively-coupled plasma mass spectrometer (ICP-MS) facility at M.I.T. These samples are thought to be representative of the approximately 25 km lithologic column exposed in the Langtang transect. They include a pelitic schist sample from the Lesser Himalayan sequence, a pelitic schist and an augen orthogneiss from the MCT zone (both samples have affinities with Lesser Himalayan rocks), and four pelitic gneiss samples, two migmatites and four granites from the Greater Himalayan sequence.

All samples were finely crushed, mechanically split to provide a representative 120 gm samples, and powdered using a shatterbox. The alkali fusion method was used to put the sample into solution: 0.1 gm of sample and 0.5 gm of lithium metaborate flux were added to a platinum crucible, mixed, and then heated over a flame for 20-30 minutes until all the sample appeared to melt. These liquid beads were dropped directly into a 5% nitric acid solution. Samples were mixed using a magnetic stirrer for 20-30 minutes, until all sample appeared to dissolve. When the sample was dissolved, the solution was diluted to 100 ml to obtain a 2% HNO_3 solution. The final solution contained 0.1 % total dissolved solids. To calibrate the ICP-MS, 50 µl of a U - Th spike was added to 10 ml of sample solution. The spike contained 1.514 ppm U and 1.577 ppm Th, with isotopic ratios of U^{235} = 0.999333, U^{238}

= 0.00066623, Th^{230} = 0.91646 and Th^{232} = 0.08354 (Jurek Blusztajn, personal communication). The samples were then ready for analysis by the ICP-MS.

U and Th concentrations of silicates can be determined with reasonable accuracy on the ICP-MS (better than ± 5%), using both open acid digestion and alkali fusion sample preparation techniques (Jackson et al., 1990; Jarvis, 1990). Certain problems have been associated with the ICP-MS, principally matrix effects, memory and blank (Jackson, et al., 1990). Matrix effects posed no interferences for analysis of the elements U and Th. Initial runs showed that memory did indeed pose a problem for Th analysis. To overcome this problem, 8 N nitric acid was flushed through the system between each sample. The nitric acid appeared to remove the vestiges of Th left on the tubing. No memory problem was encountered for U. Blanks were low during the analysis for both U and Th, usually ranging between 0.05% to 0.06% of sample concentrations.

RESULTS

Two runs per sample were analyzed on the ICP-MS, and the data was averaged. Uncertainties were estimated between 5-10%. Table 1 shows the U and Th concentration data for the gneisses and Table 2 contains the data for the granites. Both tables include results from other studies for comparison (Vidal et al., 1982; Cuney et al., 1984; Scharer, 1984; Deniel, 1985; Scharer, et al., 1986; Pinet and Jaupart, 1987; Copeland, et al., 1988; France-Lanord and Le Fort, 1988; Cuney et al., 1990; Scaillet et al., 1990). Figure 3 is a plot of U versus Th concentration for the granite and gneiss samples listed in Tables 1 and 2.

U and Th concentrations for these rocks fall within the range of values listed for leucogranites from elsewhere in the Himalayas and around the world. However, it is perhaps noteworthy that most Himalayan leucogranites have higher U than the Langtang samples. The low U content could be attributed to analytical problems

either in the preparation of the samples or in the use of the ICP-MS facility. Alternatively, low U concentrations in the granites may be due to the fact that zircons, which tend to have the highest concentrations of U, are more abundant in the Langtang gneisses than the granites.The Langtang gneisses have U and Th concentrations similar to Greater Himalayan gneisses from elsewhere in the orogen. All samples in Table 2 are characterized by Th/U > 1. With one exception, Th concentrations are higher than U concentrations in the Langtang granite samples.

Heat production values for the Langtang data were calculated from the U and Th concentration data presented in this paper assuming a K_2O concentration of 3.5% in the gneisses and 4.5 % in the granites (Le Fort, 1981; Vidal et al., 1982; Cuney et al., 1984) and a density of 2700 kg/m^3 for the gneisses and 2650 kg/m^3 for the granites (Tables 1 & 2). The results are shown graphically in Figure 4. Heat production rates for the Langtang region granites fall within the range of values quoted for other Himalayan granites, but they are on the low end of these values (Fig. 4). This is due largely to the low U concentrations in the Langtang granites. The heat production rates for the Langtang gneisses, alternatively, lie well within the range of values for other Himalayan gneisses.

DISCUSSION

From the U and Th concentration data available for the Himalaya (Tables 1 & 2) there appears to be a lateral variation along the length of the orogen. In areas with very large plutons (i.e., Manaslu and Badrinath - Gangotri), the U concentrations in the granites are very high, and thus heat production tends to be high. The Langtang area has no large plutons and the U content of the granites is lower than the Th content.

To further explore the effect of radioactivity on the thermal regime, and thus the production of the leucogranites, simple modeling of geotherms was attempted. The

model considers an initial geotherm of 10°/km upon which a radioactive heat production component is added to the upper 35 km of a 125 km column of lithosphere. Finite difference calculations based on the equation, $dT/dt = \kappa * d^2T/dz^2 + A'$, where T is temperature, z is depth, t is time, κ is thermal diffusivity and A' is heat production at a given depth, result in steady-state geotherms after 200 million years. Values for constants are listed in Table 3. The model requires temperatures at 125 km to be 1573 K. Changes in most of the initial and boundary conditions values had little affect on the conclusions of the modeling. Changes in the assumed thermal diffusivity had a significant affect on the position of the calculated geotherms, but the assumed thermal diffusivity in this model is consistent with that of other workers (e.g., Ruppel and Hodges, in press). A detailed discussion of the effects of the assumptions is given in the Appendix.

Figure 5 displays equilibrium geotherms calculated for homogeneous heat production rates of 1 $\mu W/m^3$, 2 $\mu W/m^3$, 4 $\mu W/m^3$, and 8 $\mu W/m^3$ in the top 35 km of crust. Also shown is a geotherm calculated for the Langtang area. The value of A' is calculated for Langtang assuming that the top of the Greater Himalayan sequences is at approximately 10 km depth, beneath the thickness of the Tibetan Sedimentary sequence. Heat production in the Tibetan Sedimentary sequence is assumed to be 1.0 $\mu W/m^3$, based on similar values in Pinet and Jaupart (1987). Heat production values for the Lesser through Greater Himalayan sequences span a 25 km crustal column. The heat production values assigned to this column are those calculated in this study. Heat production rates at depths for which no sample data was available were estimated by interpolation. For depths greater than those for which data was available at Langtang, values the same as those calculated for the Lesser Himalayan schists were used.

Although the modeling presented here is greatly simplified, a number of interesting observations can be made. At 20 km depth, roughly corresponding to

pressure estimates from a sample at a middle structural level in the Greater Himalayan sequence, the corresponding temperature from the Langtang geotherm is approximately 765 K. This temperature is not high enough for melting in either the dry or wet granite melting fields at 20 km. The granite wet-melting curve (Le Breton, 1988) intersects the Langtang geotherm at approximately 27 km (730 MPa) and 875 K. Pressures this high are only recorded at the base of the MCT zone by thermobarometry. Temperatures of 875 K are not recorded in the Langtang region, although the uppermost Greater Himalayan sequence samples, for which there are no good thermobarometric data, may have experienced them. Considering the heat production data and the pressure and temperature conditions of the Greater Himalayan sequence in Langtang, it appears that radioactive heating alone is not enough to account for anatexis. Although the heat production values calculated for Langtang are not high enough to cause melting, they create geotherms with high temperatures at 20 km depth. Thus, radioactivity alone raises the ambient temperature from 475 K (the initial 10 °/km geotherm) to 875 K, an increase of 400 K. The thermal modelling requires a minimum of $4\mu W/m^3$ for anatexis to occur at 20 km depth. Almost all the Himalayan gneiss samples have heat production rates well below 4 $\mu W/m^3$.

In the Langtang area, if we assume that abundances of radioactive elements brought the ambient temperature to approximately 825 K, then we must consider what other factors promoted anatexis. Fluid fluxing of the gneisses would lower the melting temperature and promote anatexis (Hyndman, 1985, p. 323). There are two issues to consider pertinent to the fluxing of fluids: the presence of water and the source of water. First of all, it appears that fluid must be have been present in the Langtang area for melting to have occurred. The assemblages present in Greater Himalayan sequence gneisses in the Langtang area are as follows: Lower Greater Himalayan sequence has quartz + plagioclase + garnet + biotite + muscovite ± kyanite ±

sillimanite, Middle Greater Himalayan sequence contains quartz + plagioclase + garnet + biotite + muscovite + sillimanite and the Upper Greater Himalayan sequence has quartz + plagioclase + garnet + biotite + K-feldspar+ sillimanite. Field relations show that anatexites were probably produced in all three levels of the Greater Himalayan sequence. Thus, the melting occurred in approximately the 900-1000 K range, based on wet melting minima curves (Le Breton, 1988). This is confirmed by thermobarometry, which gives temperature in the 700-900 K range (Macfarlane, in preparation). Dry melting occurs at much higher temperatures (minimum of 1000 K, for partial melting; (Vielzeuf and Holloway, 1988) for the 450-1000 MPa pressure range which probably existed at during anatexis, based on the approximately 10 - 15 km of Tibetan Sedimentary series overburden. If we expect to generate a reasonable amount of granite during dry melting, then we have to cross the biotite melting curve, and biotite and especially muscovite should not be present in the country rocks. In Langtang, as in all other areas of the Greater Himalayan sequence that have been described, the opposite is true. Biotite is present in abundance in all samples, suggesting that the biotite-out reaction had not been encountered (approximately 1025-1175 K; Vielzeuf and Holloway, 1988). From the above discussion, it seems likely that water-saturated melting of pelitic material probably created the leucogranites.

Le Fort (1981) suggested that the fluids originated from dewatering of the Lesser Himalayan sequence during movement on the MCT. This hypothesis is not consistent with field evidence from Langtang. In Langtang, the upper Lesser Himalayan sequence reached garnet grade during a metamorphic phase that predated movement on the MCT (Macfarlane, in preparation). During the metamorphic phase that accompanied and continued after MCT movement, the Lesser Himalayan sequence also attained garnet grade. Thus, few new dehydration reactions took place during the second metamorphic phase, and little water would have been released. As

stated before, the volume of granite in Langtang is much less than that of other areas (i.e., Manaslu, Everest). On the other hand, this volume difference could be explained by the lower grade of footwall in the other regions prior to motion on the MCT (Gansser, 1964; Le Fort, 1975). The source of fluids in these regions could have been dewatering of a low grade footwall, whereas in Langtang, little water might have come from the footwall. Thus, more melting would occur in the regions where we now see large plutons and areas such as Langtang with a higher grade footwall prior to MCT movement would have produced small volumes of granite.

One feature of the Himalaya that has not yet been considered is the role of the South Tibetan detachment system (STDS). Burchfiel et al. (1992) performed the most comprehensive study of this structure. The STDS is a collection of extensional faults, some ductile, some brittle, which have operated for at least 10 m.y. (Burchfiel, et al., 1992). In some areas the structure post-dates the leucogranites, while in others the granites cut across the STDS (Burg and Chen, 1984; Herren, 1987; Burchfiel, et al., 1992). Based on phase diagrams of water-saturated granite melting, melting temperatures increase with a decrease in pressure, because water becomes less soluble in the melt (Hyndman, 1985, p. 151). In consideration of the above discussion, beginning of melting must have occurred prior to major unroofing in the area. As suggested above, the rocks of the Greater Himalayan sequence were at depths of 10 to 30 km. From field relations in Langtang, anatexis occurred in the lower Greater Himalayan sequence rocks first, during MCT movement. The upper Greater Himalayan sequence granites were probably produced after the cessation of ductile movement of the MCT. In the Langtang area, unlike other regions with large plutons such as south of Nyalam or the Everest region, there is no evidence for large-scale granite production before movement on the STDS (Burchfiel et al., 1992). Perhaps movement on the STDS occurred earlier in the Langtang region than in other granite-rich regions, unroofing the Greater Himalayan sequence and thus curtailing the amount

of melting which occurred. This could account for the small volume of leucogranite here, as opposed to other regions where the majority of melting occurred prior to major motion on the STDS.

CONCLUSIONS

Granite genesis in the core of Nepal Himalaya appears to arise not from a single source, but more probably the combined effects of a number of important and contributing factors. Radioactive heating which occurs from a high concentration of radioactive elements in the protoliths of the granites is a necessary requirement to elevate the ambient temperatures in the metamorphic core to approximately 800-900 K. The addition of a free fluid phase will lower the melting temperature of the protolith gneisses. The majority of normal faulting must occur after the melts are produced. Extension may be caused or enhanced by anatexis, as was suggested by Burchfiel et al. (1992). The melting would produce a more ductile crust, making gravity collapse more likely to occur (Burchfiel et al., 1992). In addition to these three factors described above, it has been widely suggested that boron has lowered the melting temperature of the gneisses in the Himalayas (eg., Le Fort, 1981). In Langtang, the boron-rich mineral tourmaline is abundant in both the leucogranites and the gneisses and probably played a role in anatexis.

In the Himalayas, where there are large granite bodies such as Manaslu or Everest, I suggest that high radioactive element concentrations, large volumes of free fluid and late movement on the STDS contributed to anatexis. In granite-poor regions, such as Langtang, lower concentrations of radioelements, low volumes of water and early movement on the STDS may have precluded large amounts of melting.

ACKNOWLEDGEMENTS

The author wishes to thank John Edmond and Ed Boyle for use of the ICP-MS. Debra Colodner provided much help with sample preparation and analysis on the ICP-MS. Sample collection was done with the kind permission of the Nepali government. This research has been supported by N.S.F. grant # EAR8721403 awarded to K.V. Hodges and a G.S.A. student research grant awarded to the author.

APPENDIX

The initial and boundary conditions used in this study were examined for their affect on the results of the model by comparison with other values for these parameters. Changes in temperature at the depths of interest, between 10 and 30 km, are discussed for different values of particular parameters. The assumption of an initial 10°/km geotherm was compared with initial geotherms of 15°/km and 20°/km. At 10 km depth, an increase in temperature of 5 K occurred when the initial geotherm was either 15°/km and 20°/km. At 30 km depth, there was an increase in temperature of 14 K and 16 K for the 15°/km and 20°/km geotherms, respectively. When the depth of heat production was extended to 45 km and 55 km, no change in temperature occurred at depths of 10 km and 30 km. The assumed K_2O concentrations were tested by recalculating heat production values using K_2O concentration values of 2.5% and 4.5% for the gneisses and 3.5% and 5.5% for the granites. The increased K_2O concentration caused the temperature to increase by 6 K at 10 km and 13 K at 30 km. The decreased K_2O concentration resulted in a decrease in temperature of 7 K at 10 km and 14 K at 30 km. Although the actual rocks have not sat untouched for 200 million years, I believe that the time scale of the model is reasonable due to the existence of inherited cores in zircons, ranging in age from 970 Ma to 1.7 Ga (Parrish, 1992). From the above discussion, it should be clear that the initial geotherm, the depth of heat production, the assumed K_2O concentration and the run time used in this model were reasonable assumptions. Only slight changes in temperature, on the order of 0-15 K, resulted if different values for these parameters were used. These temperature changes do not affect the results of this study.

However, the modeling does significantly depend on the value of the thermal diffusivity. England and Thompson (1984) employ three different values of thermal diffusivity (1.2×10^{-6}, 9×10^{-7} and 6×10^{-7} m^2/s) that were calculated from experimental data for thermal conductivity. The thermal diffusivity value used in the

model presented in this paper is 1.1×10^{-6} m^2/s, which corresponds to a thermal conductivity value of 2.75 W/mK, based on an assumed heat content of 2.5×10^6 J/Km^3 (England and Thompson, 1984). If the thermal diffusivity value is changed to 9×10^{-7} m^2/s, the temperature at 10 km depth increases by 55 K, and at 30 km depth by 106 K. For a thermal diffusivity value of 6×10^{-7} m^2/s, the temperature increase at 10 km depth is 158 K and at 30 km depth is 300 K. Thus, wet granite melting would occur at approximately 25 km depth for thermal diffusivity of 9×10^{-7} m^2/s and at approximately 17 km depth for a thermal diffusivity of 6×10^{-7} m^2/s. Consequently, the results of the thermal modelling presented here are highly dependent on the assumed thermal diffusivity.

Table 1

Rock Type	Reference	location	anal. type	U ppm	Th ppm	Th/U	A μW/m3
Granite - L146b	*this study*	*Langtang*	*ICP-MS*	2.35	4.67	1.99	1.36
Granite - L145b				2.83	12.25	4.33	2.03
Granite - L156b				3.11	1.37	0.44	1.32
Granite - L38				2.92	9.47	3.24	1.85
Granite	Vidal, 82	Manaslu	INAA	4.10	0.93	0.23	1.55
				6.80	2.05	0.30	2.32
				4.30	5.60	1.30	1.93
				11.90	4.70	0.39	3.82
				3.40	4.80	1.41	1.64
				8.80	4.70	0.53	3.03
				11.90	4.10	0.34	3.78
Pegmatite	Scharer, 84	Makalu	SSMS	23.30	3.78	0.16	6.69
Granite				13.50	2.58	0.19	4.08
Granite	Deniel, thesis	Manaslu	?	28.10	9.90	0.35	8.36
Granite	Scharer, 86	Everest	SSMS	5.31	10.68	2.01	2.55
		Kangri		1.88	8.61	4.58	1.52
		Maja		2.89	10.84	3.75	1.94
		Maja		2.92	9.80	3.36	1.88
Migmatite-gr		Nyalam		2.20	36.35	16.52	3.58
Granite	Copeland, 1988	Everest	SSMS	15.00	8.00	0.53	4.90
Granite	rance-Lanord, 198	Manaslu	ICP-MS (?)	4.50	6.40	1.42	1.96
				12.00	5.70	0.48	3.86
				8.00	5.40	0.68	2.86
				13.00	5.50	0.42	4.16
Granite	Scaillet, 1990	Garhwal, India	?	19.70	2.50	0.13	5.64
		Badrinath -		21.10	3.30	0.16	6.08
		Gangotri		26.40	5.70	0.22	7.68
		plutons		22.50	4.30	0.19	6.56
				28.60	5.70	0.20	8.19
				18.90	2.50	0.13	5.39
				14.40	4.00	0.28	4.45
				19.80	2.50	0.13	5.69
Granite	Pinet, 1987	S. Norway	varies	8.00	43.60	5.45	5.58
				4.40	16.20	3.68	2.68
Granite	Cuney, 1990	Brazil	ICP-MS	7.70	32.10	4.17	4.70
		Transamazonia		14.80	3.40	0.23	4.46
				6.40	26.10	4.08	4.00
				6.90	2.00	0.29	2.29
				6.20	31.90	5.15	4.35
				40.30	5.30	0.13	11.18
				6.90	25.30	3.67	4.06
				22.40	10.50	0.47	6.95
				3.90	17.00	4.36	2.64
				4.50	10.40	2.31	2.35
				5.80	11.40	1.97	2.84
				13.70	10.40	0.76	4.75
Granite	Cuney, unpubl.	Massif Central	?	16.00	19.00	1.19	5.99

Table 2

Rock Type	Reference	location	anal. type	U ppm	Th ppm	Th/U	A μW/m3
Schist (LH) - L1	*this*	*Langtang*	*ICP-MS*	3.26	16.47	5.05	2.39
Schist (MCT) - L60a	*study*			3.28	20.47	6.24	2.68
Gneiss (MCT) - L90				5.70	15.78	2.77	2.98
Gneiss (GH) - L73a				1.45	10.12	6.98	1.45
Gneiss (GH) - L21				1.80	11.88	6.60	1.67
Migmatite (GH) - L24				2.80	4.88	1.74	1.43
Gneiss (GH) - L27				1.95	16.33	8.37	2.04
Gneiss (GH) - L39				7.94	33.58	4.23	4.86
Migmatite - L169b				0.86	8.22	9.56	1.23
Gneiss Fm 1	Vidal, 82	Manaslu	INAA	3.90	20.00	5.13	2.81
				3.00	17.50	5.83	2.40
				3.60	22.10	6.14	2.89
				2.10	15.30	7.29	2.00
				4.20	18.40	4.38	2.78
				1.60	10.60	6.63	1.53
Gneiss, Fm 1	Cuney, 1984	Manaslu	ICP-MS	1.60	10.00	6.25	1.48
				2.20	15.10	6.86	2.01
				2.90	17.20	5.93	2.35
				4.20	18.10	4.31	2.75
				4.00	20.00	5.00	2.84
Orthogneiss	Pinet, 1987	S. Norway	varies	2.80	22.90	8.18	2.79
Avg. gneiss/amphib				2.70	9.20	3.41	1.65
Felsic granulite				1.70	2.00	1.18	0.61
Archean Gneiss	Cuney, 1990	Brazil	ICP-MS	0.40	8.10	20.25	0.89
		Sete Voltas dome		6.40	12.10	1.89	2.92

Table 3: Values and Conditions for Thermal Modelling

Parameter	Definition	Value
T	Temerature	273-1573 K
z	Depth	0-125 km
t	Time	seconds
K	Thermal conductivity	3 W/m * K
κ	Thermal diffusivity	$1.11 * 10^{-6}$ m^2/s
A	Heat production	1-8 $\mu W/m^3$
Boundary Conditions:	Thickness of heat-producing layer	35 km
	Thickness of lithosphere	125 km
	T at top of lithosphere	273 K
	T at base of lithosphere	1573 K

FIGURE CAPTIONS

Figure 1: General location map of the Nepal Himalaya.

Figure 2: Map of the Langtang region. Samples used in ICP-MS analyses are denoted by the black dots and associated sample number.

Figure 3: Th versus U concentration plot for all data given in Tables 1 & 2.

Figure 4: Heat production values for all the data in Tables 1 & 2. Data is separated by region: top is areas other than the Himalaya; middle is the Himalayan data; bottom is data generated in this study.

Figure 5: Results from thermal modeling plotted as geotherms. Curves are labeled according to the input heat production for a given run.

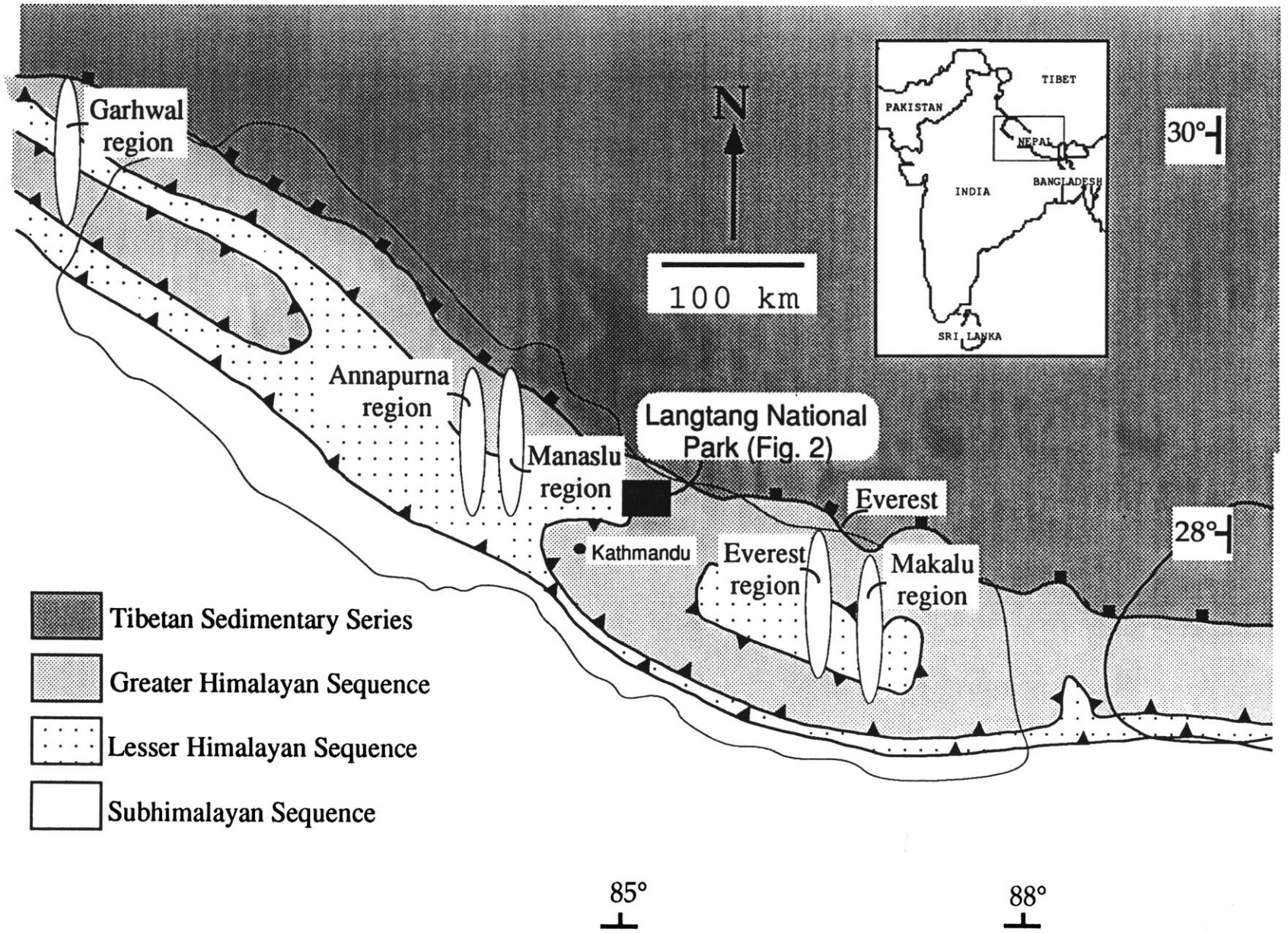
Garhwal region
Annapurna region
Manaslu region
Langtang National Park (Fig. 2)
Everest
Everest region
Makalu region
Kathmandu
N
100 km
TIBET
PAKISTAN
NEPAL
INDIA
BANGLADESH
SRI LANKA
30°
28°
85°
88°
Tibetan Sedimentary Series
Greater Himalayan Sequence
Lesser Himalayan Sequence
Subhimalayan Sequence

Figure 1

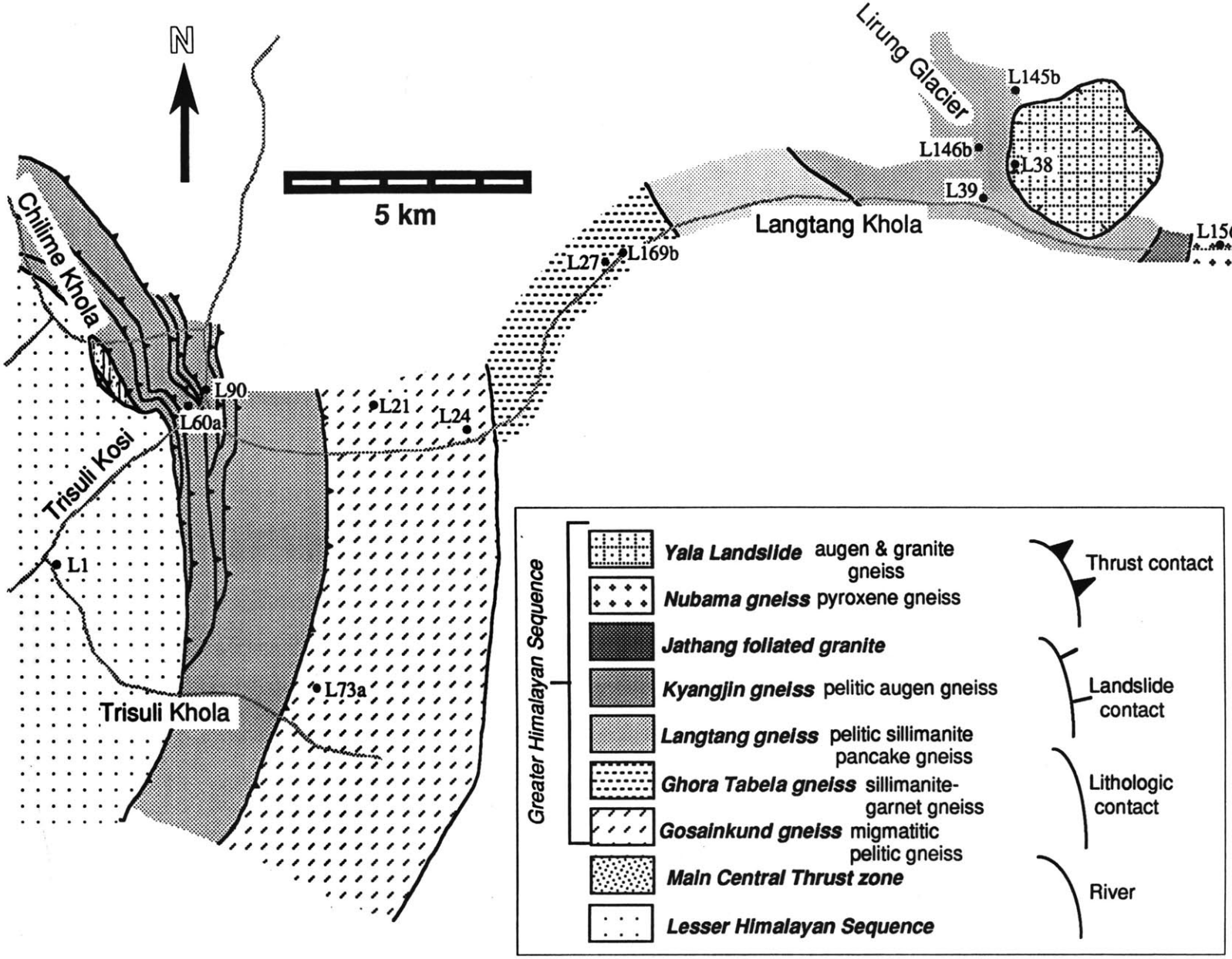
N
5 km
Lirung Glacier
L145b
L146b
L38
L39
Langtang Khola
L156b
L27
L169b
Chilime Khola
L90
L60a
L21
L24
Trisuli Kosi
L1
L73a
Trisuli Khola
Greater Himalayan Sequence
Yala Landslide augen & granite gneiss
Nubama gneiss pyroxene gneiss
Jathang foliated granite
Kyangjin gneiss pelitic augen gneiss
Langtang gneiss pelitic sillimanite pancake gneiss
Ghora Tabela gneiss sillimanite-garnet gneiss
Gosainkund gneiss migmatitic pelitic gneiss
Main Central Thrust zone
Lesser Himalayan Sequence
Thrust contact
Landslide contact
Lithologic contact
River

Figure 2

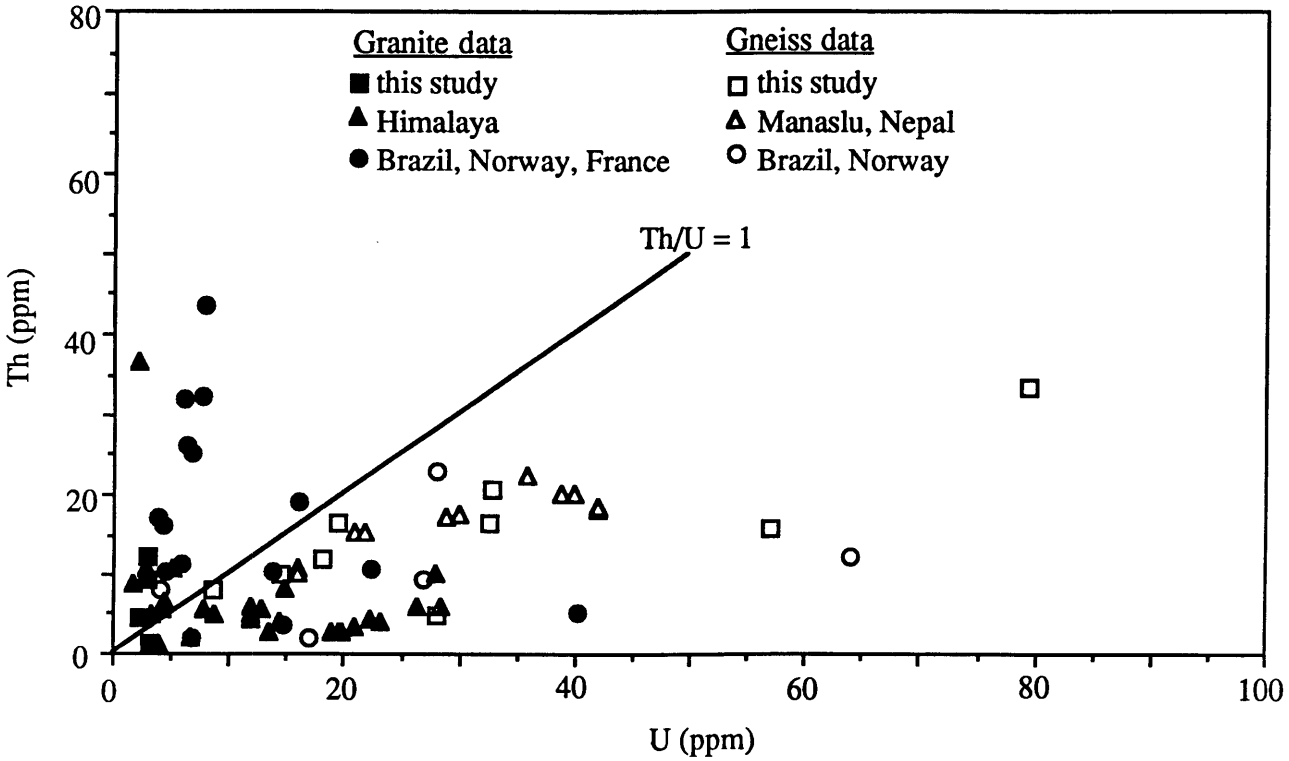
Granite data
this study
Himalaya
Brazil, Norway, France
Gneiss data
this study
Manaslu, Nepal
Brazil, Norway
Th/U = 1
Th (ppm)
U (ppm)
0
20
40
60
80
100

Figure 3

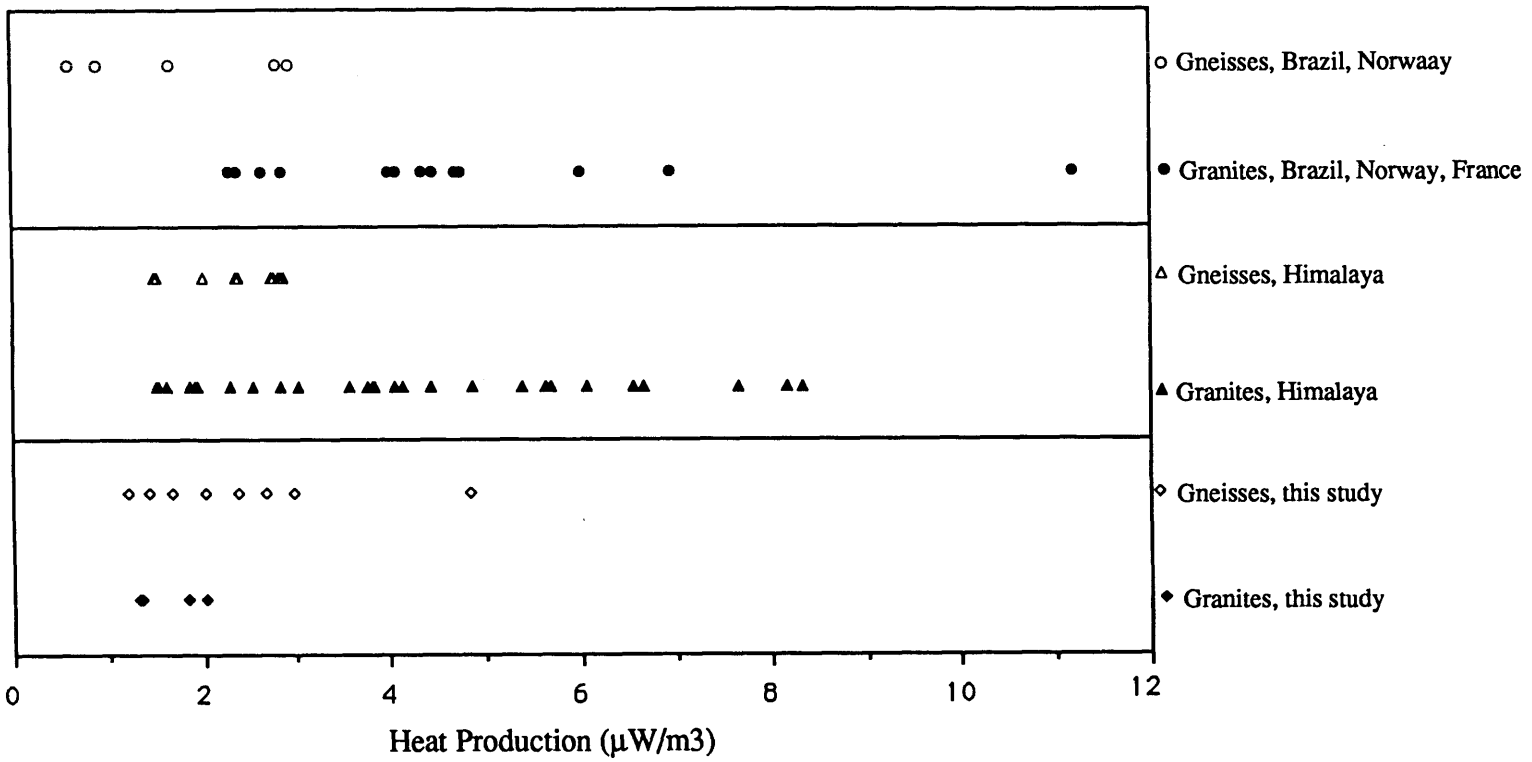
Gneisses, Brazil, Norwaay
Granites, Brazil, Norway, France
Gneisses, Himalaya
Granites, Himalaya
Gneisses, this study
Granites, this study
0
2
4
6
8
10
12
Heat Production (μW/m3)

Figure 4

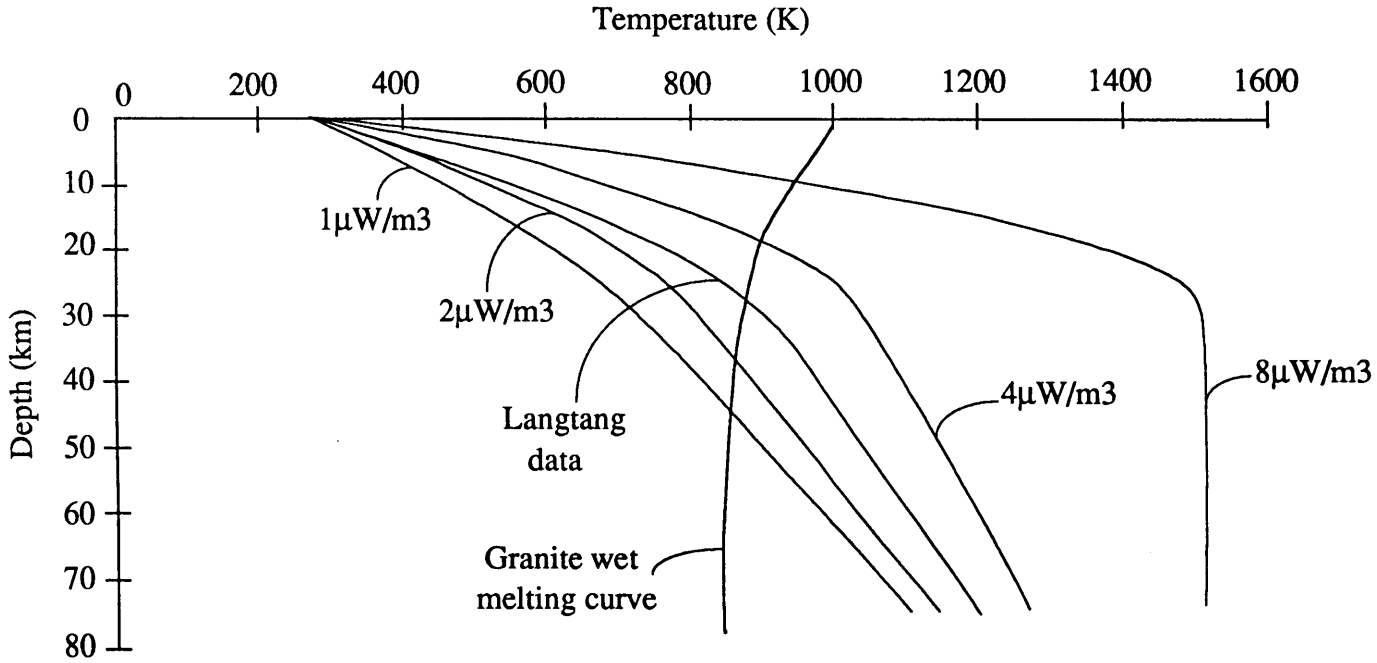
Temperature (K)
0
200
400
600
800
1000
1200
1400
1600
Depth (km)
0
10
20
30
40
50
60
70
80
1μW/m3
2μW/m3
4μW/m3
8μW/m3
Langtang
data
Granite wet
melting curve

Figure 5

CHAPTER FIVE

The Chronology of Tectonic Events in the Crystalline Core of the Himalaya, Langtang National Park, Central Nepal

ABSTRACT

The Main Central Thrust (MCT) is an important intracontinental subduction zone that accommodated a significant proportion of shortening between India and Asia during Tertiary Himalayan orogenesis. Geochronology based on the $^{40}Ar/^{39}Ar$ technique indicates at least two distinct periods of thrust movement on the MCT in the Langtang National Park region of central Nepal. Ductile deformation and associated mylonitization characterizing the earlier event, are constrained by $^{40}Ar/^{39}Ar$ dating of muscovites to have occurred sometime before 5.8 Ma. A later period of brittle deformation, resulting in the juxtaposition of rocks of different lithology within the MCT zone, occurred at approximately 2.3 Ma, based on $^{40}Ar/^{39}Ar$ dating of neoblastic muscovites from the brittle fault zones. The hanging wall of the MCT contains amphibolite to upper amphibolite grade gneisses and small leucogranite bodies assigned to the Greater Himalayan sequence. $^{40}Ar/^{39}Ar$ cooling ages of muscovite and biotite from the gneisses range from 4.6 to 9.7 Ma. These dates contrast with previously obtained 16-21 Ma U-Pb monazite and zircon ages for metasedimentary rocks from the same structural levels (Parrish, 1992), indicating relatively slow cooling over the early to middle Miocene interval for much of the MCT hanging wall. However, one 19.3 Ma biotite $^{40}Ar/^{39}Ar$ cooling age for a sample from the uppermost portion of the hanging wall is only slightly younger than U-Pb monazite ages for nearby anatexites, possibly suggesting rapid cooling of the uppermost Greater Himalayan sequence by tectonic denudation associated with the structurally higher South Tibetan detachment system. The general consistency of $^{40}Ar/^{39}Ar$ ages throughout the 11 km thick Greater Himalayan sequence suggests rapid cooling in late Miocene time, probably due to an increase in erosion rate related to ramping on the structurally lower Main Boundary Thrust. An alternative possibility would be massive hydrothermal resetting in late Miocene time of the entire sequence.

INTRODUCTION

Tectonic processes which result in major metamorphic events and include both thrust and normal-sense faulting and plutonism are characteristic of collisional orogenic belts. The timing of such processes is critical to understanding the relationship among them and has been documented to some degree in a number of major mountain belts, such as the North American Cordillera (e.g., Armstrong & Suppe, 1973; Parrish et al., 1988). The world's youngest and largest mountain belt, the Himalayan orogen, however, has been studied in less detail, especially with respect to the timing of metamorphic and deformational processes which have occurred there. Ongoing tectonic activity and the large amount of structural section exposed in the Himalayas make them a unique laboratory for geochronologists. Many of the geochronologic studies of the Himalayas to date have focussed on the western regions of Pakistan, Kashmir and Ladakh (e.g., Zeitler, 1985; Schärer et al., 1990). In the tectonically simpler eastern portion of the Himalayas, i.e., Garhwal, India, Nepal, Sikkim and Bhutan, fewer all-encompassing geochronologic studies have been done.

The core of the Himalayas consists of three major tectonostratigraphic units (Fig.1). The Tibetan Sedimentary series is the northernmost unit and is made up of Cambrian to Eocene sedimentary rocks originally deposited along the northern Indian margin and now are highly deformed but unmetamorphosed. The contact between the Tibetan Sedimentary series and the Greater Himalayan sequence to the south is the South Tibetan detachment system (STDS), a series of north-dipping, low-angle, Miocene and younger normal faults (Burchfiel, et al., 1992). The Greater Himalayan sequence consists of amphibolite to upper amphibolite grade gneisses and schists which are locally migmatitic and apparently increase in grade upsection. In some locations, the Greater Himalayan sequence has been described as polymetamorphic, experiencing at least two metamorphic events or phases (e.g., Pêcher and Le Fort,

1986; Hodges and Silverberg, 1988; Inger, 1991). Miocene leucogranites are located in the structurally higher portion of the sequence. The Main Central Thrust (MCT) forms the boundary between the Greater Himalayan sequence to the north and the Lesser Himalayan sequence to the south. It is a major north-dipping structure along which at least 100 km of shortening has occurred (Brunel, 1975; Brunel, 1986). The footwall of the MCT consists of the Lesser Himalayan sequence, Cambrian to Eocene age sedimentary and volcanic rocks which have been metamorphosed at chlorite to garnet grade near the MCT. An inverted metamorphic gradient has been described in the Lesser Himalayan sequence near the MCT (e.g., Oldham, 1883; Heim and Gansser, 1939) and movement on the MCT has been proposed as the cause (e.g., Le Fort, 1975; England, 1992). The Main Boundary Thrust (MBT), a still-active north-dipping major thrust structure that probably began moving in late Miocene time, forms the lower contact of the Lesser Himalayan sequence (Gansser, 1964).

Determining the age of movement on the MCT, the STDS, metamorphism in the Greater and Lesser Himalayan sequences and leucogranite plutonism is crucial in deciphering the tectonic evolution of the Himalaya. Field relationships indicate the relative timing of these processes. Early movement on portions of the STDS and leucogranite emplacement occurred concurrently based on cross-cutting relationships (Burg, et al., 1984; Brun, et al., 1985; Burchfiel, et al., 1992). Leucogranite plutonism appears to be associated with metamorphism in the Greater Himalayan sequence based on an increase in metamorphic grade from kyanite at the base to sillimanite + K-feldspar at the top, adjacent to the leucogranite plutons (Le Fort, 1975). The youngest metamorphism in the Greater and Lesser Himalayan sequences occurred synchronously with ductile movement on the MCT in central Nepal (Le Fort, 1975; Pêcher, 1977) and eastern Nepal near Everest (Hubbard, 1989), although in other regions such as Garhwal, India and eastern Nepal south of Makalu, at least some

movement on the MCT post-dates metamorphism (Brunel and Kienast, 1986; Hodges and Silverberg, 1988).

Quantitative data on the timing of these tectonic events is limited in the eastern portion of the Himalayas. Most geochronologic surveys in this region have been U-Pb studies of leucogranite bodies (Schärer, 1984; Schärer et al., 1986; Deniel et al., 1987; Copeland et al., 1988). Although a significant amount of reconnaissance mapping has been performed in northeastern India and Nepal, only three major thermochronometric studies of the hinterland exist: Maluski et al. (1988) in eastern Nepal, Hubbard and Harrison (1989) in eastern Nepal and Copeland et al. (1991) in central Nepal. Due to the diachronous nature of features such as the MCT, which is syn-metamorphic in some regions and demonstrably post-metamorphic in others, more detailed geochronologic studies using reliable dating systems such as U-Pb and $^{40}Ar/^{39}Ar$ are necessary to elucidate the relationship among the tectonic processes involved in mountain-building.

The Langtang National Park region of central Nepal has been recently characterized structurally and petrologically (Macfarlane et al., in press; Macfarlane, in preparation). Due to excellent roadcuts and ridgetop exposures, the location of the MCT and the structural and metamorphic nature of the footwall and hanging wall are known well. Twenty-five samples of muscovite, biotite, K-feldspar and hornblende from Langtang have been analyzed by the $^{40}Ar/^{39}Ar$ method in an attempt to place constraints on the timing of tectonic processes in that portion of the Himalayan chain. The results suggest a long and complicated movement history for the MCT that includes displacements as young as approximately 2 Ma.

LANGTANG GEOLOGY

Langtang National Park is located due north of Kathmandu at 28°10'N and 85°25'E (Fig. 1). Rocks of the upper Lesser Himalayan sequence, MCT zone and Greater Himalayan sequence are exposed within the park boundaries (Macfarlane et al., in press). In this region, the Lesser Himalayan sequence is composed of a thick monotonous unit of alternating chlorite to garnet grade metapsammites, pelitic schists and siliceous metalimestones, called the Dhunche unit (Macfarlane et al., in press). The MCT forms a 3.7 km-wide, imbricate zone of eleven different, fault-bounded, lithologic units. In this region, the base of the MCT zone is defined by the initiation of the juxtaposition of different lithologic units by brittle thrust faults. The upward disappearance of these brittle thrust faults and initiation of migmatites defines the top of the MCT zone. The MCT zone is composed of units with both footwall and hanging wall affinity and is informally divided into a lower MCT zone, containing rocks of footwall affinity, and an upper MCT zone, made up of rocks of hanging wall affinity. The Greater Himalayan sequence is at least 16 km-thick in the Langtang area. Kyanite to sillimanite + K-feldspar pelitic gneisses and schists make up the Greater Himalayan sequence. Foliation-parallel migmatites and pegmatite and aplite sills occur in the lower Greater Himalayan sequence, whereas cross-cutting dikes of pegmatite and migmatite, in addition to small discordant granite bodies, occur in the upper sequence.

A number of deformation events have affected all the major tectonostratigraphic units in Langtang (Macfarlane et al., in press). Internal foliation preserved within garnet porphyroblasts and folding of an earlier foliation provide evidence of at least two ductile events in the Lesser Himalayan sequence and lower MCT zone rocks. These ductile events may not be separate in time, but may be part of a non-coaxial deformational continuum associated with motion on the MCT. A

number of the units within the MCT zone are mylonitic and the mylonitic fabric is parallel to the dominant foliation in Langtang. These ductile structures are overprinted by discrete, brittle, thrust-sense shear zones, <10 cm to 10 m wide. The shear zones are characterized by graphitic fault gouge. We interpreted these brittle fault zones as part of a duplex structure (Macfarlane et al., in press). All kinematic indicators suggest top-to-the-south sense of shear in the Lesser Himalayan sequence and the MCT zone during both ductile and brittle phases of thrusting. The lower portion of the Greater Himalayan sequence is also dominated by top-to-the-south kinematic indicators, but in the upper portion of the sequence, some indicators suggest top-to-the-north shear sense. Although the STDS does not outcrop in Langtang, Burchfiel et al. (1992) describe it outcropping in the Gyrong region of Tibet, approximately 15 km due north of Langtang. The upper Greater Himalayan sequence also experienced an amount of late chlorite grade and brittle deformation of indeterminate shear sense.

Two metamorphic phases have affected the entire tectonostratigraphic section (Macfarlane, in preparation): an early, moderate temperature, high pressure phase followed by a high temperature, moderate pressure phase. The latest metamorphic phase affected the entire exposed section and occurred syn- to post-kinematically with respect to the most recent ductile deformation event. Although there is a significant amount of brittle faulting within the MCT zone, there appears to be no metamorphic break across it. A metamorphic field gradient is present in Langtang, going from garnet grade in the footwall to garnet-staurolite-kyanite grade in the MCT zone to garnet-kyanite grade in the lower hanging wall through sillimanite grade to sillimanite + K-feldspar grade in the upper hanging wall. Thermobarometric data associated with the second metamorphic phase do not distinguish a temperature gradient in the entire section (temperatures are 700-900K, averaging about 800K), although an increase in pressure from top (approximately 400 MPa) to bottom (approximately 650 MPa) is present (Macfarlane, in preparation).

ANALYTICAL PROCEDURE

Sample Selection and Preparation

Figure 2 shows locations of samples used in geochronological analysis. All three tectonostratigraphic units provided samples: one from the Lesser Himalayan sequence, ten from the MCT zone and fourteen from the Greater Himalayan sequence. Two hornblende samples from amphibolites were used; one from the Lesser Himalayan sequence and one from the MCT zone. Muscovite and biotite samples originated mostly from pelitic schists and gneisses in the MCT zone and the Greater Himalayan sequence. MCT zone samples L118, L127 and L51 have affinities with the Lesser Himalayan sequence, whereas samples LT33, L66 and L20a have affinities with the Greater Himalayan sequence. Fault gouge from one of the brittle faults within the MCT zone provided a syn-deformational white mica. The Syabru Bensi augen orthogneiss yielded three mineral separates: muscovite, biotite and K-feldspar. Two granites from the upper Greater Himalayan sequence produced biotite and muscovite separates.

Analytical techniques

Mineral separates were obtained by standard density and magnetic separation procedures. Samples with the prefix LT were separated by Dr. Randall Parrish at the Geological Survey of Canada. All mineral separates were prepared from the coarsest grain size fractions possible (either 60/80 or 80/100 mesh splits) and the size of prepared grains approximates the original grain size in the rocks. After the final washing and sieving, the samples were hand-picked to ensure > 99% purity.

Samples L51, L66, L20a, L43 and L36 were analyzed at the University of Maine, Orono, in the laboratory of Dr. D. Lux. Details of procedures followed in this

lab can be found in Lux (1986). These samples were irradiated in the H5 reactor at the University of Michigan for 72 hours. J-values were established with the use of in-house flux monitor SB-51. Plateau ages were determined using the critical value test outlined in Dalrymple and Lanphere (1969) and a York 2 least squares regression technique (York, 1969)was used to determine isochron ages.

The remaining samples were analyzed in the CLAIR facility at M.I.T. Samples weighing 14-34 mg for muscovite; 11-31 mg for biotite and 80-106 mg for hornblende were encapsulated in aluminum foil and then stacked in an aluminum canister, 1.35" long and 0.62" in diameter. The samples were irradiated for four hours in the core of the Omega West reactor, Los Alamos National Laboratory. The neutron flux was monitored with two interlaboratory standards (MMhb-1 hornblende - 520.4 Ma, Samson, 1987; and Fish Canyon tuff sanidine - 27.8 Ma, Cebula, 1986) and two intralaboratory standards. Samples received a mean integrated fast neutron fluence of about 5.7×10^{13} n/cm^2. The mean J/hour for irradiation was 7.1×10^{-4} and J-values varied by about 10% over the entire length of the cannister.

The CLAIR facility comprises an MAP 215-50 mass spectrometer equipped with a stainless-steel extraction line, laser sample chamber and double-vacuum resistance furnace. Sample cleaning is accomplished with SAES AP-10 Al-Zr and SAES 172 Fe-V-Zr getters. For this study, sample gas was extracted using the resistance furnace and measured with a faraday detector (sensitivity = 2.47×10^{-4} A/torr) equipped with a 10^{11} ohm resistor. Temperature in the furnace, measured with a thermocouple, is considered reproducible within 5°C. Samples were dropped into a tantalum crucible and heated to the specified increment temperature for 5 minutes. Following heating, samples were scrubbed for an additional 10 minutes and then admitted to the mass spectrometer. Data from sample analysis were corrected for mass discrimination and operational blanks. Blanks of the furnace section are relatively consistent over a wide temperature range, and increase exponentially above

1600 K. Typical system blanks observed during the course of this study were ^{40}Ar: 2.99 x 10^{-15} moles, ^{39}Ar: 5.13 x 10^{-17} moles, ^{38}Ar: 1.76 x 10^{-17} moles, ^{37}Ar: 1.77 x 10^{-17} moles and ^{36}Ar: 1.39 x 10^{-17} moles.

RESULTS

Data are presented in this paper as incremental heating schedules (Table 1), age spectra and isotope correlation plots (Figures 3-5), and compiled age data (Table 2). Figure 6 presents the distribution of ages with respect to the regional geology in Langtang. For the most part, we have based our age interpretations on the behavior of incremental release data on isotope correlation diagrams (Roddick, 1980), thereby avoiding the assumption of an initial atmospheric $^{40}Ar/^{36}Ar$ ratio for the Langtang samples. Isochron ages were calculated using both the York 1 and York 2 regression techniques (York, 1969). York 1 ages are normally quoted for this study except when the MSWD is less than 2.0. When isochron ages were not able to be determined, the minimum age from the spectrum was used to provide a maximum estimate of the closure age of the sample. For well-behaved samples, plateau ages (calculated using the criteria suggested by Fleck et al., 1977, and Dalrymple and Lanphere, 1969) are virtually indistinguishable from isochron ages. All $^{40}Ar/^{39}Ar$ age uncertainties are quoted at 2 sigma. The following discussions are arranged by tectonostratigraphic unit and within each unit, samples are discussed from structural bottom to top.

Lesser Himalayan Sequence

The only sample analyzed from the Lesser Himalayan sequence was a hornblende (KVH2). The data for this sample display no obvious linear correlation on the isotope correlation plot (Fig. 3a). In addition, this hornblende shows a complex release spectrum with a minimum age of 41 ± 6.7 Ma (Fig.3b). A plot of K/Ca versus

cumulative % 39Ar released shows a consistent K/Ca ratio with the exception of the initial heating increments, suggesting that the scatter in the data is not simply attributable to the presence of multiple phases in the sample.

MCT Zone

L118 is a sample of fault rock from an intraformational brittle fault zone located in the Trisuli unit of the MCT zone. L118 is made up of predominantly calcite, white mica and quartz. Some white micas in this sample display undulose extinction or are visibly folded, but the majority of white mica is annealed with no reaction rims. Quartz in this sample is mostly annealed, but some displays undulose extinction. An isotope correlation plot yields an age of 2.28 ± 0.04 Ma with an $^{40}Ar/^{36}Ar$ ratio of 296 ± 10 and an MSWD of 1.1 (Fig. 4a). The intercept age for L118 was calculated by dropping the data from the last increment, which contained no radiogenic argon. L118 gives a relatively flat spectrum with a plateau age of 2.3 ± 1.0 (Fig. 4b).

The only amphibole from the MCT zone is sample L127. This sample yields an isochron age of 27.2 ± 0.4 Ma associated with a $^{40}Ar/^{36}Ar$ ratio of 460 ± 56 and high MSWD (1130; Fig. 4c). Due to the wide scatter of data on the isotope correlation plot, the isochron age may be spurious. L127 yields a spectrum in which more than 60% of the gas was released during one increment that had an age of 28.0 ± 0.6 Ma (Fig.4d).

Three phases from L51, an augen orthogneiss similar to the Ulleri augen gneiss (Le Fort, 1975) and the Phaplu augen gneiss (Maruo and Kizaki, 1981), were analyzed. In Langtang, this augen gneiss is mylonitic and has good kinematic indicators suggesting top-to-the-south sense of motion. Large quartz grains display deformation lamellae with embayed edges and some subgrain formation. Small quartz grains are annealed and feldspar is undeformed. Muscovite yields no plateau age, but does provide an isochron age of 8.9 ± 0.2 Ma with an $^{40}Ar/^{36}Ar$ ratio of 306 ± 7 and an

MSWD of 3 (Fig.s 4e-f). Biotite from this sample gives both an isochron age (21 ± 0.3 Ma; calculated after omitting the data from the last increment), with an $^{40}Ar/^{36}Ar$ ratio of 290 ± 9 and MSWD of 2.8 (calcuated after dropping the data from the first and last increments) and a consistent plateau age (21 ± 0.3 Ma; Fig.s 4g-h). No intercept age was determined for K-feldspar from L51 (Fig. 4i). This sample yields a saddle-shaped spectrum (Fig. 4j). The minimum age from this spectrum, 5.5 ± 0.1 Ma, is consistent with the muscovite age and is interpreted to be the maximum age for cooling of the sample through the nominal temperature for K-feldspar closure (Zeitler and FitzGerald, 1986).

Muscovite and biotite from sample LT33, a pelitic gneiss, define the dominant foliation. The isotope correlation plot for muscovite yields an age of 5.5 ± 0.4 Ma (Fig. 4k). The intercept age for LT33 muscovite was calculated after dropping the data from the last increment. The plateau age for the muscovite is 5.8 ± 0.6 Ma (Fig.4l). The isotope correlation plot for LT33 biotite gives an age of 7.8 ± 0.1 Ma, but the $^{40}Ar/^{36}Ar$ ratio (280 ± 5) is lower than that of natural atmosphere, suggesting that the correlation diagrams may not adequately resolve the true initial $^{40}Ar/^{36}Ar$ ratio (Fig. 4m). The biotite displays a relatively flat spectrum, giving a plateau age of 7.8 ± 0.5 Ma (Fig. 4n).

Samples L66 and L20a, also from the uppermost section of the MCT zone, represent the Syabru unit which has affinities with the Greater Himalayan sequence. Both muscovite and biotite from these samples are aligned in the dominant foliation in this pelitic garnet-kyanite gneiss. Quartz is strained, exhibiting deformation lamellae, serrated edges and subgrain formation. Garnets are stretched in the foliation in both samples. L66 is mylonitic, with muscovite forming mica fish which indicate top-to-the-south shear sense. Muscovite from L66 provides an isochron age of 8.6 ± 0.2 Ma and a relatively flat spectrum, with a plateau age of 8.6 ± 0.2 Ma (Fig. 4o-p). L20a muscovite yields an isochron age of 6.9 ± 0.1 Ma which is consistent with the plateau

age of 6.9 ± 0.2 Ma (Fig.s 4q-r). Biotite from L20a gives an older isochron age (10.97 ± 0.10 Ma) and plateau age (11.0 ± 0.1 Ma; Fig.s 4s-t).

Greater Himalayan Sequence

The first ten Greater Himalayan sequence samples originate from the Gosainkund gneiss, a kyanite+sillimanite to sillimanite grade pelitic gneiss. Foliation parallel migmatites are present in this unit as well as small aplitic, pegmatitic and granitic dikes. This unit has not been significantly disrupted by any later brittle deformation. All biotites and muscovites are aligned in the dominant foliation. Quartz from these samples displays deformation lamellae, embayed grain boundaries and some subgrain formation. Increments 4 and 11 were excluded from the calculation of the isochron age for LT21 muscovite, which is 6.7 ± 0.1 Ma (Fig. 5a). An isotope correlation plot of LT21 biotite results in an age of 12.7 ± 0.3 Ma (calculated by dropping the data from the last two increments), with a high MSWD (233.8) and a large error on the $^{40}Ar/^{36}Ar$ ratio (289 ± 19; Fig. 5c). Neither the muscovite nor the biotite from sample LT21 yields plateau ages, although the spectra are relatively flat (Fig.s 5b & 5d). Muscovite from LT22 results in a wide spread on the isotope correlation diagram, giving an age of 6.7 ± 0.2 Ma and a relatively flat spectrum with a plateau age of 6.9 ± 0.7 Ma (Fig.s 5e-f). LT22 biotite is more problematic. The isochron age, calculated by omitting the data from the last two and first increments, is 16.3 ± 0.6 Ma, although the MSWD is very high (620.4) and the $^{40}Ar/^{36}Ar$ ratio is low with a large error (279 ± 42; Fig. 5g). No plateau is present for LT22 biotite although the spectrum is relatively uncomplicated (Fig. 5h). Muscovite from sample LT24 yields a good spread on the isotope correlation diagram, resulting in an intercept age of 6.1 ± 0.3 Ma (Fig. 5i). Although this sample results in an irregular spectrum, with a plateau defined by the fourth and fifth increments, the plateau age of 6.3 ± 0.3 Ma is consistent with the isochron age (Fig. 5j). The isotope correlation diagram for biotite

from LT24 reveals that most increments have similar $^{39}Ar/^{36}Ar$ and $^{36}Ar/^{40}Ar$, such that the first and second increments largely control the isochron age of 8.4 ± 0.2 Ma, calculated by omitting the data from the last two increments (Fig. 5k). This sample exhibits an irregular release spectrum, giving a plateau age of 8.3 ± 0.8 Ma (Fig. 5l). L142 muscovite yields a slightly complicated spectrum, which provides a plateau age of 9.6 ± 1.0 Ma, consistent with its isochron age of 9.7 ± 0.3 Ma, calculated by dropping the data from the last increment (Fig.s 5m-n). Biotite from L142 is much less satisfactory. Although there is a reasonable spread on the isotope correlation plot, it yields an age of 81.8 ± 11.7 Ma, (calculated by omitting the data from the first, second, fourth and fifth increments) the $^{40}Ar/^{36}Ar$ ratio is very low (244 ± 47) and the MSWD is very high (1168; Fig. 5o). The spectrum is complex, with large errors on each increment (Fig. 5p). No plateau age was obtained.

Sample LT26 is from a granitic dike within the Gosainkund gneiss. The isotope correlation plot for muscovite from this sample displays a good spread of points and results in an intercept age of 4.6 ± 0.4 Ma (Fig. 5q). The age spectrum shows an initial decreasing age gradient, which flattens over the last six steps, although no plateau was obtained (Fig. 5r). Biotite from LT26 results in an isotope correlation plot where the first and last steps are enriched in ^{36}Ar (Fig. 5s). The intercept age for the biotite is 7.6 ± 0.2 Ma. Biotite from LT26 yields a relatively flat spectrum with a plateau age of 7.6 ± 0.4 Ma (Fig. 5t).

Samples LT29 and L43 are from the Ghora Tabela gneiss, a fine-grained sillimanite + garnet gneiss. Biotite defines the dominant foliation in both these samples. Quartz in both samples is highly strained and exhibits mortar texture. The isotope correlation plot for biotite from LT29 results in a reasonable spread, giving an intercept age of 5.4 ± 0.3 Ma, a $^{40}Ar/^{36}Ar$ ratio of 295 ± 11 and an MSWD of 5.0 (Fig. 5u). This sample yields a relatively uncomplicated spectrum, although no plateau was obtained (Fig. 5v). The isotope correlation plot for biotite from L43 gives an intercept

age of 8.0 ± 0.2 Ma, an $^{40}Ar/^{36}Ar$ ratio of 291 ± 10 and an MSWD of 2.6 (Fig. 5w). A plateau age of 7.7 ± 0.2 Ma is obtained for biotite from sample L43 (Fig. 5x).

Sample L146 is the second granite dated in this study. It is composed of microcline + antiperthite + plagioclase + quartz+ biotite + muscovite, with secondary sillimanite. The contact between the granite and country rock is gradational, suggesting that this granite formed in situ from an anatectic melt of the host rock, the Kyangjin augen gneiss. Although the granite is unfoliated, the quartz exhibits mortar texture and the feldspar displays undulose extinction with embayed grain boundaries, suggesting this granite experienced some late deformation, possibly associated with motion on the STDS. The isotope correlation diagram for biotite from sample displays a good spread of points. The intercept age is 8.1 ± 0.2 Ma, with a $^{40}Ar/^{36}Ar$ ratio of 288 ± 6 and an MSWD of 18.9 (Fig. 5y). This biotite yields a flat release spectrum, with a plateau age of 7.6 ± 1.0 Ma (Fig. 5z).

The structurally highest sample, L36, originates from migmatitic garnet-bearing pelitic gneiss. Biotite defines a weak foliation in this sample and quartz displays mortar texture. This sample was taken from the Yala Landslide (Scott, 1953; Masch, 1974; Heuberger, 1984), a huge slide that occurred approximately 25,000-30,000 years ago and created a thick pseudotachylite or frictionite at its base (Heuberger, 1984). The rocks in the slide were originally located to the north, just east of Langtang Lirung, supposedly forming high peaks as part of the Langtang massif (Heuberger, 1984). Although a frictionite was formed, none of the rocks above the slide base appear to have been thermally affected by the slide. The intercept age of biotite from L36 is 19.3 ± 0.3 Ma with an $^{40}Ar/^{36}Ar$ ratio of 298 ± 7 and MSWD of 2.8 (Fig. 5aa). The sample gives a relatively flat spectrum with a plateau age of 19.4 ± 0.2 Ma (Fig. 5bb).

DISCUSSION

Data Interpretation

Figure 6 displays the cooling ages considered reasonable on the geologic map of Langtang. The complicated release spectra and wide scatter of data on the isotope correlation plots suggest that both hornblende samples were contaminated by excess Ar. In addition, the hornblende ages of 74 Ma for KVH2 and 27 Ma for L127 are geologically meaningless when considering the tectonic history of the Himalayas. There are no tectonic or plutonic events which would have resulted in the above cooling ages. From at least 150 Ma until collision at approximately 40 Ma, India drifted quietly north towards Asia (Molnar and Tapponnier, 1975). Thus, both hornblende ages are discounted.

Whenever biotite and muscovite pairs from the same sample were analyzed in this study, the biotite ages were consistently older, contrary to expectation if biotite's closure temperature to Ar is approximately 573 K and muscovite's is about 623 K (Robbins, 1972; Harrison, 1985). Biotite data for these samples were usually clustered on isotope correlation diagrams, leading to linear fits with high MSWD's indicating unusually low $^{40}Ar/^{36}Ar$ initial ratios. This behavior suggests that the non-radiogenic argon component in these samples was not adequately resolved during step heating. Although the biotite often appears to be better behaved than the muscovite with regard to the release spectrum (i.e., it exhibits a plateau), biotite may have homogenized during incremental heating whereas muscovite did not (McDougall and Harrison, 1988). A number of studies have found biotite to give older ages than muscovite (eg., Roddick, 1980; Kelley, 1988; Hubbard and Harrison, 1989). Roddick, (1980) suggested that argon was more soluble in biotite than muscovite, leading to anomalous ages for some biotite samples. Thus, the muscovites from these pairs give more reliable estimates of the cooling ages for these samples and only muscovite ages

were plotted on Figure 6. On the other hand, in the upper four Greater Himalayan sequence samples where only biotite data is available, all yield a good spread on the isotope correlation diagrams with reasonable $^{40}Ar/^{36}Ar$ ratios and relatively low MSWDs. Thus, the cooling ages of the upper four biotite samples are considered to be reliable.

The youngest muscovite cooling age from Langtang originates in fault rock from one of the brittle thrust faults associated with the duplex structure of the MCT zone (Fig.s 6 & 7). The age is a result of either muscovite growth or diffusional loss of Ar during shearing. The growth or diffusion may have occurred in response to fluid activity or frictional heating during motion on the fault. All the brittle faults contain high concentrations of graphite and are stained by Fe, most likely deposited during hydrothermal activity while movement was occurring on the fault. At least some motion must have occurred after the majority of hydrothermal activity based on the cataclastic appearance of hand samples. There are no hydrothermal deposits which cross-cut the fault gouge suggesting that there was little to no post-thrusting hydrothermal activity within these fault zones, although hydrothermal activity occurs presently at other sites. Thus, we interpret the 2.3 Ma muscovite age to represent the minimum age of brittle thrust faulting in the MCT zone at Langtang. Macfarlane et al. (in press) interpreted the brittle thrusting as the result of movement over a ramp on the MBT which caused out-of-sequence thrusting on the MCT. Therefore, 2.3 Ma is a minimum age for ramping on the MBT in the Langtang area.

The remaining muscovite ages (5.8 - 8.9 Ma) from the MCT zone originate from mylonites associated with ductile motion on the MCT and not from brittle fault zones. Microfabrics show that metamorphism outlasted ductile movement on the MCT (Macfarlane, in preparation). Thus, the muscovite ages represent minimum ages for ductile deformation and metamorphism on the MCT and maximum ages for brittle thrust-sense motion. Assuming a closure temperature of 423 K to 523 K for

argon in K-feldspar (McDougall and Harrison, 1988), the K-feldspar age of 5.5 Ma from the Syabru Bensi mylonite provides another estimate of minimum ages for metamorphism and deformation in the MCT zone. Based on the muscovite and K-feldspar cooling ages, sample L51 experienced moderate cooling rates of 29 K/m.y. to 59 K/m.y., depending on the assumed argon closure temperature of K-feldspar.

Most of the data from the Greater Himalayan sequence is consistent with cooling during unroofing. The ages span between 4.6 Ma and 9.7 Ma for muscovite and 5.4 Ma to 8.1 Ma for biotite. U-Pb ages from zircons and metamorphic monazites in gneisses and granites from samples LT22, LT24, LT26 and LT29 suggest that peak metamorphism and granite crystallization occurred concurrently from 16-20.5 Ma (Parrish, 1992). Slow cooling to 573 K-623 K results in cooling rates of 12 K-23 K/m.y. Thus, the majority of the Greater Himalayan sequence may have been dominated by erosion-controlled unroofing between 20.5 Ma and 4.6 Ma.

Sample L36 gives a much older biotite cooling age of 19.3 Ma. As stated earlier, L36 comes from an outcrop that is part of a massive landslide, which originated further to the north, closer to the likely location of the STDS and larger granite bodies (Reddy, 1992; Burchfiel, et al., 1992). The data from L36 indicate no excess argon problem. Therefore, L36 probably represents cooling from metamorphic peak temperatures. A granite sample near the contact between the Kyangjin gneiss and the Jathang foliated granite yielded a monazite U-Pb age of 20.5 to 22 Ma (Parrish, 1992). Considering a minimum crystallization temperature for the granite of 923 K (Le Breton and Thompson, 1988), a cooling rate of approximately 83 K/m.y. is calculated for L36. Compared with the cooling rates calculated for the rest of the Greater Himalayan sequence, L36 experienced rapid cooling. Based on the assumed close proximity of pre-landslide L36 to the STDS, we interpret this rapid cooling to be associated with initial movement on a portion of the STDS.

The exact timing of ductile movement on the MCT remains unconstrained. Muscovite $^{40}Ar/^{39}Ar$ data suggest that the majority of deformation and metamorphism was over by 5.8 to 8.9 Ma. Brittle thrust motion resulting in duplexing of the MCT occurred at approximately 2.3 Ma. The consistency in muscovite and biotite ages from the upper MCT zone to the upper Greater Himalayan sequence, a distance of about 11 km, suggests rapid unroofing in late Miocene time. This may be due to an increase in erosion rate spurred by movement on the structurally lower MBT.

Tectonic Significance

Figure 7 is a cartoon comparison of most of the existing $^{40}Ar/^{39}Ar$ data from the central and eastern Himalaya. The Everest region was the focus for the study by Hubbard and Harrison (1989). The data from Maluski et al. (1988) is from a transect through southern Tibet, between the villages of Nyalam and Zham. This region is just east of Langtang. The data for the research done by Copeland et al. (1991) was collected from central Nepal, west of Langtang. Relatively young ages are found in all three earlier studies of the lower and middle Greater Himalayan sequence (Fig. 7). These young ages may reflect simple slow cooling of the section or late deformation or hydrothermal fluid activity (Maluski, 1988; Hubbard and Harrison, 1989). Older cooling ages near the top of the sequence may indicate rapid tectonic denudation by movement on the STDS (Maluski, 1988).

The data from Copeland et al. (1991) are very similar to the results of this study. The ages near the MCT zone are very young and remain young through the middle of the Greater Himalayan sequence. Copeland et al. (1991) attributed their young ages to reheating by hydrothermal fluids. These fluids were released during metamorphism of the footwall of the MBT when it was buried under the Lesser Himalayan sequence after movement along the MBT (Copeland, et al., 1991). Although this is an elegant explanation, the assumption of adiabatic rise of 873 K-

temperature fluids through the thickness of the cooler Lesser Himalayan sequence to arrive at the MCT zone still retaining a temperature of 798 K seems unreasonable, given the probable thickness of the Lesser Himalayan sequence. A simpler explanation might be that Late Miocene ramping of the Greater and Lesser Himalayan sequences by movement over a step in the MBT led to rapid erosional denudation and cooling.

CONCLUSIONS

The chronology of the tectonic evolution of the core of the Langtang Himalaya can be summarized as follows. Metamorphism and granite production were concurrent at Langtang, occurring in the range of 16-22 Ma (Parrish, 1992). Early rapid cooling of the uppermost portion of the Greater Himalayan sequence may have been due to unroofing along a portion of the STDS. These early events were followed by a quiet period of slow cooling. Two distinct periods of movement occurred on the MCT in Langtang. Early ductile motion occurred prior to 5.8 Ma, based $^{40}Ar/^{39}Ar$ ages of muscovites from MCT zone mylonites. Rapid cooling of the entire sequence in Late Miocene time may have been due to increased erosion rates caused by movement over a ramp on the MBT. White micas from the brittle MCT shear zones yield $^{40}Ar/^{39}Ar$ ages which suggest that the latest stages of motion on the MCT occurred at about 2.3 Ma.

ACKNOWLEDGEMENTS

A.M.M. would like to thank the Nepali government for its kind permission to do research in Nepal. D. Lux provided his laboratory for analyses and D. West provided help during analysis in Maine. K.V. Hodges, B. Hames and B. Olszewski provided

much help with the CLAIR facility. B. Hames, M. Coleman, C.J. Northrup and M. House gave excellent reviews of the manuscript. This research has been supported by N.S.F. grant # EAR8721403 awarded to K.V. Hodges and a G.S.A. student research grant awarded to A.M.M.

Table 1

KVH2	Hornblende							
J value:	0.002963	±	0.000059					
T(K)	39Ar/40Ar	36Ar/40Ar	%39Ar	%40Ar*	K/Ca	Age		(+/- 2s)
973	0.0024	0.0007	4.4	78.3	0.52	1227.40	+/-	14.01
1073	0.0280	0.0014	8.7	59.2	1.12	109.65	+/-	6.20
1123	0.0638	0.0017	11.2	49.5	0.47	40.99	+/-	6.71
1173	0.0481	0.0010	15.2	71.5	0.21	77.68	+/-	4.71
1203	0.0380	0.0003	24.9	90.2	0.15	122.56	+/-	3.50
1233	0.0493	0.0002	69.1	93.4	0.11	98.53	+/-	0.97
1273	0.0784	0.0005	78.8	86.7	0.12	58.17	+/-	5.27
1323	0.0502	0.0004	86.2	89.0	0.11	92.28	+/-	3.74
1423	0.0419	0.0003	97.2	90.4	0.10	111.91	+/-	2.18
1523	0.0436	0.0006	98.2	82.4	0.09	98.31	+/-	37.39
1823	0.0506	0.0008	100.0	75.9	0.10	78.36	+/-	12.20

L118	Muscovite							
J value:	0.002839	±	0.000057					
T(K)	39Ar/40Ar	36Ar/40Ar	%39Ar	%40Ar*	K/Ca	Age		(+/-2s)
873	0.0139	0.0032	0.2	6.4	1	23.37	+/-	13.11
973	0.0405	0.0033	2.2	3.4	0	4.29	+/-	5.24
1023	0.3194	0.0031	5.7	9.1	12	1.46	+/-	2.74
1048	0.6015	0.0025	20.6	25.6	114	2.18	+/-	0.70
1073	1.3070	0.0014	37.4	59.1	152	2.32	+/-	0.30
1103	1.3158	0.0015	52.3	56.5	163	2.20	+/-	0.83
1173	1.1384	0.0017	68.5	48.8	178	2.19	+/-	0.85
1273	1.0314	0.0016	81.9	51.9	154	2.58	+/-	0.76
1373	1.1636	0.0017	95.0	49.4	195	2.17	+/-	0.68
1473	0.9994	0.0020	99.8	41.2	67	2.11	+/-	3.21

L127	Hornblende							
J value:	0.002839	±	0.000057					
T(K)	39Ar/40Ar	36Ar/40Ar	%39Ar	%40Ar*	K/Ca	Age		(+/- 2s)
1073	0.0011	0.0020	0.4	41.9	0.24	1336.89	+/-	86.66
1173	0.1162	0.0010	13.2	71.7	0.22	31.29	+/-	5.22
1223	0.1738	0.0001	83.6	95.7	0.26	27.95	+/-	0.62
1273	0.1562	0.0002	85.1	93.1	0.23	30.25	+/-	30.18
1323	0.1296	0.0004	91.8	87.9	0.24	34.38	+/-	3.36
1373	0.1498	0.0009	95.8	73.7	0.25	25.00	+/-	7.68
1423	0.1604	0.0013	96.5	60.9	0.24	19.34	+/-	39.00
1473	0.1641	0.0032	97.1	4.7	0.24	1.47	+/-	37.40
1523	0.1599	0.0011	98.9	68.7	0.24	21.85	+/-	19.02
1573	0.1841	0.0008	99.6	75.8	0.24	20.96	+/-	53.01
1823	0.0807	0.0019	100.0	43.6	0.27	27.45	+/-	23.47

L51	Muscovite		
J value:	0.006232	±	0.000016

Table 1

T (K)	39Ar/40Ar	36Ar/39Ar	% 39Ar	% 40Ar*	K/Ca	Age		(+/- 2 s)
923	0.0531	0.0560	0.6	12.1	67	25.35	±	5.31
1023	0.1771	0.0155	2.4	18.3	245	11.61	±	0.77
1093	0.3812	0.0060	5.5	31.3	221	9.19	±	0.24
1153	0.6158	0.0027	13.0	49.5	1550	9.01	±	0.17
1213	0.7402	0.0017	26.5	60.7	594	9.20	±	0.15
1273	0.8496	0.0012	44.9	69.1	628	9.12	±	0.16
1343	0.9191	0.0009	69.6	73.2	797	8.93	±	0.13
FUSE	0.9346	0.0007	99.8	79.2	188	9.50	±	0.13

L51	**Biotite**							
J value:	0.006033	±	0.000015					
T (K)	39Ar/40Ar	36Ar/39Ar	% 39Ar	% 40Ar*	K/Ca	Age		(+/- 2s)
923	0.1725	0.0131	4.0	33.0	251	20.73	±	1.16
1023	0.3127	0.0043	15.6	59.1	485	20.47	±	0.50
1093	0.3817	0.0024	29.8	71.8	600	20.37	±	0.22
1153	0.4115	0.0016	42.2	79.3	288	20.86	±	0.24
1213	0.4296	0.0012	51.5	83.4	171	21.02	±	0.29
1273	0.4446	0.0010	63.2	86.3	146	20.99	±	0.25
1343	0.4511	0.0008	82.5	88.6	177	21.26	±	0.24
FUSE	0.4108	0.0008	99.9	89.9	41	23.67	±	0.32

L51	**K-feldspar**							
J value:	0.006134	±	0.000015					
T (K)	39Ar/40Ar	36Ar/39Ar	% 39Ar	% 40Ar*	K/Ca	Age		(+/- 2s)
823	0.0142	0.0094	1.3	96.0	85	627.09	±	6.08
923	0.0430	0.0029	4.9	96.2	321	232.10	±	2.35
993	0.1266	0.0010	9.5	95.8	221	81.89	±	0.83
1073	0.3894	0.0003	17.5	95.4	410	26.90	±	0.35
1143	0.9276	0.0002	27.6	93.4	456	11.11	±	0.16
1193	1.5848	0.0001	38.0	89.8	566	6.26	±	0.08
1233	1.8282	0.0001	48.0	90.9	512	5.49	±	0.13
1273	1.3175	0.0001	57.2	93.4	577	7.82	±	0.12
1313	0.7067	0.0002	65.3	94.4	406	14.71	±	0.23
1353	0.3857	0.0002	71.8	97.1	343	27.64	±	0.30
1413	0.1577	0.0004	79.7	97.6	247	67.21	±	0.67
FUSE	0.0983	0.0005	100.1	98.3	242	107.37	±	1.07

L66	**Muscovite**							
J value:	0.006104	±	0.000015					
T (K)	39Ar/40Ar	36Ar/39Ar	% 39Ar	% 40Ar*	K/Ca	Age		(+/- 2s)
783	0.0376	0.0851	0.3	2.6	29	7.72	±	5.31
923	0.1004	0.0303	1.1	7.3	6	8.03	±	2.32
1023	0.2121	0.0130	4.0	15.5	165	8.02	±	0.40
1093	0.3650	0.0062	13.1	29.9	482	9.00	±	0.44

1153	0.5255	0.0035	31.1	42.6	957	8.90	±	0.25
1213	0.6293	0.0026	51.6	49.4	1511	8.62	±	0.18
1273	0.6734	0.0023	67.4	51.0	1074	8.33	±	0.14
1343	0.6270	0.0027	81.1	47.8	1259	8.37	±	0.23
FUSE	0.7289	0.0019	100.0	55.3	58	8.34	±	0.24

LT33	**Muscovite**							
J value:	0.002905	±	0.000058					
T(K)	39Ar/40Ar	36Ar/40Ar	%39Ar	%40Ar*	K/Ca	Age		(+/- 2s)
973	0.0338	0.0032	1.8	5.1	76	8.00	+/-	3.50
1023	0.0838	0.0031	15.8	9.2	1803	5.70	+/-	0.20
1048	0.4000	0.0018	38.8	46.0	0	5.50	+/-	0.50
1073	0.6000	0.0011	54.8	67.0	2469	5.80	+/-	0.60
1103	0.5000	0.0012	63.8	65.0	551	6.30	+/-	0.90
1173	0.4000	0.0019	73.8	43.0	103	6.20	+/-	0.70
1273	0.3000	0.0023	87.8	32.0	532	5.00	+/-	0.40
1373	0.7000	0.0014	97.8	59.0	341	4.60	+/-	0.90
1473	0.5000	0.0006	98.8	84.0	149	8.10	+/-	3.30
1823	0.4000	0.0025	99.8	26.0	29	3.40	+/-	7.50

LT33	**Biotite**							
J value:	0.002905	±	0.000058					
T(K)	39Ar/40Ar	36Ar/40Ar	%39Ar	%40Ar*	K/Ca	Age		(+/- 2s)
873	0.0519	0.0033	2.0	3.8	96	3.80	+/-	2.10
923	0.2000	0.0027	9.0	19.0	144	5.80	+/-	1.00
973	0.5000	0.0008	25.0	76.0	1155	7.80	+/-	0.50
1073	0.5000	0.0007	42.0	80.0	803	8.00	+/-	0.40
1143	0.5000	0.0007	53.0	78.0	66	7.80	+/-	0.80
1173	0.6000	0.0006	64.0	82.0	53	7.60	+/-	0.40
1223	0.6000	0.0005	79.0	84.0	446	7.60	+/-	0.40
1323	0.6000	0.0005	98.0	86.0	177	7.70	+/-	0.50
1423	0.5000	0.0004	99.0	89.0	31	9.20	+/-	4.00
1823	0.3000	0.0017	100.0	49.0	17	8.40	+/-	1.30

L20a	**Muscovite**							
J value:	0.006183	±	0.000015					
T (K)	39Ar/40Ar	36Ar/39Ar	% 39Ar	% 40Ar*	K/Ca	Age		(+/- 2s)
923	0.0576	0.0566	0.5	3.6	21	6.91	±	2.97
1023	0.2151	0.0133	1.8	14.9	112	7.73	±	0.56
1093	0.5015	0.0045	12.0	32.0	326	7.11	±	0.27
1153	0.7072	0.0026	26.5	44.6	587	7.02	±	0.21
1213	0.8410	0.0018	46.1	53.1	644	7.03	±	0.19
1273	0.9372	0.0015	63.1	57.5	558	6.83	±	0.11
1343	0.9497	0.0014	77.9	58.1	425	6.81	±	0.13
FUSE	1.1025	0.0009	100.1	68.7	279	6.93	±	0.09

Table 1

L20a	Biotite							
J value:	0.006222	±	0.000016					
T (K)	39Ar/40Ar	36Ar/39Ar	% 39Ar	% 40Ar*	K/Ca	Age		(+/- 2s)
923	0.3053	0.0078	13.3	28.7	124	10.53	±	0.20
1023	0.4717	0.0038	33.3	45.8	113	10.87	±	0.14
1093	0.5562	0.0027	50.4	53.8	106	10.83	±	0.19
1153	0.6329	0.0020	65.6	60.7	103	10.74	±	0.11
1193	0.6803	0.0016	77.7	65.6	80	10.79	±	0.16
1233	0.7128	0.0014	86.7	69.8	80	10.95	±	0.23
1273	0.7278	0.0013	92.9	71.2	81	10.95	±	0.17
1343	0.7413	0.0012	97.3	72.7	62	10.97	±	0.28
FUSE	0.6798	0.0016	100.1	66.8	37	11.00	±	0.52

LT21	Muscovite							
J value:	0.002839	±	0.000057					
T(K)	39Ar/40Ar	36Ar/40Ar	%39Ar	%40Ar*	K/Ca	Age		(+/- 2s)
873	0.0097	0.0034	0.1	0.8	11	4.27	+/-	26.06
973	0.0348	0.0033	1.8	3.8	38	5.57	+/-	6.30
1023	0.0588	0.0031	9.9	9.4	1224	8.20	+/-	0.66
1073	0.6036	0.0007	35.2	80.5	0	6.81	+/-	0.27
1103	0.5527	0.0009	51.5	74.7	2315	6.91	+/-	0.17
1173	0.3828	0.0017	62.5	49.9	385	6.66	+/-	0.52
1273	0.3078	0.0020	77.1	39.8	1066	6.61	+/-	0.40
1373	0.5288	0.0012	93.9	65.0	10119	6.28	+/-	0.27
1473	0.5431	0.0013	100.0	60.9	899	5.73	+/-	0.94

LT21	Biotite							
J value:	0.002839	±	0.000057					
T(K)	39Ar/40Ar	36Ar/40Ar	%39Ar	%40Ar*	K/Ca	Age		(+/- 2s)
923	0.0348	0.0032	4.5	6.5	528	9.50	+/-	0.90
973	0.2351	0.0014	24.2	57.6	906	12.50	+/-	0.52
1073	0.2917	0.0009	52.8	73.3	815	12.82	+/-	0.45
1143	0.3286	0.0004	70.9	88.5	1230	13.74	+/-	0.92
1173	0.3138	0.0008	80.1	77.1	163	12.53	+/-	0.37
1223	0.3534	0.0005	100.1	86.1	396	12.43	+/-	0.52

LT22	Muscovite							
J value:	0.00290820	±	0.00005820					
T(K)	39Ar/40Ar	36Ar/40Ar	%39Ar	%40Ar*	K/Ca	Age		(+/- 2s)
873	0.0333	0.0029	0.3	16.0	69	25.00	+/-	28.00
973	0.0319	0.0031	1.5	7.2	55	12.00	+/-	8.30
1023	0.0642	0.0030	10.0	11.0	3197	8.70	+/-	1.10
1048	0.3000	0.0021	33.0	39.0	0	6.70	+/-	0.20
1073	0.5000	0.0009	56.0	72.0	0	6.90	+/-	0.40

Table 1

1103	0.5000	0.0012	69.0	64.0	18442	6.60	+/-	0.40
1173	0.4000	0.0017	77.0	51.0	4130	7.40	+/-	1.60
1273	0.3000	0.0020	86.0	41.0	3246	7.60	+/-	1.40
1373	0.5000	0.0012	96.0	66.0	5282	6.70	+/-	0.90
1473	0.6000	0.0003	100.0	92.0	608	7.90	+/-	2.30
1823	0.2000	0.0020	100.0	40.0	74	11.00	+/-	11.00

LT22	**Biotite**							
J value:	0.002839	±	0.000057					
T(K)	39Ar/40Ar	36Ar/40Ar	%39Ar	%40Ar*	K/Ca	Age		(+/- 2s)
923	0.0596	0.0029	5.0	14.0	313	12.00	+/-	1.10
973	0.2000	0.0008	29.8	76.0	3276	17.00	+/-	0.40
1073	0.3000	0.0005	52.8	84.0	2767	17.00	+/-	0.30
1143	0.3000	0.0006	83.9	84.0	1409	16.00	+/-	0.40
1173	0.3000	0.0006	96.9	82.0	1573	14.00	+/-	1.20
1223	0.3000	0.0002	99.9	94.0	237	17.00	+/-	4.00

LT24	**Muscovite**							
J value:	0.002963	±	0.000059					
T(K)	39Ar/40Ar	36Ar/40Ar	%39Ar	%40Ar*	K/Ca	Age		(+/- 2s)
873	0.0331	0.0033	0.3	1.5	36	2.50	+/-	15.00
953	0.0237	0.0032	1.1	6.7	212	15.00	+/-	11.00
1023	0.0552	0.0030	4.7	10.0	382	9.90	+/-	3.40
1073	0.3000	0.0023	43.0	31.0	7131	6.40	+/-	0.30
1103	0.6000	0.0010	63.0	72.0	0	6.10	+/-	0.30
1133	0.5000	0.0011	73.0	68.0	9225	7.20	+/-	0.50
1173	0.3000	0.0022	78.0	36.0	579	5.50	+/-	0.90
1223	0.3000	0.0022	81.0	36.0	958	7.10	+/-	3.10
1273	0.3000	0.0027	85.0	22.0	1083	3.80	+/-	2.70
1323	0.4000	0.0014	88.0	59.0	629	7.50	+/-	1.70
1423	0.6000	0.0014	97.0	59.0	3463	5.70	+/-	1.10
1523	0.7000	0.0008	100.0	78.0	417	5.80	+/-	4.40

LT24	**Biotite**							
J value:	0.002963	±	0.000058					
T(K)	39Ar/40Ar	36Ar/40Ar	%39Ar	%40Ar*	K/Ca	Age		(+/- 2s)
873	0.0235	0.0033	1.0	3.8	106	8.46	+/-	5.84
923	0.1187	0.0027	9.5	20.2	622	8.88	+/-	1.01
973	0.4037	0.0013	25.9	63.2	0	8.19	+/-	0.66
1023	0.4680	0.0009	36.7	74.9	1332	8.37	+/-	1.64
1073	0.4562	0.0013	42.8	62.2	563	7.13	+/-	1.97
1123	0.4582	0.0007	47.5	80.3	1628	9.16	+/-	2.63
1223	0.4881	0.0007	90.2	79.4	0	8.50	+/-	0.15
1323	0.4824	0.0009	99.9	72.2	8727	7.83	+/-	1.34

Table 1

L142	Muscovite							
J value:	0.002908	±	0.000058					
T(K)	39Ar/40Ar	36Ar/40Ar	%39Ar	%40Ar*	K/Ca	Age		(+/- 2s)
873	0.0217	0.0032	0.9	5.0	40	12.02	+/-	4.15
973	0.0568	0.0031	2.3	9.0	344	8.28	+/-	8.36
1023	0.1556	0.0023	17.4	31.8	44904	10.68	+/-	0.59
1048	0.4251	0.0006	42.8	81.1	0	9.98	+/-	0.23
1073	0.4535	0.0006	58.3	81.5	1742	9.40	+/-	0.78
1103	0.4140	0.0008	67.3	75.8	4140	9.58	+/-	2.73
1173	0.3288	0.0013	73.9	62.6	2151	9.97	+/-	2.25
1273	0.3337	0.0015	82.9	54.4	2386	8.53	+/-	1.48
1373	0.4440	0.0005	93.6	84.2	3852	9.92	+/-	0.60
1473	0.4511	0.0010	99.4	69.5	1021	8.07	+/-	1.05

L142	Biotite							
J value:	0.002908	±	0.000058					
T(K)	39Ar/40Ar	36Ar/40Ar	%39Ar	%40Ar*	K/Ca	Age		(+/- 2s)
973	0.0134	0.0033	1.1	1.3	0.9	5.20	+/-	146.00
1173	0.0189	0.0028	3.3	19.0	14.0	51.00	+/-	80.00
1223	0.0218	0.0032	6.6	5.1	8.5	12.00	+/-	6.80
1323	0.0262	0.0022	17.6	35.0	68.0	68.00	+/-	25.00
1423	0.0356	0.0018	49.5	46.0	129.0	66.00	+/-	11.00
1523	0.0358	0.0018	80.3	48.0	168.0	69.00	+/-	8.00
1823	0.0240	0.0028	100.1	18.0	22.0	39.00	+/-	6.90

LT26	Muscovite							
J value:	0.002908	±	0.000058					
T(K)	39Ar/40Ar	36Ar/40Ar	%39Ar	%40Ar*	K/Ca	Age		(+/- 2s)
973	0.0389	0.0032	1.2	7.0	105	9.50	+/-	4.10
1023	0.0818	0.0029	5.6	14.0	539	8.80	+/-	0.80
1048	0.2000	0.0027	22.0	21.0	2155	6.90	+/-	0.30
1073	0.4000	0.0020	41.0	41.0	10757	5.50	+/-	0.20
1103	0.6000	0.0016	55.0	52.0	11477	4.90	+/-	0.40
1173	0.4000	0.0022	68.0	35.0	642	5.20	+/-	0.40
1273	0.3000	0.0026	78.0	23.0	523	4.70	+/-	0.30
1373	0.4000	0.0021	89.0	39.0	504	4.70	+/-	0.30
1473	0.6000	0.0014	100.0	59.0	284	5.10	+/-	0.50
1823	0.3000	0.0021	100.0	39.0	64	7.60	+/-	22.00

LT26	Biotite							
J value:	0.002905	±	0.000058					
T(K)	39Ar/40Ar	36Ar/40Ar	%39Ar	%40Ar*	K/Ca	Age		(+/- 2s)
923	0.0572	0.0032	3.5	7.1	130	6.45	+/-	2.27
973	0.3287	0.0017	25.5	48.8	711	7.76	+/-	0.23
1073	0.5238	0.0007	44.5	78.4	416	7.82	+/-	0.50

Table 1

1143	0.5191	0.0008	62.5	77.3	655	7.79	+/-	0.30
1173	0.5147	0.0009	79.7	72.5	1691	7.37	+/-	0.37
1223	0.5065	0.0011	93.6	68.4	7504	7.06	+/-	0.15
1323	0.4641	0.0011	98.6	67.6	101	7.62	+/-	1.56
1423	0.4757	0.0013	99.7	60.4	22	6.64	+/-	2.67
1823	0.1040	0.0025	99.8	24.9	2	12.50	+/-	143.75

LT29	**Biotite**							
J value:	0.002963	±	0.000059					
T(K)	39Ar/40Ar	36Ar/40Ar	%39Ar	%40Ar*	K/Ca	Age		(+/- 2s)
873	0.0000	0.0032	3.2	4.9	109	5.60	+/-	2.40
923	0.1000	0.0000	7.0	13.0	378	4.90	+/-	1.50
973	0.5000	0.0000	18.0	52.0	778	6.00	+/-	0.80
1073	0.7000	0.0010	38.0	70.0	618	5.40	+/-	0.30
1143	0.7000	0.0014	47.0	59.0	330	4.30	+/-	1.50
1173	0.7000	0.0012	53.0	64.0	833	4.70	+/-	0.80
1223	0.8000	0.0011	68.0	68.0	18055	4.80	+/-	0.40
1323	0.7000	0.0009	95.0	73.0	1101	5.70	+/-	0.20
1423	0.6000	0.0016	99.0	51.0	223	4.30	+/-	2.00
1823	0.6000	0.0012	100.0	64.0	121	5.80	+/-	4.70

L43	**Biotite**							
J value:	0.006323	±	0.000016					
T (K)	39Ar/40Ar	36Ar/39Ar	% 39Ar	% 40Ar*	K/Ca	Age		(+/- 2 s)
923	0.3164	0.0083	6.4	21.9	22	7.87	±	0.42
1023	0.5583	0.0037	18.5	38.1	50	7.77	±	0.12
1093	0.6439	0.0029	28.4	43.9	52	7.76	±	0.23
1153	0.7267	0.0023	55.6	48.9	71	7.66	±	0.15
1193	0.8569	0.0016	64.9	58.6	36	7.78	±	0.13
1223	0.9217	0.0013	73.8	62.2	28	7.69	±	0.14
1263	0.9718	0.0011	82.6	67.3	46	7.88	±	0.12
1313	1.0225	0.0009	92.6	71.7	63	7.98	±	0.11
FUSE	0.9355	0.0011	100.0	68.5	53	8.33	±	0.15

L146	**Biotite**							
J value:	0.002839	±	0.000057					
T(K)	39Ar/40Ar	36Ar/40Ar	%39Ar	%40Ar*	K/Ca	Age		(+/- 2s)
873	0.0456	0.0032	7.8	4.7	366	5.31	+/-	1.17
923	0.2346	0.0021	14.6	37.1	1165	8.09	+/-	1.36
973	0.4054	0.0012	27.5	65.0	1956	8.20	+/-	1.25
1073	0.3444	0.0014	44.2	57.9	905	8.58	+/-	0.35
1143	0.2688	0.0020	54.1	40.1	449	7.62	+/-	0.75
1173	0.4345	0.0010	65.8	70.9	4484	8.34	+/-	1.39
1223	0.4290	0.0011	83.2	67.0	13909	7.98	+/-	0.39
1323	0.4324	0.0014	97.3	60.0	481	7.09	+/-	1.48

Table 1

1423	0.3623	0.0016	99.3	53.6	381	7.57	+/-	2.57
1823	0.2395	0.0020	100.0	41.8	40	8.91	+/-	12.08

L36	**Biotite**							
J value:	0.006311	±	0.000016					
T (K)	39Ar/40Ar	36Ar/39Ar	% 39Ar	% 40Ar*	K/Ca	Age		(+/- 2 s)
923	0.1411	0.0178	3.1	25.4	96	20.41	±	2.23
1023	0.3058	0.0054	13.6	50.4	205	18.65	±	0.40
1093	0.3791	0.0030	27.8	65.3	287	19.50	±	0.30
1153	0.4149	0.0023	40.4	71.1	294	19.39	±	0.28
1213	0.4415	0.0018	50.9	75.6	368	19.40	±	0.28
1273	0.4666	0.0014	61.3	79.8	484	19.36	±	0.29
1343	0.4876	0.0011	75.9	82.8	494	19.24	±	0.20
FUSE	0.4509	0.0009	100.0	86.9	151	21.80	±	0.28

Table 2

Tectonic Unit	Unit	Sample #	Rock type	Mineral	Preferred age (Ma)	Method
Lesser Himalayan Sequence	Dhunche Unit	KVH2	amphibolite	hornblende	41 ± 6.7	Minimum age - release spectrum
MCT Zone	Trisuli gneiss	L118	fault gouge	muscovite	2.28 ± 0.04	Intercept age
	Trisuli	L127	amphibolite	hornblende	27.2 ± 0.4	Intercept age
	Syabru Bensi gneiss	L51	augen orthogneiss	muscovite	8.9 ± 0.2	Intercept age
				biotite	21.0 ± 0.3	Intercept age
				K-feldspar	5.5 ± 0.1	Minimum age - release spectrum
	Syabru gneiss	LT33	gt-kya pelitic gneiss	muscovite	5.5 ± 0.4	Intercept age
				biotite	7.8 ± 0.1	Intercept age
	Syabru gneiss	L66	gt-kya pelitic gneiss	muscovite	8.5 ± 0.2	Intercept age
	Syabru gneiss	L20a	gt-kya pelitic gneiss	muscovite	6.9 ± 0.1	Intercept age
				biotite	11.0 ± 0.1	Intercept age
Greater Himalayan Sequence	Gosainkund gneiss	LT21	migmatitic pelitic gneiss	muscovite	6.7 ± 0.1	Intercept age
				biotite	12.7 ± 0.2	Intercept age
	Gosiankund gneiss	LT22	migmatitic pelitic gneiss	muscovite	6.7 ± 0.2	Intercept age
				biotite	16.3 ± 0.9	Intercept age
	Gosainkund gneiss	LT24	migmatitic pelitic gneiss	muscovite	6.1 ± 0.3	Intercept age
				biotite	8.4 ± 0.2	Intercept age
	Gosiankund gneiss	L142	migmatitic pelitic gneiss	muscovite	9.7 ± 0.3	Intercept age
				biotite	53.7 ± 12.4	Total gas age
	Gosainkund gneiss	LT26	granite	muscovite	4.6 ± 0.4	Intercept age
				biotite	7.6 ± 0.2	Intercept age
	Ghora Tabela gneiss	LT 29	sill-gt gneiss	biotite	5.4 ± 0.3	Intercept age
	Ghora Tabela gneiss	L43	sill-gt gneiss	biotite	8.0 ± 0.2	Intercept age
	Kyangjin gneiss	L146	granite	biotite	8.1 ± 0.3	Intercept age
	Yala landslide	L36	migmatitic pel. gneiss	biotite	19.3 ± 0.3	Intercept age

gt = garnet; kya = kyanite; sill = sillimanite

FIGURE CAPTIONS

1. General location map of the Nepal Himalaya. Patterned regions are tectonostratigraphic units indicated.

2. Location geologic map of the Langtang region. Major tectonostratigraphic units are patterned as indicated. Inset box enlarges the MCT zone region for clarification of features. Locations of samples are indicated by solid circles. Abbreviations are as follows: Unit of Lesser Himalayan sequence is: **dh** = Dhunche unit. Units of the MCT zone are: **th** = Thangjet gneiss, **gol** = Goljhong unit, **gom** = Gompagong calc-quartzite, **ch** = Chilime calc-schist, **tr** = Trisuli gneiss, **bh** = Bhote carbonate, **ba** = Barabal gneiss, **sb** = Syabru Bensi augen gneiss, **ph** = Phulung augen gneiss, **ma** = Mangol metapsammite, **sy** = Syabru gneiss. Units of the Greater Himalayan sequence are: **gos** = Gosainkund gneiss, **gh** = Ghora Tabela gneiss, **lan** = Langtang gneiss, **ky** = Kyangjin augen gneiss, **ja** = Jathang foliated granite, **nu** = Nubama gneiss, **ya** = Yala landslide.

3. Isotope correlation plot (a) and age spectrum (b) for the Lesser Himalayan sequence sample KVH2. Unless otherwise indicated with error bars on the isotope correlation diagram, two-sigma errors on individual points are less than the size of the solid circles that represent them.

4. Isotope correlation plots (a, c, e ,g, i, k, m, o, q, s) and age spectra (b, d, f, h, j, l, n, p, r, t) for MCT zone samples L118, L127, L51, LT33, L66 and L20a. Intercept ages are calculated based on the data for the increments shown in the Figure. If data from increments were omitted in the age calculation, it is so indicated in the

text. Unless otherwise designated with error bars on the isotope correlation diagram, two-sigma errors on individual points are less than the size of the solid circles that represent them.

5. Isotope correlation plots (a, c, e, g, i, k, m, o, q, s, u, w, y, aa) and age spectra (b, d, f, h, j, l, n, p, r, t, v, x, z, bb) for Greater Himalayan sequence samples LT21, LT22, LT24, L142, LT26, LT29, L43, L146, L36. Intercept ages are calculated based on the data for the increments shown in the Figure. If data from increments were omitted in the age calculation, it is so indicated in the text. Unless otherwise designated with error bars on the isotope correlation diagram, two-sigma errors on individual points are less than the size of the solid circles that represent them.

6. Geologic map of the Langtang region, using Figure 2 as a base map, with realistic ages indicated by solid circles.

7. Cartoon of data from this study and the three other $^{40}Ar/^{39}Ar$ cooling-age studies from Nepal: Copeland et al. (1991), Hubbard and Harrison, (1989) and Maluski et al., (1988). All data is presented on a generalized cross section of the core of the Himalayas. Not to scale. Letters in parentheses indicate mineral used in dating; m - muscovite, b - biotite h - hornblende and K- K-feldspar.

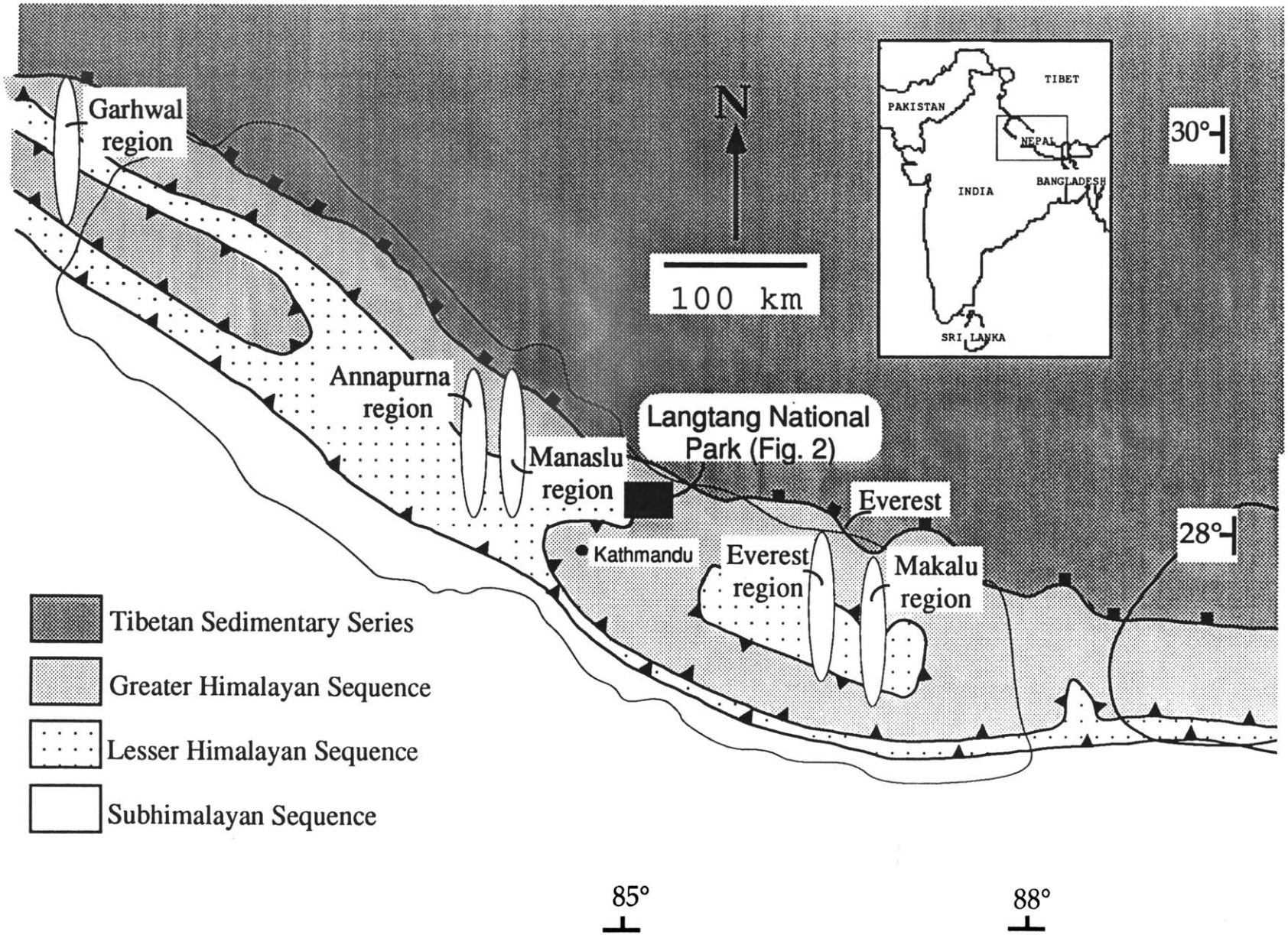
Garhwal region
Annapurna region
Manaslu region
Langtang National Park (Fig. 2)
Everest
Everest region
Makalu region
Kathmandu
N
100 km
TIBET
PAKISTAN
NEPAL
INDIA
BANGLADESH
SRI LANKA
30°
28°
85°
88°
Tibetan Sedimentary Series
Greater Himalayan Sequence
Lesser Himalayan Sequence
Subhimalayan Sequence

Figure 1

N
5 km
Chilime Khola
Trisuli Kosi
Trisuli Khola
Langtang Khola
L146
ya
L36b
ja
nu
lan
ky
L43
LT29
gh
L20a
LT21
LT22
LT24
LT26
L118
L51
KVH2
L66
LT33
gos
L127
L142
gom
gol
ch
tr
bh
ba
sy
ph
th
dh
ma
sb
Greater Himalayan Sequence
Main Central Thrust Zone
Lesser Himalayan Sequence
Thrust contact
Landslide contact
Lithologic contact
River

Figure 2

a.

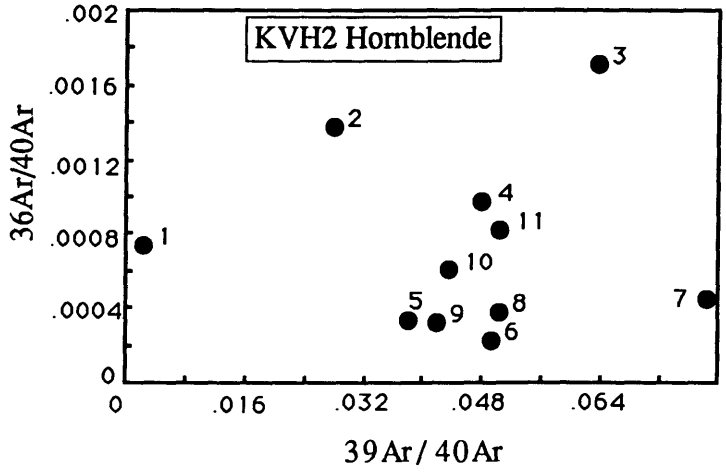
KVH2 Hornblende
36Ar/40Ar
39Ar/40Ar
.002
.0016
.0012
.0008
.0004
0
.016
.032
.048
.064
1
2
3
4
5
6
7
8
9
10
11

b.

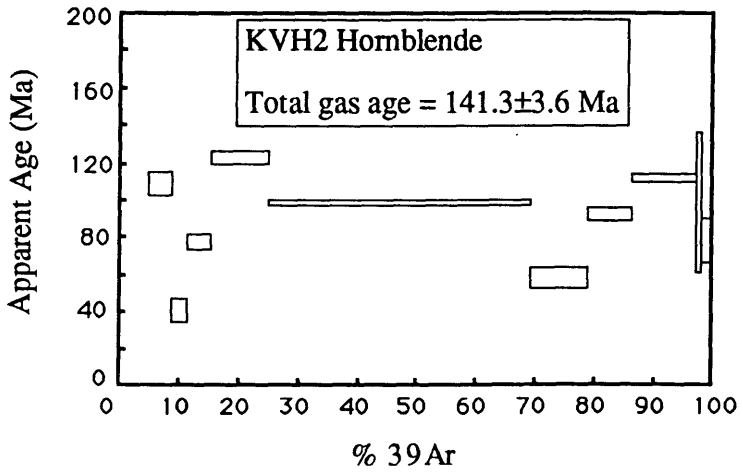
KVH2 Hornblende
Total gas age = 141.3±3.6 Ma
Apparent Age (Ma)
% 39Ar
200
160
120
80
40
0
10
20
30
40
50
60
70
80
90
100

Figure 3

a.

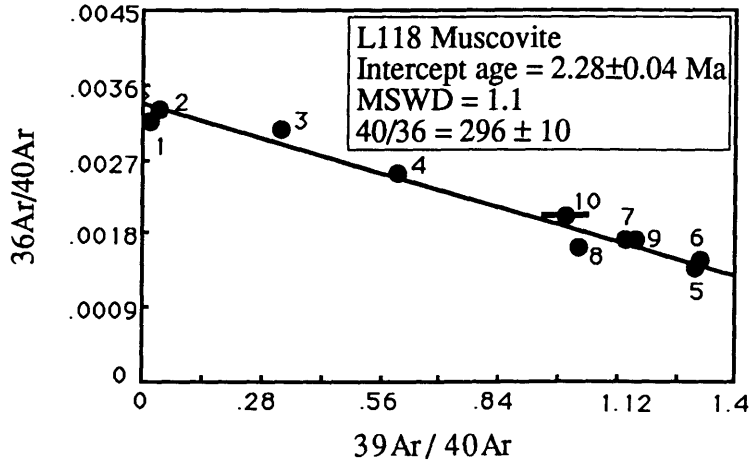
L118 Muscovite
Intercept age = 2.28±0.04 Ma
MSWD = 1.1
40/36 = 296 ± 10
36Ar/40Ar
.0045
.0036
.0027
.0018
.0009
0
0
.28
.56
.84
1.12
1.4
39Ar / 40Ar
1
2
3
4
5
6
7
8
9
10

b.

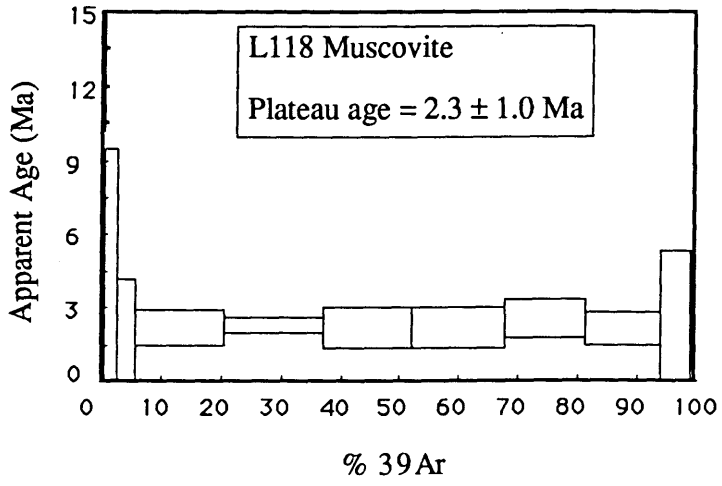
L118 Muscovite
Plateau age = 2.3 ± 1.0 Ma
Apparent Age (Ma)
15
12
9
6
3
0
0
10
20
30
40
50
60
70
80
90
100
% 39Ar

Figure 4

c.

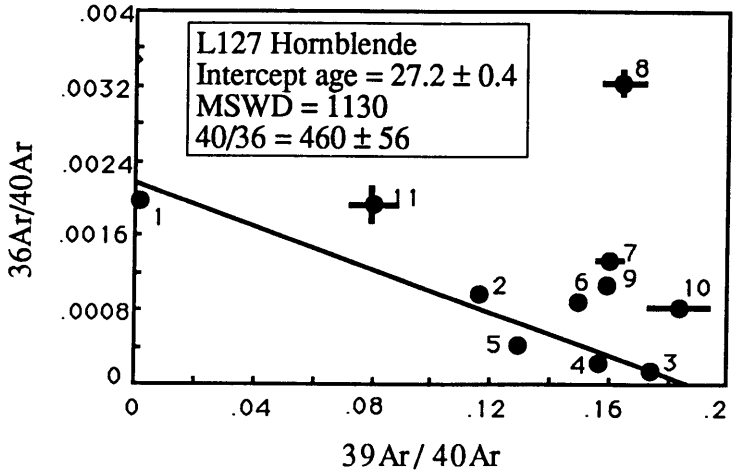
L127 Hornblende
Intercept age = 27.2 ± 0.4
MSWD = 1130
40/36 = 460 ± 56
36Ar/40Ar
.004
.0032
.0024
.0016
.0008
0
0
.04
.08
.12
.16
.2
39Ar/40Ar
1
2
3
4
5
6
7
8
9
10

d.

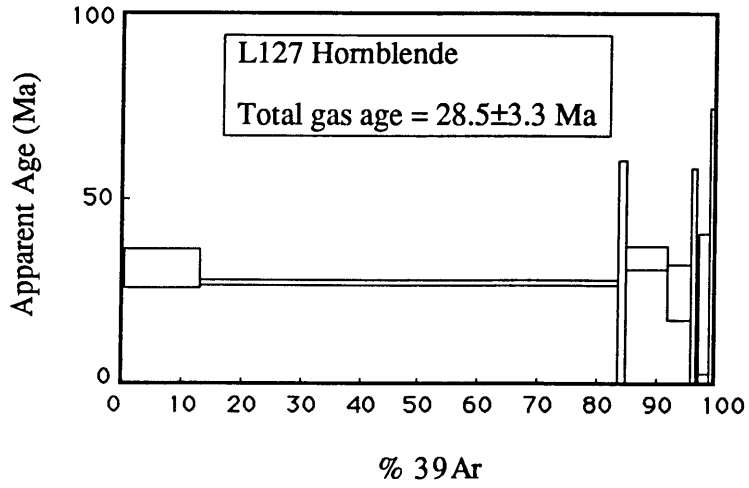
L127 Hornblende
Total gas age = 28.5±3.3 Ma
Apparent Age (Ma)
100
50
0
0
10
20
30
40
50
60
70
80
90
100
% 39Ar

Figure 4

e.

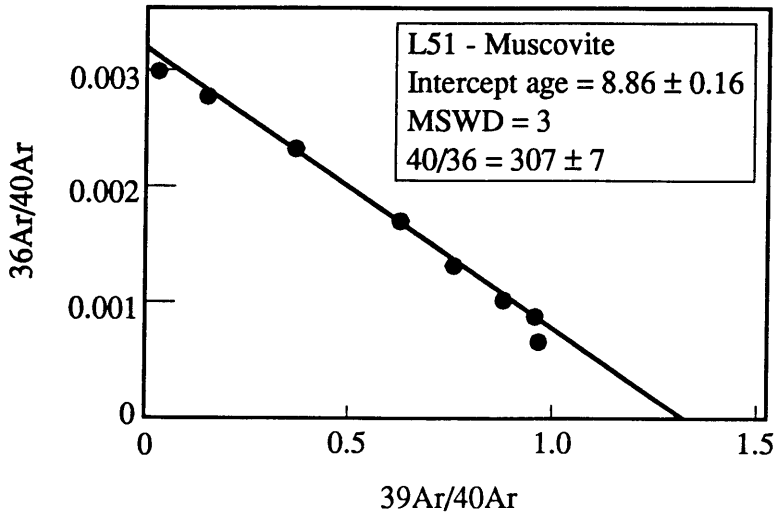
L51 - Muscovite
Intercept age = 8.86 ± 0.16
MSWD = 3
40/36 = 307 ± 7
36Ar/40Ar
0.003
0.002
0.001
0
0
0.5
1.0
1.5
39Ar/40Ar

f.

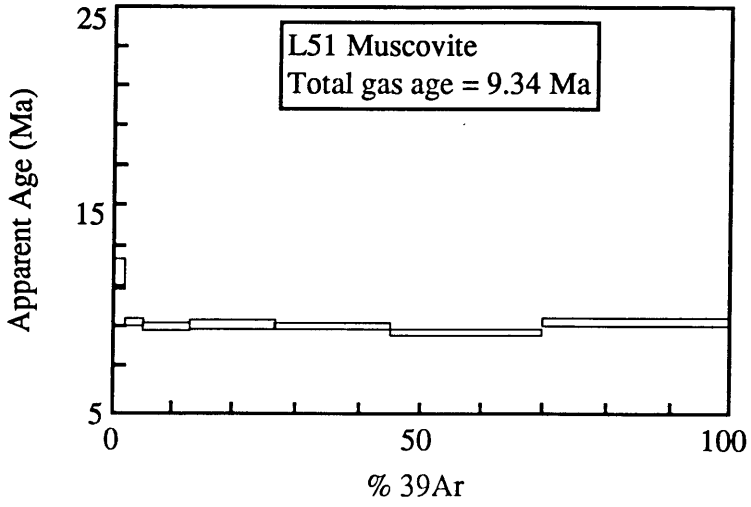
L51 Muscovite
Total gas age = 9.34 Ma
Apparent Age (Ma)
25
15
5
0
50
100
% 39Ar

Figure 4

g.

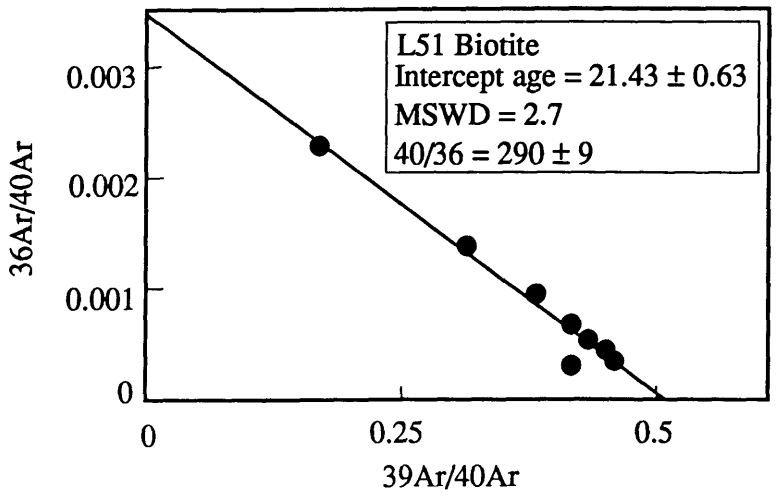
L51 Biotite
Intercept age = 21.43 ± 0.63
MSWD = 2.7
40/36 = 290 ± 9
36Ar/40Ar
0.003
0.002
0.001
0
0
0.25
0.5
39Ar/40Ar

h.

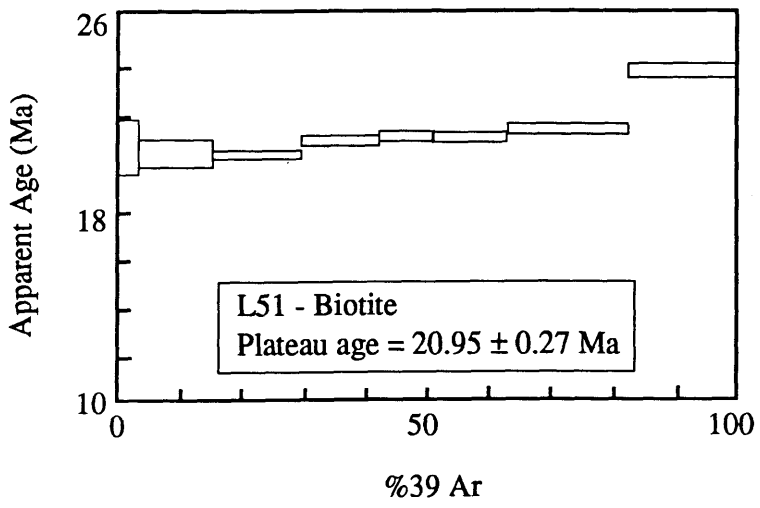
Apparent Age (Ma)
26
18
10
L51 - Biotite
Plateau age = 20.95 ± 0.27 Ma
0
50
100
%39 Ar

Figure 4

i.

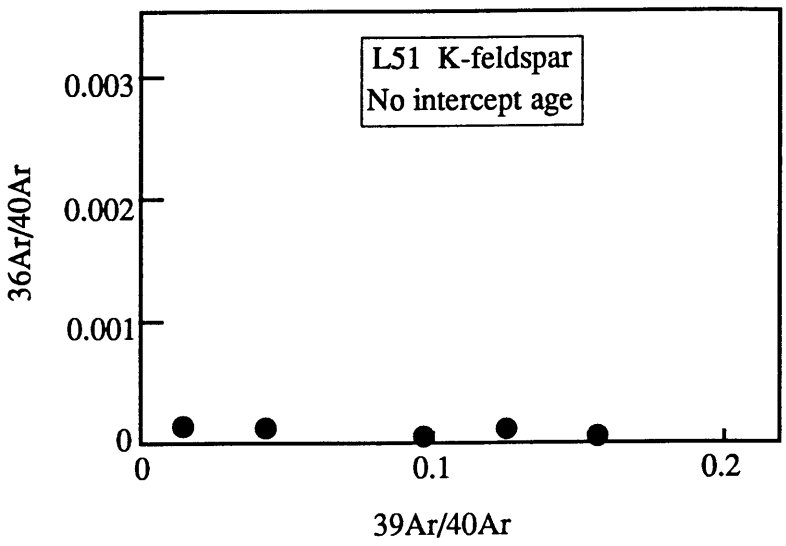
L51 K-feldspar
No intercept age
0.003
0.002
0.001
0
36Ar/40Ar
0
0.1
0.2
39Ar/40Ar

j.

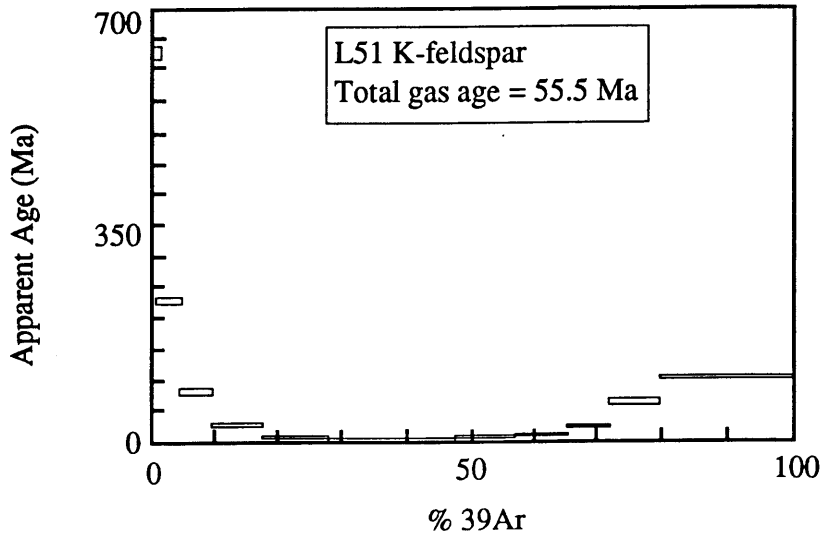
L51 K-feldspar
Total gas age = 55.5 Ma
700
350
0
Apparent Age (Ma)
0
50
100
% 39Ar

Figure 4

k.

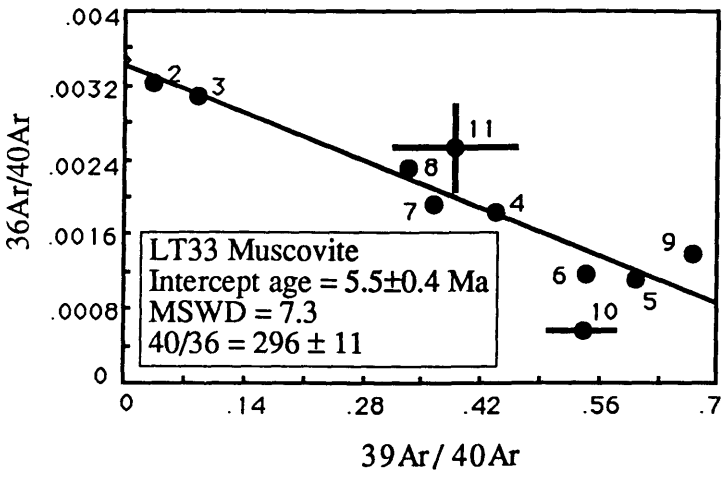
.004
.0032
.0024
.0016
.0008
0
36Ar/40Ar
0
.14
.28
.42
.56
.7
39Ar/40Ar
LT33 Muscovite
Intercept age = 5.5±0.4 Ma
MSWD = 7.3
40/36 = 296 ± 11
2
3
11
8
7
4
9
6
5
10

l.

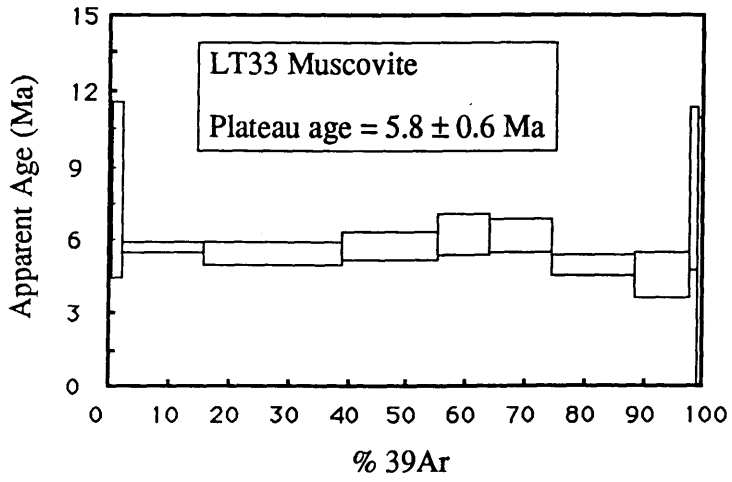
15
12
9
6
3
0
Apparent Age (Ma)
0
10
20
30
40
50
60
70
80
90
100
% 39Ar
LT33 Muscovite
Plateau age = 5.8 ± 0.6 Ma

Figure 4

m.

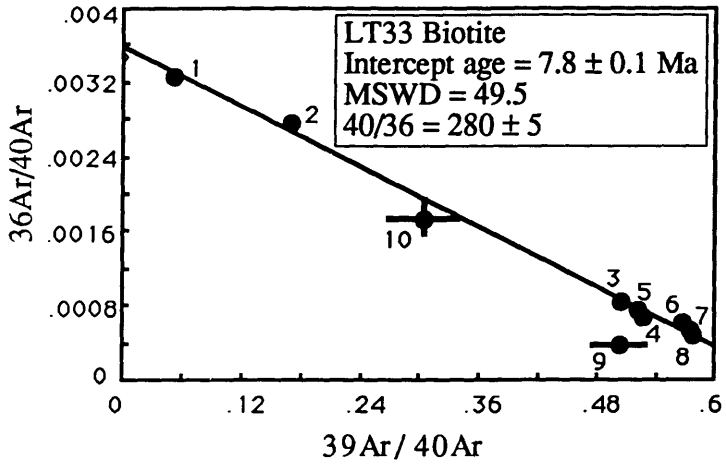
LT33 Biotite
Intercept age = 7.8 ± 0.1 Ma
MSWD = 49.5
40/36 = 280 ± 5
36Ar/40Ar
.004
.0032
.0024
.0016
.0008
0
0
.12
.24
.36
.48
.6
39Ar/40Ar
1
2
10
3
5
6
7
4
9
8

n.

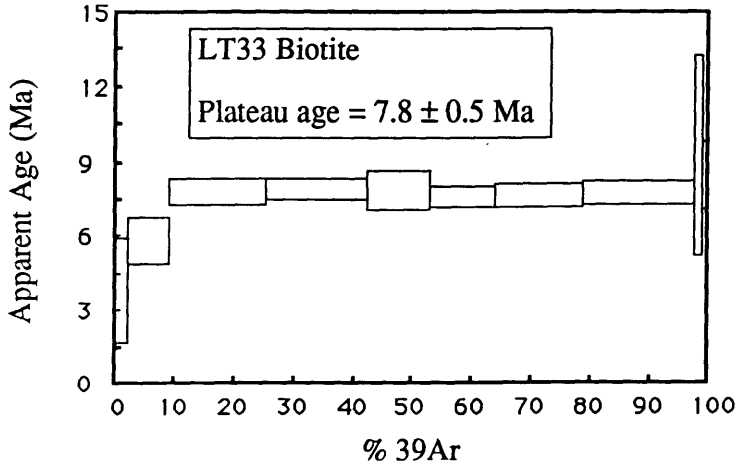
LT33 Biotite
Plateau age = 7.8 ± 0.5 Ma
Apparent Age (Ma)
15
12
9
6
3
0
0
10
20
30
40
50
60
70
80
90
100
% 39Ar

Figure 4

o.

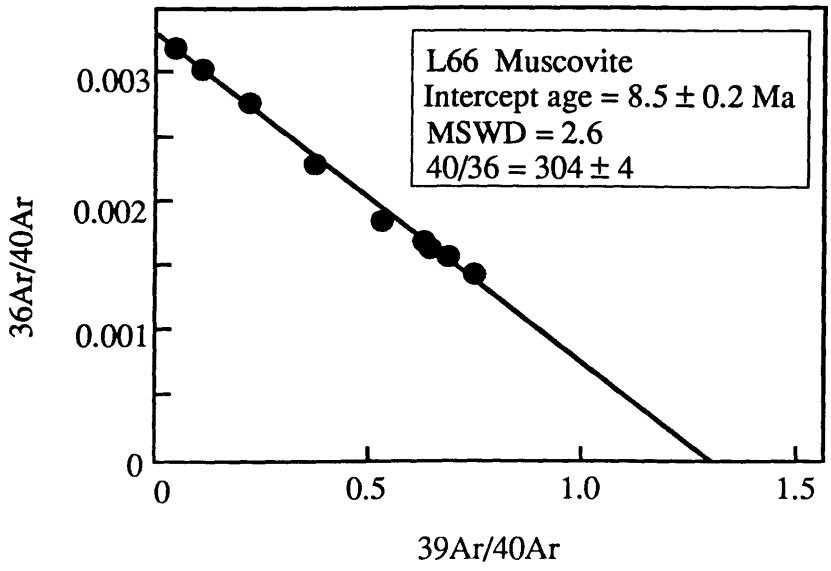
L66 Muscovite
Intercept age = 8.5 ± 0.2 Ma
MSWD = 2.6
40/36 = 304 ± 4
0.003
0.002
0.001
0
36Ar/40Ar
0
0.5
1.0
1.5
39Ar/40Ar

p.

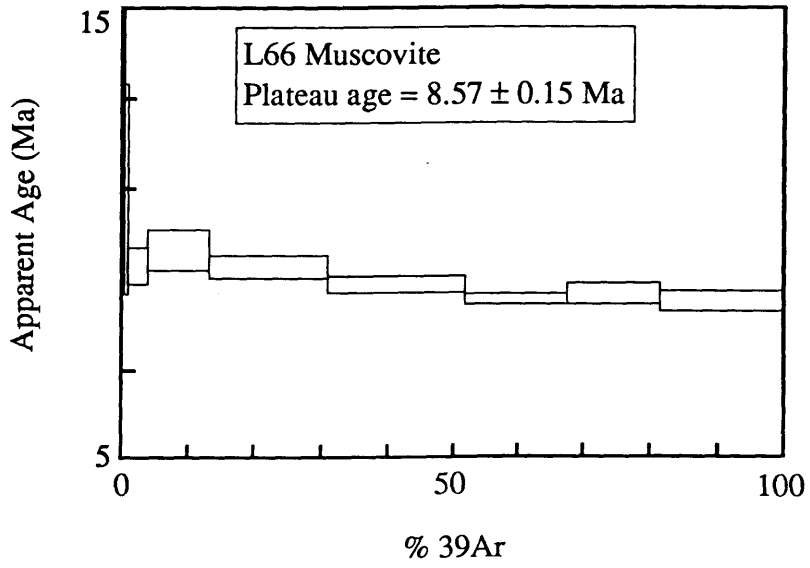
L66 Muscovite
Plateau age = 8.57 ± 0.15 Ma
15
5
Apparent Age (Ma)
0
50
100
% 39Ar

Figure 4

q.

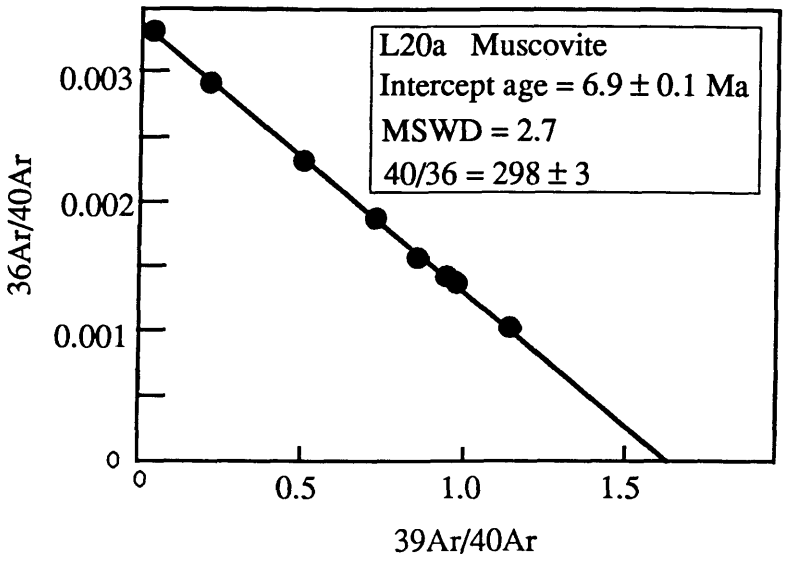
L20a Muscovite
Intercept age = 6.9 ± 0.1 Ma
MSWD = 2.7
40/36 = 298 ± 3
36Ar/40Ar
0.003
0.002
0.001
0
0
0.5
1.0
1.5
39Ar/40Ar

r.

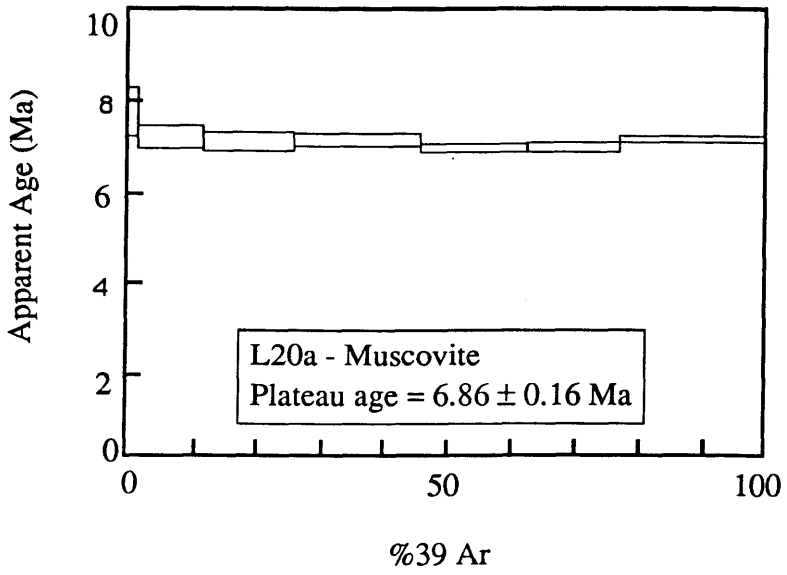
Apparent Age (Ma)
10
8
6
4
2
0
L20a - Muscovite
Plateau age = 6.86 ± 0.16 Ma
0
50
100
%39 Ar

Figure 4

s.

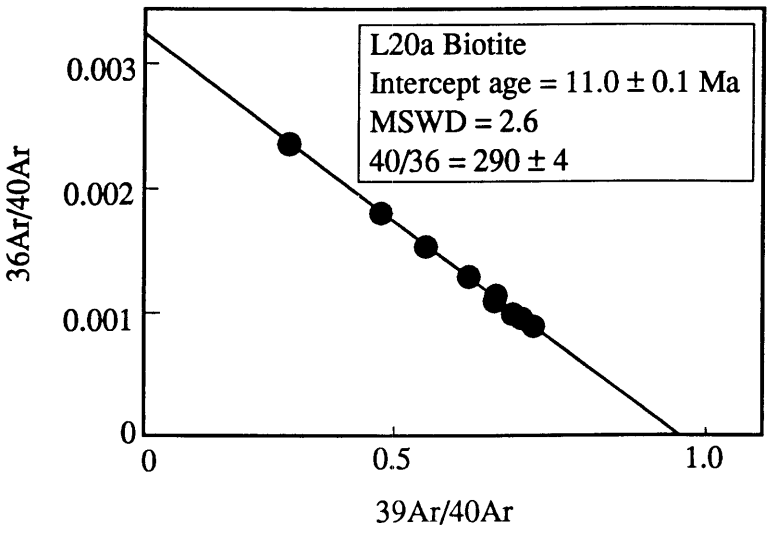
L20a Biotite
Intercept age = 11.0 ± 0.1 Ma
MSWD = 2.6
40/36 = 290 ± 4
36Ar/40Ar
0.003
0.002
0.001
0
0
0.5
1.0
39Ar/40Ar

t.

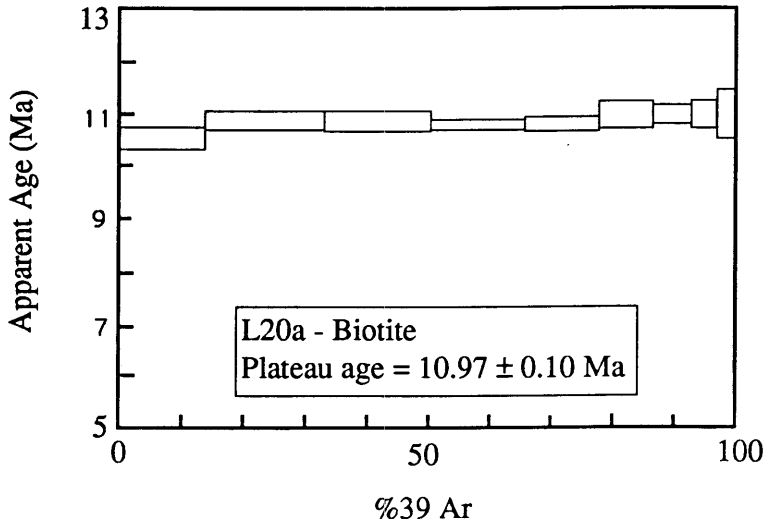
Apparent Age (Ma)
13
11
9
7
5
L20a - Biotite
Plateau age = 10.97 ± 0.10 Ma
0
50
100
%39 Ar

Figure 4

a.

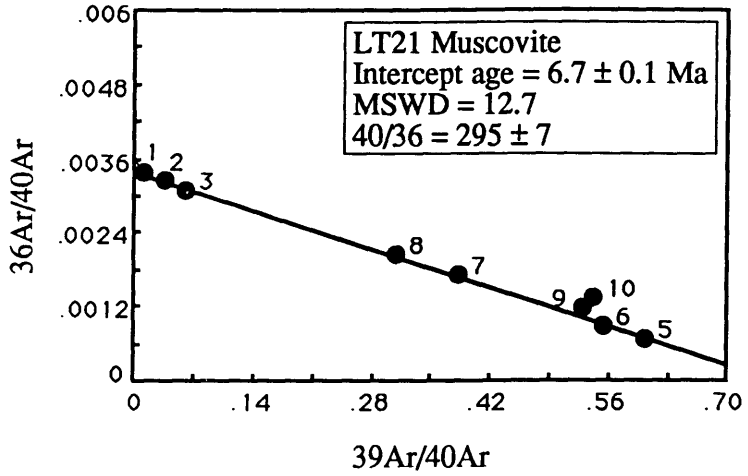
LT21 Muscovite
Intercept age = 6.7 ± 0.1 Ma
MSWD = 12.7
40/36 = 295 ± 7
36Ar/40Ar
.006
.0048
.0036
.0024
.0012
0
1
2
3
8
7
9
10
6
5
0
.14
.28
.42
.56
.70
39Ar/40Ar

b.

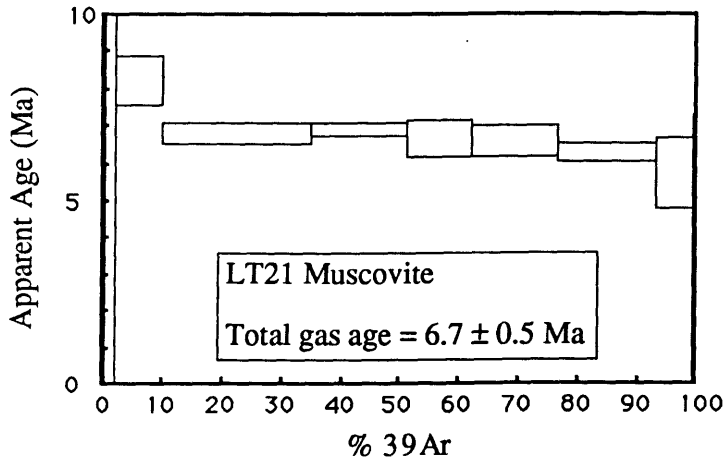
Apparent Age (Ma)
10
5
0
LT21 Muscovite
Total gas age = 6.7 ± 0.5 Ma
0
10
20
30
40
50
60
70
80
90
100
% 39Ar

Figure 5

c.

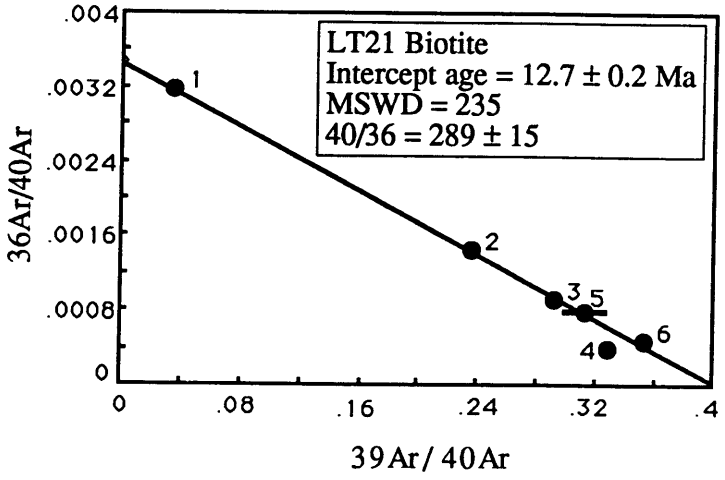
LT21 Biotite
Intercept age = 12.7 ± 0.2 Ma
MSWD = 235
40/36 = 289 ± 15
36Ar/40Ar
.004
.0032
.0024
.0016
.0008
0
1
2
3
5
4
6
0
.08
.16
.24
.32
.4
39Ar/40Ar

d.

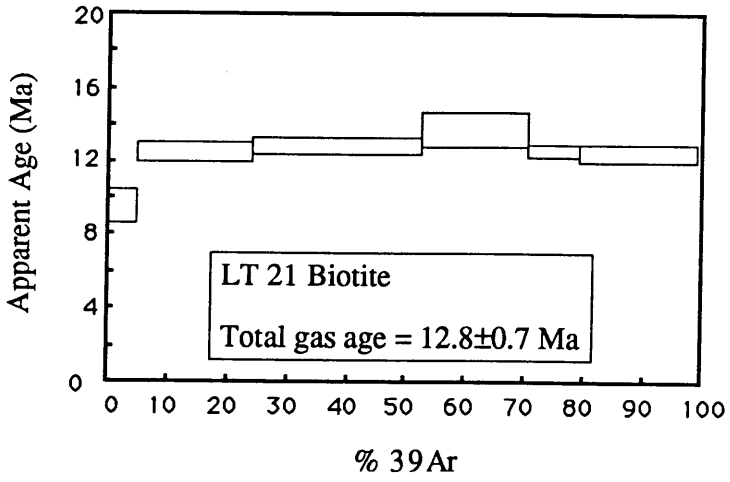
Apparent Age (Ma)
20
16
12
8
4
0
LT 21 Biotite
Total gas age = 12.8±0.7 Ma
0
10
20
30
40
50
60
70
80
90
100
% 39Ar

Figure 5

e.

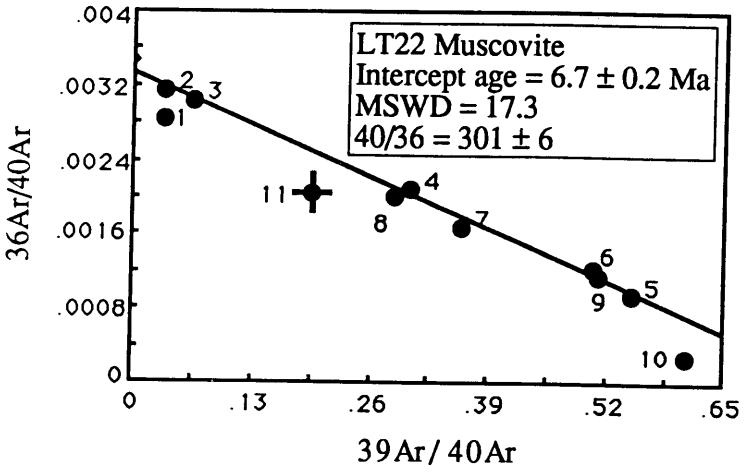
LT22 Muscovite
Intercept age = 6.7 ± 0.2 Ma
MSWD = 17.3
40/36 = 301 ± 6
36Ar/40Ar
.004
.0032
.0024
.0016
.0008
0
.13
.26
.39
.52
.65
39Ar/40Ar
1
2
3
4
5
6
7
8
9
10
11

f.

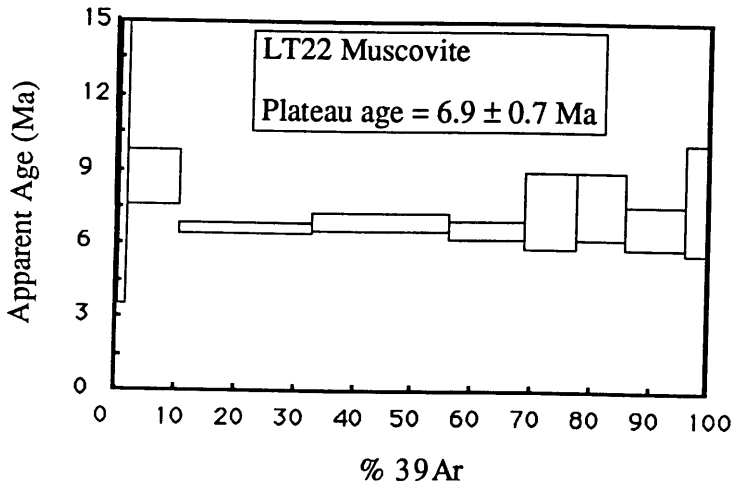
LT22 Muscovite
Plateau age = 6.9 ± 0.7 Ma
Apparent Age (Ma)
15
12
9
6
3
0
0
10
20
30
40
50
60
70
80
90
100
% 39Ar

Figure 5

g.

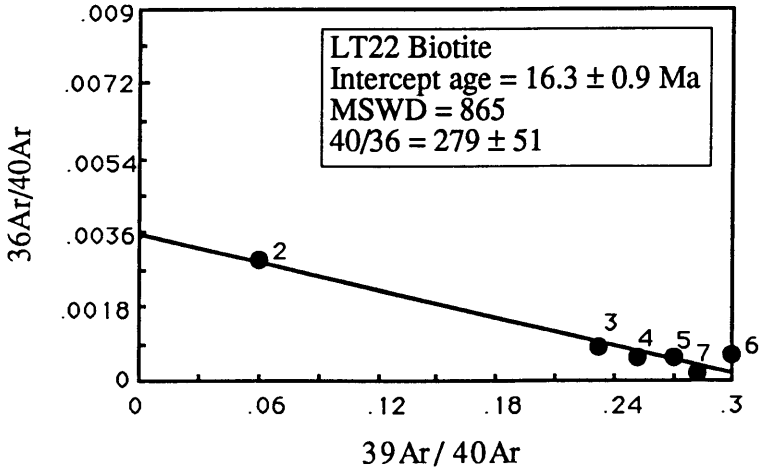
LT22 Biotite
Intercept age = 16.3 ± 0.9 Ma
MSWD = 865
40/36 = 279 ± 51
36Ar/40Ar
.009
.0072
.0054
.0036
.0018
0
2
3
4
5
7
6
0
.06
.12
.18
.24
.3
39Ar/40Ar

h.

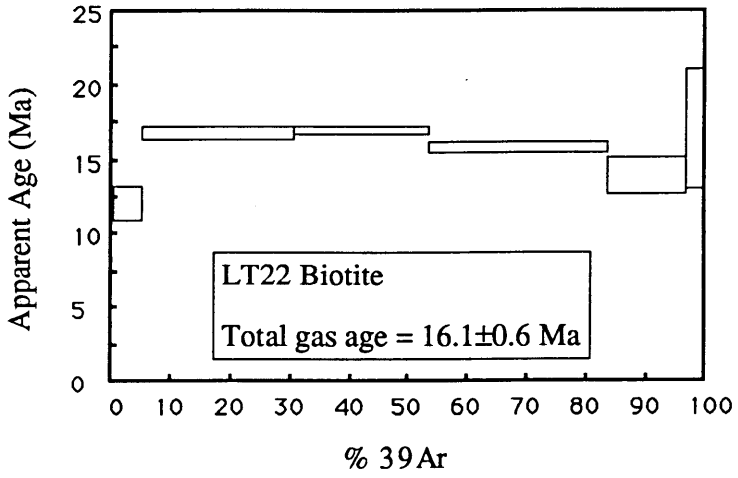
Apparent Age (Ma)
25
20
15
10
5
0
LT22 Biotite
Total gas age = 16.1±0.6 Ma
0
10
20
30
40
50
60
70
80
90
100
% 39Ar

Figure 5

i.

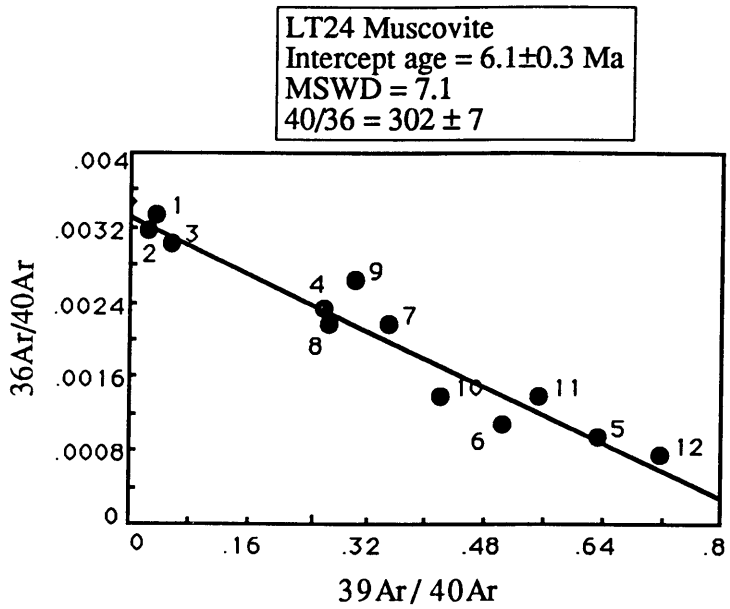
LT24 Muscovite
Intercept age = 6.1±0.3 Ma
MSWD = 7.1
40/36 = 302 ± 7
36Ar/40Ar
.004
.0032
.0024
.0016
.0008
0
0
.16
.32
.48
.64
.8
39Ar/40Ar
1
2
3
4
5
6
7
8
9
10
11
12

j.

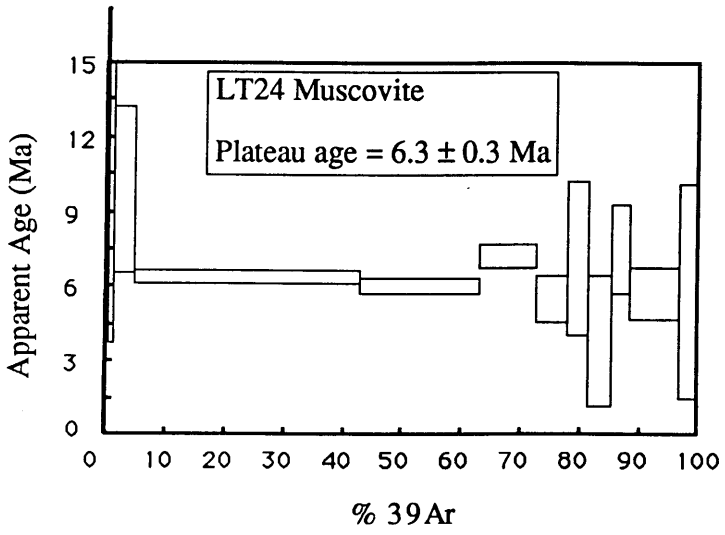
LT24 Muscovite
Plateau age = 6.3 ± 0.3 Ma
Apparent Age (Ma)
15
12
9
6
3
0
0
10
20
30
40
50
60
70
80
90
100
% 39Ar

Figure 5

k.

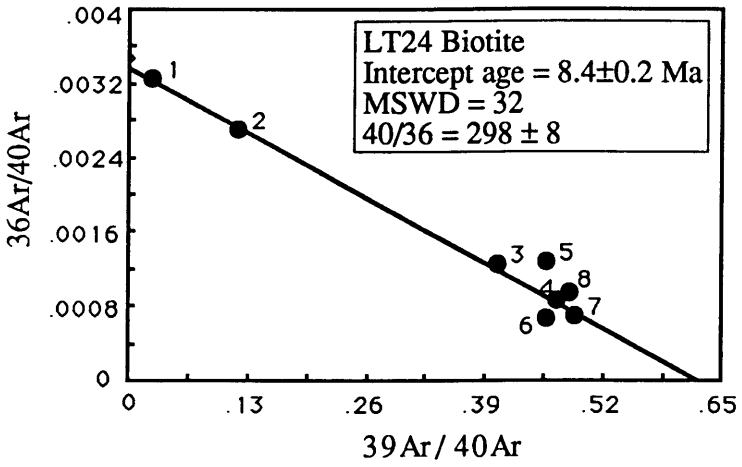
LT24 Biotite
Intercept age = 8.4±0.2 Ma
MSWD = 32
40/36 = 298 ± 8
36Ar/40Ar
.004
.0032
.0024
.0016
.0008
0
1
2
3
4
5
6
7
8
0
.13
.26
.39
.52
.65
39Ar/40Ar

l.

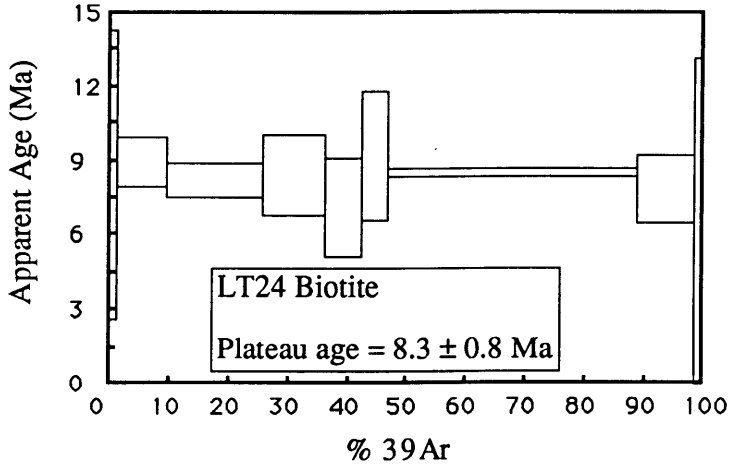
Apparent Age (Ma)
15
12
9
6
3
0
LT24 Biotite
Plateau age = 8.3 ± 0.8 Ma
0
10
20
30
40
50
60
70
80
90
100
% 39Ar

Figure 5

m.

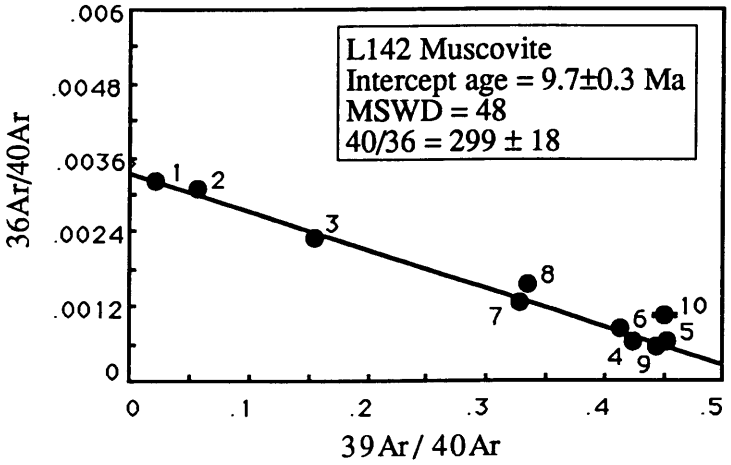
L142 Muscovite
Intercept age = 9.7±0.3 Ma
MSWD = 48
40/36 = 299 ± 18
36Ar/40Ar
.006
.0048
.0036
.0024
.0012
0
0
.1
.2
.3
.4
.5
39Ar/40Ar
1
2
3
8
7
6
10
5
4
9

n.

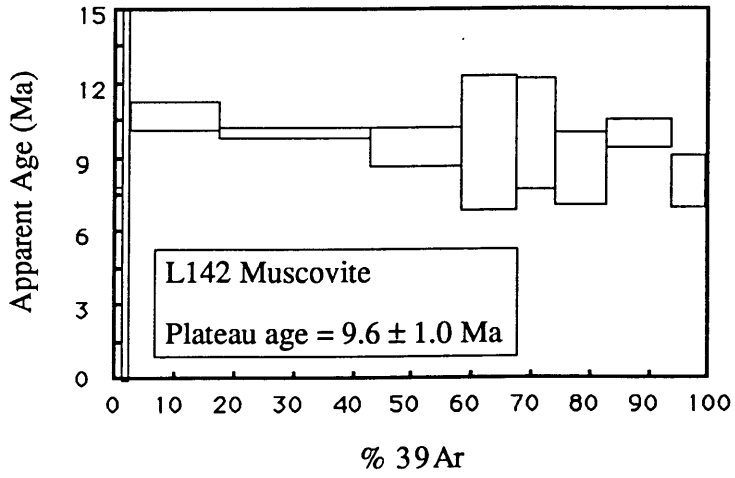
Apparent Age (Ma)
15
12
9
6
3
0
L142 Muscovite
Plateau age = 9.6 ± 1.0 Ma
0
10
20
30
40
50
60
70
80
90
100
% 39Ar

Figure 5

o.

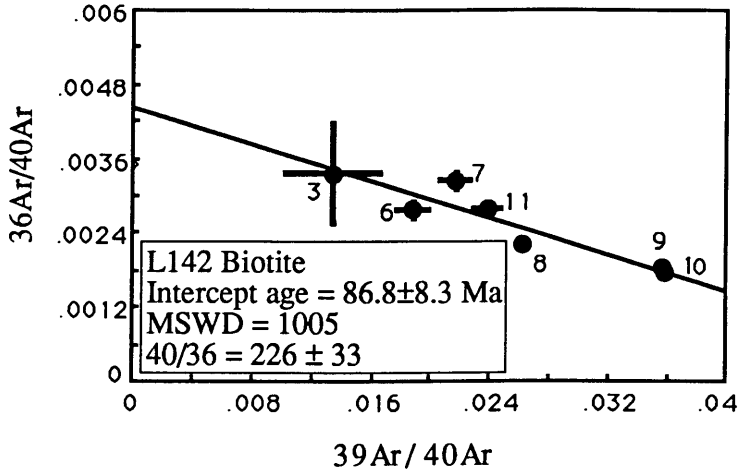
.006
.0048
.0036
.0024
.0012
0
36Ar/40Ar
3
6
7
11
8
9
10
L142 Biotite
Intercept age = 86.8±8.3 Ma
MSWD = 1005
40/36 = 226 ± 33
0
.008
.016
.024
.032
.04
39Ar/40Ar

p.

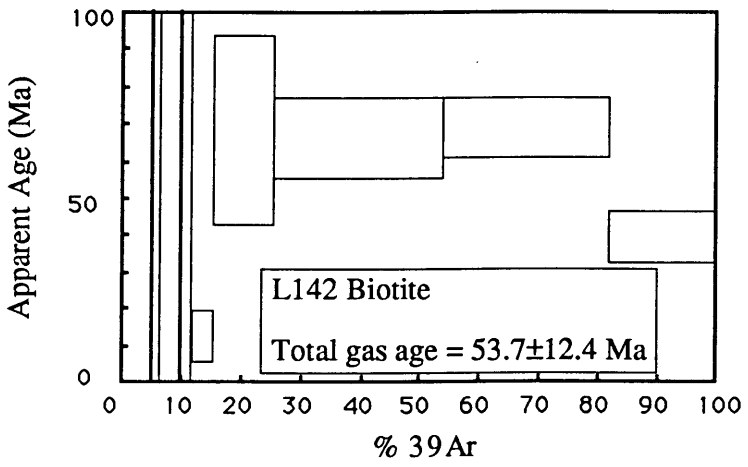
100
50
0
Apparent Age (Ma)
L142 Biotite
Total gas age = 53.7±12.4 Ma
0
10
20
30
40
50
60
70
80
90
100
% 39Ar

Figure 5

q.

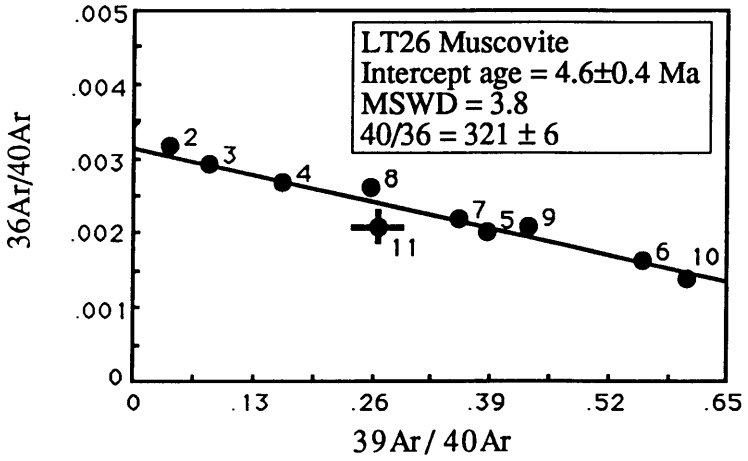
LT26 Muscovite
Intercept age = 4.6±0.4 Ma
MSWD = 3.8
40/36 = 321 ± 6
36Ar/40Ar
.005
.004
.003
.002
.001
0
2
3
4
8
11
7
5
9
6
10
0
.13
.26
.39
.52
.65
39Ar/40Ar

r.

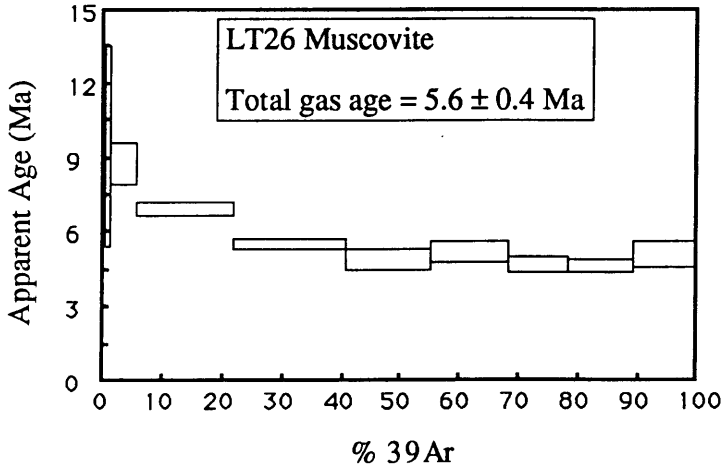
LT26 Muscovite
Total gas age = 5.6 ± 0.4 Ma
Apparent Age (Ma)
15
12
9
6
3
0
0
10
20
30
40
50
60
70
80
90
100
% 39Ar

Figure 5

s.

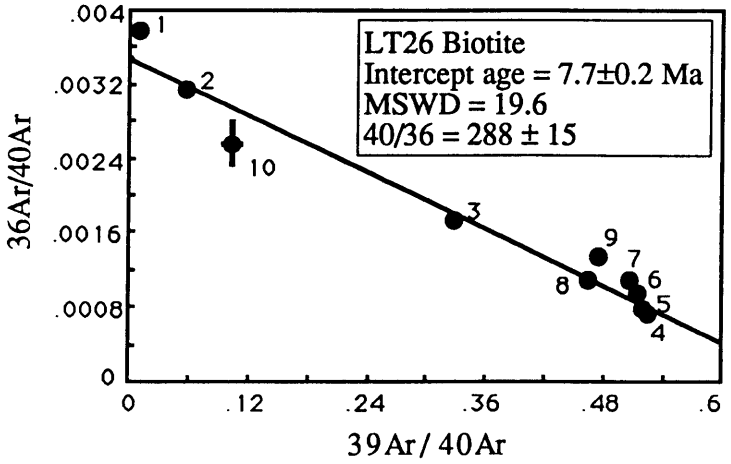
LT26 Biotite
Intercept age = 7.7±0.2 Ma
MSWD = 19.6
40/36 = 288 ± 15
36Ar/40Ar
39Ar/40Ar
.004
.0032
.0024
.0016
.0008
0
.12
.24
.36
.48
.6
1
2
10
3
9
7
8
6
5
4

t.

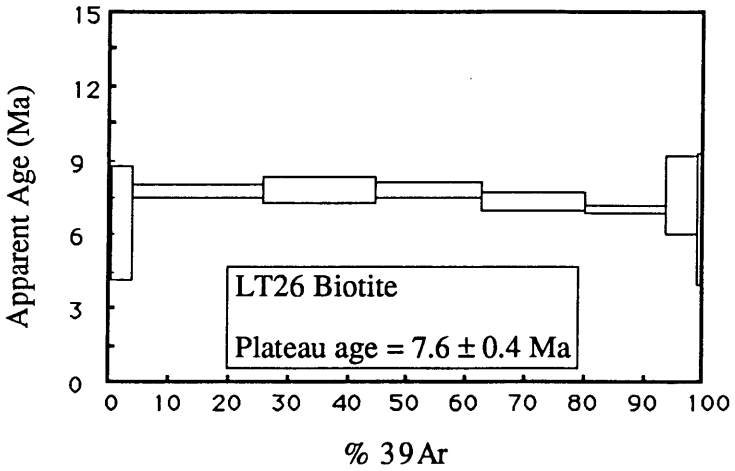
Apparent Age (Ma)
% 39Ar
LT26 Biotite
Plateau age = 7.6 ± 0.4 Ma
15
12
9
6
3
0
0 10 20 30 40 50 60 70 80 90 100

Figure 5

u.

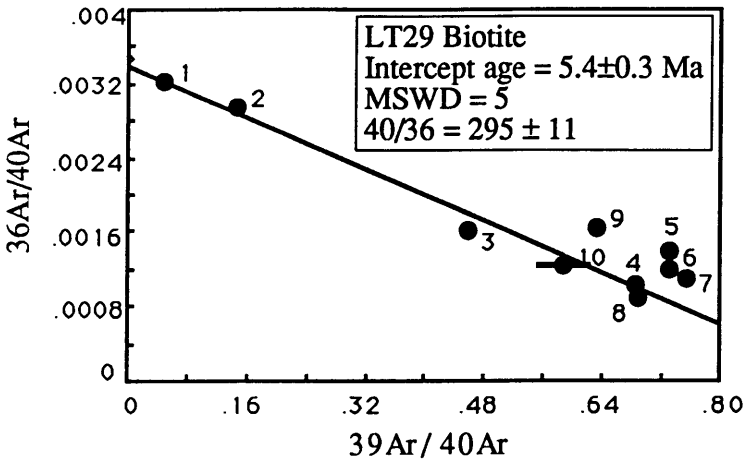
LT29 Biotite
Intercept age = 5.4±0.3 Ma
MSWD = 5
40/36 = 295 ± 11
36Ar/40Ar
.004
.0032
.0024
.0016
.0008
0
0
.16
.32
.48
.64
.80
39Ar/40Ar
1
2
3
4
5
6
7
8
9
10

v.

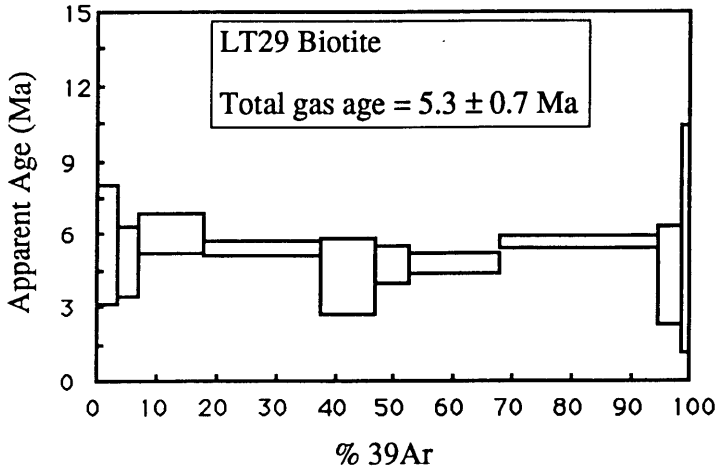
LT29 Biotite
Total gas age = 5.3 ± 0.7 Ma
Apparent Age (Ma)
15
12
9
6
3
0
0
10
20
30
40
50
60
70
80
90
100
% 39Ar

Figure 5

w.

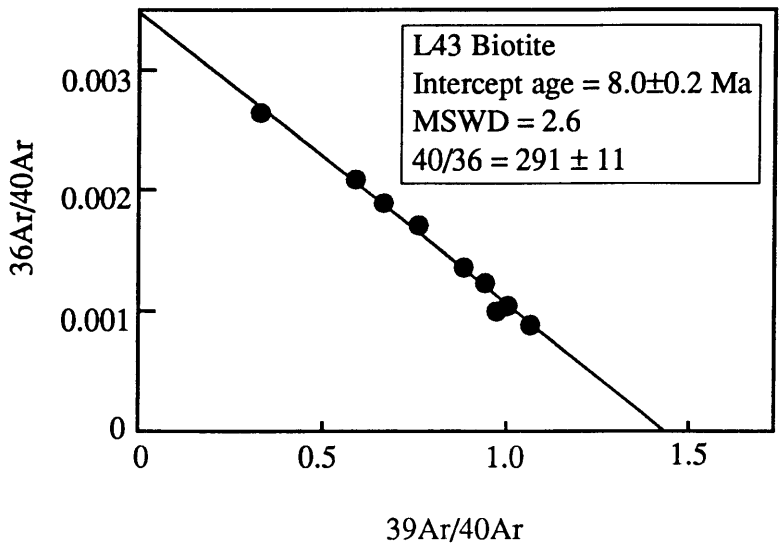
L43 Biotite
Intercept age = 8.0±0.2 Ma
MSWD = 2.6
40/36 = 291 ± 11
36Ar/40Ar
0.003
0.002
0.001
0
0
0.5
1.0
1.5
39Ar/40Ar

x.

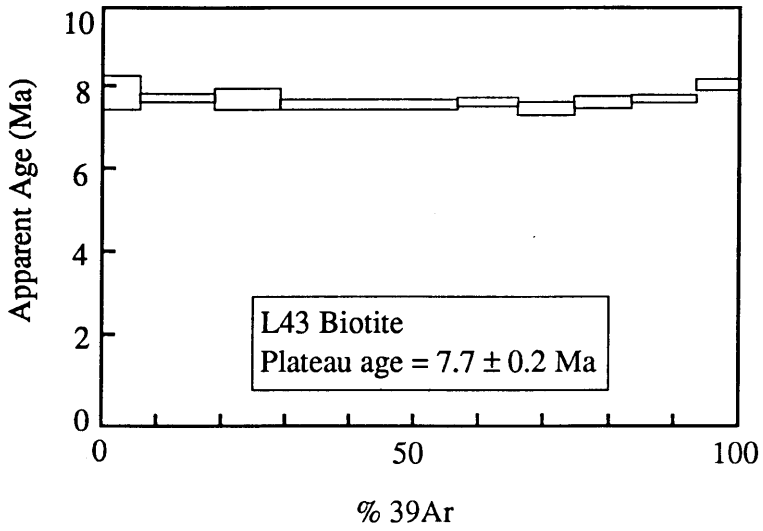
Apparent Age (Ma)
10
8
6
4
2
0
L43 Biotite
Plateau age = 7.7 ± 0.2 Ma
0
50
100
% 39Ar

Figure 5

y.

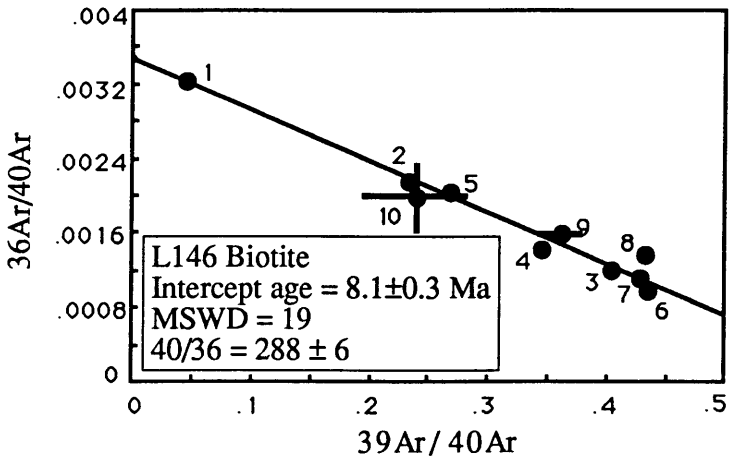
.004
.0032
.0024
.0016
.0008
0
36Ar/40Ar
1
2
5
10
9
8
4
3
7
6
L146 Biotite
Intercept age = 8.1±0.3 Ma
MSWD = 19
40/36 = 288 ± 6
0
.1
.2
.3
.4
.5
39Ar/ 40Ar

z.

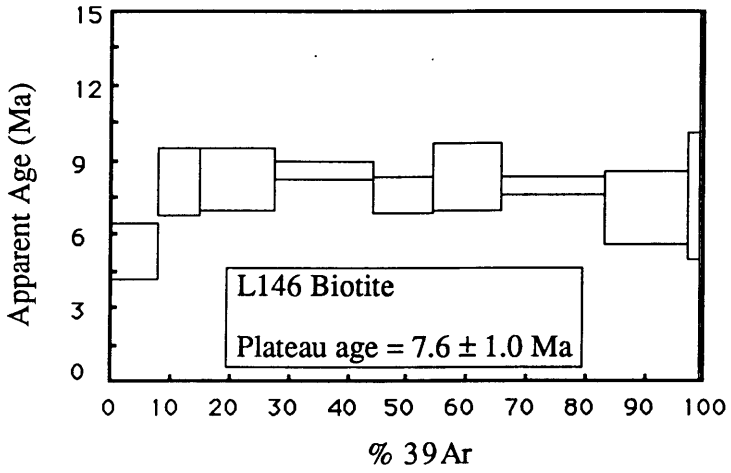
15
12
9
6
3
0
Apparent Age (Ma)
L146 Biotite
Plateau age = 7.6 ± 1.0 Ma
0 10 20 30 40 50 60 70 80 90 100
% 39Ar

Figure 5

aa.

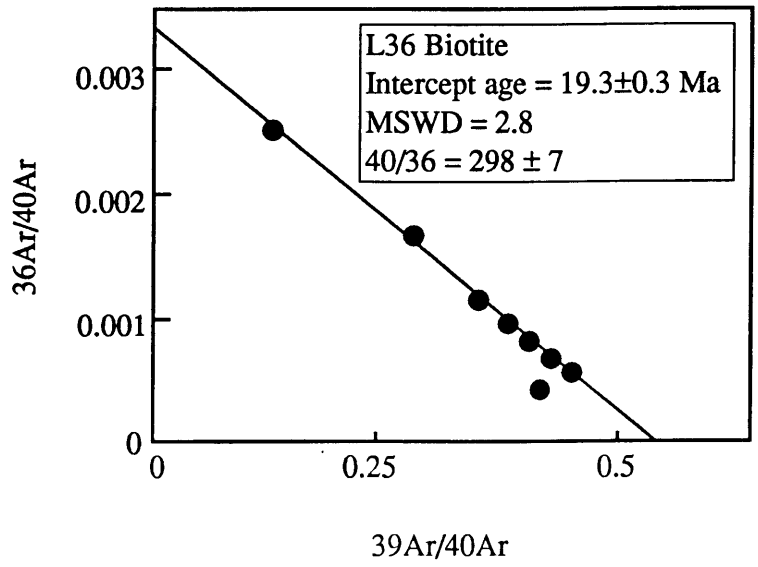

bb.

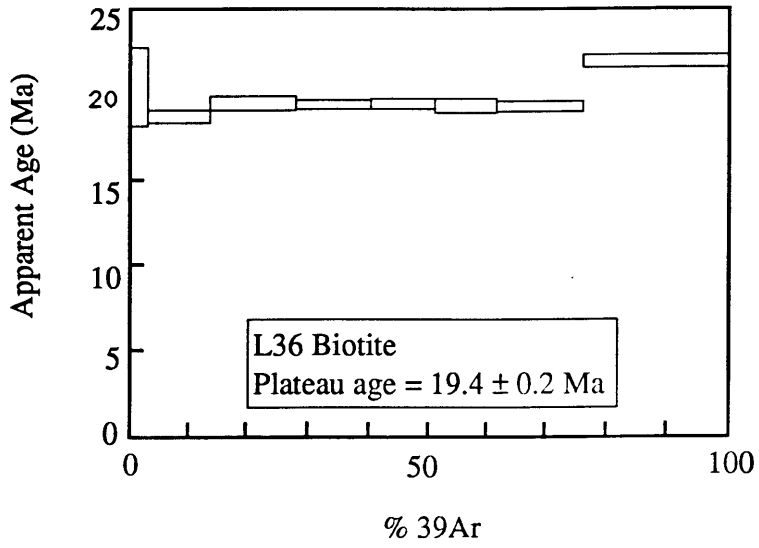

Figure 5

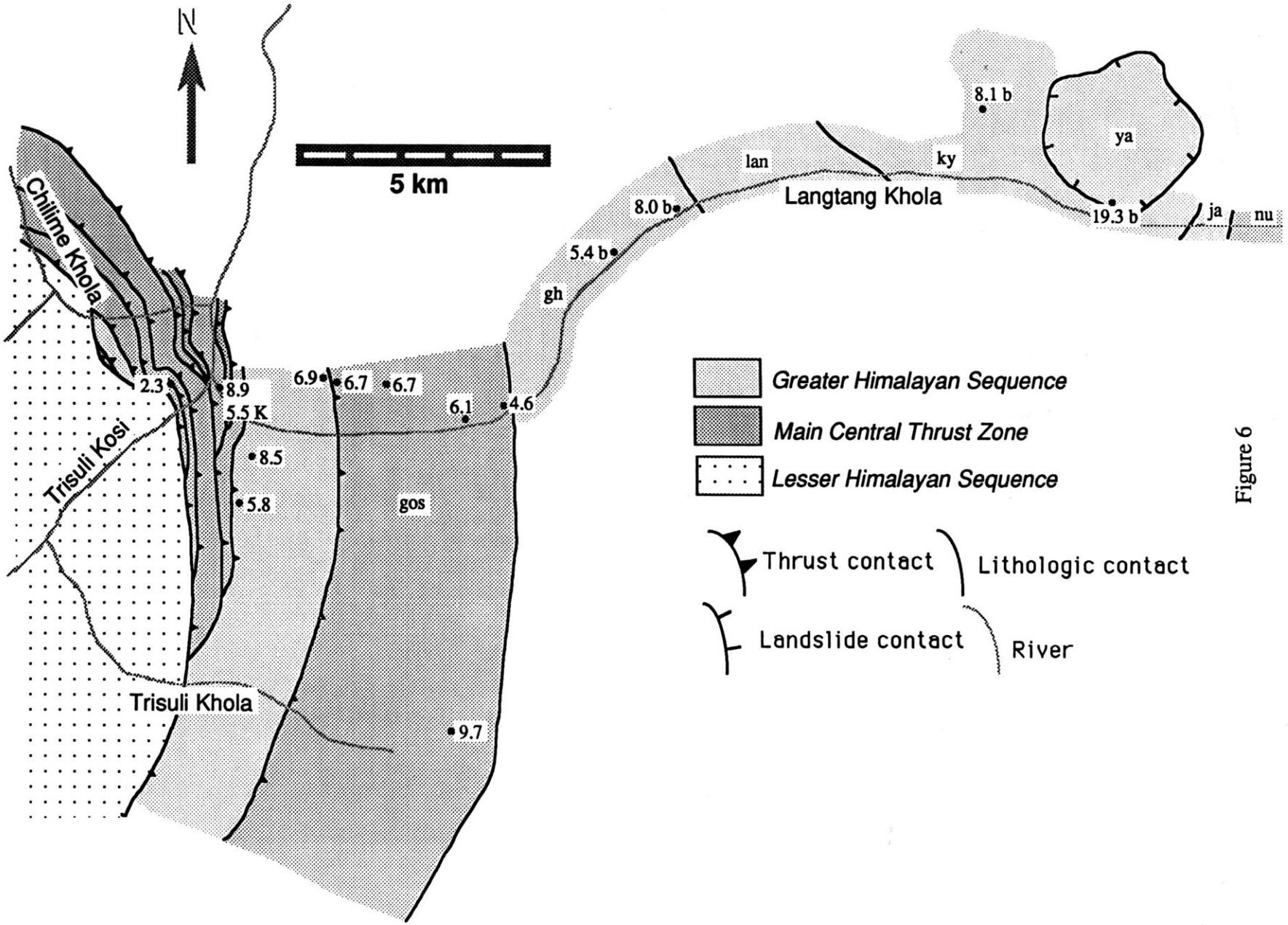
N
5 km
Chilime Khola
Trisuli Kosi
Trisuli Khola
Langtang Khola
2.3
8.9
5.5 K
8.5
5.8
6.9
6.7
6.7
6.1
4.6
5.4 b
8.0 b
8.1 b
19.3 b
lan
ky
ya
ja
nu
gh
gos
9.7
Greater Himalayan Sequence
Main Central Thrust Zone
Lesser Himalayan Sequence
Thrust contact
Lithologic contact
Landslide contact
River

Figure 6

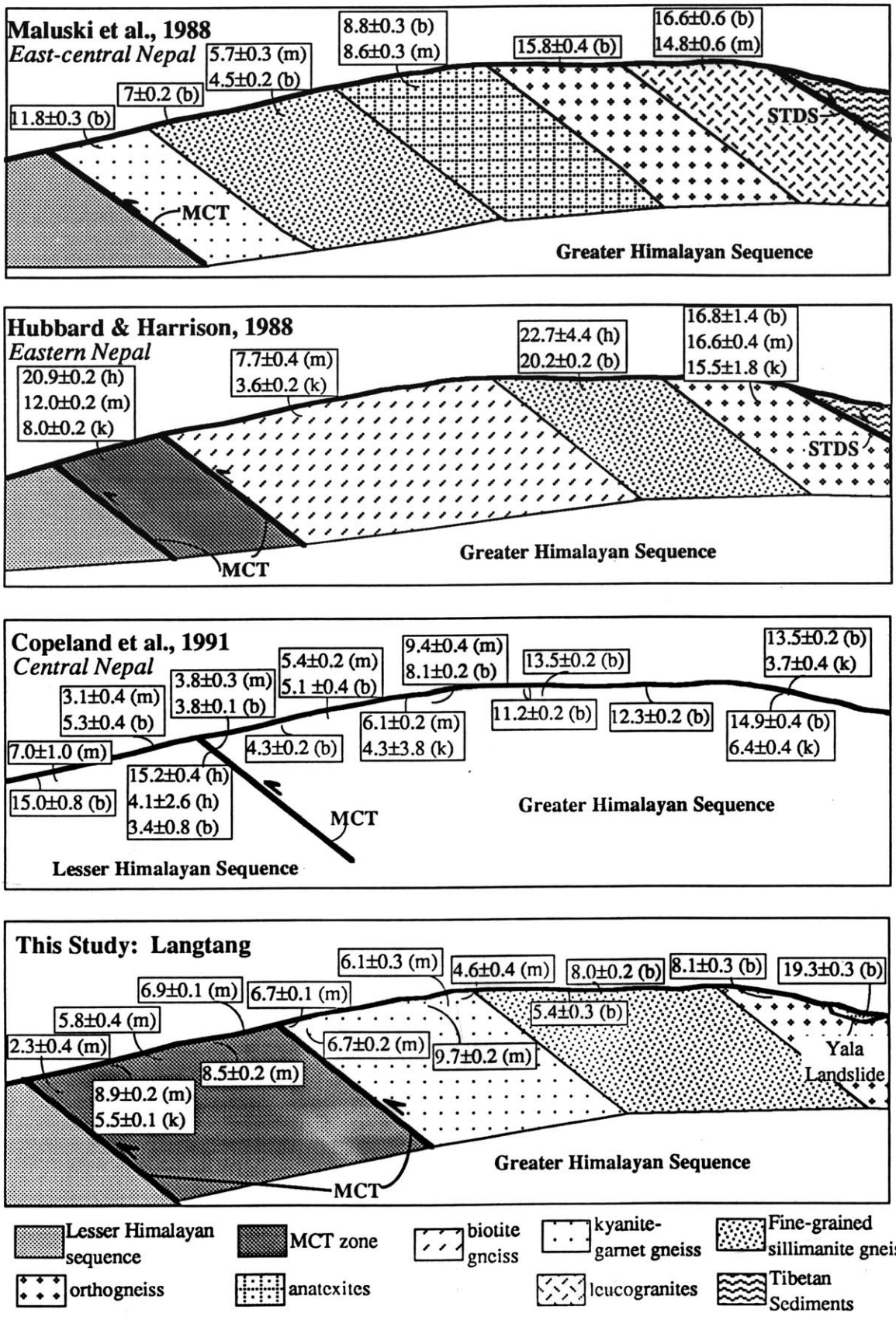
Maluski et al., 1988
East-central Nepal
5.7±0.3 (m)
4.5±0.2 (b)
7±0.2 (b)
11.8±0.3 (b)
8.8±0.3 (b)
8.6±0.3 (m)
15.8±0.4 (b)
16.6±0.6 (b)
14.8±0.6 (m)
STDS
MCT
Greater Himalayan Sequence
Hubbard & Harrison, 1988
Eastern Nepal
20.9±0.2 (h)
12.0±0.2 (m)
8.0±0.2 (k)
7.7±0.4 (m)
3.6±0.2 (k)
22.7±4.4 (h)
20.2±0.2 (b)
16.8±1.4 (b)
16.6±0.4 (m)
15.5±1.8 (k)
STDS
MCT
Greater Himalayan Sequence
Copeland et al., 1991
Central Nepal
3.1±0.4 (m)
5.3±0.4 (b)
3.8±0.3 (m)
3.8±0.1 (b)
5.4±0.2 (m)
5.1 ±0.4 (b)
9.4±0.4 (m)
8.1±0.2 (b)
13.5±0.2 (b)
13.5±0.2 (b)
3.7±0.4 (k)
11.2±0.2 (b)
12.3±0.2 (b)
14.9±0.4 (b)
6.4±0.4 (k)
6.1±0.2 (m)
4.3±3.8 (k)
4.3±0.2 (b)
7.0±1.0 (m)
15.0±0.8 (b)
15.2±0.4 (h)
4.1±2.6 (h)
3.4±0.8 (b)
MCT
Greater Himalayan Sequence
Lesser Himalayan Sequence
This Study: Langtang
6.1±0.3 (m)
4.6±0.4 (m)
8.0±0.2 (b)
8.1±0.3 (b)
19.3±0.3 (b)
6.9±0.1 (m)
6.7±0.1 (m)
5.8±0.4 (m)
5.4±0.3 (b)
2.3±0.4 (m)
6.7±0.2 (m)
9.7±0.2 (m)
Yala
Landslide
8.5±0.2 (m)
8.9±0.2 (m)
5.5±0.1 (k)
Greater Himalayan Sequence
MCT
Lesser Himalayan sequence
orthogneiss
MCT zone
anatexites
biotite gneiss
kyanite-garnet gneiss
leucogranites
Fine-grained sillimanite gneiss
Tibetan Sediments

Figure 7

REFERENCES

Armstrong, R.L. and J. Suppe, 1973. K-Ar geochronometry of Mesozoic igneous rocks in Nevada, Utah and southern California. *G.S.A. Bulletin*, **84**, 1375-1392.

Bordet, P., 1961. *Recherches geologiques dans l'Himalaya du Nepal, region du Makalu.* Centre Nationale Recherche Scientifique, Paris, 275p.

Bouchez, J. L. and A. Pêcher, 1976. Microstructures and quartz preferred orientations in quartzites of the Annapurna area (Central Nepal), in the proximity of the Main Central Thrust. *Himalayan Geology*, **6**, 118-132.

Boyer, S. and D. Elliott, 1982. Thrust Systems. *American Association of Petroleum Geologists Bulletin*, **66**, 1196-1230.

Brun, J.P., J.P. Burg, and C.G. Ming, 1985. Strain trajectories above the Main Central Thrust (Himalaya) in southern Tibet. *Nature*, **313**, 388-390.

Brunel, M., 1975. La nappe du Mahabharat, Himalaya du Nepal central. *D.Sc.*, C.R. Acad. Sci., Paris.

Brunel, M., 1986. Ductile thrusting in the Himalayas: Shear sense criteria and stretching lineations. *Tectonics,* **5**, 247-265.

Brunel, M., 1989. Comment on "Possible thermal buffering by crustal anatexis in collisional orogens: Thermobarometric evidence from the Nepalese Himalaya". *Geology*, **17**, 573-575.

Brunel, M. and J. R. Kienast, 1986. Etude petro-structurale des chevauchements ductiles himalayens sur la transversale de l'Everst-Makalu (Nepal oriental). *Canadien Journal of Earth Sciences*, **23**, 1117-1137.

Burchfiel, B. C. and L. Royden, 1985. North-south extension within the convergent Himalayan region. *Geology*, **13**, 679-682.

Burchfiel, B. C., C. Zhiliang, K. V. Hodges, L. Yuping, L. H. Royden, D. Changrong and X. Jiene, 1992. The South Tibetan detachment system, Himalayan orogen:

Extension contemporaneous with and parallel to shortening in a collisional mountain belt. *Geologic Society of America Special Paper*,.no. **269**.

Burg, J. P., M. Brunel, D. Gapais, G. M. Chen and G. H. Liu, 1984. Deformation of leucogranites of the crystalline Main Central Sheet in southern Tibet (China). *Journal of Structural Geology*, **6**, 535-542.

Burg, J.P. and G.M. Chen, 1984. Tectonics and structural zonation of southern Tibet, China. *Nature*, **311**, 219.

Caby, R., A. Pêcher and P. Le Fort, 1983. Le M.C.T. Himalayen: nouvelles donnees sur la metamorphisme inverse a la base de la Dalle du Tibet. *Revue de Geographie Physique et de Geologie Dynamique*, **24**, 89-100.

Cebula, G.T., M.J. Kunk, H.H. Mehnert, C.W. Naeser, J.D. Obradovich, and J.F. Sutter, 1986. The Fish Canyon tuff, a potential standard for the 40Ar/39Ar and fission track methods [abstr]. *Terra Cognita*, **6**, 139-140.

Chamberlain, C.P.and Leslie J. Sonder, 1990. Heat-producing elements and the thermal and baric patterns of metamorphic belts. *Science*, **250**, 763-769.

Colchen, M., P. Le Fort and A. Pêcher, 1981. Geologic map of Annapurna-Manaslu-Ganesh Himal, Nepal Himalaya; scale 1:2000000. In *Zagros-Hindu Kush-Himalaya geodynamic evolution* (ed. Gupta and Delany), American Geophysical Union, Geodynamic Series, 136p.

Colchen, M., P. Le Fort and A. Pêcher, 1986. *Notice explicative de la carte geologique Annapurna-Manaslu-Ganesh (Himalaya du Nepal) au 1/2000.000*: (bilingue: francais-english). Centre National de Resecherches Scientifiques, Paris, 136p.

Copeland, P., T.M. Harrison, R. Parrish, B.C. Burchfiel, K.V. Hodges and W.S.F. Kidd, 1987. Constraints on the age of normal faulting, north face of Mt. Everest: Implications for Oligo-Miocene uplift. *Eos*, **68**, 1444.

Copeland, P., R. Parrish and T.M. Harrison, 1988. Identification of inherited radiogenic Pb in monazite and its implications for U-Pb systematics. *Nature,* **333**, 760-763.

Copeland, P., T.M. Harrison, K.V. Hodges, P. Mauejol, P. Le Fort, and A. Pêcher, 1991. An early Pliocene thermal disturbance of the Main Central Thrust, central Nepal: Implications for Himalayan tectonics. *Journal of Geophysical Research*, **96**, no. B5, 8475-8500.

Cuney, M., P. Le Fort, and W. Zhixiang, 1984. Uranium and Thorium geochemistry and mineralogy in the Manaslu Leucogranite (Nepal, Himalaya). *Conference Uranium and Thorium geochemistry and mineralogy in the Manaslu Leucogranite (Nepal, Himalaya)*, Beijing. 853-873.

Cuney, M., P. Sabate, P. Vidal, M.M. Marinho, and H. Conceicao, 1990. The 2 Ga peraluminous magmatism of the Jacobina - Contendas Mirante Belt (Bahia) Brazil: Major and trace-element geochemistry and metallogenic potential. *Journal of Volcanology and Geothermal Research*, **44**, 123-141.

Dalrymple, R.D. and M.A. Lanphere, 1969. *Potassium-argon dating*. W.H. Freeman, San Francisco, 258p.

Deniel, C., 1985. Apport des isotopes du Sr, du Nd et du Pb a la connaissance de l'age et de l'origine des leucogranites himalayens. Exemple du Manaslu (Himalaya, Nepal). *DSc*, University of Clermont-Ferrand.

Deniel, C., P.F. Vidal, A. Fernandez, P. Le Fort and J.-J. Peucat, 1987. Isotopic study of the Manaslu granite (Himalaya, Nepal): inferences on the age and source of the Himalayan leucogranites. *Contributions to Mineralogy and Petrology*, **96**, 78-92.

England, P.C. and A.B. Thompson, 1984. Pressure-temperature-time paths of regional metamorphism I. Heat transfer during the evolution of regions of thickened continental crust. *Journal of Petrology*, **25**, 894-928.

England, P., P. Le Fort, P. Molnar, and A. Pêcher, 1992. Heat sources for Tertiary metamorphism and anatexis in the Annapurna-Manaslu region central Nepal. *Journal of Geophysical Research*, **97**, 2107-2128.

Ferry, J. M. and F. S. Spear, 1978. Experimental calibration of the partitioning of Fe and Mg between garnet and biotite. *Contributions to Mineralogy and Petrology*, **66**, 113-117.

Fleck, R.D., J.F. Sutter, and D. Elliot, 1977. Interpretation of discordant $^{40}Ar/^{39}Ar$ age spectra of Mesozoic tholeiites from Antarctica. *Geochimica Cosmochimica Acta*, **41**, 15-32.

France-Lanord, C. and P. Le Fort, 1988. Crustal melting and granite genesis during the Himalayan collision orogenesis. *Transactions of the Royal Society of Edinburgh: Earth Sciences*, **79**, 183-195.

Gansser, A., 1964. *Geology of the Himalayas*. Interscience Publishers, London, 289 p.

Gansser, A., 1966. The Indian Ocean and the Himalaya: A geologic interpretation. *Ecologae Geologicae Helveticae*, **59**, 832-848.

Ghent, E. D. and M. Z. Stout, 1981. Geobarometry and geothermometry of plagioclase - biotite - garnet - muscovite assemblages. *Contributions to Mineralogy and Petrology*, **76**, 92-97.

Ghent, E. D., 1976. Plagioclase - garnet - Al_2SiO_5 - quartz: A potential geobarometer - geothermometer. *American Mineralogist*, **61**, 710-714.

Hagen, T., 1969. Report on the geological survey of Nepal. *Denkschr. Schweiz. Naturf. Gesell.*, **86**, 185p.

Harrison, T.M., I. Duncan, and I. McDougall, 1985. Diffusion of ^{40}Ar in biotite: Temperature, pressure and compositional effects. *Geochimica Cosmochimica Acta*, **49**, 2461-2468.

Heim, A. and A. Gansser, 1939. *Central Himalaya: Geologic observations of the Swiss expedition, 1936*. Mem. Soc. Helv. Sci. Nat., Zurich, 245p.

Herren, E., 1987. Zanskar shear zone: northeast-southwest extension within the Higher Himalayas (Ladakh, India). *Geology*, **15**, 409-413.

Heuberger, H., L. Masch, E. Preuss, and A. Schröcker, 1984. Quarternary landslides and rock fusion in central Nepal and in the Tyrolean Alps. *Mountain Research and Development*, **4**, 345-362.

Hodges, K. V. and L. Royden, 1984. Geologic thermobarometry of retrograded metamorphic rocks: An indication of the uplift trajectory of a portion of the northern Scandinavian Caledonides. *Journal of Geophysical Research*, **89**, 7077-7090.

Hodges, K. V. and P. D. Crowley, 1985. Error estimation and empirical geothermobarometry for pelitic systems. *American Mineralogist*, **70**, 702-709.

Hodges, K. V. and L. W. McKenna, 1987. Realistic propagation of uncertainties in geologic thermobarometry. *American Mineralogist*, **72**, 673-682.

Hodges, K. V. and D. S. Silverberg, 1988. Thermal evolution of the Greater Himalaya, Garwhal, India. *Tectonics*, **7**, 583-600.

Hodges, K. V., M. S. Hubbard and D. S. Silverberg, 1988. Metamorphic constraints on the thermal evolution of the central Himalayan orogen. *Philosophical Transactions of the Royal Society of London*, **A326**, 257-280.

Hodges, K. V., P. Le Fort and A. Pêcher, 1988. Possible thermal buffering by crustal anatexis in collisional orogens: thermobarometric evidence from the Nepalese Himalaya. *Geology*, **16**, 707-710.

Hodges, K. V., P. Le Fort and A. Pêcher, 1989. Reply to comment on "Possible thermal buffering by crustal anatexis in collisional orogens: Thermobarometric evidence from the Nepalese Himalaya". *Geology*, **17**, 575-576.

Hubbard, M. S. and T. M. Harrison, 1989. $^{40}Ar/^{39}Ar$ constraints on deformation and metamorphism in the Main Central Thrust zone and Tibetan Slab, eastern Nepal Himalaya. *Tectonics*, **8**, 865-880.

Hubbard, M. S., 1988. Thermobarometry, 40Ar/39Ar geochronology, and structure of the Main Central Thrust zone and Tibetan Slab, eastern Nepal Himalaya. *Ph.D.*, M.I.T.

Hubbard, M. S., 1988, Thermobarometry, $^{40}Ar/^{39}Ar$ geochronology, and structure of the Main Central Thrust zone and Tibetan Slab, eastern Nepal Himalaya [Ph.D. thesis]: Massachusetts Institute of Technology, 169 p.

Hubbard, M. S., 1989. Thermobarometric constraints on the thermal history of the Main Central Thrust Zone and Tibetan Slab, eastern Nepal Himalaya. *Journal of Metamorphic Geology*, **7**, 19-30.

Hubbard, M. S., 1989. Thermobarometric constraints on the thermal history of the Main Central Thrust Zone and Tibetan Slab, eastern Nepal Himalaya. *Journal of metamorphic Geology*, **7**, 19-30.

Hyndman, D.W., 1985. *Petrology of Igneous and Metamorphic Rocks*. McGraw-Hill Book Company, New York, 786p.

Inger, S., 1991. Metamorphism and granite genesis in the Langtang region, north-central Nepal. *PhD*, The Open University.

Jackson, S.E., B.J. Fryer, W. Gosse, H.P. Healey, H.P. Longerich and D.F. Strong, 1990. Determination of the precious metals in geological materials by inductively coupled plasma-mass spectrometry (ICP-MS) with nickel sulphide fire-assay collection and tellurium coprecipitation. *Chemical Geology*, **83**, 119-132.

Jarvis, K.E., 1990. A critical evaluation of two sample preparation techniques for low-level determination of some geologically incompatible elements by inductively coupled plasma-mass spectrometry. *Chemical Geology*, **83**, 89-103.

Jaupart, C. and A. Provost, 1985. Heat focussing, granite genesis and inverted metamorphic gradients in continental collision zones. *Earth and Planetary Science Letters*, **73**, 385-397.

Kelley, S., 1988. The relationship between K-Ar mineral ages, mica grain sizes and movement on the Moine Thrust Zone, NW Highlands, Scotland. *Journal*, **143**, 1-10.

Le Breton, N. and A. B. Thompson, 1988. Fluid-absent (dehydration) melting of biotite in pelites in the early stages of crustal anatexis. *Contributions to Mineralogy and Petrology*, **99**, 226-237.

Le Fort, P., 1975. Himalaya: the collided range. Present knowledge of the continental arc. *American Journal of Science*, **275A**, 1-44.

Le Fort, P., 1981. Manaslu leucogranite: a collision signature of the Himalaya, a model for its genesis and emplacement. *Journal of Geophysical Research*, **86**, 10545-10568.

Le Fort, P., 1986. Metamorphism and magmatism during the Himalayan collision. In *Collision Tectonics* (ed. M. P. Coward and A. C. Ries), Geological Society, 159-172.

Le Fort, P., 1988. Granites in the tectonic evolution of the Himalaya, Karakorum and southern Tibet. *Philosophical Transactions of the Royal Society of London*, **A 326**, 281-299.

Lombard, A., 1953. Les grandes lignes de la Geologie du Nepal oriental. *Bull. Soc. Belge Geol. Pal. Hydr.*, **41**, 260-264.

Lombard, A., 1958. Un intineraire geologique dans l'Est du Nepal (massif du Mont Everest). *Memoires de la Societe Helvetique Sciences Naturelles*, **82**, 107p.

Lux, D.R., 1986. 40Ar/39Ar ages for minerals from the amphibolite dynamothermal aureole, Mont Albert, Gaspe, Quebec. *Canadian Journal of Earth Sciences*, **23**, 21-26.

Lyon-Caen, H. and P. Molnar, 1983. Constraints on the structure of the Himalaya from an analysis of gravity anomolies and a flexural model of the lithosphere. *Journal of Geophysical Research*, **88**, 8171-8191.

Macfarlane, A.M., 1992, The tectonic evolution of the core of the Himalaya, Langtang National Park, Nepal [abstr.]: for the 7th Himalaya - Karakorum - Tibet Workshop, Oxford, England, April, 1992.

Macfarlane, A.M., in preparation. A petrologic examination of the metamorphic core of the Himalayan orogen, Langtang National Park, Nepal.

Macfarlane, A.M., K.V. Hodges and D. Lux, in press. A structural analysis of the Main Central Thrust zone, Langtang National Park, central Nepal Himalaya. *Geological Society of America Bulletin.*

Mallet, F.R., 1875. On the geology and mineral resources of the Darjiling District and Western Duars. *India Geologic Survey Memoirs* **11**, 1-50.

Maluski, H., Matte, Philippe, Brunel, Maurice and Xusheng Xiao, 1988. Argon 39-Argon 40 dating of metamorphic and plutonic events in the north and high Himalaya belts (southern Tibet - China). *Tectonics*, **7**, 299-326.

Marshak, S. and G. Mitra, 1988. *Basic Methods of Structural Geology*. Englewood Cliffs, NJ, Prentice Hall, 446 p.

Maruo, Y., B. M. Pradhan and K. Kizaki, 1979. Geology of eastern Nepal: between Dudh Kosi and Arun. *Bulletin of the College of Science*, University of Ryukus, **28**, 155-191.

Maruo, Y. and K. Kizaki, 1981. Structure and metamorphism in eastern Nepal, In *Metamorphic Tectonites of the Himalaya*, P. S. Saklani, ed. Today and Tomorrow's Printers & Publishers, New Dehli, 175-230.

Masch, L., 1974. Neue Untersuchung an einem Beispiel von Aufschmelzung auf euner Verschiebungsflache im Langtang Himal, Nepal. *Neues Jahrbuch Mineralogie Monatsch.*, **52**, 66-67.

Massey, J.A., N.B.W. Harris, R.S. Harmon and S Reddy., 1992. Thermal evolution and fluid movement in the High Himalayan crystallines, Langtang valley, central Nepal [abstr.]. Oxford, England, April, 1992.

McDougall, I. and T.M. Harrison, 1988. *Geochronology and Thermochronology by the $^{40}Ar/^{39}Ar$ Method.* Oxford University Press, New York, 208p.

McKenna, L. W. and K. V. Hodges, 1988. Accuracy versus precision in locating reaction boundaries: Implications for the garnet - plagioclase - aluminum silicate - quartz geobarometer. *American Mineralogist*, **73**, 1205-1208.

Molnar, P., 1984. Structure and tectonics of the Himalaya: constraints and implications from geophysical data. *Annual review of Earth Planetary Science*, **12**, 489-518.

Molnar, P. and P. Tapponnier, 1975. Cenozoic tectonics of Asia: effects of a continental collision. *Science*, **183**, 419-426.

Molnar, P. and P. England, 1990. Temperatures, heat flux, and frictional stress near major thrust faults. *Journal of Geophysical Research*, **95**, 4833-4856.

Oldham, R. D., 1883. Notes on a traverse between Almora and Mussooree in October 1882. *Geologic Survey of India Reconnaissance*, **16**, 162-164.

Parrish, R.R., Carr, S.D. and Parkinson, D.L., 1988. Eocene extensional tectonics and geochronology of the southern Omineca Belt, British Columbia and Washington. *Tectonics*, **7**, 181-212.

Parrish, R. R., K.V. Hodges and A.M. Macfarlane, 1992. U-Pb geochronology of igneous and metamorphic rocks near the Main Central Thrust in the Langtang area, central Nepal Himalaya [abstr]. 7th Annual Himalayan-Karakorum-Tibet Workshop, Oxford, England, April, 1992.

Pêcher, A., 1977. Geology of the Nepal Himalaya: deformation and petrography in the Main Central Thrust zone [abstr.]: Colloq. int. 268, *Ecologie et geologie de l'Himalaya*, Paris, 301-318.

Pêcher, A., 1978. Deformations et metamorphisme associes a une zone de cisaillement: Exemple du grand chevauchement central Himalayen (MCT). *D.Sc.*, Grenoble.

Pêcher, A., 1989. The metamorphism in the Central Himalaya. *Journal of Metamorphic Geology*, **7**, 31-41.

Pichavant, M., 1987. The effects of B and H_2O on liquidus phase relations in the haplogranite system at 1 kbar. *American Mineralogist*, **72**, 1056-1070.

Pêcher, A. and P. Le Fort, 1986. The metamorphism in central Himalaya, its relation with the thrust tectonic. *Sciences de la Terre*, **47**, 285-309.

Pinet, C. and C. Jaupart, 1987. A thermal model for the distribution in space and time of the Himalayan granites. *Earth and Planetary Science Letters*, **84**, 87-99.

Pinet, C. and C. Jaupart, 1987. The vertical distribution of radiogenic heat production in the Precambrian crust of Norway and Sweden: Geothermal implications. *Earth and Planetary Sciences,* **14**, 260-263.

Reddy, S., M. Searle and J. Massey, 1992. Structural evolution of the High Himalayan Crystalline sequence of the Langtang Valley, Nepal [abstr]. Himalaya-Karakorum-Tibet Conference, Oxford, England, April, 1992.

Robbins, G.A., 1972. Radiogenic argon diffusion in muscovite under hydrothermal conditions. *M.Sc.*, Brown University.

Roddick, J.C., Cliff, R.A. and Rex, D.C., 1980. The evolution of excess argon in alpine biotites - a $^{40}Ar/^{39}Ar$ analysis. *Earth and Planetary Science Letters*, **48**, 945-960.

Royden, L. H. and B. C. Burchfiel, 1987. Thin-skinned N-S extension within the convergent Himalayan region: gravitational collapse of a Miocene topographic front. In: *Continental Extensional Tectonics*, M.P. Coward, J.F. Dewey and P.L. Hancock, editors, Geological Society Special Publication, **28**, 611-619.

Samson, S.D.and. E.C. Alexander Jr., 1987. Calibration of the interlaboratory 40Ar/39Ar dating standard, MMhb-1. *Geochimica Cosmochimica Acta,* **66**, 27-34.

Scaillet, B., C. France-Lanord and P. Le Fort, 1990. Badrinath - Gangotri plutons (Garhwal, India): petrological and geochemical evidence for fractionation

processes in a high Himalayan leucogranite. *Journal of Volcanology and Geothermal Research*, **44**, 163-188.

Schärer, U., 1984. The effect of initial 230Th disequilibrium on young U-Pb ages: the Makalu case, Himalaya. *Earth and Planetary Science Letters*, **67**, 191-204.

Schärer, U., R. Xu and C. Allègre, 1986. U-(Th)-Pb systematics and ages of Himalayan leucogranites, South Tibet. *Earth and Planetary Science Letters*, **77**, p. 35-48.

Schärer, U., P. Copeland, T.M. Harrison and M.P. Searle, 1990. Age, cooling history and origin of post-collisional leucogranites in the Karakorum Batholith: a multisystem isotope study. *Journal of Geology*, **98**, 233-251.

Schelling, D., 1987. The geology of the Rolwaling-Lapchi Kang Himalayas, east-central Nepal: Preliminary findings. *Journal of the Nepal Geological Society*, **4**, 1-19.

Scott, J.S.and H.I. Drever, 1953. Frictional fusion along a Himalayan thrust. *Proceedings of the Royal Society of Edinburgh*, **65 B**, 121-142.

Spear, F. S. and J. Selverstone, 1983. Quantitative P-T paths from zoned minerals: theory and tectonic applications. *Contributions to Mineralogy and Petrology*, **83**, 348-357.

Spear, F. S. and S. M. Peacock, 1989. *Metamorphic Pressure-Temperature-Time Paths*. American Geophysical Union.

Stöcklin, J., 1980. Geology of Nepal and its regional frame. *Journal of the Geological Society of London*, **137**, 1-34.

Thompson, J. B., 1957. The graphical analysis of mineral assemblages in pelitic schists. *American Mineralogist*, **42**, 842-858.

Tullis, J. and R.A. Yund, 1977. Experimental deformation of dry Westerly granite. *Journal of Geophysical Research*, **82**, 5705-5718.

Valdiya, K. S., 1979. An outline of the structural set-up of the Kumaun Himalaya. *Journal of the Geological Society of India*, **20**, 145-157.

Valdiya, K. S., 1980. *Geology of Kumaun Lesser Himalaya.* Dehra Dun, India, Wadia Institute of Himalayan Geology, 291 p.

Vidal, P., A. Cocherie and P. Le Fort, 1982. Geochemical investigations of the origin of the Manaslu leucogranite (Himalaya, Nepal). *Geochimica Cosmochimica Acta*, **46**, 2279-2292.

Vielzeuf, D.and J.R. Holloway, 1988. Experimental determination of the fluid-absent melting relations in the pelitic system. *Contributions to Mineralogy and Petrology*, **98**, 257-276.

York, D., 1969. Least squares fitting of a straight line with correlated errors. *Earth and Planetary Science Letters,* **5**, 320-324.

Zeitler, P.K., 1985. Cooling history of the northwest Himalaya, Pakistan. *Tectonics*, **4**, 127-151.

Zeitler, P.K. and J.D. Fitzgerald, 1986. Saddle-shaped $^{40}Ar/^{39}Ar$ age spectra from young, microstructurally complex potassium feldspars. *Geochimica Cosmochimica Acta*, **50**, 1185-1199.

Plate 1a

Geologic Map of Langtang National Park Central Nepal

Allison M. Macfarlane, 1992

Greater Himalayan sequence

- ya — ***Yala Landslide*** augen & granite gneiss
- nu — ***Nubama gneiss*** pyroxene gneiss
- aug — ***Augen gneiss***
- amg — ***Amphibolite gneiss***
- ja — ***Jathang foliated granite***
- ky — ***Kyangjin gneiss*** pelitic augen gneiss
- la — ***Langtang gneiss*** pelitic sillimanite "pancake" gneiss
- gt — ***Ghora Tabela gneiss*** fine-grained sillimanite-garnet gneiss
- gos — ***Gosainkund gneiss*** migmatitic pelitic gneiss

Main Central Thrust zone

- sy — ***Syabru gneiss & schist*** kyanite-garnet gneiss & schist
- ma — ***Mangol metapsammite*** garnet-bearing quartzite
- ph — ***Phulung augen gneiss*** pelitic augen gneiss
- sb — ***Syabru Bensi orthogneiss*** augen orthogneiss
- ba — ***Barabal schist & gneiss*** pelitic garnet schist
- bh — ***Bhote carbonate*** siliceous metalimestone
- tr — ***Trisuli gneiss & schist*** kyanite-garnet schist & gneiss
- ch — ***Chilime calc-schist*** calcareous graphitic schist
- gom — ***Gompagong calc-quartzite*** calcareous psammite & pelitic schist
- gol — ***Goljhong unit*** quartzite, marble, calcareous & pelitic schist
- th — ***Thangjet gneiss*** augen gneiss

Lesser Himalayan sequence

- dh — ***Dhunche schist & metapsammite*** pelitic schist, quartzite & metalimestone

- lithologic contact
- brittle fault within MCT zone
- approximate boundary of Yala landslide
- 45 — dominant schistosity
- 32 — stretching/mineral lineation

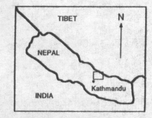

1:25000

1 km

The topographic base used for this map is the Helambu-Langtang map from the E. Schneider series. The approximate outline of the Yala landslide was taken from Heuberger et al., 1984 (Fig. 7).

85° 30'

85° 40'

Ghenge Liru

Pangsang Lekh

Morimoto Peak

Yala Peak

Tsangbu

Chh

Tarng

Langtang

Mund

Singdem

Nesapali

Patpal

Thangsep

Chamki

Ghora Tabela

Pangame Lung

Chhona

Chaldhang Gompa

Kyangchinghyang

Tharchd Pisa

Thangdemo

Tserko

Yala

Pi'ung

Pangari Goldum

Kijung Phu

Pemdang Karpu

Langsisa Kharak

Nubama Dhang

Thikyapsa

Lathang

Marku

Kingur Chin

Mendang

Branchen

La'ung

Nääkhang

Naya Kanga (Nasum Khang)

Kongja La

Gangchenpo

Syarpa

Dhokache

Chadang

Danda

Gosain Kund

Laurebina Pass

Chimisedang Lekh

Urkin Kangari

Kangjava Himal

Dhukpu Danda

Tenbathang

(Drosakhang)

Doaley Himal

Thorke

Pokhari Lo

Plate 1b

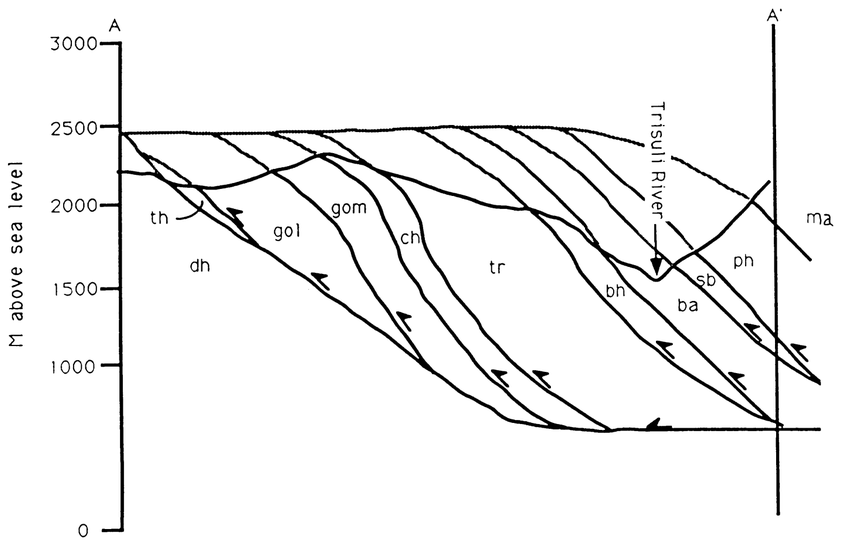

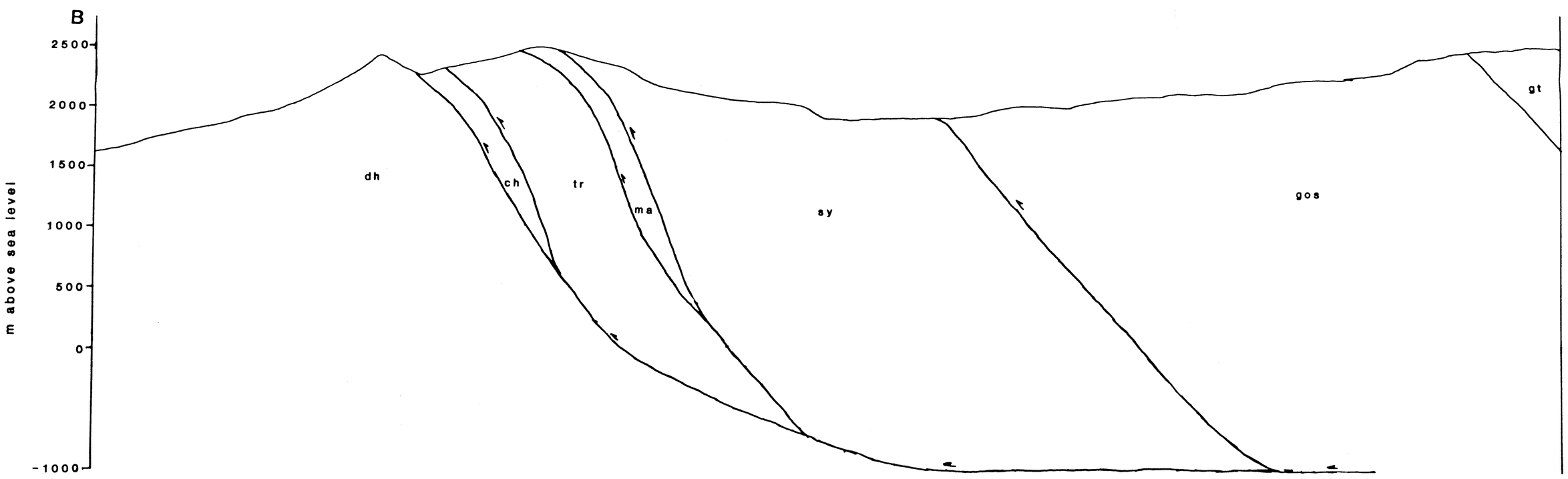

PLATE 2